



Unadkat, Ricky Ashok (2020) *Growth by stretch: an interdisciplinary approach*. PhD thesis.

<http://theses.gla.ac.uk/81624/>

Copyright and moral rights for this work are retained by the author

A copy can be downloaded for personal non-commercial research or study, without prior permission or charge

This work cannot be reproduced or quoted extensively from without first obtaining permission in writing from the author

The content must not be changed in any way or sold commercially in any format or medium without the formal permission of the author

When referring to this work, full bibliographic details including the author, title, awarding institution and date of the thesis must be given

Enlighten: Theses

<https://theses.gla.ac.uk/>  
[research-enlighten@glasgow.ac.uk](mailto:research-enlighten@glasgow.ac.uk)

# GROWTH BY STRETCH: AN INTERDISCIPLINARY APPROACH



**Ricky Ashok Unadkat**

**MEng, MRes**

Submitted in fulfilment of the requirements of the Degree of Doctor of  
Philosophy in:

The Institute of Molecular, Cell and Systems Biology,  
University of Glasgow

## Abstract

Tissue expansion is a technique used by plastic and restorative surgeons to cause the body to grow additional skin, bone or other tissues. Distraction osteogenesis (DO) is an example of tissue expansion which has been widely applied in lower limb surgery (trauma/congenital), and congenital upper limb reconstruction (e.g. radial dysplasia). This complex and tightly regulated expansion process has resulted in adverse effects such as severe soft-tissue contractures and loss of nerve function as well as microtrauma and micro-haematoma formation (Natu et al., 2014). Thus far, the procedure can only be optimised by long-term animal or human experimentation. This thesis explains the development of an in vitro model that will allow extension regimes ( $\mu\text{m}/\text{h}$ , continuous/ intermittent) and molecular pathways involved in soft tissue damage related to DO to be explored.

Cells cultured onto polycaprolactone (PCL) polymer films can be stretched at very low, adjustable speeds, using a stepper motor and various 3D printed and laser cut designs. The idea here is that plastic flow of PCL can be utilised to enable the material to stay extended upon strain being released, to represent permanent stretching of soft tissue. PCL film for the purposes of this project was made using a solvent in conjunction with a spin-coating process; A semi-crystalline and amorphous derivative of the polymer was made (C-PCL and A-PCL respectively). Testing the two polymer sheets indicated that C-PCL is a more rigid material and that strain occurs in more localised regions when it is stretched in comparison to A-PCL. The profile of the stress-strain curve for both C-PCL and A-PCL closely resemble that of a typical soft tissue after it has passed its yield point (33% strain).

Due to the known involvement of fibroblasts in mechanical loading of tissue (B. Hinz, 2004), they were used as an initial cell line to develop an in vitro model for growth by stretch. Both A-PCL and C-PCL were used as substrates and were stretched passed their yield point (33% strain) before cells were cultured on. Following fibroblast proliferation to confluency substrates were further stretched by 1mm (2.5% strain) over 24 hours (stepped stretching at 0.04mm per hour). Orientation analysis indicated that cells grown on C-PCL initially elongate and orient to the direction of pre-stretch (when substrates are initially stretched

passed their yield point), then contract upon being further stretched by 1mm over 24 hours. Cells cultured on A-PCL, under the same stretching regime initially align to the direction of pre-stretch; after being further stretched by 1mm the majority of cells remain aligned, but also elongate in the direction of stretch. Initial alignment on both materials was deemed a result of tension in the material and/or topographical features which formed during stretching of substrates before cells were cultured on. The alignment was more pronounced on the C-PCL substrate and cell nuclei were analysed to be more elongated indicating the topography caused the fibroblasts to reside in a stressed state. This aligned cell effect was lost on C-PCL during further 1mm stretching due to; stress relaxation after each step of stretching; and/or localised strain regions causing cells to round during the stepped 1mm stretch. A-PCL was further investigated as a substrate to model soft tissue expansion in relation to DO where MRTF-A nuclear translocation was shown to increase in response to stretch (by 3-fold). F-actin texture analysis further implied cytoskeletal involvement in the stretching regime utilised for this project.

Based on the results obtained, it was concluded that A-PCL with the stretching regime detailed (where plastic flow is utilised), provides the basis for a representative in vitro model of stretching soft tissue in relation to DO. Future work outlined to build on this model would be to: further investigate the relation between strain and cell response at the cell level for both materials using live imaging (in conjunction with fiducial markers in the substrate) and atomic force microscopy methods; and to develop understanding of extracellular matrix (ECM) interactions with cells in response to the stretching in the plastic flow region by again using live imaging methods (fluorescently tagging ECM components).

# Table of Contents

Abstract.....	2
List of Tables.....	7
List of Figures.....	8
Acknowledgement.....	17
Author’s Declaration.....	18
Definitions/Abbreviations .....	19
1 Introduction .....	22
1.1 Distraction Osteogenesis.....	23
1.2 Composition of Soft Tissue Determining its Mechanical Properties .....	26
1.3 Cell-Matrix Interactions.....	29
1.4 Cellular Mechanisms Involved in Stretching of Tissue .....	31
1.5 Growth Factor Involvement .....	32
1.6 Fibroblasts and their Importance in Tissue Expansion.....	35
1.7 Current Methods Used for Inducing Stretch to Cells .....	38
1.8 Project Aims .....	41
1.9 Thesis Outline .....	42
2 Characterisation of Polymer Film to Investigate Stretching of Soft Tissue..	43
2.1 Introduction.....	43
2.1.1 Stress, Strain and Stress-Relaxation .....	46
2.1.2 Poly- $\epsilon$ -caprolactone .....	50
2.1.3 Crystal Formation Process .....	51
2.1.4 Film Formation .....	53
2.1.5 Surface Treatment.....	54
2.1.6 Chapter Aims and Objectives .....	55
2.2 Methods.....	58
2.2.1 C-PCL Film Development .....	58
2.2.2 A-PCL Film Development .....	58
2.2.3 Tensile Testing .....	58
2.2.4 Digital Image Correlation.....	60
2.2.5 Light Microscopy and Scanning Electron Microscopy.....	63
2.2.6 Polarised Light Microscopy .....	64
2.2.7 Plasma Treatment and Water Contact Angle Measurements.....	66
2.3 Results .....	67
2.3.1 Tensile Testing .....	68
2.3.2 DIC.....	74
2.3.3 Microscopy, and SEM Imaging.....	77

2.3.4	Polarised Light Microscopy Imaging .....	79
2.3.5	Water Contact Angle .....	81
2.4	Discussion and Conclusion .....	83
3	Devices Developed for Experimentation.....	85
3.1	Introduction.....	85
3.1.1	Defining the Mechanism of Stretch .....	85
3.1.2	Devices Used for Cell Substrate Stretching .....	87
3.1.3	Devices to be Developed .....	94
3.2	Results .....	95
3.2.1	Cell Sheet Stretching Device.....	95
3.2.2	Live Cell Sheet Stretching Device.....	106
3.3	Discussion and Conclusion .....	112
4	Fibroblast Response to a Continuously Stretched Substrate .....	114
4.1	Introduction.....	114
4.1.1	Fibroblast Mechanotransduction and Cell Morphology .....	115
4.1.2	Myocardin related transcription factor A.....	118
4.1.3	Chapter Aims and Objectives .....	121
4.2	Methods.....	123
4.2.1	Mechanical Testing of PCL .....	123
4.2.2	Finite Element Analysis .....	123
4.2.3	Optimising Cell Proliferation on PCL .....	125
4.2.4	Cell Culture and Analysis Methods in Relation to the Stretching Device	129
4.2.5	Statistical Analysis.....	139
4.3	Results .....	140
4.3.1	Mechanical Characterisation of Crystalline and Amorphous Polycaprolactone .....	140
4.3.2	Nuclei morphological analysis .....	143
4.3.3	Live Imaging of Cell Remodelling .....	154
4.3.4	MRTF-A Nuclear Translocation.....	156
4.3.5	F-Actin Texture Analysis.....	158
4.4	Discussion.....	163
4.4.1	Conclusion.....	167
5	Final Discussion and Project Perspectives .....	169
5.1	Material Topography.....	169
5.2	Material Rigidity and Stress-Relaxation .....	171
5.3	Material Strain Homogeneity.....	173
5.4	Overall Perspective on Utilising Plastic Flow to Stretch Cell-Substrates 175	
5.5	Future Work to Further Elucidate Findings.....	179

Appendices .....	181
Appendix A- Image Processing to Analyse MRTF-A Nuclear to Cytoplasmic Ratio .....	181
References .....	186

## List of Tables

Table 4.1. Optimum parameters used on the Ultimaker 2 3D printer for printing wells onto PCL 126

Table 4.2. Haralick texture features and how they are calculated on 'Orange'. Mathematical formulae (right column) using the GLCM values (see Figure 4.26) can be used to determine defined texture measurements (left column).  $P(i,j)$  is the probability value at position  $(i,j)$  in the generated GLCM.  $P_{ij}$  values in the GLCM are therefore a measure of commonness of occurrence between neighbouring pixel values; as it is a probability measure, the value ranges between 0 and 1. Contrast (CO) measures similarity of pixels. When  $i$  and  $j$  are equal,  $(i-j=0)$ , this represents pixels entirely similar to their neighbour, so they are given a weight of 0 (no contrast). The weights increase exponentially as  $(i-j)$  increases. Homogeneity (HO) increases with less contrast as essentially homogeneity weights values by the inverse of the contrast weight. Entropy (EN) is a measure used to determine the unpredictability of the grey level distribution; the  $\ln$  of the probability will always be 0 or negative as the probability range is between 0 and 1. the  $(-1)$  multiplier in makes each term positive. Therefore, the smaller the  $P_{ij}$  value, the greater the weight, and the greater the value of entropy. The GLCM Mean (ME) is not simply the average of all the original pixel values in the image window. The pixel value is weighted by its frequency of its occurrence in combination with a certain neighbour pixel value. The equation can calculate the mean based on the reference pixels ( $i$ ) or the neighbour pixels ( $j$ ). GLCM variance (VA) uses the GLCM, therefore it deals specifically with the combinations of reference and neighbour pixel; it is not the same as the variance of grey levels in the original image. The Correlation (CO) texture measures the linear dependency of grey levels on those of neighbouring pixels; it is expressed by the regression equation. 160

## List of Figures

Figure 1-1. Phases of distraction osteogenesis. The latency phase is the healing phase which begins straight after fracture. The distraction phase is when the 2 pieces of bone are pulled apart. The consolidation phase is when mineralisation occurs in the separation gap, and the remodelling phase is where repair is completed (Birch & Samchukov, 2004). 23

Figure 1-2. Schematic of cells residing in connective tissue matrix with elastin and collagen fibrils. The extracellular matrix determines tissue mechanical properties and is comprised of collagen, elastin and reticular fibers. Collagen fibers determine tensile properties of the tissue, while elastin forms low stiffness cross-linked networks across the extracellular matrix. Reticular fibers are thin collagen fibers which support early synthesized extracellular matrix. The ground substance is an unstructured material that fills the space between cells and fibres; it is primarily composed of water, proteoglycans and cell adhesion proteins (Mescher, 2010). 27

Figure 1-3. Schematic representing how Integrins bind to extracellular matrix components initiating focal adhesion complexes and actin filament formation (Image taken from: [www.nature.com/scitable/topicpage/cell-adhesion-and-cell-communication-14050486](http://www.nature.com/scitable/topicpage/cell-adhesion-and-cell-communication-14050486)). 29

Figure 1-4. Summary of biochemical pathways that may be involved in stretching due to mechanotransduction. Tensile stresses cause stretching of intracellular junctions, activation of membrane ion channels, or release of growth factors that leads to activation of secondary messengers. Secondary messenger activation leads to activation of factors such as NF- $\kappa$ B that binds to promoter sequences in genes such as those expressed for tenascin-C and type XII collagen. Stretching of ECM-integrin contacts and cell intercellular junctions are known to trigger MAP kinase pathways (MAPKK, and MAPK) via GTPase Ras. MAPKs translocate to the nucleus and activate transcription factors such as AP-1. Alternately, members of the MAP kinase kinase kinase (MAPKKK) family have been shown to activate the I- $\kappa$ B kinase (IKK) complex, which phosphorylates I- $\kappa$ B and leads to the release of NF- $\kappa$ B, which in turn, translocates to the nucleus. In the nucleus, NF- $\kappa$ B binds to its target promoter sequence. Another putative route for MAPK activation is via autocrine release of growth factors and activation of protein kinase C (PKC). Mechanical stretch also leads to activation of stretch response promoter regions in tenascin-C and type XII collagen genes (Chiquet, 1999). 33

Figure 1-5. Fibroblast regulation of extracellular matrix structure and function through feedback loop. Increased mechanical loading or matrix stiffness causes cell responses which either work towards matrix homeostasis (negative feedback loop), or develops fibrotic conditions (positive feedback loop). In both cases, stabilized focal adhesions of greater number or size and increased actomyosin contractility through Rho–Rho kinase pathway is key. (figure adapted from Humphrey et al., 2014). 37

Figure 1-6. Schematic of current methods used for mechanically deforming cells. A) Probing single cells using AFM. B) Probing individual cells using magnetic beads, C) Deforming single cells using micropipette aspiration. D) Deforming individual cells using optical traps. E) Using shear flow to stimulate entire cell populations. F) Stretching substrates cultured with cells to stimulate cell populations (Bao & Suresh, 2003). 40

Figure 2-1. Stiffness of tissue compared to polymers used for the purposes of cellular mechanotransduction studies. A) Illustrates the range of various tissue stiffnesses, and B) illustrates stiffnesses of different polymers used for cellular mechanotransduction studies (H. N. Kim et al., 2012). 44

Figure 2-2. Illustration of the feedback loop between cells and biomechanical signals from the ECM. The loop is depicted by red arrows and the green are the various biomechanical cues. Purple regions on the diagram indicate ECM receptors to the biomechanical cues, which in turn trigger intracellular responses; it can be seen that stiffness, topography and stretching of the ECM can combine to set off varying cell responses, such as migration, proliferation, apoptosis and differentiation, alongside the release of certain proteins (MMPs, TIMPs and other proteins which can impact the ECM) (Urbanczyk et al., 2019). 45

Figure 2-3. Typical stress strain for polymers that undergo plastic deformation. Stress is plotted against strain as a material is elongated. The initial linear region is the elastic region of the material, where the gradient of the line is a measure of the Young's Modulus (E) of the material. The yield point is the top of the linear region; when extended beyond this, deformation of the material is plastic (image taken from [www.orthobullets.com](http://www.orthobullets.com)). 47

Figure 2-4. Schematic illustrating difference between elastic and viscoelastic materials held at the same strain (top curve). In the elastic material, stress remains constant after it initially increases to reach the strain level achieved. The spike seen for the viscoelastic material is the initial stress required to reach that level of strain before molecular rearrangement occurs through time to reduce stress when held at that same strain (Naemi et al., 2016). 48

Figure 2-5. Stress/strain profile of skin tissues strained at different rates and orientations in different studies. (T) refers to the direction of strain being transverse to the tissue orientation and (L) refers to the direction being longitudinal to the orientation of the tissue. Tissue in the 'Jansen & Rottier' study was obtained from the human abdomen; from the 'Ni'Annaidh' study it was obtained from the human back; from the 'Ankersen' study from pig skin (Ankersen, 1999; Gallagher et al., 2012; Payne et al., 2014) 49

Figure 2-6. Schematic diagram of the change in free energy during nucleation (Beaupere et al., 2018). 52

Figure 2-7. Schematic of tensile testing apparatus (Zwick Roell z2. The specimen to be tested (PCL films in this case) is gripped at each end by the holding grips. The gauge length is the distance between the end of each grip. When the crosshead moves up it stretches the material and the load cell records the force required to stretch the material. 59

Figure 2-8. Example of strain measurements of a single point on a material undergoing deformation. A) Point A displaces along the x and y axis to A'; its perpendicular line elements B and C change length and angle in relation to A during this deformation (B', and C'). The change in angle for C is defined by  $\lambda$  and for B the change in angle is defined by  $\theta$ . B) These are the equations for normal strain in the x and y direction ( $\epsilon_{xx}$ ,  $\epsilon_{yy}$ ) and the shear strain ( $\epsilon_{xy}$ ) which is defined by the angle change in elements (Figure adapted from Kelly, 2015). 61

Figure 2-9. Illustration of what DIC tracks as a specimen deforms. A) Schematic of speckles to be tracked during material deformation. B) Schematic of speckles moving relative to their original position upon material deformation. 62

Figure 2-10. DIC set up. A) Speckled specimen clamped between rubber grips on Zwick Roell z2, and brought into focus using Vic-Snap camera. B) Specimen zoomed into and region of interest manually created using Vic-2D software. 63

Figure 2-11. Schematic of how light travels during polarised light microscopy. A polariser filters light to only enable light oriented in a specific direction through (polarising direction). There are two polarisers in a polarizing optical microscope and they are oriented perpendicularly to one another. The polarising direction of the first polariser is oriented vertically to the incident beam, enabling only waves with vertical direction to pass through. This is then blocked by the second polarizer as it is horizontal to the incident wave unless an object between the polarisers causes the light to diffract (Image taken from chem.libretexts.org). 65

Figure 2-12. Contact angles were measured using the static drop technique on PCL surfaces with different plasma treatment times, and fitted with a circular line to determine angles. The contact angle varies depending on the hydrophobicity of the surface. 66

Figure 2-13. Developed PCL films. A) C-PCL, as the polymer is crystalline its translucency can be seen against a black background. B) A-PCL. 67

Figure 2-14. Stress strain curves for 2 versions of PCL. A) Semicrystalline (C-PCL), tensile characteristics are outlined here. The initial slope where stress and strain increase is the Young's modulus. This slope leads into a peak called 'the yield point', the material is no longer elastic after being stretched further than this point. The drop in stress while strain increases is known as stress relaxation. The flat region following stress relaxation is known as 'plastic flow'. The increase in stress alongside strain after the flat region is known as strain hardening; the peak reached at the end of strain hardening is where the material breaks (fracture point). B) Amorphous (A-PCL). Deformation for both materials was applied at 60mm/min (n=4 spin coated samples for both sample types). 68

Figure 2-15. Example of polymer necking after yield point. A) Image of PCL before yield point reached; width of sample is uniform. B) Image of PCL after yield point is reached; width of PCL is non uniform due to necking of sample. 69

Figure 2-16. Difference in Young's Modulus and yield point between CPCL and APCL. A) Young's Modulus. B) Yield Point. (n=4 for both C-PCL and A-PCL. (Error bars represent 95% confidence intervals based on standard deviations. P values indicating significance, \*\*\*  $\leq$  0.001). 70

Figure 2-17. Difference in plastic flow regions between C-PCL and A-PCL. A) C-PCL plastic flow and B) A-PCL plastic flow. For both graphs, the mean region of plastic flow is plotted between 4 samples (black); a polynomial equation has been fit to each mean line. The grey lines represent the 95% confidence interval. 71

Figure 2-18. Difference between C-PCL and A-PCL in A) Linear strain hardening and B) Fracture point. (n=4 for both C-PCL and A-PCL. Error bars represent 95% confidence intervals based on standard deviations. P values indicating significance, \*\*  $\leq$  0.01). 73

Figure 2-19. DIC tensile testing comparison between C-PCL and A-PCL. Images taken at 50% Engineering Strain for A) C-PCL B) A-PCL, and at 167% strain for C) C-PCL and D) A-PCL. The bar on the right of each image is a scale for the colours present (red=high strain, purple=low strain) on the material and is not equal between images. This is depicted by the min and max strains highlighted in each image. 75

Figure 2-20. Difference between C-PCL and A-PCL when looking and localised strain (A) and stress (B). (n=3 for both C-PCL and A-PCL. Error bars represent 95% confidence intervals based on standard deviations. P values indicating significance, \*  $\leq$  0.05). 76

Figure 2-21. Light Microscopy images of C-PCL being stretched. A) At 0% strain, the initial crystal structure can be seen. B) At 35% strain, just after the yield point of the material, a clearly stretched region can be seen; crystals outside of this region also look deformed in comparison to the 0% image. C) At 50% strain, the strain can be seen to propagate through the clearly stretched region; further deformation of crystals outside of this area continues to be seen. D) At 200% strain, the stretched region has propagated further through the material. Scale bar is equal to 100um in each image. 77

Figure 2-22. SEM images of A-PCL (A) unstretched (B) Stretched at 50% strain. Small oval nodes ~5um in size develop on the stretched sample. 78

Figure 2-23. Polarised light microscopy images of C-PCL and A-PCL under crossed polarised light. A-C are images of unstretched C-PCL when the stage is turned from 0-50°. D-F are images of stretched C-PCL (50% strain) when the stage is turned from 0-50°. G-I are images of unstretched A-PCL when the stage is turned from 0-50°. J-L are images of stretched A-PCL (50% strain) when the stage is turned from 0-50°. The circles in the top right corner in each image determine how much the stage has been rotated for each image. Scalebar represent 50um. 80

Figure 2-24. Quantification of light intensity generated by polarised light microscopy imaging of unstretched and stretched C-PCL and A-PCL samples. Samples were rotated under polarised light microscopy from 0-90°. Unstretched samples of C-PCL and A-PCL show no difference in light intensity between rotations. Stretched samples have low light intensity at 0°, this increases through rotation, and peaks at 50° before intensity drops from 50 to 90° rotation again. 81

Figure 2-25. Water contact angle measurements for C-PCL treated at different air plasma times. n=4 samples with n=5 droplet measurements on each sample for each plasma treatment time. (Error bars represent 95% confidence intervals based on standard deviations. P values indicating significance, \*\*\*  $\leq$  0.001). 82

Figure 3-1. Schematic depicting typical device fixation points for distraction osteogenesis procedure. Although the distraction site for bone is isolated to a small region, the soft tissue being stretched is over the length of the whole bone (image taken from: [www.jnjmedicaldevices.com/en-EMEA/product/distraction-osteogenesis-ring-system](http://www.jnjmedicaldevices.com/en-EMEA/product/distraction-osteogenesis-ring-system)). 86

Figure 3-2. CellScale devices used to uniaxially stretch cell cultured substrates. A) The MCJ1 has vertically orientated culture chambers with a load cell attached to each chamber alongside individual actuators. substrates are attached via outlined clamps. B) The MCT6 has horizontally oriented chambers with one actuator for all chambers, substrates are attached via outlined clamps (images taken from: <https://cellscale.com/products/>). 89

Figure 3-3. Example pneumatic actuator mechanisms. A) Positive pressure used to inflate series of ballon membranes, thereby stretching cell cultures. B) Negative pressure applied to each end of cell cultured membrane to stretch from each end. 90

Figure 3-4. Example piezoelectric actuator mechanisms to stretch cell cultured substrates. A) Microwell substrates placed over piezoelectric pin, displacement controlled via power input. B) Stretching of cell cultured PDMS membrane through moving stages; the linear stage moves away from the spring stage upon piezoelectric actuation, upon relaxation, the spring helps the PDMS recoil back to its original shape. 91

Figure 3-5. Motor mechanisms to create linear displacements. A) Timing-belt pulley; size of pulley dictates displacement. B) Engaged gears; size of gears dictates displacement. C) Camshaft; Non-concentricity of cam dictates displacement. D) Screw pitch, length, and direction of motor rotation dictate displacement (Lei & Ferdous, 2016). 93

Figure 3-6. Schematic depicting a concept of how a substrate material for cells may be stretched with precision. 96

Figure 3-7. Stepper motor driven by arduino to achieve precision stretching of cell culture substrates. A) Arduino configuration with Adafruit V2 motorshield fitted on top. B) Nema-17 Stepper motor with welded leadscrew (6.35mm diameter, 2mm lead length). 98

Figure 3-8. Example script uploaded to Arduino to provide 1mm stretch over 24 hours. Before the 'void loop' line, certain libraries are being selected, and the motor and which port it's connected to have been defined, as well as the speed that it will go through the amount of steps that are input within the 'void loop'. The delay function stops the motor from turning and is defined in milliseconds. The line highlighted defines how many steps (2) it takes in one cycle before the next delay; which way the motor rotates the lead screw (FORWARD), and which method it uses to turn the lead screw (MICROSTEP). 99

Figure 3-9. Frame assembly for cell substrate stretcher. A) Assembled Makerbeam beams (30cm x4, 15cm x 5, 6cm x 4), corner cubes (x8), M3 12mm square headed screws (12mm x 20, 6mm x 16), and L-brackets (x10). B) Blowout of a corner joint to connect 2 beams at a right angle. 2 x 6mm M3 screws are required. They are each pushed in through the large hole on the cube through to the small which sits against an M3 threaded hole on the end of the beam. C) Blowout of how an L-bracket connects the 15cm beams to the 30cm ones. A screw slotted into each beam goes through one of the holes on the bracket and is kept in place by screwing down a nut on each screw. D) Blow of the L-bracket joint again. Different view to show how screws slot into T-beams. 100

Figure 3-10. Motor/leadscrew assembly on frame. A) Full assembly with motor fitted onto bottom 2 15cm brackets. B) Blowout showing how the motor attaches to the brackets, 4x 12mm M3 screws go through 4 corners of the front of the bracket into 4 threaded corners into the motor. The bracket is attached via 4x 6mm M3 screws (2 slotted in each 15 cm beam before being tightened with M3 nuts). 101

Figure 3-11. 4-well-plate assembly on frame. A) Full assembly with well-plate fitted on. B) Blowout of just the well-plate and the frame fixture which keeps the well-plate locked onto the frame. The ridges of the fixture fit over the spacers between each well. The M4 threaded holes are for components described next. C) Blowout depicting how the well-plate frame, well-plate and Makerbeam frame fit together. 2x 12mm flat headed M3 screws are slotted into the 2 15cm beams surrounding the well-plate. The 4 holes on the corners of the well-plate frame are placed over the screws and bolted down onto the frame. 102

Figure 3-12. Leadscrew block assembly on frame. A) Full assembly with leadscrew block fitted. B) Blowout showing how the block attaches to the leadscrew nuts. The leadscrew nut has 3 holes on it 120 degrees apart on the larger circle side of it. The block has 3 holes corresponding to them. The arch of the block fits over the smaller part of the leadscrew nut; the holes are aligned and 3x 12mm M3 screws are pushed through the aligned holes before being bolted off. 102

Figure 3-13. Assembly of lid on frame. A) Blowout diagram to show how lid fits onto the leadscrew block. Holes between the 2 are aligned. The 2 holes on the leadscrew block are manually threaded to allow a 12mm M3 screw to be screwed in. B) Full assembly with lid. 103

Figure 3-14. Assembly of how substrates fit into the well plate. A) View of how a small block (a substrate would be attached) screws into the frame. B) The larger block sits opposite the fixed in small block (the other end of the substrate would be attached to it). C) The full assembly; the lid fits over, where the large block protrudes through one of the lid's rectangular holes. 104

Figure 3-15. Overall assembly and functionality of the device designed. A) Picture of components assembled to make stretcher. B) Top view of device with PCL (20mm length) attached in all 4 wells

of the well-plate. C) Top view of stretcher after 20 rotations of the lead screw is applied through 4000 steps of the stepper motor. 105

Figure 3-16. Schematic depicting a concept of how a substrate material for cells may be stretched with precision under a microscope for live imaging. 107

Figure 3-17. Partial assembly of petri-dish device. A) Blowout diagram; A substrate guide component is used to keep substrates in the petri-dish. The OD of this (50.5mm) is slightly larger than the petri-dish's (50mm), and this allows for an interference fit in the dish. A slider component screws down into the tramlines of the substrate guide component, and the leadscrew pushes through the hole in the column. B) Assembly showing that the leadscrew pushes all the way through till the knob is against the column. 108

Figure 3-18. Subassembly of components in petri-dish. A) Blowout diagram showing how blocks clamping the substrate down attach. The sliding block screws into the slider, and the fixed block screws into the substrate guide component. The leadscrew then screws into the sliding block after it has been pushed up against the column of the substrate guide component. 108

Figure 3-19. Side view of components attached to substrate. On both blocks, there is a part designed to make the substrate sit at the bottom of the petri-dish. 109

Figure 3-20. Assembly of Petri-dish device stretcher. A) Blowout of components fitting together. The well plate with the subassembly that fits inside sits in the ring of the microscope stage fixture. The sides of the petri-dish are clamped down by being screwed to the microscope stage fixture, which fits directly onto the microscope stage. B) Diagram of the petri-dish device fully assembled. 110

Figure 3-21. Overall assembly and functionality of the live-imaging stretcher device designed. A) Top view of stretcher with PCL film attached. B) Image and length of PCL film before being stretched through 10 rotations of the leadscrew. C) Image and length of PCL film after being stretched through 10 rotations of leadscrew. The film stretched by 2mm. 110

Figure 4-1. Cycling of RhoA between active and inactive forms: Switching of RhoA between inactive GDP-bound form to the active GTP-bound form is regulated by GEFs, GAPs and GDIs. Binding to GTP changes the conformation of the molecule, thus allowing the binding of various downstream effectors of RhoA such as ROCK, thereby facilitating various downstream signaling pathways (Figure adapted from Thomas et al., 2019). 116

Figure 4-2. Schematic representation of RhoA mediated formation of F-Actin. RhoA-GTP 117

Figure 4-3. Schematic representation of MRTF-A activity regulation by ECM tension and TGF- $\beta$  signalling via activation of RhoA GTPase . In response to stimulation, integrins and TGF- $\beta$  receptors activate Rho GEFs. Active Rho GEFs mediate exchange of GDP for GTP activating RhoA. RhoA-GTP upregulates actin polymerisation via mDia1 and downregulates depolymerisation via ROCK pathway. Increased actin filament growth reduces concentration of monomeric actin in the cytoplasm, leading to G-actin dissociation from MRTF-A. MRTF-A is translocated to the nucleus, where it binds SRF and activates gene transcription (Olson & Nordheim, 2010) . 119

Figure 4-4. Cartoon representation of MRTF-A RPEL domain bound to 5 actin monomers. Actin monomers that are bound to RPEL motifs 1-3 are shown in grey, monomers recruited to spacer regions – in cyan. RPEL motifs are shown in magenta, spacer regions in yellow and nuclear localization sequences 1 and 2 (NLS) in green (Mouilleron et al., 2011). 120

Figure 4-5. Wells developed to keep PCL taut for cell culture. A) AutoCAD design of the wells. B) How the wells look printed onto the PCL. 126

Figure 4-6. Optimising plasma treatment time of C-PCL for cell growth. A) Graph depicting percentage nuclei coverage on C-PCL plasma treated between 0.5 and 2.5 minutes (Glass = positive control, 0 = negative control). B) Image of cell nuclei on PCL (plasma treated for 1 minute); nuclei attachment after 2 hours. C) Image of cells on PCL (plasma treated for 1 minute); cells have increased markedly after 4 days. Curves show mean of 3 repeats. 128

Figure 4-7. Cell proliferation on C-PCL, plasma treated for 1 minute vs 0 minutes over 2 weeks. A) Graph showing cell numbers increase over a 2 week period when cells cultured onto C-PCL which has been plasma treated for 1 minute. The exponential curve provides a fit for the data till it reaches a plateau (confluence) where cell density (y) can be approximated by culture time (x). B), C) Immunofluorescent images at 2 hours after culture, DNA and F-actin respectively. D), E)

Immunofluorescent images at 2 days after culture, DNA and F-actin respectively. F), G) Immunofluorescent images at 5 days after culture, DNA and F-actin respectively. H), I) Immunofluorescent images at 8 days after culture, DNA and F-actin respectively. All scale bars are 50 $\mu$ m. Curves show mean of 3 repeats. 129

Figure 4-8. Example script uploaded to Arduino to provide 1mm stretch over 24 hours. Before the 'void loop' line, certain libraries are being selected, and the motor and which port it's connected to have been defined, as well as the speed that it will go through the amount of steps that are input within the 'void loop'. The delay function stops the motor from turning and is defined in milliseconds (3600000 = 1hour). The line highlighted defines how many steps (4) it takes in one cycle before the next delay; which way the motor rotates the lead screw (FORWARD), and which method it uses to turn the lead screw (MICROSTEP). 131

Figure 4-9. FIJI Macro used to open image stacks and process them into one focussed image for an entire sample. Text on the right explains key elements of the macro. 135

Figure 4-10. Example of processed image of cells cultured to confluence on stretched C-PCL. A) DNA and B) F-actin. Six consecutive image stacks have been processed using an EDF filter here for images taken at two different wavelengths of light 405nm, to image DAPI bound to DNA and 561.4nm to image F-actin. 136

Figure 4-11. Example of part of PCL substrate with cells attached. A) Image of nuclei (DAPI stained) after images have been run through macro and stitched. This image highlights how some nuclei blend in with the background. B) Same image processed through CLAHE. 137

Figure 4-12. Illustration of what the Feret, Min Feret and Feret Angle are. The Feret is the maximum diameter of the particle. The Min Feret is the smallest diameter of the particle. The Feret Angle is the angle between the Feret and Normal. 138

Figure 4-13. Stress relaxation in C-PCL and A-PCL when stretching materials by 1mm after pre-stretch has been applied. A) Image of A-PCL being stretched from 30-40mm, before being stretched by 1mm to 41mm. B) Top: Force drop (stress-relaxation) deforming 40mm C-PCL to 41mm. Bottom: Force drop (stress-relaxation) deforming 40mm A-PCL to 41mm. Stress-relaxation gradient for is 0.08N/mm for C-PCL and 0.02 for A-PCL. 140

Figure 4-14. Finite strain analysis comparison between C-PCL and A-PCL when both materials are stretched by 1mm after being pre-stretched by 10mm from a 30mm gauge length. A) Finite element Y-strain ( $\epsilon_{yy}$ ) plotted in the Eulerian configuration shows a more localised strain region on C-PCL to A-PCL. The strain propagates on from one point on C-PCL. Although strain is still localised to the necked region on A-PCL, the profile is more homogenous in comparison to C-PCL (see light blue and yellow regions on films). B) Finite element shear-strain ( $\epsilon_{xy}$ ) plotted in the Eulerian configuration again shows to highly localised points of shear on C-PCL, whereas shear strain is more evenly distributed on A-PCL). 142

Figure 4-15. Histogram plotting aspect ratio of cell nuclei when cells grown to confluence on C-PCL that has been pre-stretched, and then further stretched for xmm over yhours for one experiment. The distribution of nuclei aspect ratio for both conditions indicates that the median should be used to gauge the centre point of the data rather than the mean as the median in both cases is closer to the peak of the data than the mean. 144

Figure 4-16. Summarised data for aspect ratio of cell nuclei when cells grown to confluence on C-PCL that has been pre-stretched, and then further stretched for three experiments. A) Boxplot of individual experiments. The bottom of each box represents the first quartile and the top is the third quartile. The centre point in each box is the median for each experiment. The whiskers extend from either side of the box. The whiskers represent the ranges for the bottom 25% and the top 25% of the data values. The median of the pre-stretch data is 1.76 and the median of the further stretched data is 1.53. These median aspect ratios are significantly different ( $p < 0.001$ , using the Mann-Whitney Test)).  $n_{\text{cells}} = 61836$  for pre-stretch and  $n_{\text{cells}} = 74482$  for the further stretched condition. Point estimate for  $\eta_1 - \eta_2$  is 0.2087, 99.9 Percent CI for  $\eta_1 - \eta_2$  is (0.2025, 0.2149), Test of  $\eta_1 = \eta_2$  vs  $\eta_1 \neq \eta_2$  is significant at 0.0000. B) Histogram of pooled aspect ratios of nuclei on pre-stretched C-PCL vs further stretched C-PCL. An overall shift can be seen where nuclei are more elongated in the pre-stretch condition in comparison to the further stretched condition. C) Example of nuclei analysed in pre-stretched condition on C-PCL. D) Example of nuclei analysed in further stretched condition on C-PCL. Nuclei can be seen to be more elongated in C) than D). Scalebars in white in C and D are 20 $\mu$ m in length. 145

Figure 4-17. Aspect ratio of nuclei of cells grown to confluence on pre-stretched A-PCL, compared to cells grown to confluence on pre-stretched A-PCL and then further stretched. A) Boxplot of individual experiments. The bottom of each box represents the first quartile and the top is the third quartile. The centre point in each box is the median for each experiment. The whiskers extend from either side of the box. The whiskers represent the ranges for the bottom 25% and the top 25% of the data values. When pooled median aspect ratios are significantly different ( $p < 0.001$ , Mann-Whitney U test).  $n_{\text{cells}}=92864$  for the pre-stretch condition and  $n_{\text{cells}}=91514$  for the further stretched condition. Point estimate for  $\eta_1 - \eta_2$  is  $-0.3477$ , 99.9 Percent CI for  $\eta_1 - \eta_2$  is  $(-0.3548, -0.3406)$ , Test of  $\eta_1 = \eta_2$  vs  $\eta_1 \neq \eta_2$  is significant at  $0.0000$ . B) Histogram of pooled aspect ratios of nuclei on pre-stretch A-PCL vs further stretched A-PCL. An overall shift can be seen where nuclei are more elongated in the further stretched condition in comparison to the pre-stretched condition. C) Example of nuclei analysed in pre-stretched condition on A-PCL. D) Example of nuclei analysed in further stretched condition on A-PCL. Nuclei can be seen to be more elongated in D) than C). Scalebars in white are  $20\mu\text{m}$  in length. 146

Figure 4-18. Transformation of orientation Feret angle values. A) Example data point to be transformed to avoid bimodal data sets. B) Data point from A) transformed by subtracting original value from  $180^\circ$ . 147

Figure 4-19. Orientation of cell nuclei grown to confluence on pre-stretched C-PCL, compared to cells grown to confluence on pre-stretched C-PCL and then further stretched. A) Boxplot of individual experiments. The bottom of each box represents the first quartile and the top is the third quartile. The centre point in each box is the median for each experiment. The whiskers extend from either side of the box. The whiskers represent the ranges for the bottom 25% and the top 25% of the data values. When pooled, median orientation angles are  $19.9^\circ$  in pre-stretch, and  $50.2^\circ$  when further stretched ( $p < 0.001$ , Mann-Whitney U-test).  $n_{\text{cells}}=61836$  for pre-stretch and  $n_{\text{cells}}=74482$  for the further stretched condition. Point estimate for  $\eta_1 - \eta_2$  is  $-21.404$ , 99.9 Percent CI for  $\eta_1 - \eta_2$  is  $(-21.866, -20.947)$ . Test of  $\eta_1 = \eta_2$  vs  $\eta_1 \neq \eta_2$  is significant at  $0.0000$ . B) and C) are circular histograms for C-PCL, pre-stretched and stretched data respectively; the red line is a mean vector indicating how well the distribution is spread around the mean. D) Example of cells orienting in the direction of stretch on the pre-stretched material and E) Example of cells losing orientation to stretch direction when C-PCL is further stretched. Scalebars in white are  $20\mu\text{m}$ . 148

Figure 4-20. Orientation of cell nuclei grown to confluence on pre-stretched A-PCL, compared to cells grown to confluence on pre-stretched A-PCL and then further stretched. A) Boxplot of individual experiments. The bottom of each box represents the first quartile and the top is the third quartile. The centre point in each box is the median for each experiment. The whiskers extend from either side of the box. The whiskers represent the ranges for the bottom 25% and the top 25% of the data values. When pooled, median orientation angles are  $30.5^\circ$  in pre-stretch and  $38^\circ$  when further stretched ( $p < 0.001$ , Mann-Whitney U-test).  $n_{\text{cells}}=92864$  for the pre-stretch condition and  $n_{\text{cells}}=91514$  for the further stretched condition. Point estimate for  $\eta_1 - \eta_2$  is  $-8.54$ . 99.9 Percent CI for  $\eta_1 - \eta_2$  is  $(-8.8, -8.2)$ . Test of  $\eta_1 = \eta_2$  vs  $\eta_1 \neq \eta_2$  is significant at  $0.0000$ . B), C) Circular histograms for A-PCL, pre-stretched and stretched data respectively; the red line is a mean vector indicating how well the distribution is spread around the mean. D) Example of cells on pre-stretched A-PCL orienting towards stretch direction. E) Example of cells on further stretched A-PCL continuing to orient in the direction of stretch. Scalebar in white are  $20\mu\text{m}$ . 150

Figure 4-21. Nuclei direction analysis indicative of F-actin fiber direction. A) Immunofluorescent F-actin staining of confluent cells cultured on A-PCL, stretched for 1mm over 24hours after pre-stretching of material. Arrows indicate direction of nearby fibers. B) Immunofluorescent DNA staining of confluent cells in the same region as A). Arrows indicate direction of nuclei represents direction of F-actin fibers. 151

Figure 4-22. Heat maps plotting Feret angle of cells to their aspect ratios on C-PCL. A) For all pre-stretched samples ( $n_{\text{cells}}=61836$ ), and B) for all further stretched samples ( $n_{\text{cells}}=74482$ ). Schematic nuclei have been drawn into the them most populated bins. Their circularity and orientation represents circularity and orientation for the bin that they are in. The schematic nuclei show that cells are responding to the surface being plastically stretched by becoming more circular and orienting against the direction of stretch. 152

Figure 4-23. Heat maps plotting Feret angle of cells to their aspect ratios on A-PCL. A) For all pre-stretched samples ( $n_{\text{cells}}=92864$ ), and B) for all further stretched samples ( $n_{\text{cells}}=91514$ )  $n=3$  biological repeats?. Schematic nuclei have been drawn into the them most populated bins. Their circularity and orientation represents circularity and orientation for the bin that they are in. The schematic nuclei

show that cells are responding A-PCL being plastically stretched by becoming more elongated and are slightly orienting against the direction of stretch. 153

Figure 4-24. Live images using a live/dead stain of: A) Directly after 4% strain has been applied to C-PCL substrate, B) 0.5 hours after image A taken. C) Is the same image as B, but with remodelled areas outlined in green, cells are made blue so that the green is better visualised. The green areas are a subtraction of image B from A. D) Directly after 15% strain has been applied to substrate, E) 0.5 hours after image D taken. F) Is the same image as E, but with remodelled areas outlined in green. Scalebars in red are 50 $\mu$ m. 155

Figure 4-25. MRTFF-A translocation from cytoplasm to nuclei for cells grown to one-tenth confluence on pre-stretched A-PCL, compared to translocation on further stretched A-PCL. A) Box plot showing when 3 experiments pooled, median MRTF-A ratio from nucleus to cytoplasm in the pre-stretch control condition is 0.35 whereas when stretch is further applied this increases to 0.99 ( $p < 0.001$ , Mann-Whitney U-test).  $n_{\text{cells}}=7238$  for the pre-stretch condition and  $n_{\text{cells}}=7606$  for the further stretched condition. The bottom of each box represents the first quartile and the top is the third quartile. The centre point in each box is the median for each experiment. The whiskers extend from either side of the box. The whiskers represent the ranges for the bottom 25% and the top 25% of the data values. Point estimate for  $\eta_1 - \eta_2$  is -0.63947. 99.9 Percent CI for  $\eta_1 - \eta_2$  is (-0.65097, -0.62806). Test of  $\eta_1 = \eta_2$  vs  $\eta_1 \neq \eta_2$  is significant at 0.0000. B) All cells MRTF-A translocation ratio (log10) plotted against aspect ratio showing there is still an increase in aspect ratio of nuclei in response to stretch. C) MRTF-A in the cytoplasm with very little in the nucleus in the pre-stretch condition. D) MRTF-A in the cytoplasm as well as the nucleus in the further stretched condition. (Nuclear regions for images C and D defined by black outline, scalebar is 10 $\mu$ m). 157

Figure 4-26. Schematic of how a normalised GLCM is developed. A region of interest is selected and each pixel is assigned a grey value. A GLCM is developed with respect to neighbouring pixels in a specified direction (in this case to the right); for each pixel, its value and the neighbouring pixel value are counted in a specific GLCM element. The value of the reference pixel determines the column (i) of the GLCM and the neighbour value determines the row (j). As an example, there are two instances when a reference pixel of 3 “co-occurs” with a neighbour pixel of 2 (blue), and there is one instance of a reference pixel of 3 with a neighbour pixel of 1 (red). The normalised GLCM represents the estimated probability of each combination to occur in the image (Figure adapted from L6fstedt, Brynolfsson, Asklund, Nyholm, & Garpebring, 2019). 159

Figure 4-27. F-actin texture difference on A-PCL, pre-stretch vs further stretch. Texture homogeneity (a), contrast (b), entropy (c) and correlation (d) values were measured in 4 different directions. Homogeneity (a) and correlation (d) decreased after stretching, while contrast (b) and entropy (c) increased. All measurements, except for entropy, also varied dependent on direction. Box plots show inter-quartile range (25% above and below the median), whiskers show 10-90 percentile of the data, \*\*\* indicates  $p < 0.0001$  by Welch’s t-test. Data shown from 2 independent repeats and 22095 cells. (Figure courtesy of undergraduate student Egle Antanaviciute). Image (e) is an image of 2 phalloidin stained cells on the pre-stretch control condition. The areas indicated by the yellow arrows are areas that are highly homogenous which would have a low entropy. Image (f) is an image of 2 phalloidin stained cells on the further stretched condition. The areas indicated by the red arrows are areas that will lead to higher contrast and entropy values. Scalebar is 10 $\mu$ m in each case. 162

Figure 5-1. Schematic depicting fibroblast behaviour on C-PCL. When C-PCL is pre-stretched, fibroblasts align to the direction of pre-stretch in an elongated manner. When a further 1mm stretch is applied over a 24 hour period in a stepped manner of 0.04mm each hour, C-PCL undergoes large changes in tension due to stress-relaxation occurring between steps; furthermore the strain transferred is very localised on the material. This leads to cells rounding on the material as a result. 176

Figure 5-2. Schematic depicting fibroblast behaviour on A-PCL. When A-PCL is pre-stretched, fibroblasts align to the direction of pre-stretch. When a further 1mm stretch is applied over a 24 hour period in a stepped manner of 0.04mm each hour A-PCL undergoes small changes in tension as stress-relaxation is lower in comparison to C-PCL between steps; furthermore the strain transferred is more homogenous on the material in comparison to C-PCL. This leads to cells elongating on the material as a result. 177

Figure 5-3. Prototype AFM stretcher Device. A) CAD drawing of the main base which was 3D printed (Ultimaker 2). B) Final version of the device with attached parts. The base fits on top of the Nanowizard 4 (jpk.com). The PCL is clamped between ‘Clamp 1’ and ‘Clamp 2’. ‘Clamp 2’ has a thread through the middle of it, through which a screw with a lead of 1mm is tightly fitted; the end of this screw also goes through a loose hole in the ‘Block’, where it is met by a threaded hole in the

'Extender'. When the 'Extender' is turned clockwise the screw tightens, increasing the gap between 'Clamp 1' and 'Clamp 2', thereby stretching the PCL by 1mm/rotation. The 'Coverslip holder' fits on the bottom of 'Clamp 1' and has screws going through the holes on its margins which connect to the 'Guides' ensuring smooth movement. 179

Figure A.1. Imaging pipeline main components. Primary objects were to be cell nuclei masks. Secondary objects were to be entire cell masks (determined by MRTF images). Tertiary objects were to be cell cytoplasm masks where nuclei were subtracted from cell masks. Nucelus and cell dimensions were out put alongside MRTF intensities in the nuclei and cytoplasm. 182

Figure A.2. Primary objects parameters for cell profiler pipeline. The input here is a stitched image of nuclei on the film. When the pipeline is run, if an image is output at this point it will output a mask image for the nuclei input. 182

Figure A.3. Secondary objects parameters for cell profiler pipeline. The input here is a stitched image of MRTF on the film. When the pipeline is run, if an image is output at this point it will output a mask image for the MRTF input. This was used as a mask representing the entire cell. 183

Figure A.4. Tertiary objects, definining an output cytoplasmic mask via the subtraction of the nuclei mask from its corresponding cell mask. 183

Figure A.5. MRTF intensity measurements output defined. 184

Figure A.6. Example of Cell Profiler image pipeline outputs. A) Input nuclei image. B) Input F-Actin image. C) MRTF to have cytoplasmic and nuclear intensity measured. D) Output nuclei mask. E) Output cell mask. F) Output cytoplasmic mask. All scale bars in white are 50 $\mu$ m. 185

## Acknowledgement

I would like to show my deepest appreciation to my supervisors, Dr Mathis Riehle and Dr Richard Burchmore, who have guided me well through the PhD. At times it felt like Mathis, you were a bit of a dad to me (The amount of times I got told to tidy up in the kitchen. It wasn't always me!). On a serious note, I could not have wished for a better 1st supervisor, so I thank you for that.

The lab I worked in (CCE) was an absolute pleasure to work in. I made friends here that I will keep for life. Anil, never stop being a "Duff-er", nothing will come close to replacing the lab memories we created!

To my flatmates Jake and Mark, I feel if we hadn't bonded the way we did then Pasquale would not exist. Jake, I miss watching 2 laptop screens when we could not decide which football match to watch. Mark, I still don't know how you got the better of me in FIFA (all the time). I always dominated you. In all honesty, thank you both for 3 great years; I am sure we're friends for life.

To my wonderful family. Mum you pushed me into being a normal human being; without you I would be a lazy slob who would have gone to football college, so thank you! Dad, you are relaxation personified; speaking to you makes me calm and any feeling of stress filters away, so thank you! And sister, I can't thank you enough for always being there for me and helping me dissect through any problems I have come to you with. I'm lucky to have the family that I do.

Finally, to the DTC thanks, I could not have wished for a better group to start my PhD quest with!

#SomethingMResYear!

## **Author's Declaration**

“I declare that, except where explicit reference is made to the contribution of others, this thesis is the result of my own work and has not been submitted for any other degree at the University of Glasgow or any other institution”

Ricky Unadkat

## Definitions/Abbreviations

ABBREVIATION	DEFINITION
<b>2D</b>	Two-dimensional
<b>3D</b>	Three-dimensional
<b>AFM</b>	Atomic force microscopy
<b>A-PCL</b>	Amorphous polycaprolactone
<b>BSA</b>	Bovine serum albumin
<b>CAMP</b>	Cyclic adenosine monophosphate
<b>C-PCL</b>	Semi-crystalline polycaprolactone
<b>DAG</b>	Diacylglycerol
<b>DAPI</b>	4',6-diamidino-2-phenylindole
<b>DIC</b>	Digital image correlation
<b>DMEM</b>	Dulbecco's Modified Eagle Medium
<b>DNA</b>	Deoxyribonucleic Acid
<b>DO</b>	Distraction osteogenesis
<b>ECM</b>	Extracellular matrix
<b>EGF</b>	Epidermal growth factor
<b>ERK</b>	Extracellular signal-regulated protein kinase

<b>FA</b>	Focal adhesion
<b>F-ACTIN</b>	Filamentous actin
<b>FAK</b>	Focal Adhesion Kinase
<b>FEA</b>	Finite element analysis
<b>FITC</b>	Fluorescein isothiocyanate
<b>FN</b>	Fibronectin
<b>G-ACTIN</b>	Globular actin
<b>GAG</b>	Glycos-amino-glycan
<b>GAP</b>	GTPase activating proteins
<b>GDIS</b>	Guanine dissociation inhibitors
<b>GDP</b>	Guanosine Diphosphate
<b>GEF</b>	Guanine nucleotide exchange factors
<b>GLCM</b>	Gray-Level Co-Occurrence Matrix
<b>GTP</b>	Guanosine triphosphatase
<b>HDL</b>	high density lipoprotein
<b>HSA</b>	Human serum albumin
<b>IGF</b>	Insulin like growth factor
<b>IGG</b>	Human serum immunoglobulin
<b>MAPK</b>	Mitogen activated protein kinase

<b>MLCK</b>	Myosin Light Chain Kinase
<b>MRTF-A</b>	myocardin-related transcription factor A
<b>PCL</b>	polycaprolactone
<b>PDGF</b>	Platelet derived growth factor
<b>PDMS</b>	Polydimethylsiloxane
<b>PGE2</b>	Prostaglandin E2
<b>PKC</b>	Protein kinase c
<b>PLC</b>	Phospholipase C
<b>PLM</b>	Polarised light microscopy
<b>PTFE</b>	Polytetrafluoroethylene
<b>ROCK</b>	Rho associated kinase
<b>SEM</b>	Scanning Electron Microscopy
<b>SRE</b>	Serum response element
<b>SRF</b>	Serum response factor
<b>TGFB</b>	Transforming growth factor beta
<b>TRITC</b>	Tetramethylrhodamine
<b>WCA</b>	Water contact angle
<b>A -SMA</b>	$\alpha$ -smooth muscle actin

# 1 Introduction

The ability of human tissue to stretch and expand over time can be seen in physiological and pathological situations. Laxity of the abdominal wall following 9 months of pregnancy is a typical example of the body's ability to adapt to tensile forces. Stretching of chest skin to form a ptotic breast mound following puberty under hormonal influence is also another one of many forms of physiological tissue expansion. Skeletal tissues also demonstrate such characteristics; an example is the stretching of the calvaria at the level of the cranial sutures during infant brain growth. In pathological situations, skin and soft-tissues over benign tumours such as lipomas and malignant tumours such as soft-tissue sarcomas also show stretching and expansion. Tissue expanders extend this natural principle to create excess tissue bulk by utilising the ability of tissue under constant strain to stretch and expand over a period of time. (Wagh et al., 2014).

The first attempts at tissue expansion were directed at bone where Codvilla reported femoral elongation using an external pin and traction load of 25-30 kg, followed by Magnuson in 1908, who reported the use of an external traction device to surgically lengthen bones in the leg (Jordan et al., 2013). He also reported that this could be used to successfully and concomitantly stretch the soft tissues of the leg as well. Thereafter Putti in 1921 showed that sustained traction on bone over a month's period could result in 8-10 cm of lengthening not only of bone, but also soft-tissue structures such as the muscles, nerves and blood vessels (Wagh et al., 2013).

## 1.1 Distraction Osteogenesis

Distraction osteogenesis (DO) is the gradual lengthening of bone by applying controlled mechanical force in order to separate osteotomised bone segments (Djasim et al., 2009). DO induces new bone formation along the vector of pull without requiring the use of bone graft (Jiang et al., 2010). It takes place over the course of three phases (Figure 1.1). The first phase is the latency period immediately following the fracture of the bone (either osteotomy or corticotomy) which allows for healing. As the bone is healing, the two pieces are slowly pulled apart in a controlled manner, a process known as the distraction phase. If the bone is pulled apart too quickly, it may not be able to form in between the two pieces and a fibrous cartilage union will result. If the bone is distracted too slowly, it will result in an early consolidation with bone forming across the distraction gap before the desired length is reached (G. Kumar & Narayan, 2014). New bone forms centripetally from the edges of the bone towards the middle of the distraction gap (Rowe et al., 1998). The consolidation phase is the final phase of DO, occurring when the bone that has formed centripetally between the two bone segments becomes mineralized.

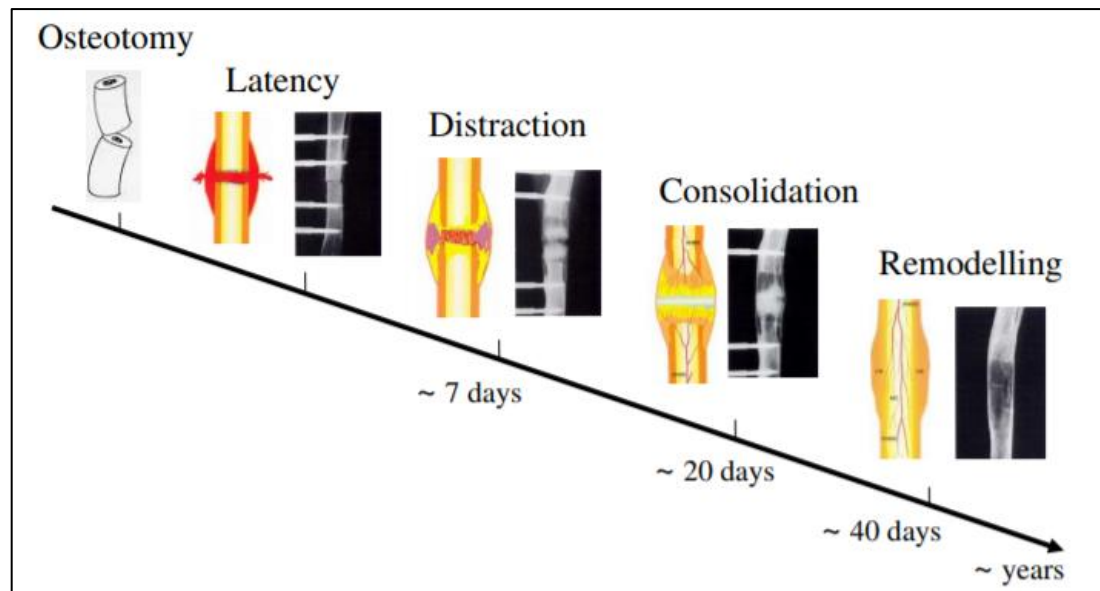


**Figure 1-1. Phases of distraction osteogenesis.** The latency phase is the healing phase which begins straight after fracture. The distraction phase is when the 2 pieces of bone are pulled apart. The consolidation phase is when mineralisation occurs in the separation gap, and the remodelling phase is where repair is completed (Birch & Samchukov, 2004).

Gavril Ilizarov was a Soviet physician who popularized distraction osteogenesis of the long bones of the legs. Through his research and clinical procedures, he created the Law of Tension-Stresses, which states that gradual traction on living tissues creates stresses that can stimulate and maintain the regeneration and active growth of certain tissue structures (M. Li et al., 2018). His procedure and techniques using an external ring fixator came to be known as the Ilizarov method and formed the basis of distraction rates used today. The daily extension rate and regime is still however disputed (G. Kumar & Narayan, 2014). In many cases, the overall distraction takes place over several distractions per day, but it is not uncommon to see the use of anywhere from 1-4 distractions per day to achieve an overall distraction length. The distraction length that is most commonly used is 1mm/day (Farhadieh et al., 2000; King et al., 2003; Reina-Romo et al., 2009); higher rates have resulted in a higher incidence of adverse effects such as severe soft-tissue contractures and loss of nerve function as well as microtrauma formation and micro-haematoma formation (Natu et al., 2014). Another possible distraction method is automated continuous distraction, where distraction is applied continuously in small increments over a 24 hour period (Djasim et al., 2009). Using continuous DO in rabbits has shown significantly more regenerated bone volume in the central part of the regenerated area than the use of discontinuous DO, while also producing higher osteoblastic activity and more blood vessels (Djasim et al., 2009). Decreasing the distraction rate to 0.5mm/day has also shown to have an adverse effect in that premature consolidation occurs.

Frequently recommended values such as distraction rates of 1 mm/day distributed over two increments per day (i.e. 0.5 mm every 12 hours) ultimately rely on intuition, experience and anecdotal evidence rather than a systematic understanding of the involved processes (Askari et al., 2006; Bhatt et al., 2007; Saunders et al., 2010). Optimal distraction parameters might very well depend on factors such as age, sex, localization and general health status of the patients; generic recommendations do not regard any of those factors (Niemeyer et al., 2018). A better understanding of the mechanobiological processes governing tissue differentiation during DO might therefore provide an opportunity to identify improved procedures that could reduce the rate of complications and failure.

Distraction forces applied to bone create tension in surrounding soft tissues, initiating a sequence of adaptive changes in skin, blood vessels, nerves, muscle, ligament, tendon, and cartilage. Part of the long-term success of DO depends on the ability of the surrounding soft tissues to tolerate distraction forces and to adapt to the resulting increase in skeletal length and volume. Imaging has shown that bone trabeculae and fibrous tissue align in the direction of the vector of distraction (Djasim et al., 2009). Furthermore cells residing within the distraction gap have also shown to align parallel to the vector of distraction (Karaharju-Suvanto et al., 1992). This adaptive process requires better understanding in order to combat the high incidence of soft tissue complications in relation to the process (Natu et al., 2014).

Gradual bone lengthening has a negative impact on the surrounding muscles through stretch; impalement by pins and wires; pain and inflammation. The speed of the gain in length with a 1mm/day rate is about 4 to 8 times faster than during the adolescent growth spurt (Aronson & McCarthy, 1994). The elastic limit of stretched muscles (stress-strain curve) is 10-15 % of the length at rest; excessive stretch leads to plastic deformation and subsequent contractures which commonly affect muscles spanning two joints (rectus femoris, hamstrings). Nerves, vessels and skin adapt to a certain degree in length during the distraction process; however the recovery time from temporary degenerative changes can be expected to be in the region of 2 months after halting distraction (Ippolito et al., 2011). Excessive gradual (>20-30 %) or acute distraction (>15 %) may both lead to partial or complete loss of nerve potentials (Lee et al., 2018; Strong et al., 1994). Expansion rate used in DO is mainly determined by observation; furthermore, only long-term animal or human experimentation/studies have been used to evaluate different DO rates and loading regimes.

This chapter will discuss important components to consider when developing a top-down model for soft tissue damage in DO. Top-down models involve isolating cells lines which are relevant to the problem defined and culturing them on substrates to apply the physiological mechanism that they are being investigated for. The global aim of the model in this instance is to help understand relatable cell and molecular pathway responses better with a view to optimising the DO procedure.

The components will be discussed in the following order:

- Structure and composition of soft tissue governing mechanical properties.
- Proteomic pathways and inflammatory molecules involved in soft tissue stretching.
- Fibroblast importance in mechanically stretched tissue.
- Current in vitro methods which can be utilised to investigate soft tissue stretching.

Following the consideration of these components, a strategy for the development of this model will be outlined, leading into project aims. This chapter will then conclude by giving an outline of what each chapter succeeding this one comprises.

## **1.2 Composition of Soft Tissue Determining its Mechanical Properties**

Soft tissues vary in their constitutive structures and composition, yielding vast differences in characteristic form and function between types. However, in soft tissues there are surprisingly few base structural components that significantly affect overall biological or mechanical function. Constituents of tissue can typically be classified as either extracellular or cellular. For most soft tissues with load-bearing function, the proteins collagen and elastin are dominant components of the extracellular matrix (Goth et al., 2016); Figure 1.2 illustrates how these major structural components reside in connective tissue amongst other components to make up the majority of soft tissues.

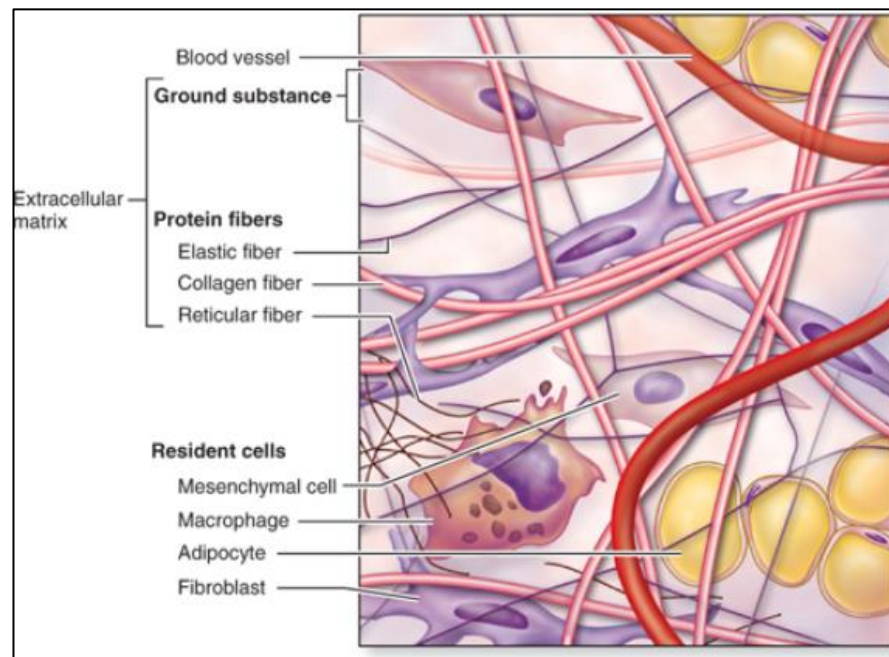


**Figure 1-2. Schematic of cells residing in connective tissue matrix with elastin and collagen fibrils. The extracellular matrix determines tissue mechanical properties and is comprised of collagen, elastin and reticular fibers. Collagen fibers determine tensile properties of the tissue, while elastin forms low stiffness cross-linked networks across the extracellular matrix. Reticular fibers are thin collagen fibers which support early synthesized extracellular matrix. The ground substance is an unstructured material that fills the space between cells and fibres; it is primarily composed of water, proteoglycans and cell adhesion proteins (Mescher, 2010).**

Type I collagen is the most abundant protein in the body and is the major determinant of mechanical behaviour of soft tissues (Gelse et al., 2003). At the molecular level, tropocollagen molecules are composed of a triple helix of three  $\alpha$  chains that arrange themselves into a quarter-staggered array to form collagen fibrils (Gelse et al., 2003). Collagen fibrils form the functional subunits of the collagen fibers, as described by the Hodge-Petruska model (Petruska & Hodge, 2006). Like the fibrils from which their functional properties are derived, collagen fibers exhibit high tensile but low flexural stiffness (Sacks et al., 2009). Thus, the fiber longitudinal axial direction is the primary determinant of the stiffness of the tissue composite. Collagen fibers typically have a stiffness of 1 GPa and extend by no more than 4-5% (Z. L. Shen et al., 2008). The way fibrils form and arrange themselves in tissue determines the tissues functional mechanical properties. In tendons and ligaments for example, collagen fibrils are densely packed in a parallel form where a localised direction change acts as a hinge to allow for crimping of the tissue (Gathercole & Keller, 1991). In tissues such as skin and nerve, the fibrils arrange in a thinner, more uniform manner with a helical subfibrillar arrangement. These fibrils appear in a parallel and sinusoidal manner (Franchi et al., 2008). The stiffer, crimped fibrils associated with tendons and

ligaments enable compliance to high unidirectional tensional forces (Gathercole & Keller, 1991). This is in contrast to the flexible thinner fibrils with helical subfibrils in skin and nerve, which adapt to extreme curvatures without damage to enable multidirectional compliance at lower loads (Franchi et al., 2008).

Although collagen fibrils are the principal source of tensile strength in soft tissues, elastin forms complex cross-linked fibrous networks of comparatively low modulus that assist in tissue recoil as well as maintenance of collagen fibre crimp (Debelle & Tamburro, 1999). The arrangement, structure and organisation of elastic fibres are again reflected in the function of the tissue. For example, in arteries, elastic fibres are organised in concentric rings, while in the lung elastic fibres form fine branched network throughout the organ. In ligaments and tendons, fibres are oriented longitudinally, parallel to collagen fibrils (Mithieux & Weiss, 2005). Finally, glycosaminoglycans (GAGs) are known to affect water retention in soft tissues (Lovekamp et al., 2006); the loss of GAGs reduces tissue thickness and diminishes rehydration capacity. GAGs are not a primary load-bearing component but do maintain tissue volume and act as a dampening agent to smooth rapid motions (Eckert et al., 2013).

It can be seen from the above that structure determines function and structure is controlled by the soft tissue microenvironment where cell growth, cell death, differentiation, propagation, protein production/alteration signalling via mechanical stimulation all impact tissue structure (Chanet & Martin, 2014; Fulda et al., 2010; Kubow et al., 2015). It is therefore important to understand how cells interact with their extracellular matrix (ECM) components, and furthermore how these interactions can result in damaging of soft tissue when it is placed under tension during DO.

## 1.3 Cell-Matrix Interactions

The way in which cells communicate with the ECM is through focal adhesions (FAs), which are specialized adhesion organelles that mediate various biological functions and responses through integrin surface receptor binding. Integrins are a family of alpha-beta heterodimer transmembrane receptors that bind extracellular matrix or cell surface-bound ligands. Activation of integrins and ligand binding leads to FA-associated proteins being recruited from the cytosol to bind to integrin cytoplasmic tails as well as one another. Together, these proteins form thin (200 nm), distinct, plasma membrane-associated FA plaques (0.1-10  $\mu\text{m}^2$  surface area) which connect the ECM to intracellular F-actin of the cytoskeleton (Bershadsky et al., 2003) (Figure 1.3). Talin and vinculin provide one linkage between integrins and actin; the ILK-PINCH-parvin pathway provides another, as do filamin and  $\alpha$ -actinin (Humphrey et al., 2014).

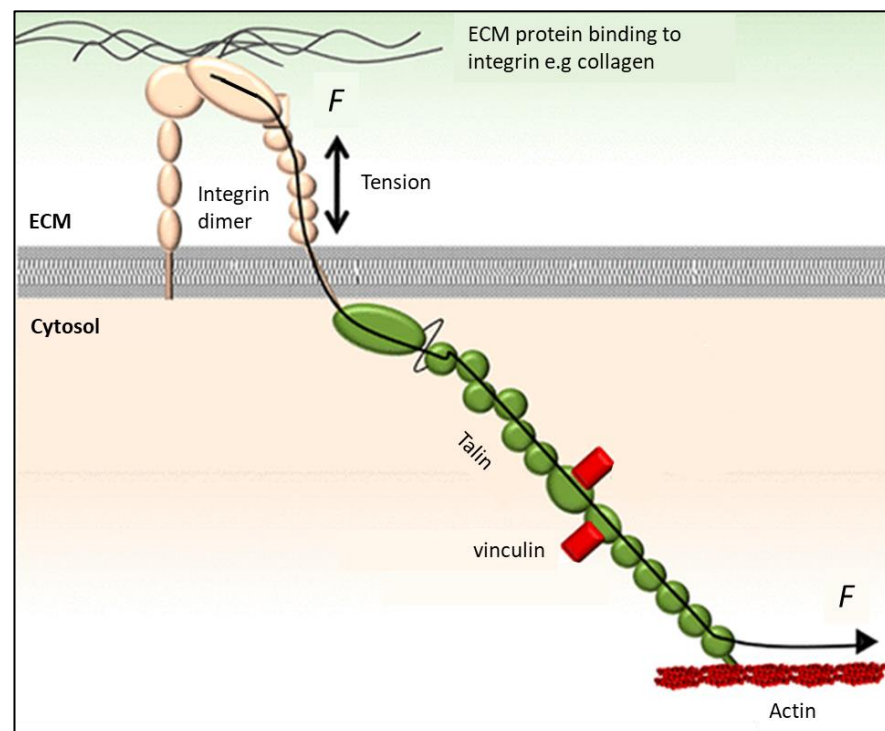


**Figure 1-3. Schematic representing how Integrins bind to extracellular matrix components initiating focal adhesion complexes and actin filament formation; the example depicted shows how Talin and vinculin provide one linkage between integrins and actin (adapted from Chakraborty et al., 2019).**

Integrins in conjunction with FA-associated proteins perform four basic functions: First, the integrins bind extracellular ligands to mediate cell adhesion to ECM or other cells. Second, integrin engagement leads to signalling from FAs to induce different cellular responses (e.g. proliferation/differentiation/apoptosis). Third, FA proteins link the cytoskeleton to integrins, allowing cells to transduce force generated in the actomyosin system to the ECM or other cells, e.g. to drive tissue morphogenesis or cell movement. Finally, FAs act as cytoskeletal regulators, controlling cytoskeletal organization via physical interactions with actin filaments and regulating dynamics through signalling to control the activity of actin-binding proteins and myosin motors. FAs can mediate responses through the same class of receptor by varying FA protein composition (Geiger et al., 2009).

Force transmission across the matrix can strengthen integrin-mediated adhesions (Bershadsky et al., 2003; Moore et al., 2010). Signals are transmitted as a result of unfolding protein domains and a change in binding affinities. The matrix component fibronectin was the first protein for which this was shown; forces expose binding sites in fibronectin that promote its self-assembly into fibrils upon stretching (Zhong et al., 1998). Research demonstrated fibronectin unfolding within fibrils in response to actomyosin-dependent forces through FRET (Baneyx et al., 2002). Further work in this field showed that integrin-cytoskeletal linkers such as talin and filamin undergo domain unfolding upon stretching. Stretching talin enables it to bind vinculin (Del Rio et al., 2009; Patel et al., 2006), which in turn binds actin and reinforces the link between integrins and actin (Dumbauld et al., 2010; Grashoff et al., 2010).

Single molecule studies show that upon application of a load between 2 and 5 pN to isolated filamin A constructs binding to integrin, glycoprotein, and migfilin peptides increases (Rognoni et al., 2012). This work is supported by studies in live cells using fluorescence-based molecular force sensors, which demonstrated tension across filamin and the talin-vinculin assembly (Grashoff et al., 2010; Meng et al., 2011). Such studies indicate unfolding of protein domains due to tissue deformation can impact protein interactions leading to signalling cascades important in mechanosensing.

## 1.4 Cellular Mechanisms Involved in Stretching of Tissue

As well as integrins and focal adhesions, membrane proteins such as G proteins may also be involved in mechanotransduction (Silver et al., 2003). Mechanical stimulation has shown to change the conformation of G protein that leads to growth factor changes which initiates secondary messenger cascades leading to cell growth (Vandeburgh, 1992). Cyclic strain has shown to significantly decreased steady state levels of G protein and adenylate cyclase activity (Wiersbitzky et al., 1994).

Furthermore, mechanical stress triggers activation of stretch-activated ion channels (Silver et al., 2003). Stretch activated channels reportedly allow the passage of cations such as  $\text{Ca}^{2+}$ ,  $\text{K}^+$  and  $\text{Na}^+$ . In muscle cells  $\text{Ca}^{2+}$  influx through voltage-gated channels induces a transient elevation in intracellular  $\text{Ca}^{2+}$  levels (Davis et al., 1992).  $\text{Ca}^{2+}$  influx is activated by mechanical stimulation and leads to membrane depolarization and cell contraction. Strain induced  $\text{Ca}^{2+}$  signal transmission is likely to involve the actin microfilament system as an actin polymerization inhibitor was found to abolish  $\text{Ca}^{2+}$  responses that were induced by mechanical strain (Diamond et al., 1994).  $\text{Ca}^{2+}$  ion involvement in phospholipase C (PLC) activation has been proposed; this involves catalysing the generation of PLC-derived inositol phosphates and diacylglycerol (DAG) necessary for PKC activation (Rhee et al., 1992). The presence of mechanical forces at the cell-ECM interface may not only affect stretch-activated ion channels but may also modulate changes in cell membrane structure with membrane associated changes in the cell cytoskeleton. Actin binding proteins, including vinculin, and gelsolin, are related to the phosphoinositide and the Protein Kinase C (PKC) pathways and may undergo or lead to conformational changes during membrane activation (Silver et al., 2003).

PKC has been proposed to play a pivotal role in signal transduction by mediating a variety of biological responses (Nishizuka et al., 1995). Hydrolysis of phospholipids in cell membranes, catalysed by PLC, produces inositol phosphates

and diacylglycerol, leading to PKC activation (Takei et al., 1998). Mechanical strain in muscle cells activates PLC, phospholipase A2 and phospholipase D, DAG and inositol triphosphate (Silver et al., 2003). Inhibition of PLC activation abolishes the strain-induced responses in endothelial cells (Diamond et al., 1994). PLC $\gamma$ 12 is stimulated by the receptor tyrosine as well as the EGF receptor, suggesting that EGF exhibits its stimulatory effect through the PLC and PKC pathway. PLCB is also activated in association with G protein that could activate mitogen-activated kinase (MAPK) through PKC-related pathways (Blumer et al., 1994). The mitogen-activated kinase (MAPK), also known as extracellular signal-regulated protein kinase (ERK), plays an important role in cell signalling (Cobb et al., 1995). Changes in ERK and MAPK activities have been observed in aged human skin (Chung et al., 2000). Secondary messengers implicated in strain-induced cellular responses include cyclic adenosine monophosphate (cAMP) and prostaglandin E2 (PGE2). cAMP is reported to influence protein cell growth, differentiation and protein synthesis (Takei et al., 1997). Cyclic strain results in increased protein production by keratinocytes and a decrease in cAMP and cAMP-dependent protein kinase A activity (Takei et al., 1997).

## **1.5 Growth Factor Involvement**

Growth factors such as platelet derived growth factor (PDGF) and angiotensin II have been implicated in strain-induced cellular growth in vascular tissues (Wilson et al., 1993, Sudhir et al., 1993). The below schematic (Figure 1.4) provides a basic outlay as to how growth factors may promote responses in response to mechanical stretch.

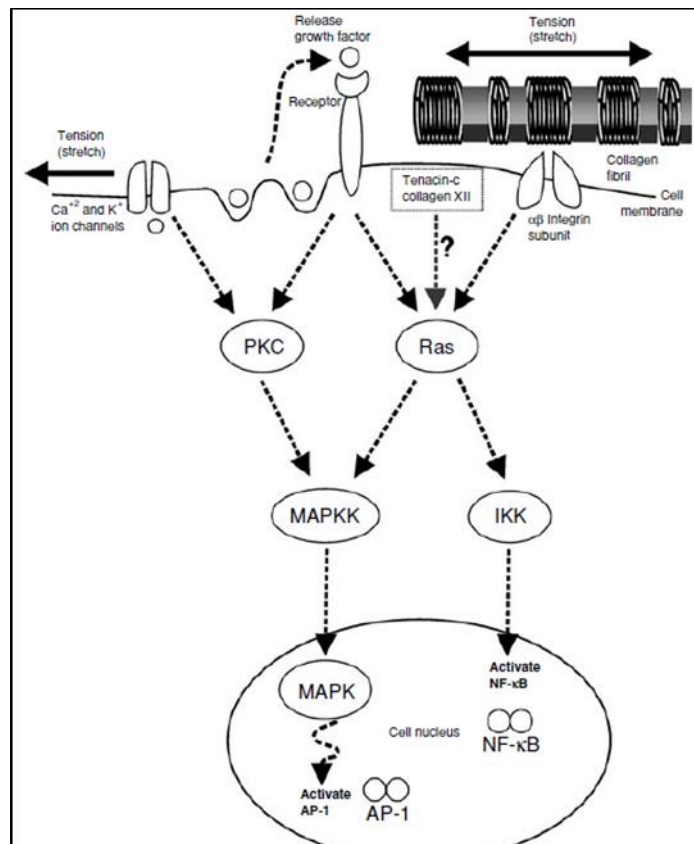


**Figure 1-4. Summary of biochemical pathways that may be involved in stretching due to mechanotransduction. Tensile stresses cause stretching of intracellular junctions, activation of membrane ion channels, or release of growth factors that leads to activation of secondary messengers. Secondary messenger activation leads to activation of factors such as NF-κB that binds to promoter sequences in genes such as those expressed for tenascin-C and type XII collagen. Stretching of ECM-integrin contacts and cell intercellular junctions are known to trigger MAP kinases pathways (MAPKK, and MAPK) via GTPase Ras. MAPKs translocate to the nucleus and activate transcription factors such as AP-1. Alternately, members of the MAP kinase kinase kinase (MAPKKK) family have been shown to activate the I-κB kinase (IKK) complex, which phosphorylates I-κB and leads to the release of NF-κ, which in turn, translocates to the nucleus. In the nucleus, NF-κB binds to its target promoter sequence. Another putative route for MAPK activation is via autocrine release of growth factors and activation of protein kinase C (PKC). Mechanical stretch also leads to activation of stretch response promoter regions in tenascin-C and type XII collagen genes (Chiquet, 1999).**

The epidermal growth factor (EGF) receptor has been shown to bind to actin binding proteins, which could lead to actin polymerisation and further membrane ruffles (Diakonova et al., 1995). Platelet derived growth factor (PDGF) and insulin-like growth factor (IGF) have also shown to be associated with membrane ruffling; this suggests that growth regulation by these factors is likely to be mediated by cytoskeletal pathways. Upon addition of EGF, it has been demonstrated that the

tyrosine residues on the EGF receptor become phosphorylated and there is a strong co-localisation of F-actin suggesting that cytoskeleton linked EGF receptors seem to be important in inducing cell proliferation through the microfilament system (van Bergen et al., 1992). Membrane ruffling sites have shown to consist of high levels of actin, EGF receptors, PLCygl, and tyrosine phosphorylated proteins (Payraastre et al., 1991).

The EGF receptor is a member of the tyrosine kinase receptor family, and two types have been identified; high affinity and low affinity. Effects so far seem to occur upon binding of the high affinity receptor. This stimulates ligand-induced dimerization, activating the intrinsic protein-tyrosine kinase activity of the receptor. The tyrosine kinase activity, in turn, initiates a signal transduction cascade that results in a variety of biochemical changes within the cell; a rise in intracellular calcium levels, increased glycolysis and protein synthesis, and increases in the expression of certain genes including the gene for EGFR, ultimately leading to DNA synthesis and cell proliferation (Defize et al., 1989). Keratinocytes stretched *in vitro* using silicon substrates coated with collagen 1 have recently shown that mechanical stretching induces proliferative signals via phosphorylation of the EGF receptor. Substrates were stretched by 20% and EGFR phosphorylation was significantly higher to control groups between 2 and 5 minutes of stretching (Yano S et al., 2006).

Transforming growth factor-beta (TGFB) is a family of multifunctional 25 kDa proteins. Members of the TGFB superfamily are multifunctional cytokines, which include TGFBs, activins, and bone morphogenetic proteins (BMPs). These cytokines bind to two different types of serine/threonine kinase receptors (type I and type II), and activate intracellular substrates, e.g. SMAD proteins. The type II receptor kinases are constitutively active, and transactivate the type I receptor kinases, which then transmit signals inside cells. Thus, the type I receptors act downstream of the type II receptors and determine the specificity of intracellular signals (Heldin et al., 1997). TGFB is known to regulate the differentiation of cells, induce chemotaxis of cells, and to induce the accumulation of extracellular matrix proteins. *In vivo*, TGFB stimulates the repair of soft as well as hard tissues. It also acts as a potent immunosuppressant. TGFB is produced as latent high molecular weight complexes; since it is produced by many different cell types, and most

cells have receptors for TGF $\beta$ , the activation of latent TGF $\beta$  is likely to be an important step in the regulation of its action (Sporn et al., 1990). There are currently 5 isoforms of TGF $\beta$ ; TGF $\beta$ 1 has been shown to have a role in re-epithelisation of skin whereas TGF $\beta$ 3 is implicated in epidermal differentiation (Schmid et al., 1993).

## **1.6 Fibroblasts and their Importance in Tissue Expansion**

Fibroblasts are mesenchymal cells that are responsible for normal connective tissue production and turnover. Fibroblasts can secrete elastin, different types of collagens, glycoproteins, and GAGs; they coordinate their synthetic and mechanical machinery to organize the constituents that give rise to the overall structural organization, and thus mechanical properties, of the tissues. They can also secrete proteases, most notably members of the matrix metalloproteinase family, that degrade various structural constituents (Nagase et al., 2006).

Under normal physiological circumstances, soft tissues typically contain relatively few active fibroblasts. By actively synthesizing and cross-linking fibrillar ECM proteins such as collagen, fibroblasts establish a resting tension, ensuring that normal connective tissue retains its shape after application of external mechanical load (Grenier et al., 2005). The ECM is continually subjected to mechanical tension; however, this tension is minimally transmitted to fibroblasts. The fibroblasts are protected, even from relatively sizeable external loads, by the mechanical properties of the surrounding ECM; fibroblasts are therefore stress shielded by the ECM that they deposit and remodel (Tomasek et al., 2002).

Despite stress shielding, a feedback loop exists between the fibroblasts and the ECM to register and regulate the tensional homeostasis (Tomasek et al., 2002). The fibroblast may respond to ongoing structural change in the tensional state of the surrounding ECM by adapting the molecular composition (collagen type I) and density, the diameter of the collagen fibril and the organisation (architecture) of the collagen network. Thus, to understand the fibroblasts' responses to

mechanical forces properly, the fibroblast must be considered together with the ECM as one operational unit (Eastwood et al., 1998).

Taking skin as an example, fibroblasts in the dermis are mechano-responsive; as the tensional homeostasis of the surrounding ECM is interrupted, the fibroblasts are activated to reconstruct damaged ECM and restore the initial tensional homeostasis (Chiquet et al., 2003). However, before this occurs, fibroblasts migrate to the defect site. Therefore, they make contact with the ECM and pull themselves along the collagen fibrils, generating traction forces in the ECM (Pellard, 2006). Thus, the fibroblasts, as well as the collagen fibrils, will be reorganized along the lines of tension (Tomasek et al., 2002). Research has shown that fibroblasts migrating along the ECM initiate traction forces that are sufficient to close small defects by themselves in a process called cell traction (Ehrlich et al., 1989). Upon reaching their defect site, fibroblasts proliferate on a large scale and start synthesizing a new collagen-containing matrix called granulation tissue. Furthermore, the fibroblasts transform to myofibroblasts (Tomasek et al., 2002). Differentiation of fibroblasts into myofibroblasts is induced by growth factors, such as TGF $\beta$ 1, specialized ECM molecules, the cellular fibronectin (FN) splice variant ED-A and mechanical tension in the surrounding tissue (Eastwood et al., 1998). This transformation process is characterized by the development of intracytoplasmic stress fibres, which confer to these cells the capacity of developing tension (Eastwood et al., 1998).

It has been shown that  $\alpha$ -smooth muscle actin ( $\alpha$ -SMA) expression is essential for the acquisition of a high contractile activity by myofibroblasts. The contractile activity of myofibroblasts is a crucial factor for connective tissue remodelling where a stressed matrix is created, this can further promote myofibroblast differentiation in a mechanical feedback loop (Hinz et al., 2003). The interaction between the fibrillar collagen network of the ECM and the myofibroblasts is critical for the mechanical regulation of the cell activity, resulting in connective tissue homeostasis. Cell-matrix junctions are key in the perception and transduction of mechanical tension signals. An altered mechanical load of the ECM stimulates the myofibroblasts to adjust their contractile activity and collagen deposition to achieve tensional homeostasis (Eastwood et al., 1998). A fibroblast

that does not experience extracellular tension, will not transform to a myofibroblast (Grinnell et al., 1999).

Under normal circumstances the collagen network is organized again and takes over the mechanical load, releasing the embedded myofibroblasts from stress (Tomasek et al., 2002). Under normal physiological circumstances, at this stage the contractile and synthesizing activity of myofibroblasts is terminated and their number is dramatically reduced by apoptosis (Grinnell et al., 1999). However, in certain cases such as chronic pathological wound healing this feedback loop fails and apoptosis of myofibroblasts does not occur (Figure 1.5). Thus, the excessive contractile and synthesizing activity continues, resulting in continuous matrix remodelling and retraction (Aarabi et al., 2007).

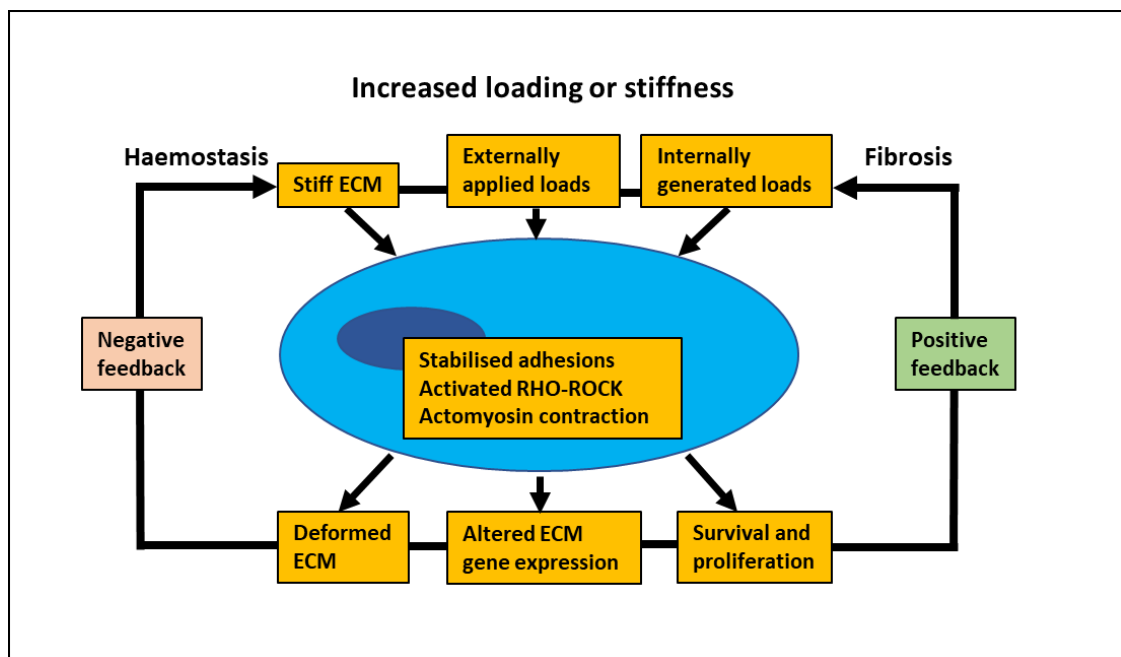


**Figure 1-5. Fibroblast regulation of extracellular matrix structure and function through feedback loop. Increased mechanical loading or matrix stiffness causes cell responses which either work towards matrix homeostasis (negative feedback loop) or develops fibrotic conditions (positive feedback loop). In both cases, stabilized focal adhesions of greater number or size and increased actomyosin contractility through Rho–Rho kinase pathway is key. (figure adapted from Humphrey et al., 2014).**

Although many other cell types, including macrophages, contribute either directly or indirectly to mechanical homeostasis in connective tissues, as a starting point for the model to be developed, fibroblasts will be the focus.

## 1.7 Current Methods Used for Inducing Stretch to Cells

There are many ways of investigating the impact of deformation on cells within soft tissue, ranging from measurements of stress-strain data by deforming parts of a single cell to stretching substrates with entire cell populations cultured on. These methods of investigation can broadly be classified by 3 experimental techniques (Figure 1.6): first, local probing of small parts of a single cell; second, mechanical loading of an entire cell; and third, simultaneous mechanical stressing of a population of cells.

Probing single cells can be achieved by techniques such as atomic force microscopy (AFM) and magnetic twisting cytometry. With an AFM, it is possible to cause a local deformation in the cell with a sharp tip at the free end of a flexible cantilever. The deflection of a laser beam at the top of the calibrated cantilever tip can be measured, and the applied force then estimated (Mathur et al., 2001). In the case of MTC, magnetic beads with functionalized surfaces are attached to a cell. An applied magnetic field creates a twisting moment on the beads, thereby deforming parts of the cell. With this method, one can estimate the elastic or viscoelastic properties of the deformed cellular part (Puig-De-Morales et al., 2001); this may be a useful technique in being able to contribute to a model for soft tissue stretching in terms of defining cell mechanical properties.

Mechanical Loading of entire cells has been done by micropipette aspiration or using optical tweezers. Micropipette aspiration deforms the cell via suction and the mechanical response is quantified by recording geometric changes in response to the suction (Evans & Yeung, 1989); the elastic shear modulus can be derived from the relation between the aspirated length and the aspiration pressure. In the case of optical tweezers, an attractive force is created between a dielectric bead

of high refractive index and a laser beam, pulling the bead toward the focal point of the trap. Two microbeads in such a laser trap can operate as tweezers and deform a cell (Falleroni et al., 2018). This method produces only small forces in the range of pico Newton and is therefore more often used for studies of molecule mechanics than for cells. Also, single cell methods such as these negate the effect of matrix deformation in response to tissue being stretched; therefore, for the purposes of this project, a method where populations of cells can be stretched alongside their relative matrix will be considered.

Shear-flow devices and substrate stretching devices are typical methods used for deformation of cell populations. Shear-flow devices either use a cone-and-plate viscometer, consisting of a stationary flat plate and a rotating, inverted cone where laminar and turbulent flows can be applied; or a parallel-plate flow chamber, in which cells are subjected to laminar flow (Usami et al., 1993). This technique is applicable in providing outputs for modelling certain in vivo behaviours (such as lung ischaemia), however stretching cell attached substrates is a more representative approach.

In terms of substrate stretching, uniaxial, biaxial and pressure-controlled elastic membrane stretching devices have historically been used (Banes et al., 1985; Neidlinger-Wilke et al., 1994; H. Wang et al., 1995). In brief, cells are cultured on a thin, transparent polymer substrate such as elastic polydimethylsiloxane (PDMS) which is coated with an ECM protein to make the surface adhesive for cells. The substrate is then mechanically deformed while cells are cultured on, and the effects of mechanical load on cell morphology and phenotype are then examined by means of microscopy.

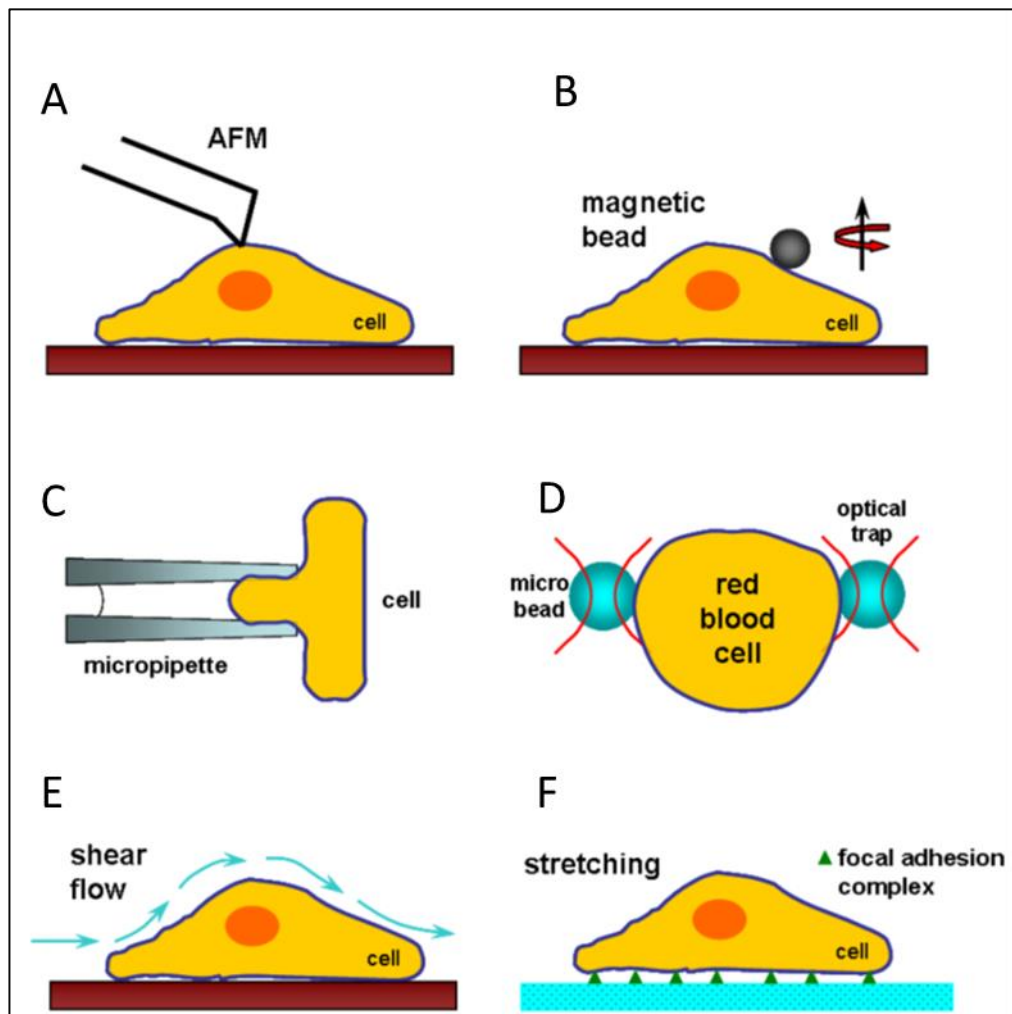


**Figure 1-6. Schematic of current methods used for mechanically deforming cells. A) Probing single cells using AFM. B) Probing individual cells using magnetic beads, C) Deforming single cells using micropipette aspiration. D) Deforming individual cells using optical traps. E) Using shear flow to stimulate entire cell populations. F) Stretching substrates cultured with cells to stimulate cell populations (Bao & Suresh, 2003).**

PDMS has been widely used in substrate stretching approaches as it offers significant advantages as a cell culture substrate, including a high optical transparency and easy manipulation of stiffness and surface coating. Elastomers that include PDMS are able to reliably deform their dimensions under applied forces. However elastomers upon being stretched retain tension in the material, and if the material is not gripped and held at the deformation applied, the material will return back to its original dimensions; this is unrepresentative of how a soft tissue would stretch and eventually permanently deform. Rectangular 3D gels such as collagen have also been used. Collagen gels are difficult to handle, and due to this, methods surrounding the application of tension to them face challenges. For example, a method developed where collagen gel was attached to

glass rods via Velcro strips inside a mini-incubator was subject to high friction loss in transmission of strain to strain gauges making the set up relatively insensitive (Delvoye et al., 1991). Eventually the system was developed where better feedback on strain was achieved (Kolodney & Wysolmerski, 1992) and subsequent quantitative investigations were performed with fibroblasts in a collagen lattice. Such techniques however focus on the application of adjustable, physiologically relevant mechanical load (Brown et al., 1998; Eastwood et al., 1998) where the final strain percentage is relatively low compared to what is required when investigating for the purposes of DO.

Current substrates used to model soft tissue stretching are therefore not applicable to what the model wishes to achieve in this project, therefore other polymer alternatives will be investigated in the subsequent chapter.

## **1.8 Project Aims**

The global project aim of this thesis is to understand how the cell response is impacted by mechanical stretching of tissues through a polymer substrate model, with a mind as to how this can be used to optimise stretching regimes (or even intervention therapies) for the purposes of DO. To this end, the aims of this thesis can be defined as:

- 1) Characterise a polymer which is ideal to model growth by stretch, before defining how its properties will be utilised to appropriately stimulate cells.
- 2) Design, develop and prototype devices relevant to the type of data acquisition required.
- 3) Elucidate cell responses in relation to the stretching mechanism of the polymer defined for studying soft tissue stretching.

## 1.9 Thesis Outline

Chapter 2 shows the production and characterisation of the polymer films to be used for the model of 'growth by stretch' through mechanical tensile testing, finite element analysis, and various imaging methods, with the chapter concluding how the deformation characteristics of the films will be used as a substrate for modelling soft tissue growth by stretch.

Chapter 3 outlines requirements before detailing devices designed and developed for cell culture experiments requiring substrate stretching.

Chapter 4 defines methods developed to culture and image cells on substrates defined in Chapter 2 using devices described in Chapter 3 to apply relevant stretch to substrates before and after culture. The cell response is subsequently analysed in terms of morphology, orientation and protein translocation. This chapter concludes by attributing the cell responses seen to the mechanics of the substrate they are cultured on.

Chapter 5 is a general discussion of the findings of this thesis, and neatly concludes what this work contributes to the field of cell mechanotransduction.

## 2 Characterisation of Polymer Film to Investigate Stretching of Soft Tissue

### 2.1 Introduction

When creating a system to model stretching of soft tissue, polymer films can be utilised to mimic a stretching profile typical of soft tissues. This would enable a representative mechanical load application to cells and their matrix of that incurred when soft tissue is stretched. For this artificial polymer based system to be useful, any substrate will have to be biocompatible, which in the case of polymers often requires surface modification. In the following I will introduce polymers used for the purposes of modelling soft tissue with the intent of defining key mechanical variables that are to be considered in the design of a model for stretching soft tissue. Material stiffness, and how biopolymers and tissues deform will be extensively described, before the processing of a rigid polymer: polycaprolactone (PCL) to form a cell substrate film is outlined; where the intent will be to explain how mechanical properties of it can be tailored by altering bond strength within the material via crystallinity to fit the purpose of the model to be developed.

Material stiffness in bioengineering has proved to be an important component when assessing biomaterial selection for various purposes. At the cellular level, key research has shown the ability to vary stiffness of materials to control stem cell differentiation amongst other cell responses (Engler et al., 2006). Polyacrylamide or gelatin gels are widely used in this aspect as the stiffness of them can be controlled within a range of 150Pa-150kPa (Flanagan et al., 2002; Leach et al., 2007; Mih & Tschumperlin, 2008) and 1-100kPa (Domke & Radmacher, 1998; Hall et al., 1997) respectively. Figure 2.1 below outlines polymers used in cell mechanotransduction studies alongside the range in stiffness that they can be made to. As a comparison the range of stiffness attributed to certain tissues is also provided in the same figure.

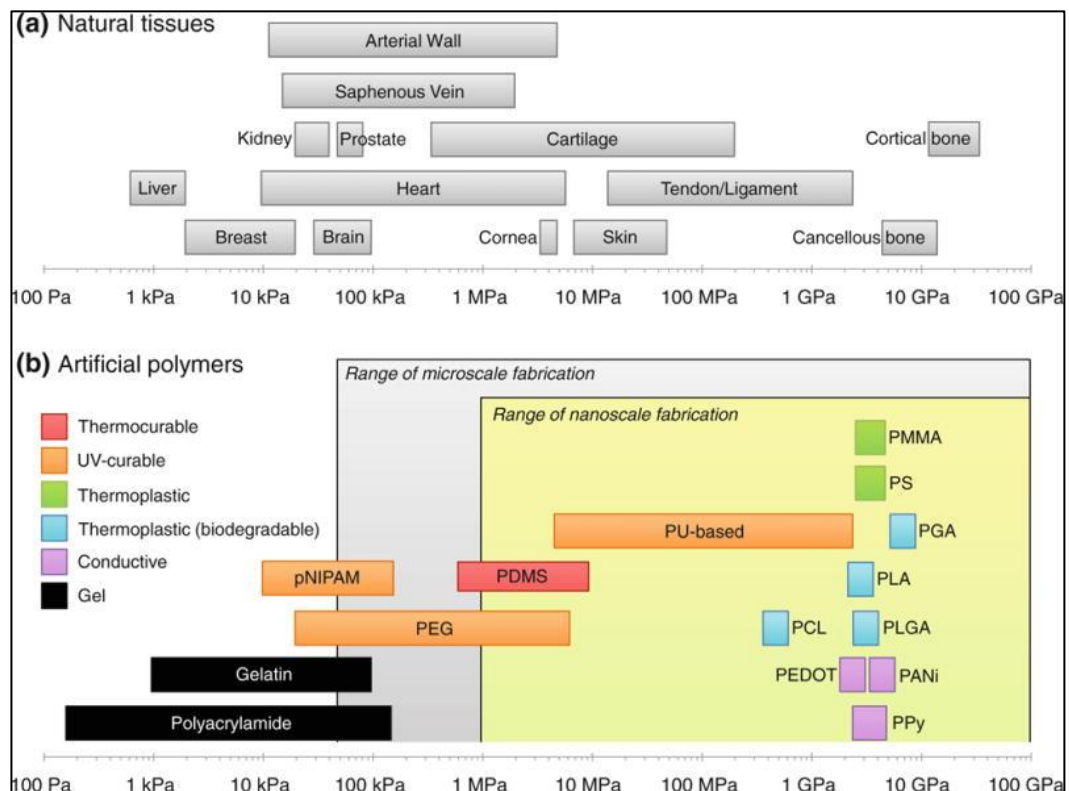


**Figure 2-1. Stiffness of tissue compared to polymers used for the purposes of cellular mechanotransduction studies. A) Illustrates the range of various tissue stiffnesses, and B) illustrates stiffnesses of different polymers used for cellular mechanotransduction studies (H. N. Kim et al., 2012).**

The stiffness of tissue is dictated by cell types within that tissue and structural organization of proteins and mineralisation levels in the ECM surrounding it; tissue stiffnesses range from a few kilopascals (kPa) to tens of gigapascals (GPa). The liver and breast display very low elastic stiffness around ~1 kPa, which is similar to that of polyacrylamide (150 Pa-150 kPa) or gelatin (1-100 kPa) (Nemir & West, 2010). Whereas cortical and cancellous bones are a lot stiffer at ~10 GPa, which corresponds to poly(methyl methacrylate) (PMMA) (2-4 GPa)(Nemir & West, 2010).

Stiffness has a direct influence on cell differentiation (Engler et al., 2006), however topography has also been shown to affect stem cell differentiation as well as other cell responses (Dalby et al., 2007; Meredith et al., 2007). In vivo, structure and alignment of cells and their ECM proteins within tissue contributes to function and mechanical properties of that tissue (for example alignment of cells and matrix in muscle allows for directional contraction). Material topography in cell culture models has demonstrated the ability to align cells and promote in vivo like properties as a result; for example, pre-aligned ligament cells have shown more efficient calcium wave propagation compared to randomly oriented ligament

cells undergoing stretch on PDMS substrates (Jones et al., 2005). From studies such as this, it can also be seen that material deformation can initiate certain cell responses. PDMS is a material which has regularly been used in ‘stretch’ investigations related to cells due to its high elongation at break (~160%) (Choi & Rogers, 2003). This property enables an application of cyclic stretching (stretching and releasing) onto single or multiple cells with desired tensions and frequency. This material has been useful in evaluating responses at the cellular level for tissues such as muscle (W. Kim et al., 2018), heart (Camelliti et al., 2005), cartilage (Beaupré et al., 2000), ligament and tendon (J. H. C. Wang et al., 2005), due to these tissues being inherently exposed to mechanical loads. It is therefore important to understand topography as well as stiffness and deformation all contribute to cell responses grown on a substrate. Figure 2.2 below summarises how a combination of the three variables contribute to cell responses.

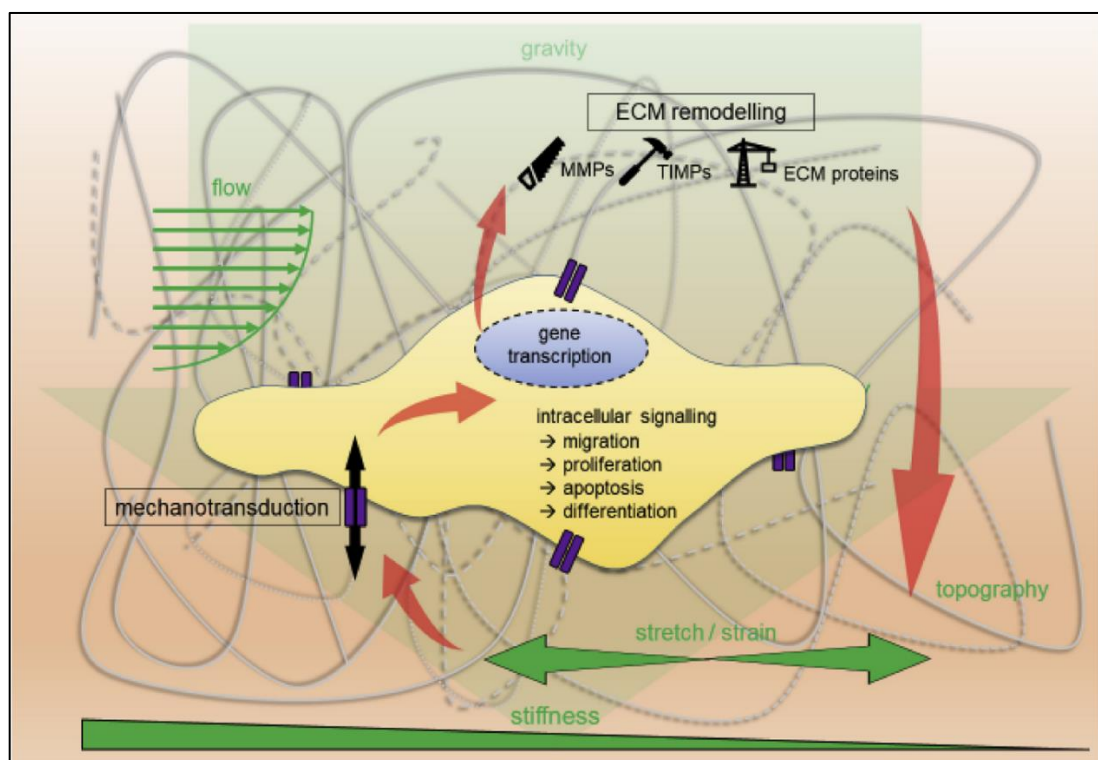


**Figure 2-2. Illustration of the feedback loop between cells and biomechanical signals from the ECM. The loop is depicted by red arrows and the green are the various biomechanical cues. Purple regions on the diagram indicate ECM receptors to the biomechanical cues, which in turn trigger intracellular responses; it can be seen that stiffness, topography and stretching of the ECM can combine to set off varying cell responses, such as migration, proliferation, apoptosis and differentiation, alongside the release of certain proteins (MMPs, TIMPs and other proteins which can impact the ECM) (Urbanczyk et al., 2019).**

Several studies have shown synergy between stiffness and topography in cell behaviours, where differences were demonstrated for cell migration, spreading and alignment compared to presence of just a single physical cue of stiffness or topography (C. C. Chen et al., 2009; Sochol et al., 2011; Tzvetkova-Chevolleau et al., 2008).

So far, stiffness has been mentioned as a main physical cue sensed by cells, and it is important to understand that the value for stiffness in these cases applies to the material in its elastic region when being put under compression or strain. To understand what is meant by ‘stiffness in the elastic region’ more clearly, the next section will focus on explaining mechanobiology terms such as stress and strain before describing the relevance of stress relaxation in a model for stretching soft tissue.

### **2.1.1 Stress, Strain and Stress-Relaxation**

Stress is the amount of force applied to an area to change its shape and is normalized to the area over which the force is applied to; it is reported in Newtons per square meter ( $\text{N/m}^2$ ), or Pascal (Pa). There are different types of stress: tensional (also known as tensile) stress, compressive stress, torsional stress and shear stress (Love, 2017). For example, pulling on an object would cause tensional stress, pressing on the object creates compressive stress, twisting on objects causes torsional stress, and applying forces parallel to an object, such as blood flow to an artery wall, is shear stress (N. Shen et al., 2017). For the purposes of this project, when stress is mentioned, it refers to tensional stress. Strain is the deformation of an object to an applied stress, and it is calculated by the change in length of material, divided by its original length. As it is a ratio, it has no units, but is commonly reported out as a percentage (Love, 2017). Stiffness is simply a measure for the change in stress required for a change in strain; this can be seen in the slope region outlined in Figure 2.3.

There are two main types of strain deformations: elastic deformation and plastic deformation. Elastic deformation is a temporary deformation that is recoverable

once a force is removed. For example, pulling on skin will cause a temporary deformation of the elastic fibers until the skin is released. The stiffness during elastic deformation is known as the Young's modulus, and is the measurement reported out for stiffness so far in the previous sections of this chapter. The soft polymers such as hydrogels and PDMS mentioned in the above section, break after a certain amount of elastic deformation, however, certain polymers which are more rigid and non-brittle may undergo plastic deformation if they are strained further than their elastic limit which is termed the yield point of the material (Figure 2.3). Plastic deformation is a permanent deformation where the material will remain at the length that it has been stretched to, after the stress has been released (Wilhelmi et al., 1998).

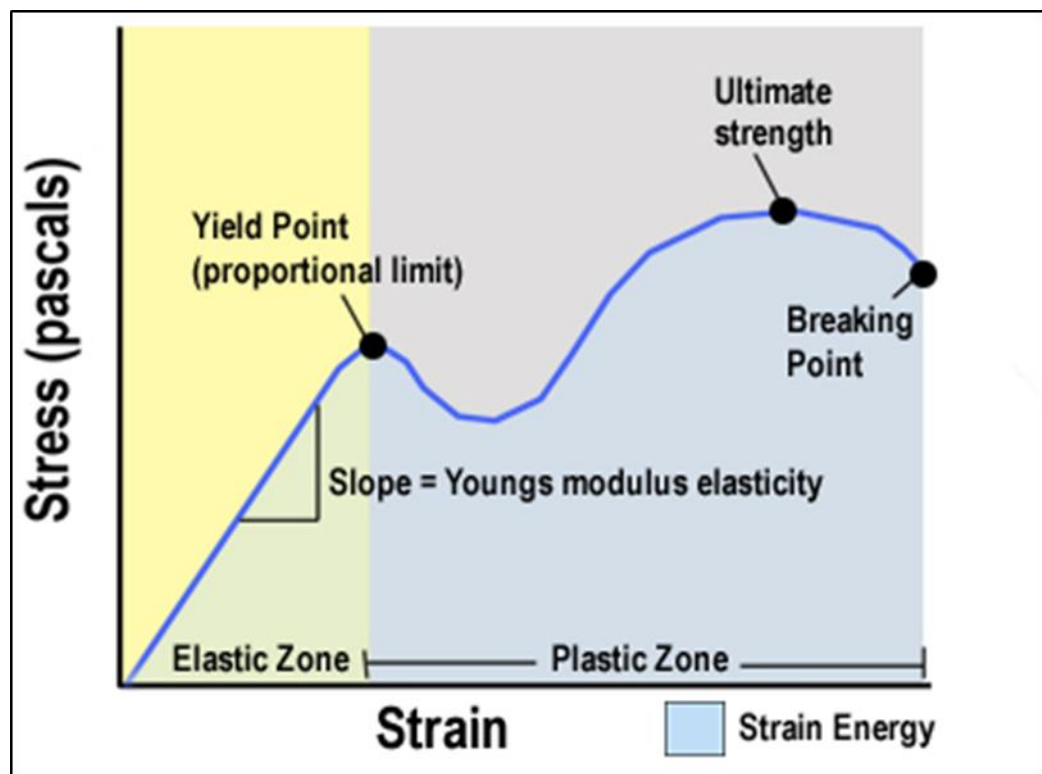
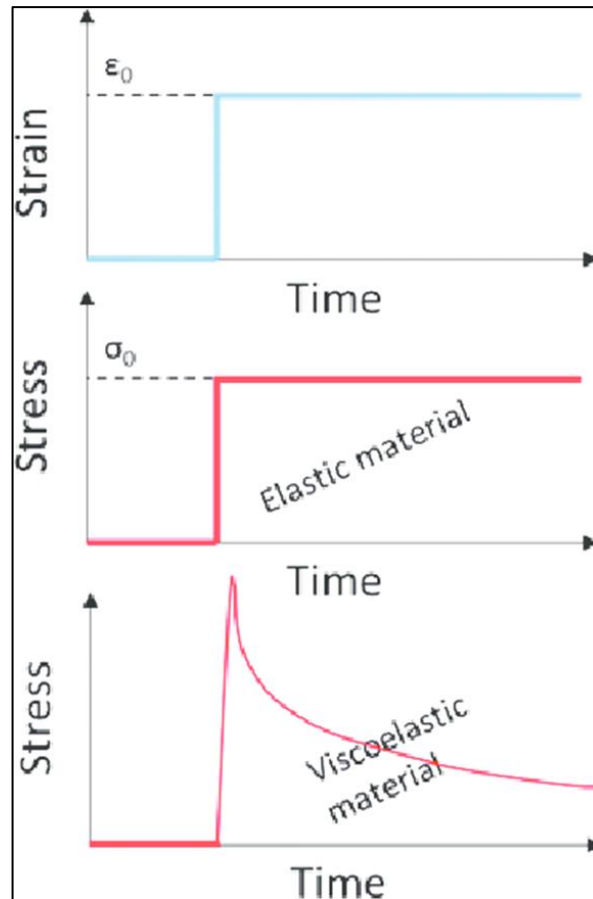


Figure 2-3. Typical stress strain for polymers that undergo plastic deformation. Stress is plotted against strain as a material is elongated. The initial linear region is the elastic region of the material, where the gradient of the line is a measure of the Young's Modulus ( $E$ ) of the material. The yield point is the top of the linear region; when extended beyond this, deformation of the material is plastic (image taken from [www.orthobullets.com](http://www.orthobullets.com)).

Soft tissues in vivo, when stretched exhibit viscoelastic behaviour. Viscoelastic materials undergo stress-relaxation; in the case of soft tissues, ECM molecules such as collagen and elastin extend and rearrange in response to mechanical forces

to decrease stress as strain is applied; however, they do not permanently deform and return to their original shape after the force is removed. Figure 2.4 below, highlights the difference between a viscoelastic material and an elastic material held for the same amount of time at a particular strain.



**Figure 2-4. Schematic illustrating difference between elastic and viscoelastic materials held at the same strain (top curve). In the elastic material, stress remains constant after it initially increases to reach the strain level achieved. The spike seen for the viscoelastic material is the initial stress required to reach that level of strain before molecular rearrangement occurs through time to reduce stress when held at that same strain (Naemi et al., 2016).**

The aim when stretching tissue during distraction osteogenesis is to stimulate tissue to grow due to the strain applied. This involves utilising the viscoelastic nature of tissue where applied deformation during the process turns permanent over time due to a combination of cell responses (such as proliferation/differentiation and protein secretion) where the ECM is remodelled to provide overall tissue extension.

The ability of tissue to stress relax upon loading is therefore key for it to adapt to continuous deformation (Chauduri et al., 2015, 2016; Bauer et al., 2017; Vining et al., 2019). Therefore for the purposes of developing a model for permanently

stretching soft tissue (as is done during distraction osteogenesis), the material selected as a substrate must be able to plastically deform so that tension is not held in the material during stretch and hold cycles. Furthermore, developing a polymer film with a relevant stretching profile to a typical soft tissue (Figure 2.5) is also important to enable cells and their matrix to be mechanically loaded in a manner similar to what they would incur when soft tissue is stretched. Figure 2.5 illustrates how tensile curves for soft tissues vary based on speed and what orientation the tissue is tested in; however, the profile in each case is similar where the curve gradient gradually increases as deformation is increased.

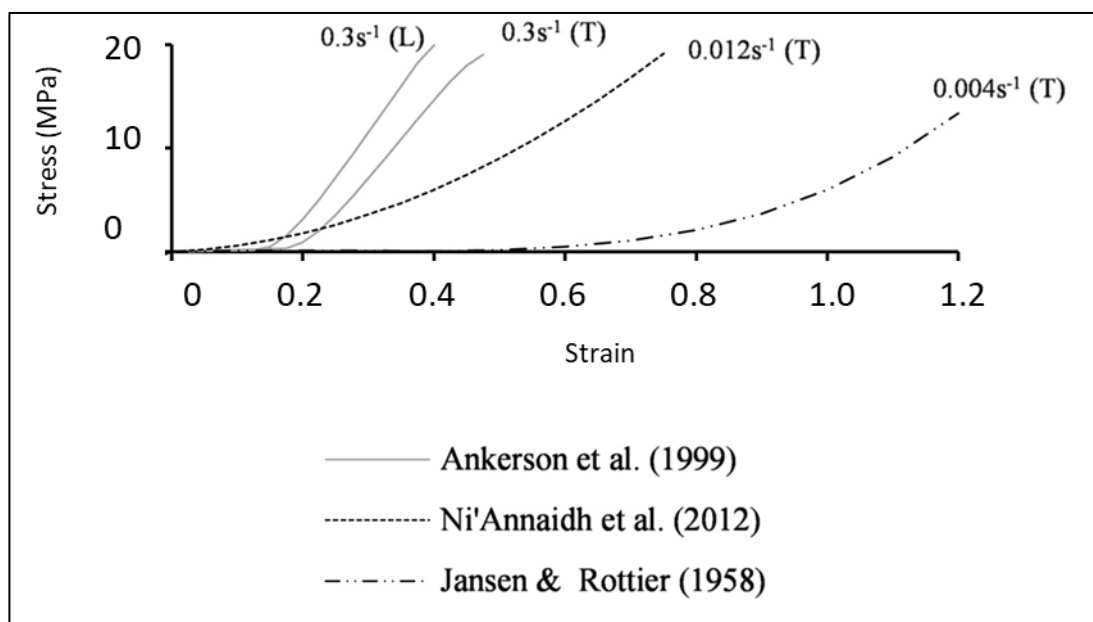


**Figure 2-5. Stress/strain profile of skin tissues strained at different rates and orientations in different studies. (T) refers to the direction of strain being transverse to the tissue orientation and (L) refers to the direction being longitudinal to the orientation of the tissue. Tissue in the 'Jansen & Rottier' study was obtained from the human abdomen; from the 'Ni'Annaidh' study it was obtained from the human back; from the 'Ankersen' study from pig skin (Ankersen, 1999; Gallagher et al., 2012; Payne et al., 2014)**

For the purpose of developing a similar stress/strain under tension to the curves above as well as the requirement around the polymer being able to plastically deform and stress relax under a held stress, the more rigid polymers that can be seen in Figure 2.1 were looked into, namely polycaprolactone (PCL).

### 2.1.2 Poly- $\epsilon$ -caprolactone

PCL is a biocompatible polyester which has been explored for forming various medical devices (Van der Giessen et al., 1996), templates for tissue regeneration (Htay et al., 2004; W. J. Li et al., 2006) and drug delivery systems (Aliabadi et al., 2005). It has a low melting point (70°C) and mechanical properties can be tailored by altering its molecular chain length and crystallinity (Engelberg & Kohn, 1991); the fact that PCL matrices formed after dissolution in chloroform have shown elongation up to 1000% before breaking makes this an interesting material to investigate for the purposes of using it as a substrate to model soft tissue stretching on (Averous et al., 2000).

The simple chain architecture of polymers such as PCL forces them to crystallize to a certain extent, normally between 10 and 60% overall crystallinity. The reason for this partial crystallinity is the kinetic hindrance of entanglements among the polymer chains, which cannot be abolished but can lead to the formation of amorphous layers during solidification. Stacked lamellar crystals with entangled amorphous polymeric chains in between lamellae form what is known as a semicrystalline state (Strobl, 2007).

The periodicity between the lamellar crystals and amorphous layers in the bulk semicrystalline state occurs typically at a length scale of 10–50 nm. The hard crystalline and soft amorphous parts provide rigidity to the material and toughness to the system respectively. The presence of these two phases results in complex deformation behaviour (Strobl, 2007), where polymer chain entanglement, crystallite structure and percentage will affect the mechanical deformation properties of the film. With sufficient understanding of this behaviour it may be possible to tailor PCL for the purpose of being a stretchable sheet to induce a mechanical stimulus on cells and their matrix, in a manner similar to that incurred by soft tissue.

### 2.1.3 Crystal Formation Process

As stated above, the crystalline regions of a polymer are the harder parts of the polymer in comparison to its amorphous parts. Therefore, the higher the crystallinity of a polymer, the stiffer it is too due to the strong bonding within crystallites. To tailor PCL to be representative of soft tissue from a mechanical deformation perspective, it may be necessary to reduce its crystallinity.

Polymer crystallization is assumed to be a multistep process with many influencing aspects. Usually the resultant polymer is semi-crystalline due to chain structure, which can cause geometric hindrance during local ordering which is driven thermodynamically. Temperature, pressure, shearing and various other parameters can drive non-equilibrium to induce other changes to polymer structure e.g. crystal morphology, and degree of crystallinity (Androsch et al., 2010).

Nucleation represents the starting point for crystallization. Macromolecules arrange themselves in an organised pattern, forming a site onto which additional polymer chains can deposit, allowing crystals to grow at a characteristic crystalline growth rate. Nucleation can be either homogeneous or heterogeneous. Homogeneous nuclei are formed due to thermodynamic driving forces by the polymer chains themselves, whereas heterogeneous nuclei are often supported on interfaces, usually on intentionally added foreign materials or often on impurities (such as catalyst residues, processing enhancers, or stabilizers) (Schmelzer et al., 1995; Turnbull, 1950; Wunderlich & Mehta, 1974).

An important driving force for crystallisation is the Gibbs free energy difference between the solid and the liquid ( $\Delta G$ ).  $\Delta G$  is a temperature dependent parameter, which can be related to the change in enthalpy ( $\Delta H$ ) and the entropy difference ( $\Delta S$ ) between the solid and the liquid as detailed in equation 1, where 'T' represents the current temperature of the system.

$$\Delta G = \Delta H - T\Delta S$$

(Equation 1)

The melt temperature of the polymer is defined as 'T<sub>m</sub>', and at this temperature  $\Delta G = 0$  where

$$T_m = \Delta H / \Delta S$$

(Equation 2)

Crystallisation cannot occur above T<sub>m</sub> where  $\Delta G > 0$ ; however, crystallisation can occur below T<sub>m</sub> where  $\Delta G < 0$ . As T decreases,  $\Delta G$  becomes more negative, increasing the driving force for crystallisation.

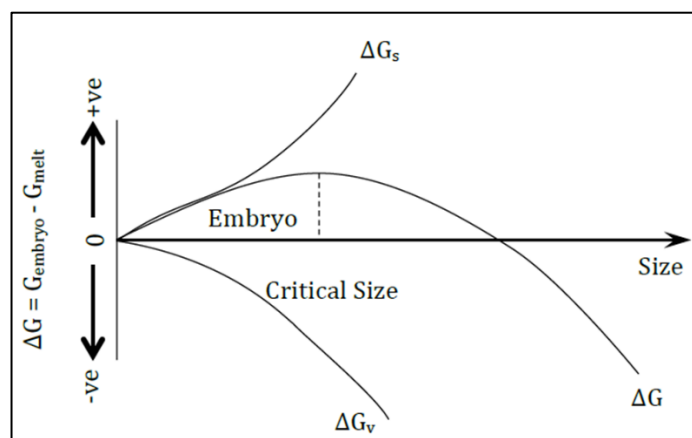


Figure 2-6. Schematic diagram of the change in free energy during nucleation (Beaupere et al., 2018).

$\Delta G$  is the sum of the surface free energy ( $\Delta G_s$ ); the excess free energy between the surface and the bulk of the nucleus, and volume free energy  $\Delta G_v$ ; the excess free energy between an infinitely large nucleus and the nucleus in the liquid (Figure 2.6).  $\Delta G_s$  is a positive quantity, proportional to  $r^2$  (where  $r$  is nuclei radius);  $\Delta G_v$  is a negative quantity, proportional to  $r^3$ . The dependence of  $\Delta G$  on the nuclei radius causes  $\Delta G$  to pass through a maximum corresponding to the critical nuclei (figure 2.6). For a spherical nucleus the critical free energy,  $\Delta G^*$ , can be described through Equation 3, where  $\sigma$  is the surface tension and  $r_c$  is the critical radius (Schultz, 2001).

$$\Delta G^* = 4/3 \pi \sigma r_c^2$$

(Equation 3)

The crystallisation process from a solution involves ordered regions originating from disordered entanglements. Temperature here plays a key role; cooling slowly from the polymer's melting temperature will give the polymer chains time to crystallise. The crystallites are formed by the reeling in of polymer chains from the entanglement accompanied by a loss of the entanglements (Hamilton et al., 2012; J. Y. Park & McKenna, 2000). This crystallisation process is called adjacent re-entry and results in the formation of highly ordered lamellae as a result of the process reaching thermodynamic equilibrium. Conversely, fast deep quenching of the temperature from the melt temperature will result in the entangled polymer being unable to reach its thermodynamic equilibrium resulting in an amorphous structure (Hamilton et al., 2012; J. Y. Park & McKenna, 2000).

#### **2.1.4 Film Formation**

A PCL thin film can be produced via solution processing methods such as spin-coating, where a polymer solution is deposited on a substrate that is rotated at high speed (typically between 1000 and 10 000 rpm), resulting in the formation of a thin polymer film in a matter of seconds. There then exists a trade-off between the ideal physical processing steps required to produce a film of the required thickness and the structure and morphology of the film itself.

Film thinning can be simplified as a two-stage process; hydrodynamic thinning and evaporative thinning. The initial hydrodynamic thinning takes place due to the centrifugal force acting on the solution, which is then proceeded by film thinning dominated by solvent evaporation (Meyerhofer, 1978). Hydrodynamic thinning is dependent upon the solution viscosity, radial speed and acceleration (Emslie, Bonner, & Peck, 1958,), while evaporative thinning is dependent upon the vapor pressure of the solvent (Birnie, 2001).

The crystallinity can then be temperature controlled as described above where a shallow quench (when solvent is lost slowly) will result in the morphology evolving towards thermodynamic equilibrium, while for deep quenches (when solvent is

removed rapidly), the morphology may become frozen far from thermodynamic equilibrium (Mellbring et al., 2001).

### 2.1.5 Surface Treatment

Despite its tailorable mechanical properties and biodegradability, the low hydrophilicity of PCL does not make it biocompatible and hence suitable for cell adhesion and proliferation. Hydrophobic scaffolds tend to conform adsorbed proteins into sub-optimal configurations (with hydrophobic residues displaced towards the scaffold surface), hydrophilic polymers adsorb protein in a hydrated interfacial phase wherein the proteins are more likely to retain their native conformation (Vogler, 1998). Research has shown that introduction of different functional groups to surfaces changes the conformation of adsorbed fibronectin leading to altered integrin binding, such that indices of osteoblastic differentiation (expression of bone markers, alkaline phosphatase activity and mineralization) become significantly upregulated on OH- and NH<sub>2</sub>-functionalized surfaces compared with CH<sub>3</sub> and COOH (Keselowsky et al., 2005).

Recent papers describe surface modification processes applied to scaffolds, using O<sub>2</sub> and N<sub>2</sub> low pressure plasmas (Djordjevic et al., 2008; H. Shen et al., 2007; Wan et al., 2004) and Dielectric Barrier Discharge (DBD) plasmas (Safinia et al., 2007; Yildirim et al., 2008). These plasma processes have also shown to be effective in 3D scaffold constructs to create homogeneously distributed cells within scaffolds to reconstruct tissues such as cartilage or bone (Hardingham et al., 1999; Meijer et al., 2007).

Plasma treated PCL scaffolds have demonstrated surface modification of the material. XPS analysis showed presence of nitrogen on the scaffold surface and section. Two new contributions appear with respect to untreated PCL, the first being a peak for the N-C=O (BE 288.1 eV) and the second being a peak for C-N (BE 286.0 eV). This makes the surface more hydrophilic resulting in better attachment of ECM proteins and cells.

Previous work has demonstrated that amounts of human serum albumin (HSA), human serum immunoglobulin (IgG) and human serum high density lipoprotein (HDL) adsorbed from 20% serum-containing culture medium to plasma-treated polymer films were much larger than those adsorbed to unmodified polymer films. The amounts of adsorbed HSA and HDL to nitrogen and oxygen plasma-treated Polytetrafluoroethylene (PTFE) films were independent of measured contact angle. However, the amount of IgG adsorbed to polymer films treated with oxygen plasma increased with decreasing contact angle. Fn adsorbed to treated PTFE films treated with oxygen plasma increased with decreasing contact angle (Dekker et al., 1991). Therefore, quantification of hydrophilicity will be used as an initial signal for how long PCL films should be treated for before cells are cultured onto them.

### **2.1.6 Chapter Aims and Objectives**

This chapter aims to characterise PCL film as a substrate for modelling stretching of soft tissue.

As PCL can be formed in either a crystalline (C-PCL) or amorphous (A-PCL) manner, the aim here was to compare mechanical and structural properties which may influence cell responses between the 2 forms of the material before determining how the mechanical behaviour (ideally plastic deformation) can be utilised to model stretching of soft tissue.

In order to meet these aims the following objectives were outlined:

- Make a crystalline and amorphous version of PCL (C-PCL and A-PCL) through a spin coating process using temperature modifications.
  - C-PCL will be created by allowing natural crystallisation to enable thermodynamic equilibrium during solidification.

- A-PCL will be created by keeping the polymer at its melt temperature before applying a fast-deep temperature quench to solidify it in an amorphous state.
- Define the substrates mechanical properties and differences between them to identify which version of the material (if either) is a better representation of soft tissue being stretched.
  - Tensile testing (in adherence with ASTM standard testing for polymer films) will first be used to outline differences between stress/strain profiles.
  - Finite element analysis (FEA) will then be used to determine differences in strain profile homogeneity.
- Analyse structural differences between the 2 materials to understand if surface topography, as well as structural changes induced by stretching, will eventually impact cell responses in a different manner for each substrate.
  - Initial observations will be made using microscopy, before polarised light microscopy and SEM are used to better understand structural changes of the materials in response to stretch.
- Determine surface hydrophilicity of PCL in response to varying plasma treatment times, with the view of optimising cell attachment on the substrate.

It was hypothesised that C-PCL would significantly differ in its appearance as well as mechanical properties from A-PCL. It is expected to be stiffer than A-PCL due to high bond strength between molecules in its crystal structure, and is likely to be more opaque in appearance than A-PCL; amorphous materials are transparent as light can pass through the medium of disorderly distributed macromolecules without being diffracted. Polymer crystals however will diffract the light leading to a degree of opaqueness.

As C-PCL will have amorphous regions within the material, it was predicted that upon being stretched, the strain would manifest from a localised region on the material, whereas this would not be the case for A-PCL as the material would be

homogenous; furthermore stretching has been shown to initiate crystallisation via nucleation in amorphous polymers which would further lead to strain being more evenly distributed.

Structural differences were expected to be seen under microscopy between the 2 materials, where visible crystal structures should be able to be seen for C-PCL and nothing should be able to be seen for the A-PCL (as it is transparent). Under polarised light microscopy (PLM), C-PCL is hypothesised to diffract light enabling crystal imaging through the second polariser; this should not be the case with A-PCL, where no light should pass through the second polariser.

It is expected that after C-PCL has been stretched passed its yield point, crystals will begin to stretch, and this should be visible under microscopy and is likely to give a change in observation in PLM. A-PCL upon stretching past its yield point may remain transparent with no light passing through the second polariser under PLM, however light passing through would be indicative of a change in structure within the material.

With regards to hydrophilicity of PCL in response to being plasma treated; water contact angle is hypothesised to decrease as plasma treatment time increases, indicating an increase in hydrophilicity of the surface in response to treatment.

## 2.2 Methods

### 2.2.1 C-PCL Film Development

C-PCL films were made by dissolving PCL beads (80, 000 MW, Sigma) in chloroform at a 12% weight/weight (wt/wt) ratio before 5 ml of the solution was spin coated onto a hydrophobic silanised silicon wafer (78.55cm<sup>2</sup>) at 1500 RPM with acceleration of 200 RPM/s for 30 seconds to give a uniformly thick film (20µm) of area 0.157cm<sup>3</sup>. The film was left to dry for 20 minutes.

### 2.2.2 A-PCL Film Development

The above spin coating parameters were kept the same to produce an amorphous version of the film, however upon spin completion, the silicon wafer was removed and placed on a hotplate at 80°C. This would allow the polymer to melt and again become entangled upon evaporation of the chloroform as PCL melt temperature is 70°C; it was important to keep the temperature close to the T<sub>m</sub> of the polymer and not too far above it as this could break the long monomer chains. The wafer was kept on the hotplate for 5 minutes.

Whilst the silicon wafer (7855cm<sup>2</sup>) was on the hotplate, a brass block (350g) was left to cool to the temperature of liquid nitrogen (-196°C). Once the 5 minutes were completed, the silicon wafer was taken off the hotplate, and instantly the cooled brass block placed on top to apply a deep temperature quench to the PCL. The silicon wafer has a high thermal conductance of 1.3 W cm<sup>-1</sup> °C<sup>-1</sup> enabling a quick transition between temperatures. The thickness of the A-PCL was 20µm resulting in an area of 0.157cm<sup>3</sup>.

### 2.2.3 Tensile Testing

Tensile testing of C-PCL and A-PCL was conducted to evaluate mechanical properties of the materials when they are being stretched. Tensile testing involves the application of force to stretch a material. The displacement and force

required to displace are 2 of the raw data outputs. As the materials being investigated are 2 thin polymer films which are less than 1mm in thickness, ASTM guidelines for tensile testing thin plastic sheets were adhered to (ASTM, 2002).

Samples were cut from PCL developed films using a mould (15mm x 70mm rectangle) and scalpel before the thickness of each sample was measured using a micrometer screw gauge. For the tensile test each sample was clamped using pneumatic rubber grips in a tensile testing system (Zwick Roell z2) so that the gauge length (length between the 2 grips) was 30mm (See Figure 2.7). Samples were then stretched at 60mm per minute till breaking point using a 2kN load cell (Figure 2.7).

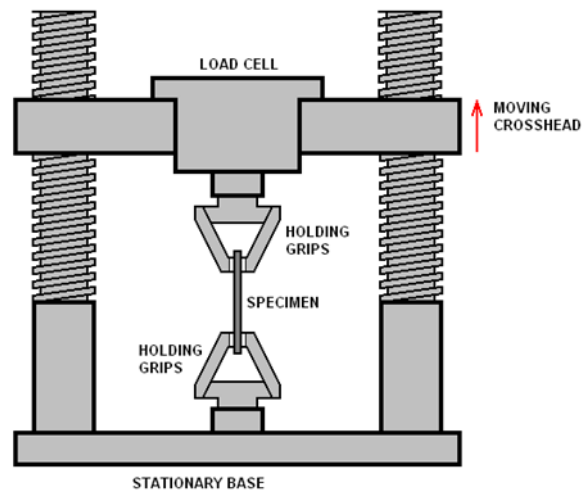


**Figure 2-7. Schematic of tensile testing apparatus (Zwick Roell z2. The specimen to be tested (PCL films in this case) is gripped at each end by the holding grips. The gauge length is the distance between the end of each grip. When the crosshead moves up it stretches the material and the load cell records the force required to stretch the material.**

Force and displacement values were exported through the Zwick software (TestXpert II) and these values were converted to stress and strain respectively. Stress is calculated by dividing the force by the cross-sectional area of the specimen, and strain is calculated by dividing the displacement by the original gauge length of the specimen.

## 2.2.4 Digital Image Correlation

DIC is a method used to assess how during mechanical testing, samples/specimen are being deformed using an optical flow approach. DIC uses a mathematical correlation analysis to examine digital image data taken while samples are in mechanical tests. This technique involves capturing consecutive images with a digital camera during the deformation period to evaluate the change in surface characteristics and understand the behaviour of the specimen while it is subject to incremental loads. The deformation readout during tensile testing enables calculation of the engineering strain which is what strain has referred to so far in this chapter. However, analysing the optical flow of the material undergoing deformation allows the calculation of finite strains (through FEA) within the material as it is undergoing deformation.

Material deformation can be described by depicting the material to be a collection of small line elements. As the material is deformed, the line elements stretch, or get shorter and can also rotate in space relative to each other. Strain at a point is characterised by the movement of any two mutually perpendicular line-segments. If it is known how these perpendicular line segments are stretching, contracting and rotating, it will be possible to determine how any other line element at the point is behaving, by using a strain transformation rule. This is analogous to the way the stress at a point is characterised by the stress acting on perpendicular planes through a point, and the stress components on other planes can be obtained using the stress transformation formulae (Kelly, 2015).

The surface of the PCL film is a two-dimensional case. If 2 perpendicular line-elements emanating from the same point are considered during a deformation, two things happen in conjunction: The line segments will change length; and the angle between the line-segments can change. The change in length of line elements is called normal strain and the change in angle between initially perpendicular line segments is called shear strain (Kelly, 2015). Normal strain in direction  $x$  is denoted as  $\epsilon_{xx}$ , whereas normal strain in  $y$  direction is denoted as  $\epsilon_{yy}$ . Shear strain is then denoted by  $\epsilon_{xy}$ . Figure 2.8 depicts  $\epsilon_{yy}$ ,  $\epsilon_{xx}$  and  $\epsilon_{xy}$  for a single point when a material has been deformed.

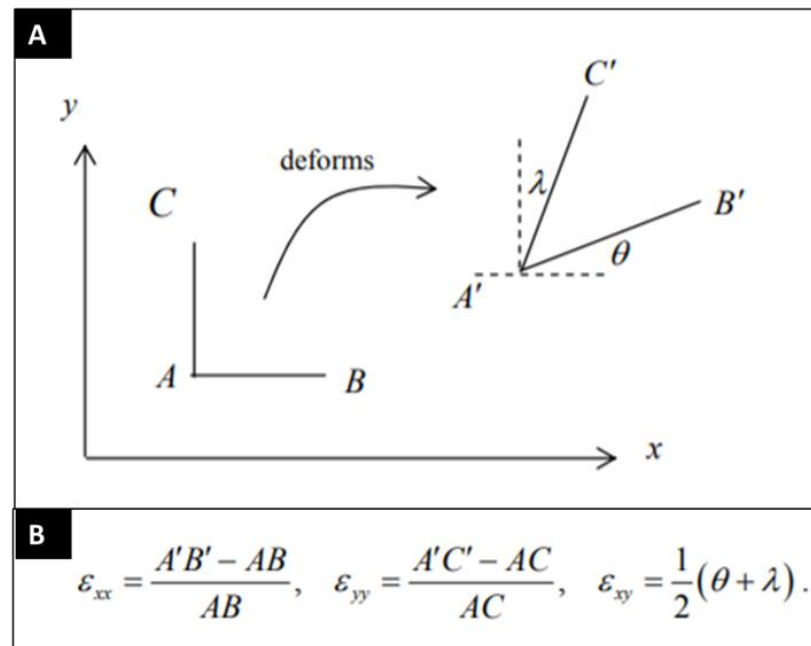


**Figure 2-8.** Example of strain measurements of a single point on a material undergoing deformation. **A)** Point A displaces along the x and y axis to A'; its perpendicular line elements B and C change length and angle in relation to A during this deformation (B', and C'). The change in angle for C is defined by  $\lambda$  and for B the change in angle is defined by  $\theta$ . **B)** These are the equations for normal strain in the x and y direction ( $\epsilon_{xx}$ ,  $\epsilon_{yy}$ ) and the shear strain ( $\epsilon_{xy}$ ) which is defined by the angle change in elements (Figure adapted from Kelly, 2015).

Finite element analysis maps several of these points as a heat map on a material. This displacement field can be a function of the coordinates of the material particles in the reference/undeformed state or the coordinates in the deformed state. If the displacement is a function of the coordinates of the material particles in the reference configuration it is called the Lagrangian representation of the displacement field. If the displacement is a function of the coordinates of the material particle in the deformed state, it is said to be Eulerian (Kelly, 2015). For the purposes of the results displayed in this chapter, the Eulerian strain fields for samples are depicted and analysed.

To be able to use DIC to map strains, specimens need to be prepared by the application of a random dot pattern (speckle pattern) to its surface. This method was used in conjunction with tensile testing of the samples on the Zwick Roell z2. The initial image taken before loading is used as a reference image, and a 'region of interest' is defined on here; this is to be the region of material to be strained. A series of pictures are then taken during the deformation process and the

displacement of the dots is tracked by software (Vic-2D, Correlated Solutions Inc, USA) to create a strain distribution map through loading (Figure 2.9).

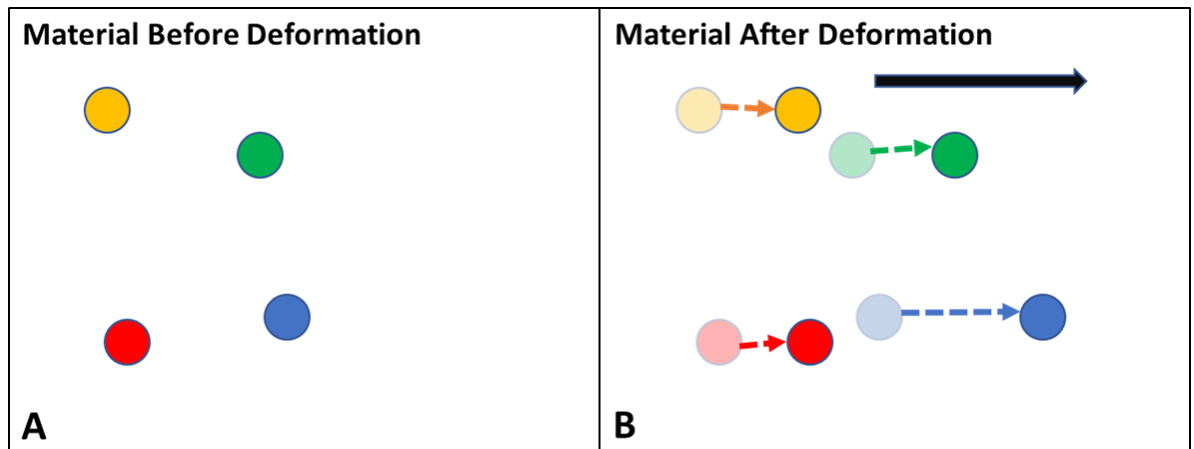


**Figure 2-9.** Illustration of what DIC tracks as a specimen deforms. A) Schematic of speckles to be tracked during material deformation. B) Schematic of speckles moving relative to their original position upon material deformation.

The speckle pattern is therefore essential as it permits the software to be able to identify and calculate displacements with accuracy. To obtain accurate results with the digital image correlation it is important to get an adequate speckle pattern. An adequate speckle pattern must have a considerable quantity of black speckles with different shapes and sizes. The effectiveness of the speckle pattern can be determined by the quantity of pixels per black speckle. A good speckle pattern must have small black speckles (10 pixels), medium black speckles (20 pixels) and large black speckles (30 pixels). To generate this pattern Holts car spray paint (matt black) was used. Samples were placed flat on a table and the spray can was held approximately 50cm away from the samples. The spray was lightly applied by applying a small amount of pressure on the nozzle while moving the spray can from left to right.

The sample was then clamped between rubber grips in the Zwick Roell z2, and a digital camera was set up on a tripod to image specimens (2048×2448 pixels, Vic-Snap, Correlated Solutions, Inc., Columbia, SC). A white sheet was placed behind the specimen to maximise the contrast on the speckle pattern. Regions of interest were manually defined (see Figure 2.10).

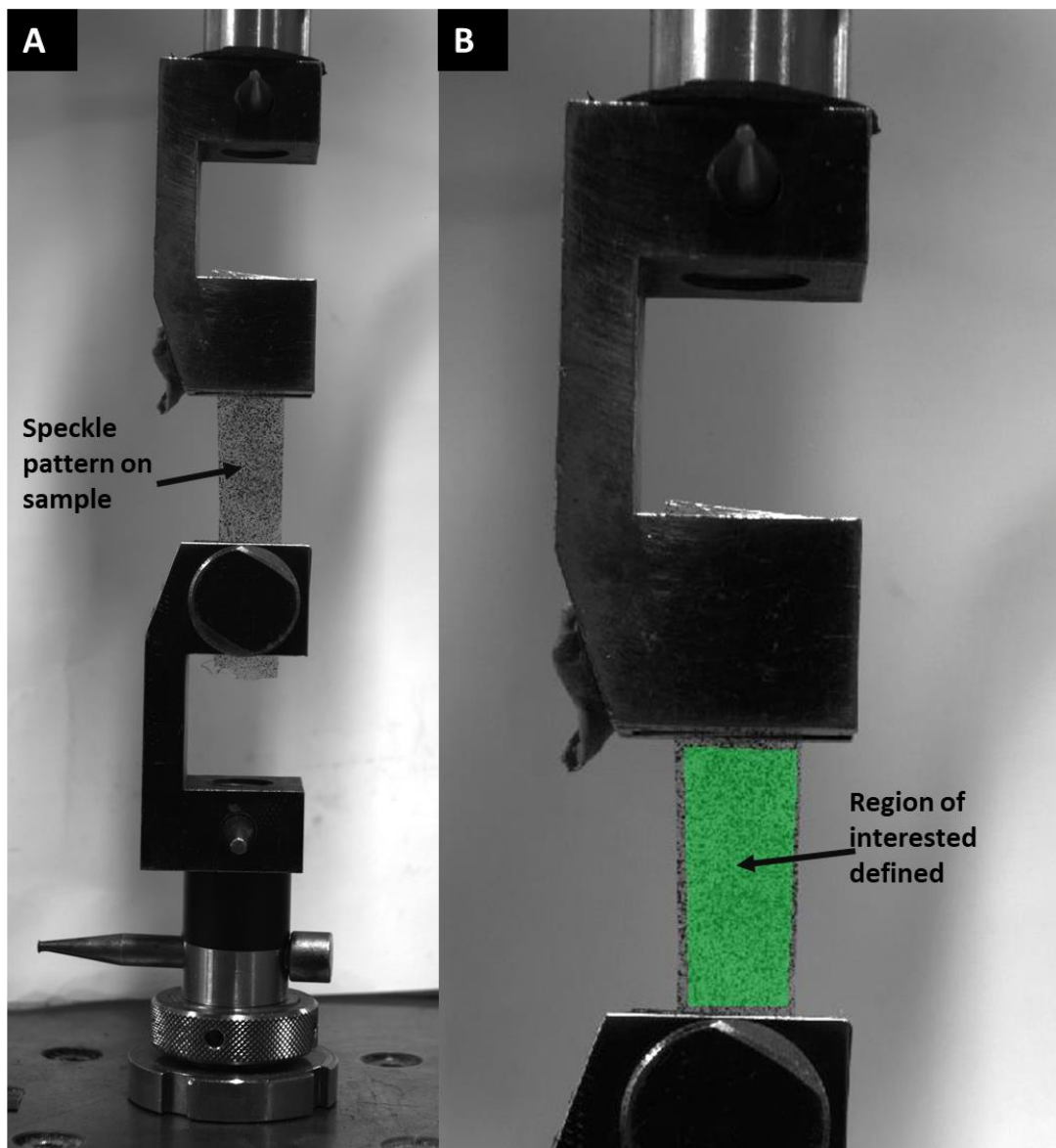


Figure 2-10. DIC set up. A) Speckled specimen clamped between rubber grips on Zwick Roell z2, and brought into focus using Vic-Snap camera. B) Specimen zoomed into and region of interest manually created using Vic-2D software.

Data were tracked (Vic-2D Version 2009, Correlated Solutions, Inc., Columbia, SC) using a seed point defined near the stationary grip (Vic-2D parameters, subset: 40, step size: 5), with the results used to compute Eulerian strains.

## 2.2.5 Light Microscopy and Scanning Electron Microscopy

C-PCL samples were observed under microscopy to link deformation behaviour observed at a finite level in DIC to structural changes that may be occurring in the material throughout various points in its deformation; imaging was conducted on a Olympus BX51, under 10x/0.30 magnification lens. Samples were cut (1cm x

2cm) and stretched to various levels of deformation; each end of the films were then stuck down to microscope slides using tape, ensuring the sample lay flat and taut over the slide. Due to the random molecular arrangement of A-PCL samples (as described in the introduction section), these samples could not be observed under light microscopy as they are completely transparent.

A-PCL was therefore observed under scanning electron microscopy (SEM), and C-PCL was used as a comparison. SEM is useful in this case as light wavelength is a limiting factor when analysing the A-PCL surface. Electrons have much shorter wavelengths, enabling better resolution. Both sample types were cut (and stretched for analysing the polymers stretched) and attached to aluminium stubs with double-sided conductive carbon tape and sputter coated with gold-palladium to a thickness of 15-20 nm (Polaron SC515 SEM coater). Sputter coating and image acquisition were performed with kind assistance from Margaret Mullin (University of Glasgow) using a JEOL JSM 6400 scanning electron microscope with Olympus Scandium software at an accelerating voltage between 5 and 20kV.

### **2.2.6 Polarised Light Microscopy**

Polarised light microscopy is another useful tool in analysing A-PCL, particularly when analysing whether it displays a change in structure in response to being stretched. Light is initially vertically polarised before travelling through a sample. If it passes through the sample without diffracting (such as in an amorphous material such as glass or the A-PCL) it does not travel through the second polariser as this polarises in the perpendicular direction to the first polariser (Figure 2.11). However, if structures cause the light to diffract, they will pass through the second polariser.

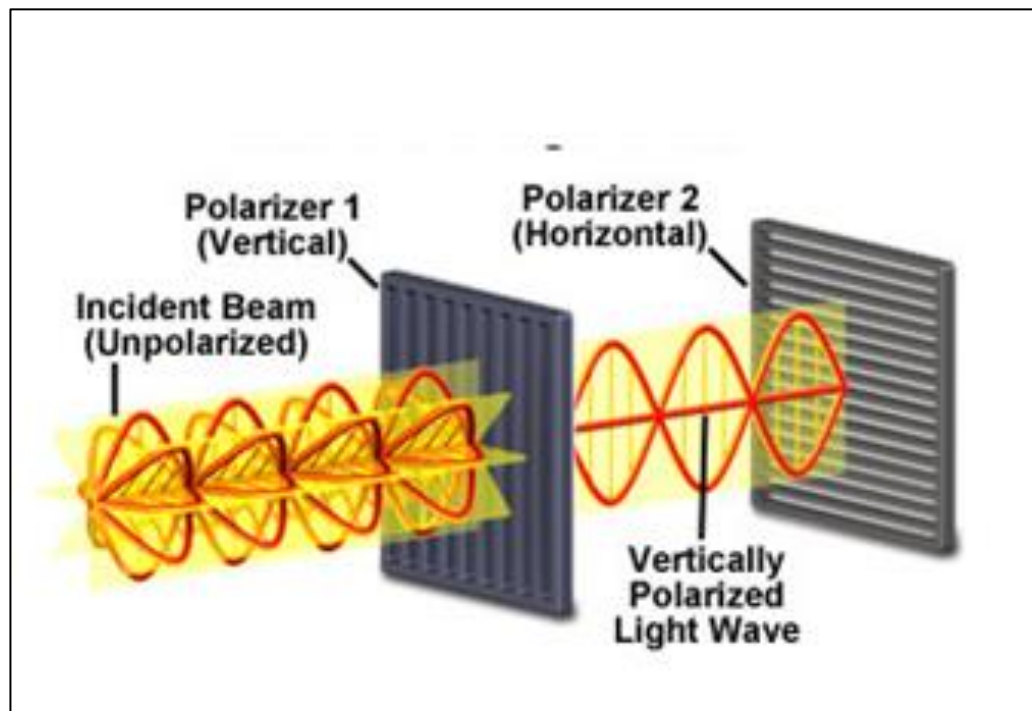
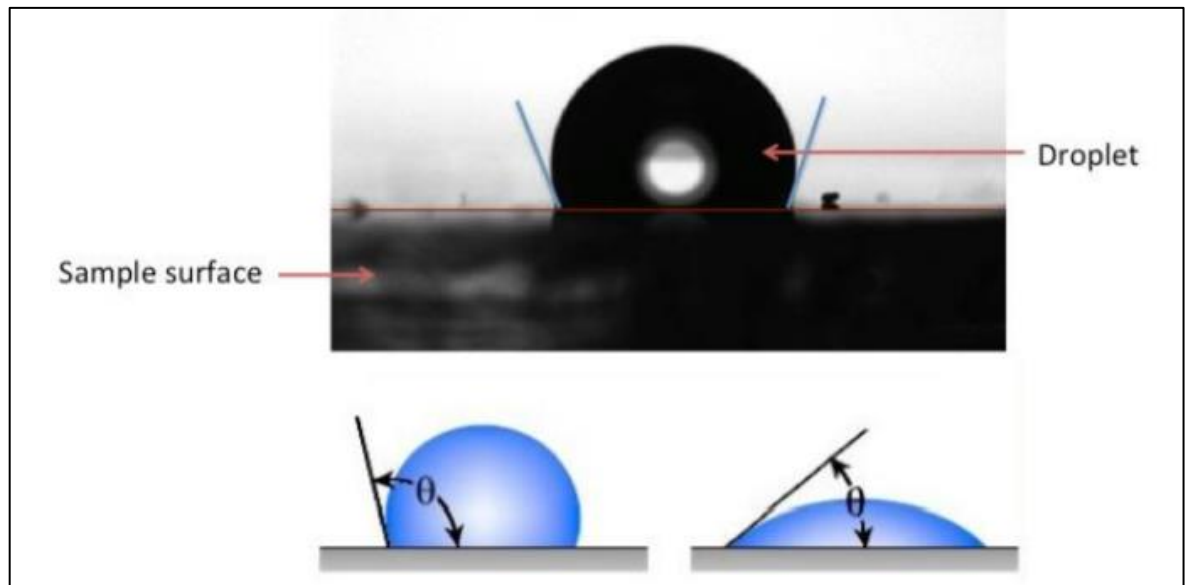


Figure 2-11. Schematic of how light travels during polarised light microscopy. A polariser filters light to only enable light oriented in a specific direction through (polarising direction). There are two polarisers in a polarizing optical microscope, and they are oriented perpendicularly to one another. The polarising direction of the first polariser is oriented vertically to the incident beam, enabling only waves with vertical direction to pass through. This is then blocked by the second polarizer as it is horizontal to the incident wave unless an object between the polarisers causes the light to diffract (Image taken from chem.libretexts.org).

C-PCL and A-PCL samples were cut (1cm x 2cm) and each end of the films were stuck down to microscope slides using tape, ensuring the sample lay flat and taut over the slide. Stretch samples to be analysed were stretched at 50% strain prior to being stuck down. Samples were imaged under 40x magnification with crossed polarised light. The microscope stage was slowly rotated through 90° with images being captured every 10°. Rotating the stage enables analysing of whether structures are orienting in a particular direction, based on the intensity of light that passes through as the stage is rotated.

## 2.2.7 Plasma Treatment and Water Contact Angle Measurements

To determine the effect of plasma treatment on PCL, samples of C-PCL were treated for a range of times between 0 and 5 minutes with air plasma generated using a Harrick Plasma PDC-002 cleaner at 29.6 W. WCA measurement was carried out using the static drop technique with an Attension Theta (Biolin Scientific) instrument.



**Figure 2-12.** Contact angles were measured using the static drop technique on PCL surfaces with different plasma treatment times and fitted with a circular line to determine angles. The contact angle varies depending on the hydrophobicity of the surface.

High contrast images were recorded for 30 seconds after a droplet was placed on the surface. OneAttension software was used to define the contact angle by fitting a circular equation around the droplet to determine the contact angles across the series of images taken (Figure 2.12).

## 2.3 Results

The 2 types of PCL (C-PCL and A-PCL) appeared visually different upon formation (Figure 2.13). C-PCL was spin-coated and left to dry at room temperature, allowing crystal formation during drying; this causes the film to be translucent. A-PCL was spin-coated, before being kept just above its melt temperature prior to being rapidly quenched below its glass transition; this causes it to be amorphous and completely transparent. Both films consistently had a uniform thickness of 20 $\mu$ m.

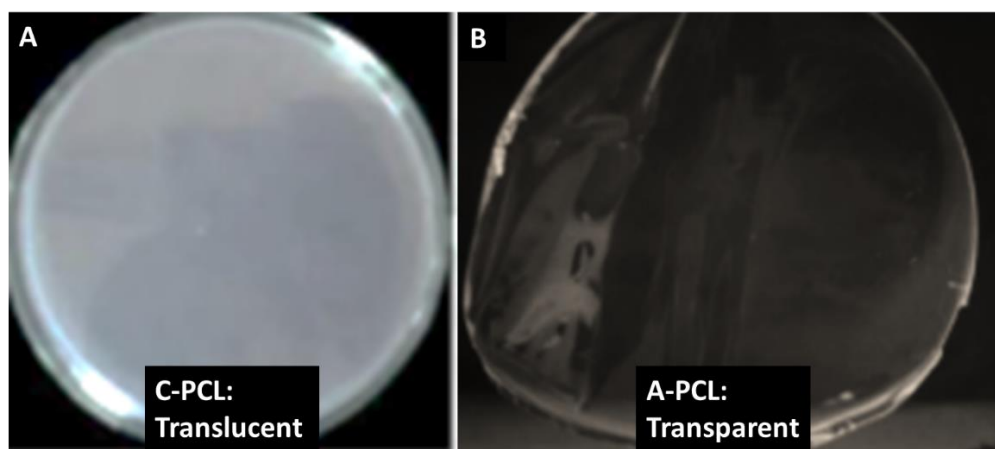


**Figure 2-13. Developed PCL films. A) C-PCL, as the polymer is crystalline its translucency can be seen against a black background. B) A-PCL.**

Having developed 2 variations of PCL film, a series of tests were conducted to characterise the differences between the 2 versions of the film and to outline whether cell behaviour in general may be impacted by certain characteristics such as force required to stretch the films, surface deformation behaviour, and topographical influences (as described in aims and objectives section of this chapter).

### 2.3.1 Tensile Testing

Tensile testing was first used to evaluate the force required to stretch C-PCL and A-PCL. Figure 2.14 below show the stress/strain curves obtained for 4 tested samples of each variant of the polymer.

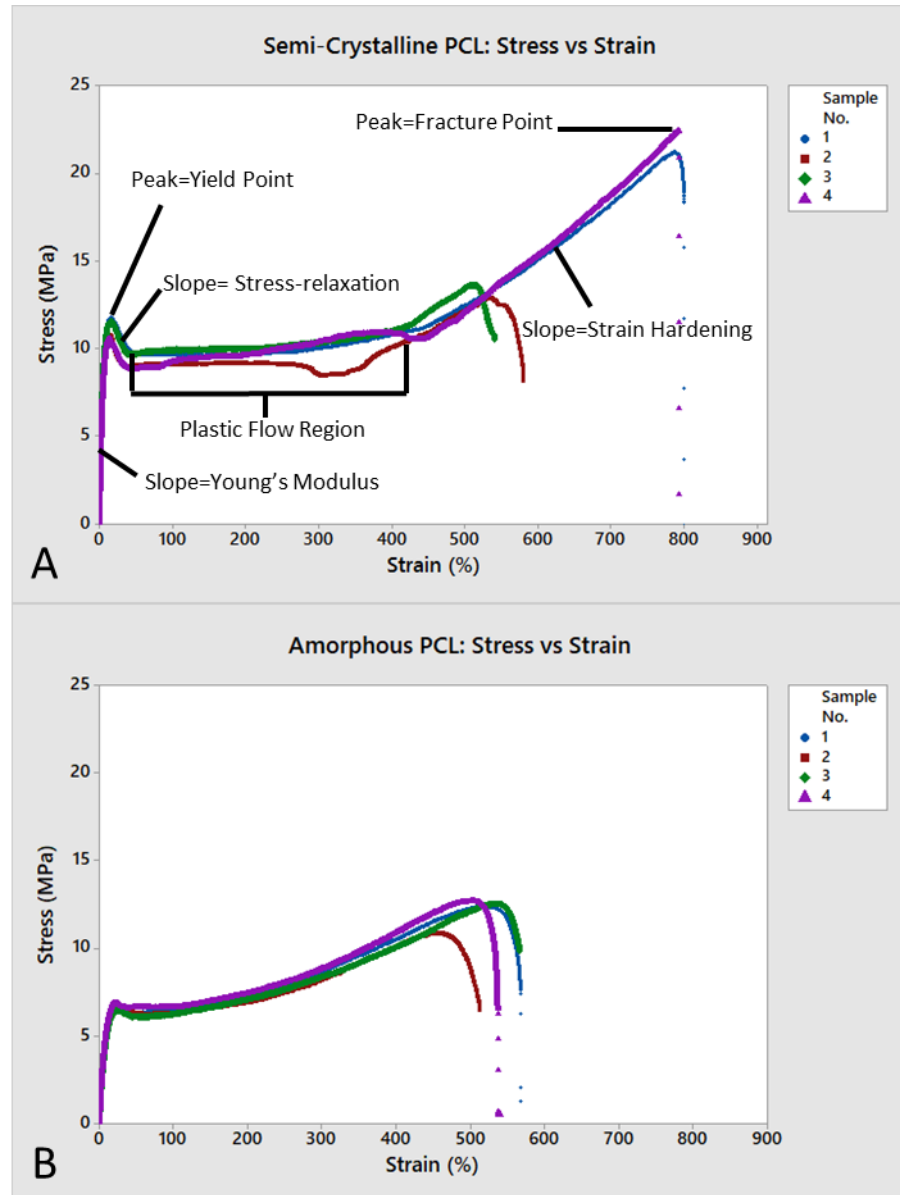


**Figure 2-14. Stress strain curves for 2 versions of PCL. A) Semicrystalline (C-PCL), tensile characteristics are outlined here. The initial slope where stress and strain increase is the Young's modulus. This slope leads into a peak called 'the yield point', the material is no longer elastic after being stretched further than this point. The drop in stress while strain increases is known as stress relaxation. The flat region following stress relaxation is known as 'plastic flow'. The increase in stress alongside strain after the flat region is known as strain hardening; the peak reached at the end of strain hardening is where the material breaks (fracture point). B) Amorphous (A-PCL). Deformation for both materials was applied at 60mm/min (n=4 spin coated samples for both sample types).**

The initial slope between stress and strain is the Young's modulus and is the elasticity of the material. In this region bonds are stretched, and energy is stored in a reversible manner (Hookean elasticity, linear viscoelasticity). As the stress rises further, the response becomes nonlinear; energy is still recoverable on release of the stress, but at a slow rate (Milisavljević et al., 2012). Eventually, the yield point is reached, accompanied by the onset of components of irreversible deformation. During this deformation, energy is dissipated in a viscous manner (plastic flow). The stress drops initially in this period (stress relaxation) and extension proceeds easily; necking of the polymer is seen here and this continuously undergoes drawing through increased strain (Milisavljević et al., 2012) (Figure 2.15).

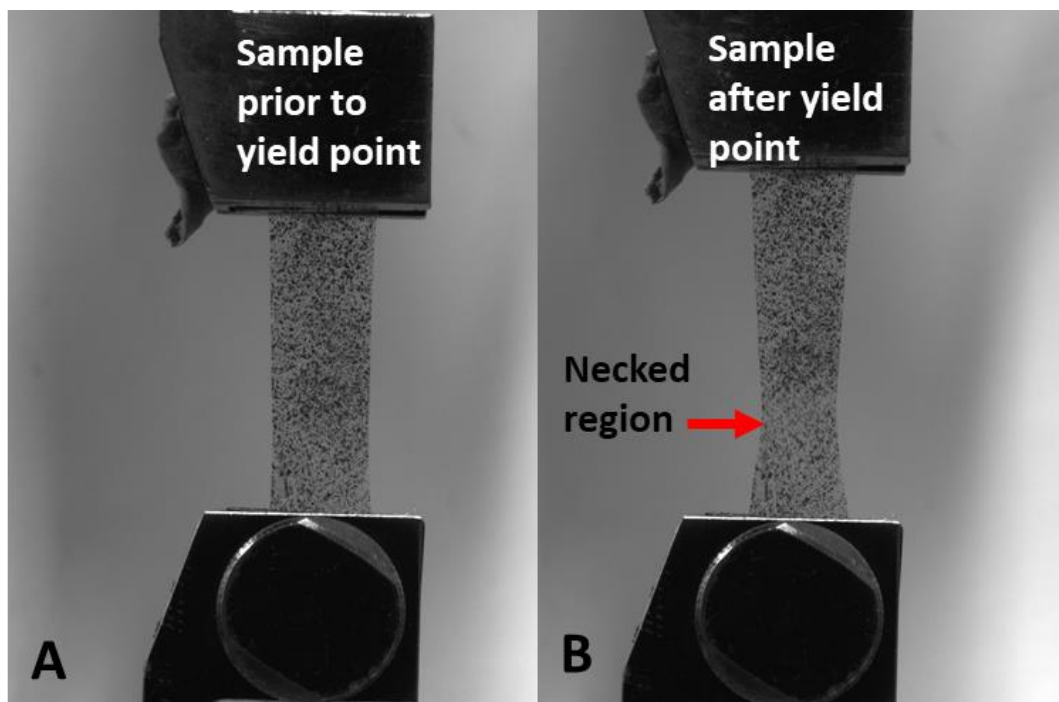


**Figure 2-15. Example of polymer necking after yield point. A) Image of PCL before yield point reached; width of sample is uniform. B) Image of PCL after yield point is reached; width of PCL is non uniform due to necking of sample.**

Towards the end of the plastic flow region, the material strain hardens before reaching its fracture point. The tensile curves for C-PCL and A-PCL can be seen to differ in figure 2.15. The differences between the curves are highlighted and explained in the figures and paragraphs below.

The Young's modulus is higher for C-PCL than A-PCL (91.98 vs 47.04MPa, Figure 2.16). Crystalline structures are generally very ordered, which is what gives them strength and rigidity; the molecular chains are largely locked in place against one another. The polymer chains are easier to uncoil for the A-PCL on the application of stress; the entropy is reduced as the chains have fewer conformations available. When the stress is removed the chains increase their entropy by readopting the random conformations. As the chains can move across each other the material remains elastic for larger strains, which is why the strain at which the yield point occurs for A-PCL is greater than that of C-PCL (20.9 vs 14.34%, Figure 2.16).

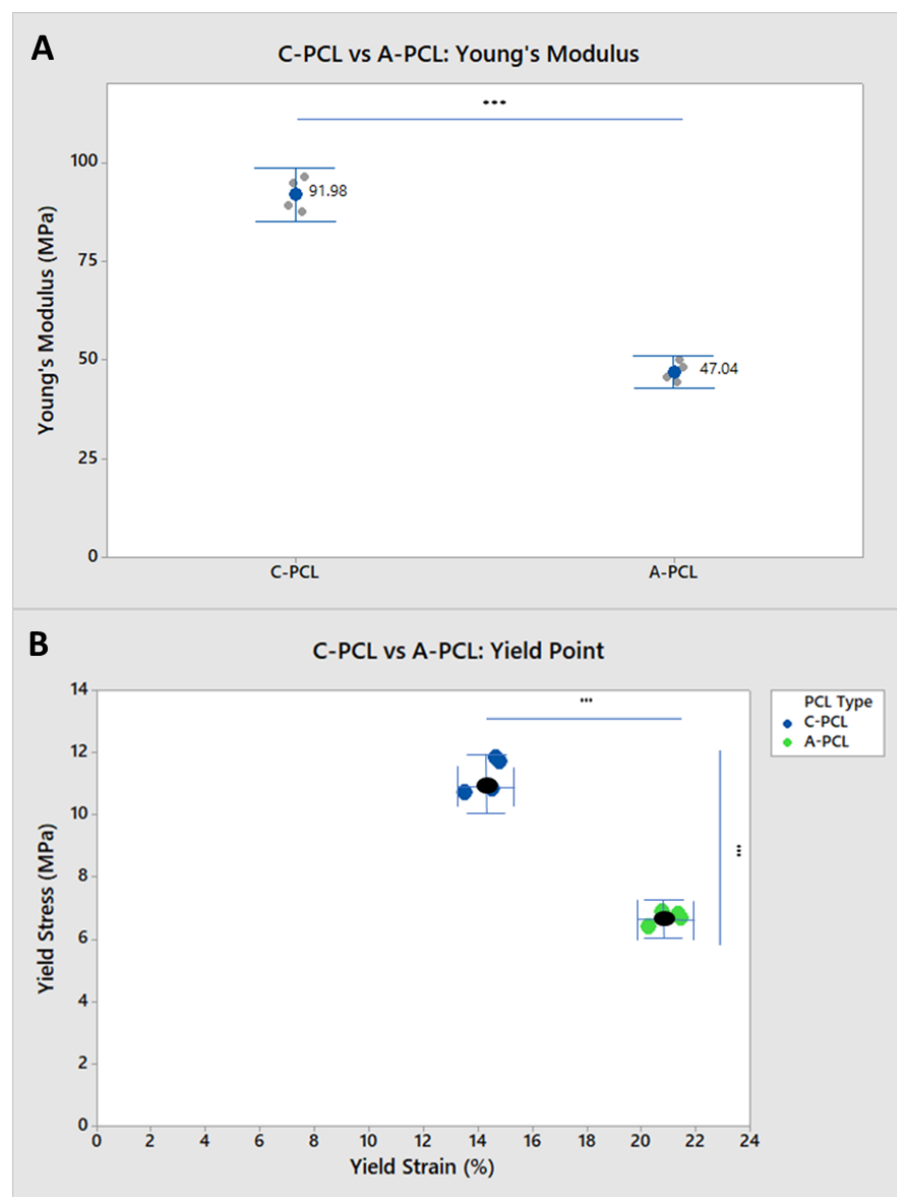


**Figure 2-16.** Difference in Young's Modulus and yield point between CPCL and APCL. **A)** Young's Modulus. **B)** Yield Point. (n=4 for both C-PCL and A-PCL. (Error bars represent 95% confidence intervals based on standard deviations. P values indicating significance, \*\*\*  $\leq$  0.001).

Both C-PCL and A-PCL are in plastic flow after the yield point, and both polymers show a degree of stress relaxation. Following stress relaxation the two polymers respond differently to being further stretched (Figure 2.17). C-PCL exhibits a stress plateau before it starts to strain harden. Conversely, A-PCL immediately begins to strain harden. Strain-hardening is generally attributed to the amorphous behaviour of the fibrillar structure and is assumed to increase with content of tie molecules (Bartczak, 2005; Makke et al., 2012). The probability to form tie molecules decreases as a function of crystallinity (Jabbari-Farouji et al., 2015). As a result, the onset of strain hardening occurs at a higher strain in C-PCL.

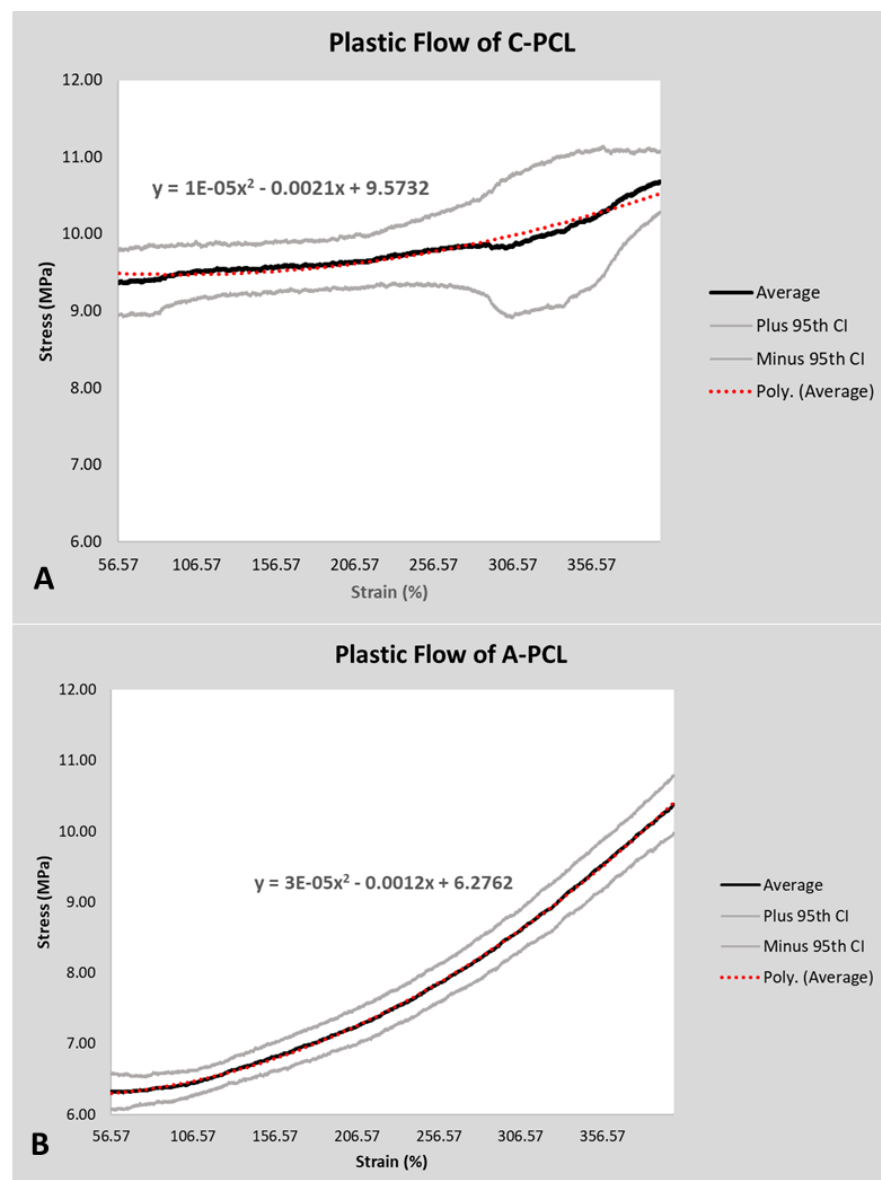


**Figure 2-17. Difference in plastic flow regions between C-PCL and A-PCL. A) C-PCL plastic flow and B) A-PCL plastic flow. For both graphs, the mean region of plastic flow is plotted between 4 samples (black); a polynomial equation has been fit to each mean line. The grey lines represent the 95% confidence interval.**

The rate at which stress increases during the plastic flow period analysed in Figure 2.17 for C-PCL and A-PCL can be calculated by differentiating the respective equations ( $y=3E-5x^2-0.0012x+6.2762$  and  $y=1E-5x^2-0.0021x+9.5732$ , see Figure 2.17) for each:

C-PCL:

$$dy/dx = 2E-5x - 0.0021 \quad (1)$$

A-PCL:

$$dy/dx = 6E-5x - 0.0012 \quad (2)$$

A relevant use of these equations here would be to compare C-PCL and A-PCL film when extended to similar strains. For example, when both are displaced to a strain of 300%, the rate of stress increase in the of C-PCL would be 3.9kPa per 1% strain and for A-PCL this would be 16.8 kPa per 1% strain, showing how different the polymers behave in plastic flow.

The strain hardening modulus (the linear portion of the graph after plastic flow) is higher for C-PCL than A-PCL (1.32 vs 2.53MPa, Figure 2.18) after the initial stress plateau shown above. This lines up with previous research which shows influence of crystalline content in strain hardening behaviour (Hiss et al., 1999). At strains beyond the yield point, the chain-folded structures align partially in the direction of tensile stress. At larger deformations in the strain hardening regime, chains in crystalline domains are unfolded as a result of tensile stress, and both chains in amorphous and crystalline domains are stretched and aligned (Hiss et al., 1999).

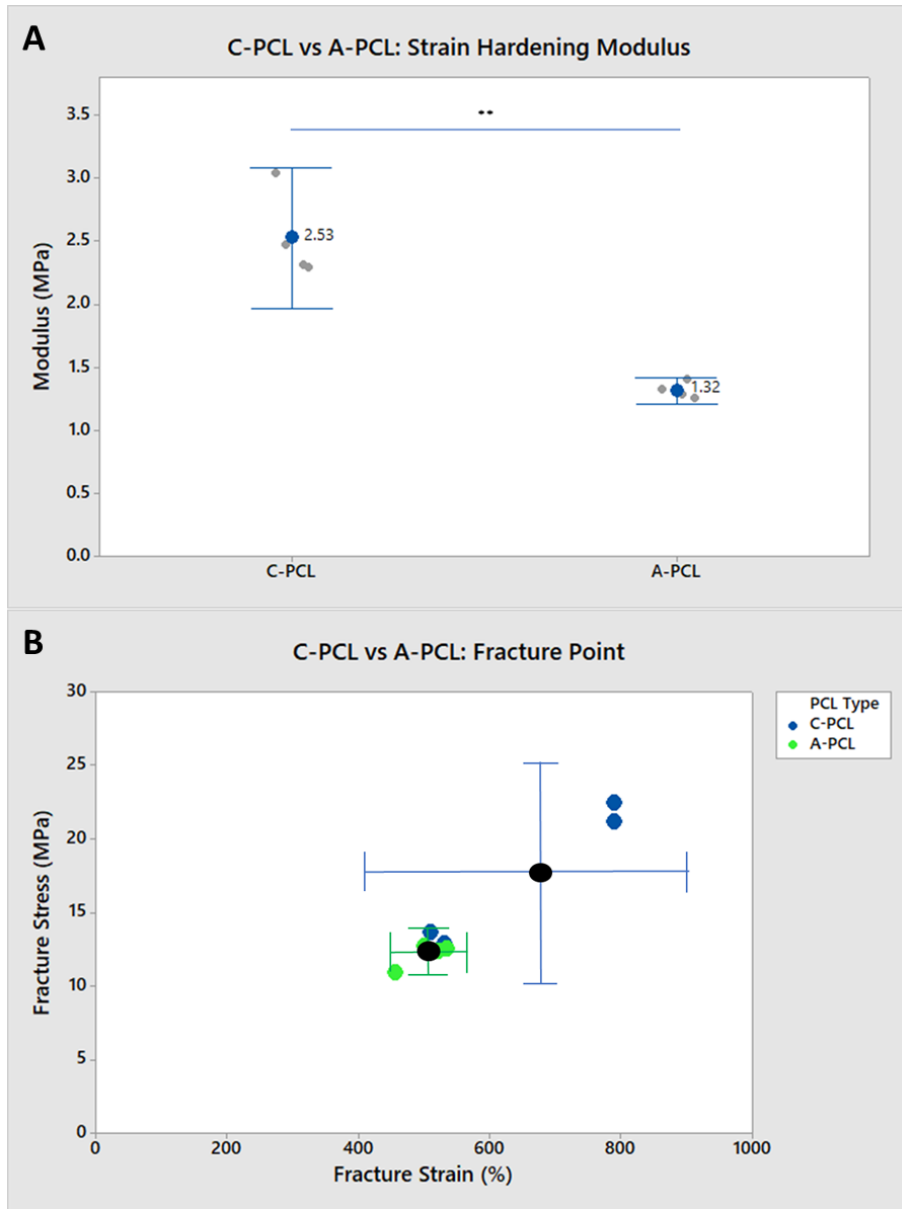


**Figure 2-18. Difference between C-PCL and A-PCL in A) Linear strain hardening and B) Fracture point. (n=4 for both C-PCL and A-PCL. Error bars represent 95% confidence intervals based on standard deviations. P values indicating significance,  $** \leq 0.01$ ).**

To summarize, plastic deformation of C-PCL is more complex than that of A-PCL; it involves tilting of crystallites and separation of crystalline blocks during stress relaxation/plateau followed by stretching and alignment of both amorphous and folded chains in the strain-hardening regime.

### 2.3.2 DIC

To investigate whether the difference in force profile between C-PCL and A-PCL affects the way in which the material deforms, DIC was next used to track the materials as they were being stretched using the same set up as the tensile testing in the above section. The below figure is an example of the output Eulerian strains ( $\epsilon_{yy}$ ) for one test sample per polymer variation (figure 2.11).

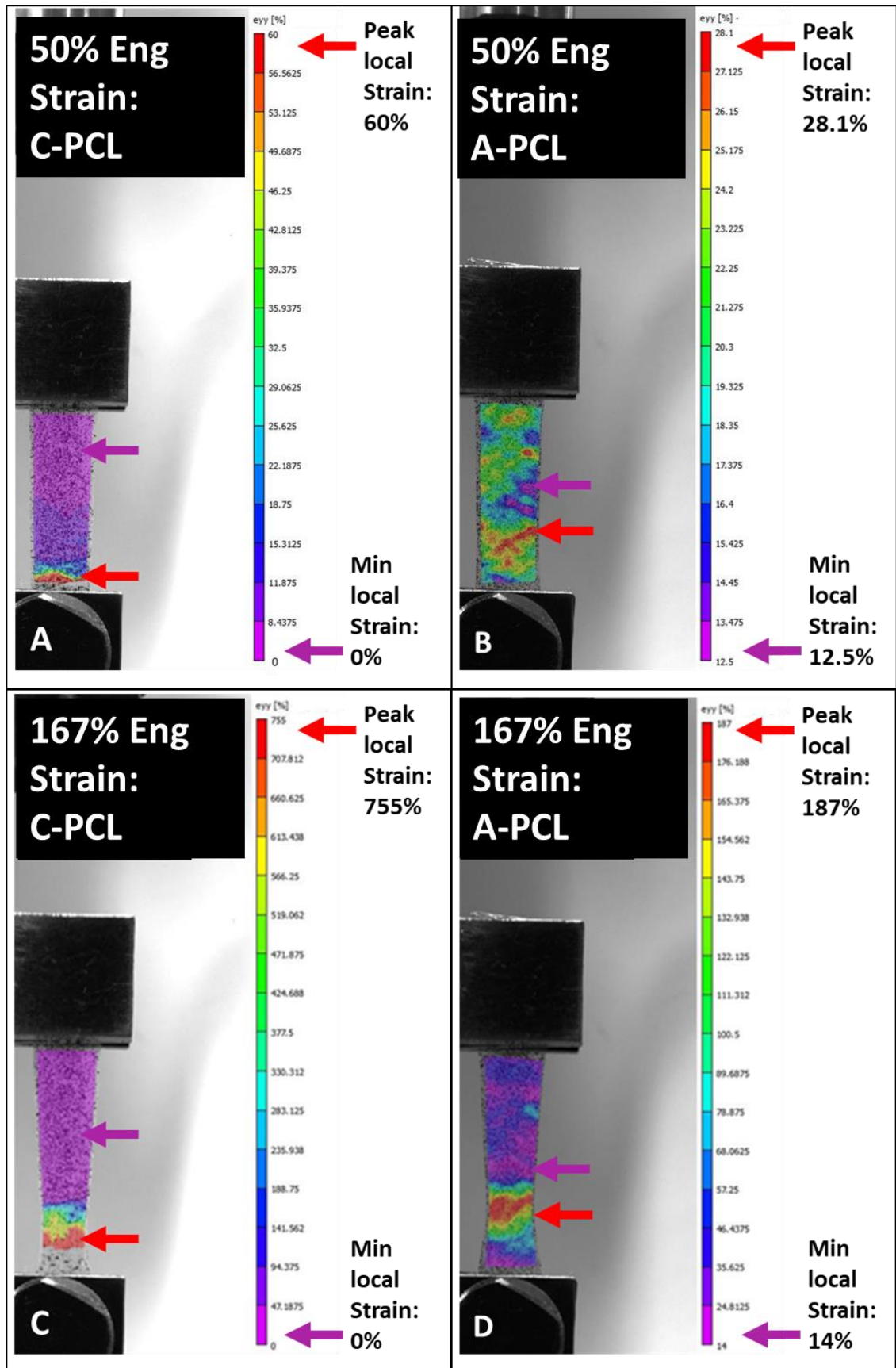
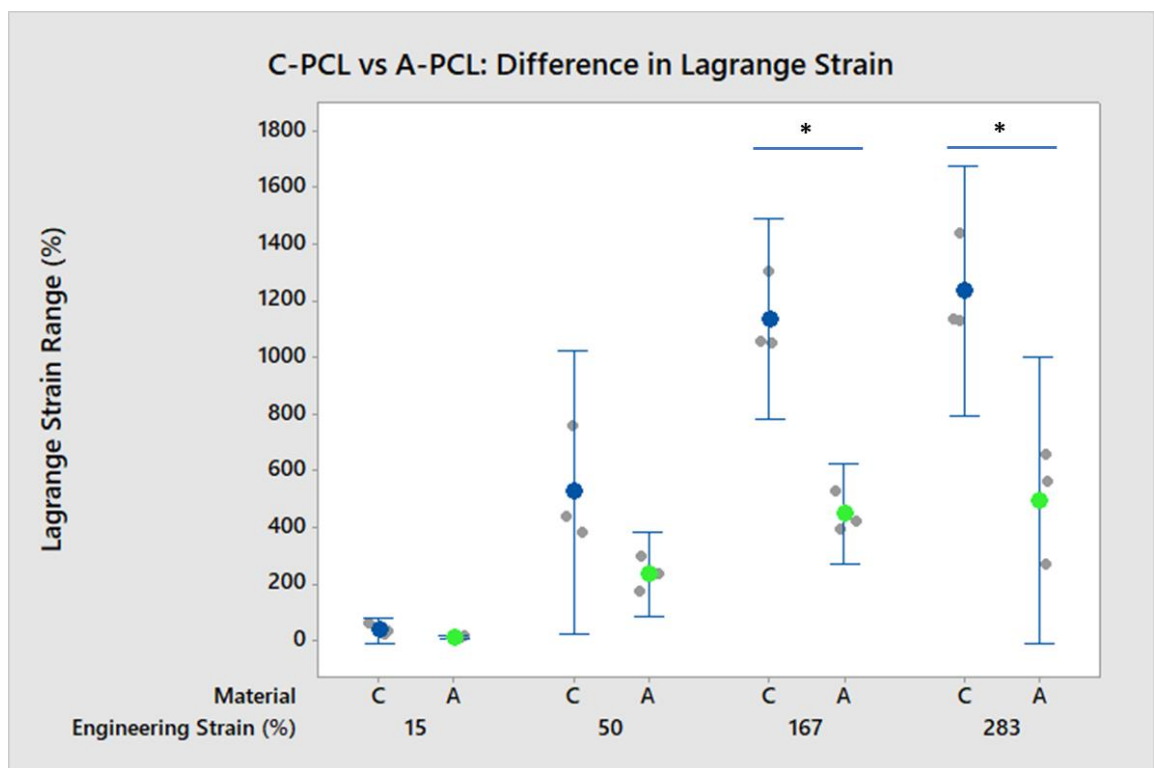


Figure 2-19. DIC tensile testing comparison between C-PCL and A-PCL. Images taken at 50% Engineering Strain for A) C-PCL B) A-PCL, and at 167% strain for C) C-PCL and D) A-PCL. The bar on the right of each image is a scale for the colours present (red=high strain, purple=low strain) on the material and is not equal between images. This is depicted by the min and max strains highlighted in each image.

A clear difference can be seen by looking at the heat map of local strains across the 2 PCL variations. The range in strain values between each sample is a good indicator for how homogenous the strain distribution is in each material; the material displaying a lower range (at the same level of Engineering Strain) would be evaluated to have a more homogenous strain profile, as this would indicate that the strain is more evenly distributed through the material, as a pose to a localised point on the material taking the bulk of the strain. Figure 2.20 quantifies the range in Eulerian strains ( $\epsilon_{yy}$ ) obtained from DIC images across 3 samples of each polymer variant.



**Figure 2-20. Difference between C-PCL and A-PCL when looking and localised strain (A) and stress (B). (n=3 for both C-PCL and A-PCL. Error bars represent 95% confidence intervals based on standard deviations. P values indicating significance, \*  $\leq 0.05$ ).**

The first range value was taken at 15% as this is towards the end of the elastic range for both materials. The remaining quantifications are made through the plastic flow/strain hardening region of the curve. After 283% strain, tracking could not continue on the CPCL material due to the deformed crystals refracting light.

The initial strain ranges don't significantly differ, and it is clear in both cases that stress and strain localise to a 'necking' region (Figure 2.19). The localisation of this strain is greater in C-PCL during the plastic flow stage at 167% and 283% Engineering Strain where the difference in Eulerian Strain range is significantly higher than in A-PCL.

### 2.3.3 Microscopy, and SEM Imaging

To understand the stretching behaviour illustrated in the above section of C-PCL, microscopy images were taken while the material was stretched underneath it. Figure 2.21 illustrates how the crystalline structure changes throughout being stretched. Crystals are initially closely packed with small amorphous spaces between. Just after the yield point (35% strain) noticeable stretching can be seen, however the crystalline structure around the region which looks unstretched also has changed; this is due to tilting of crystallites and separation of crystalline blocks during stress relaxation/plateau. This is followed by stretching and alignment of both amorphous and folded chains propagating along the necked region (Jabbari-Farouji et al., 2015).

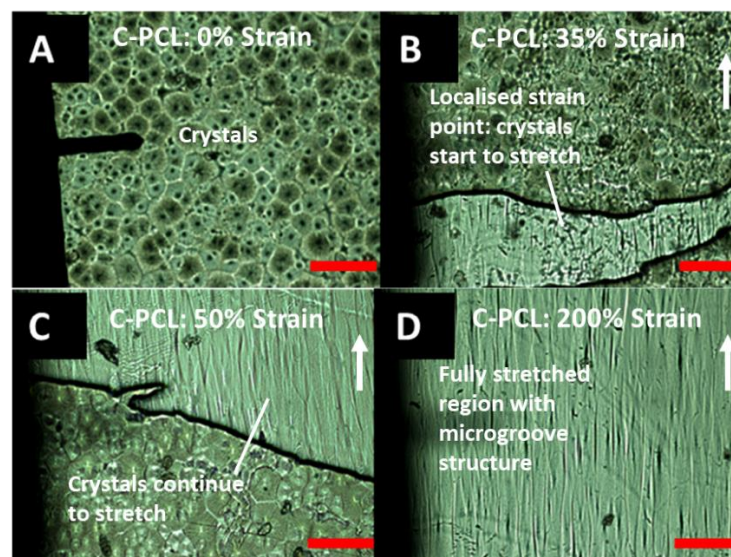
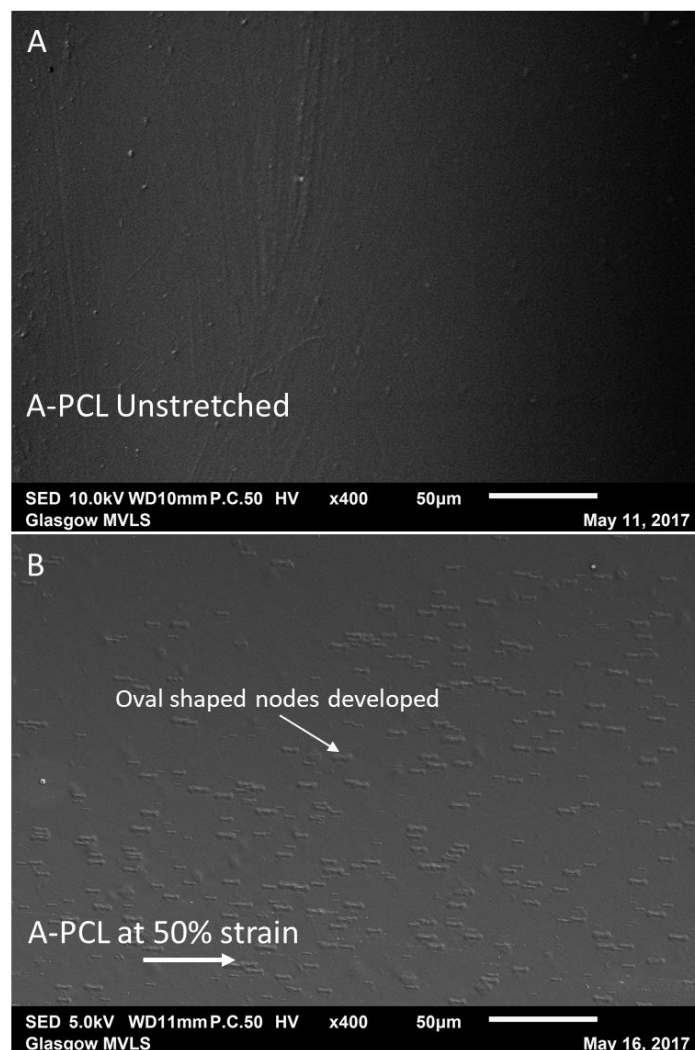


Figure 2-21. Light Microscopy images of C-PCL being stretched. A) At 0% strain, the initial crystal structure can be seen. B) At 35% strain, just after the yield point of the material, a clearly stretched region can be seen; crystals outside of this region also look deformed in comparison to the 0% image. C) At 50% strain, the strain can be seen to propagate through the clearly stretched region; further deformation of crystals outside of this area continues to be seen. D) At 200% strain, the stretched region has propagated further through the material. Scale bar is equal to 100 $\mu$ m in each image.

A-PCL structural changes cannot be determined in the same way under a light microscope as the light just passes through the sample. A-PCL structural changes due to stretch were therefore first investigated through SEM imaging. Unstretched samples were imaged followed by samples stretched to 50% strain (within the plastic flow range). Figure 2.22 shows how no structure could be identified under SEM for unstretched A-PCL samples, however at 50% strain, small elongated oval structure features (~5 $\mu$ m maximum diameter) can be seen to be developed.



**Figure 2-22. SEM images of A-PCL (A) unstretched (B) Stretched at 50% strain. Small oval nodes ~5 $\mu$ m in size develop on the stretched sample.**

These features may be nucleation points of crystallisation developing due to strain on the amorphous material; this could contribute as to why A-PCL displayed more strain homogeneity. The nucleation points may act as a series of anchor points

developing through the material as it's strained providing a more homogenous strain profile through the material.

### **2.3.4 Polarised Light Microscopy Imaging**

Polarised light microscopy was used to further analyse the structural changes occurring in both materials. Specifically, this technique will provide information on the orientation of the structures within both materials. Unstretched versions of both C-PCL and A-PCL were first put on the stage of the microscope before the stage was rotated through  $90^\circ$ . C-PCL, as expected produced a rotating image of crystals as the stage was turned (Figure 2.23, A-C); this is due to the crystals diffracting light through the second polariser. Conversely, A-PCL produced an unchanging image of darkness, due to light not diffracting through it and hence not passing through the second polariser (Figure 2.23, G-I).

However, upon stretch (50% strain), both materials give a different output. Initially neither material enables light to pass through the second polariser, however upon the stage being turned, light passes through and increases in intensity as the stage is turned to  $50^\circ$  (Figure 2.23, D-F, J-L). The light intensity then drops back down as the stage is turned from  $50^\circ$  to  $90^\circ$  (Figure 2.24). In both cases, this suggests that the structures are monoaxially oriented in each film in the direction of stretch.

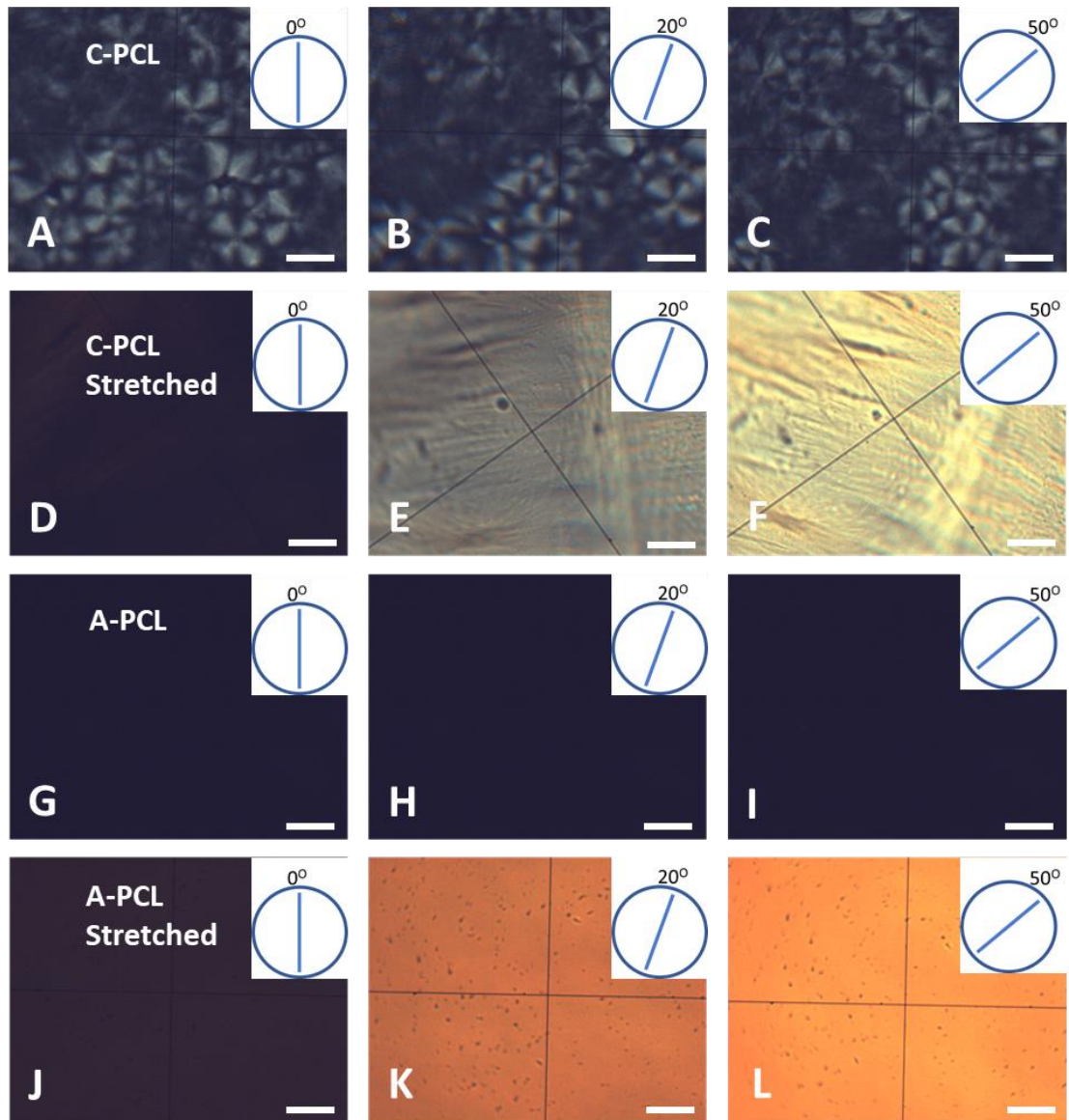


**Figure 2-23. Polarised light microscopy images of C-PCL and A-PCL under crossed polarised light. A-C are images of unstretched C-PCL when the stage is turned from 0-50°. D-F are images of stretched C-PCL (50% strain) when the stage is turned from 0-50°. G-I are images of unstretched A-PCL when the stage is turned from 0-50°. J-L are images of stretched A-PCL (50% strain) when the stage is turned from 0-50°. The circles in the top right corner in each image determine how much the stage has been rotated for each image. Scalebar represent 50um.**

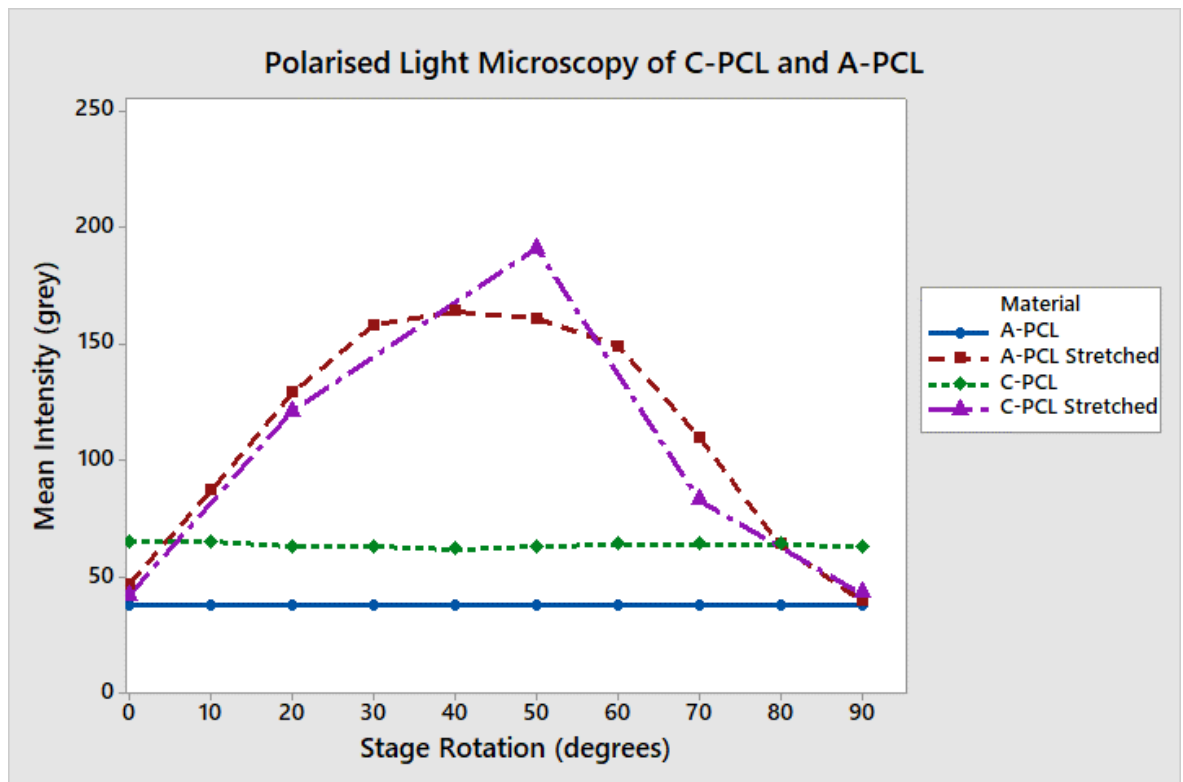
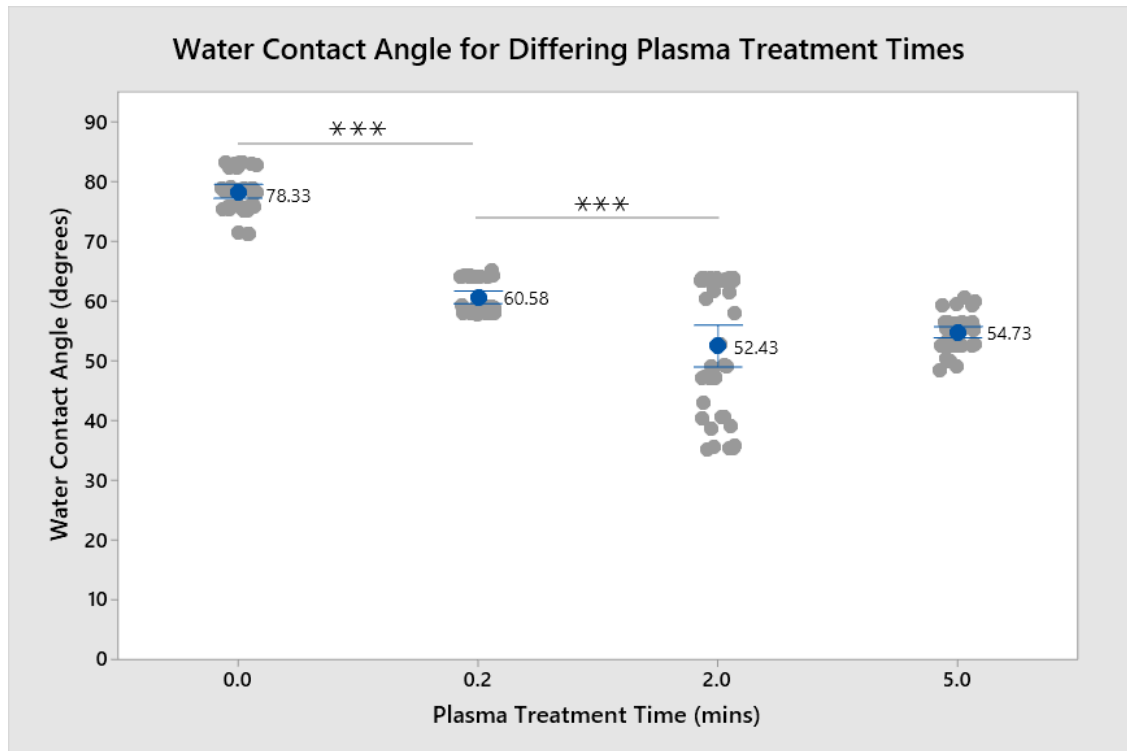


Figure 2-24. Quantification of light intensity generated by polarised light microscopy imaging of unstretched and stretched C-PCL and A-PCL samples. Samples were rotated under polarised light microscopy from 0-90°. Unstretched samples of C-PCL and A-PCL show no difference in light intensity between rotations. Stretched samples have low light intensity at 0°, this increases through rotation, and peaks at 50° before intensity drops from 50 to 90° rotation again.

### 2.3.5 Water Contact Angle

Having characterised mechanical and structural differences between the 2 versions of PCL, the effect of surface treatment on material hydrophilicity was then determined for future cell attachment studies. The aim here was to determine a range of plasma treatment times to test against cell attachment and proliferation so that the surface could be optimised to support cell attachment and proliferation over long time frames required for investigating tissue growth via stretch.

WCA measurements were taken for C-PCL plasma treated under a range of times (0-5 minutes). Figure 2.25 shows that as plasma treatment time is increased WCA decreases due to the surface becoming more hydrophilic as a result of nitrogen and oxygen bonding to the surface of the material. However, there is no significant difference between WCA for samples treated for 2 minutes and samples treated for 5 minutes.



**Figure 2-25.** Water contact angle measurements for C-PCL treated at different air plasma times.  $n=4$  samples with  $n=5$  droplet measurements on each sample for each plasma treatment time. (Error bars represent 95% confidence intervals based on standard deviations. P values indicating significance,  $*** \leq 0.001$ ).

As WCA decreases for plasma treatment times up to 2 minutes, samples tested for optimisation of cell attachment and proliferation will be treated for varying times up to 2 minutes before being evaluated.

## 2.4 Discussion and Conclusion

This chapter characterised differences between 2 types of PCL film, amorphous and crystalline. The stress/strain profile for C-PCL correlates with previous data for tensile testing of PCL (Duling, 2008; Ragaert et al., 2014). Utilisation of the polymer for modelling stretching of soft tissue for the purposes of growth is however unexplored. Both versions of the polymer (A-PCL and C-PCL) initially have an elastic period which is unrepresentative of the deformation characteristics of soft tissue, firstly because the polymers are stiffer than most soft tissues at this point (Young's Modulus 91.98 and 47.04 MPa for C-PCL and A-PCL respectively), and secondly soft tissue is viscoelastic and therefore stress-relaxes upon being stretched. Stretching in the elastic phase of both C-PCL and A-PCL maintains a consistent tension over time.

The ultimate goal of considering stiffness in tissue engineering strategies is the recapitulation of qualities of living tissue. Static mechanical properties are initially considered by trying to mimic the stiffness and/or softness of the native structure. However, in the case of this project the elasticity (Young's modulus) is not as important as the deformation behaviour of the material. This is because the dynamic nature of tissue stretching is aimed to be captured and the Young's Modulus does not consider the coming together of several molecular components to remodel tissue in response to stretching. Furthermore, certain tissues are multi-layered, where each layer has its own elastic property, which enables functional nonlinearity of the stress-strain curve (Levental et al., 2007). It is therefore important to incorporate the dynamic nature of change in response to stretch of biological tissues in this model.

To capture this element of stretching soft tissue, it was decided that both substrates would be pre-stretched past their yield points and held at that point before cells are cultured on, so that any stretching regime conducted after cells are cultured on is in the plastic flow region of each material and more representative of the change in tension soft tissue would undergo. It is important to realise the degree of stress-relaxation is different in C-PCL compared to A-PCL, where C-PCL exhibits more stress-relaxation after the yield point; furthermore, the stress plateau displayed in the plastic flow region (Figure 2.17) also signals

that it will stress-relax more compared to A-PCL (Duling, 2008). This property difference may be utilised in the future for the purposes of modelling different tissues which stress-relax/deform differently.

There are also differences between C-PCL and A-PCL in terms of how each material deforms (Figure 2.19, and 2.20) and structural topography of each material before stretch and after stretch. However, in both cases the material structures align to the direction of stretch. Previous work on pre-stretched PDMS has shown that cells align in the direction of 'highest stiffness' in the direction of stretch, where topography impact was negated by deposition of a non-fibrous poly-L-lysine matrix for cells to be cultured on (Liu et al., 2014). Work prior to that suggested topographical changes aligned fibrous collagen to the direction of stretch to determine cell orientation (Haston et al., 1983). Pre-stretched semi-crystalline PCL shown to develop microgroove like structures has also shown cells to align in the stretched direction when the material was not held under tension (Z. Y. Wang et al., 2014). Therefore, the structural change and tension in the material are likely to contribute to cell alignment if both materials are taken and held past their yield point prior to cells being seeded on.

The WCA measurements taken for different plasma treatment times indicate that a range between 0 and 2 minutes should be tested as part of a cell attachment/proliferation study in Chapter 4.

## **3 Devices Developed for Experimentation**

### **3.1 Introduction**

Stretching substrates with attached cells has been used as a means of investigation for various mechanobiological applications; many of which use cyclic stretching of elastic substrates. Examples involve investigation of cells subjected to a dynamic stimulation; such as cells in the connective tissue of heart or lung. The focus of this chapter is to detail how PCL substrates are to be stretched under cell culture conditions. Chapter 2 of this thesis concluded that PCL films will be used as a model substrate for stretching soft tissue cells. Furthermore, it was concluded that substrates were to be stretched past their yield point prior to cells being cultured on. As the current rate of distraction osteogenesis in surgery is ~1 mm every 24 hours, the rate at which substrates cultured with cells are stretched will not exceed 1 mm over 24 hours. This is not designed to be a stretching mechanism which is cyclic, and the substrates will be continuously stretched over long periods of time ( $\geq 1$  day), where they will be permanently deformed.

This chapter will first define parameters around stretching that the substrate must undergo in relation to cell culture, before outlining and comparing devices used so far in the application of stretch to cell cultured substrates. These devices will be analysed with the view of either applying them or using features of them for the purposes of this project. Subsequent sections of the chapter will then describe the development of devices and how they compare to the aforementioned devices.

#### **3.1.1 Defining the Mechanism of Stretch**

Research studies in relation to stretch are commonly cultured under stretch regimens that mimic the physiological mechanical strain of the tissue of interest. For example, to condition engineered bladders, the pattern of stretch was set based on the bladder activity within a period of 24 hours. Four sets of filling/

emptying were defined to occur in a 16-hour period followed by 8 hours of rest. In each fill-empty cycle, stretching increased from 0 to 2.5% equibiaxially for the first 3 hours, this was followed by 1 hour with larger strain ranges (5% to 25%). To simulate the rest period, the construct was relaxed back to 0% strain (Luo et al., 2015). Looking at neurons at the opposite end of the scale; axons were grown under stretch by taking 1 $\mu$ m steps uniaxially every minute over 1000 iterations resulting in 1mm elongation growth each day (Loverde et al., 2011).

By the same principle, the stretching regimen used to stretch PCL constructs with cells cultured on must be uniaxial and done in small increments. The stretching regime will be uniaxial as during DO the stretching is done in one axis. The length usually between the fixation points for the fracture sight in a DO procedure is ~40-60mm (Figure 3.1). However, there are further fixture points at each end of the bone (Figure 3.1); as the soft tissue is the primary concern for this project, the model should be scaled to the entire length of the bone being distracted.

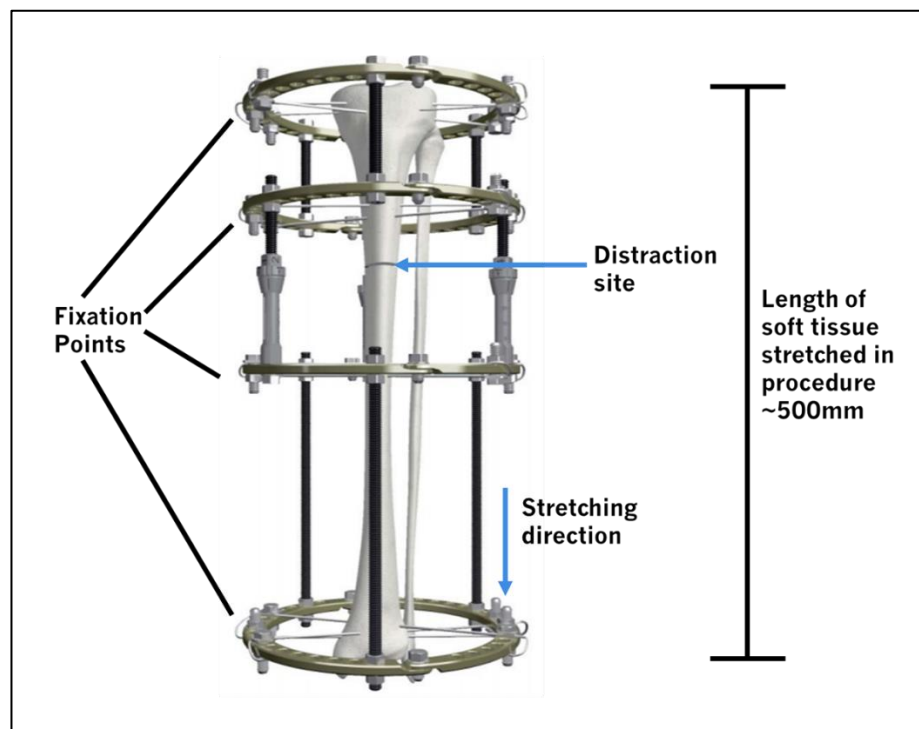


**Figure 3-1. Schematic depicting typical device fixation points for distraction osteogenesis procedure. Although the distraction site for bone is isolated to a small region, the soft tissue being stretched is over the length of the whole bone (image taken from: [www.jnjmedicaldevices.com/en-EMEA/product/distraction-osteogenesis-ring-system](http://www.jnjmedicaldevices.com/en-EMEA/product/distraction-osteogenesis-ring-system)).**

The substrates are likely to be significantly smaller than bone (50mm compared to ~500mm) and the 1mm over 24 hours rate of distraction (G. Kumar & Narayan, 2014) should therefore be scaled down. However a 1mm stretch over 24 hours was still aimed to be the starting rate of stretching substrates after cells have been cultured on and this was to be done in small hourly increments; stretching during DO is usually done in 1-4 increments over the 24 hours (G. Kumar & Narayan, 2014). The significantly higher deformation (x10 relatively) alongside the increase in steps should provide a strong signal when analysing cell responses to ensure plastic deformation of PCL has an effect on cell populations. However, for the purposes of experiments beyond the scope of this project, the device should be able to administer 0.1mm deformation over 4 steps in 24 hours to substrates 50mm in length to directly simulate DO for the purposes of limb lengthening. This equates to a minimum strain of 0.05% being able to be applied (for each increment) by the device/devices to be used.

Furthermore, as the substrate needs to be stretched passed its yield point into the plastic flow region (see chapter 2 conclusions), the machine must be able to initially strain substrates by 25% at 1mm per second. If substrates are to be 50mm in length for when cells are to be cultured on, they can be stretched from 40mm to 50mm prior to culture. The needs of the device/devices are specific in relation to the stretching regimen, however a scan of devices used to date can be used to provide direction and input into what should be developed and how it should be developed.

### **3.1.2 Devices Used for Cell Substrate Stretching**

Flexcell (<https://www.flexcellint.com>) is one of the most used type of device for cell mechanotransduction studies; they have 3 main devices which come into consideration with regards to application of tension on a substrate cultured with cells. The 'FX-6000T™' and 'Flex Jr.™' tension systems are designed to cyclically stretch silicone substrates whereas the 'Tissue Train®' 3D culture systems strain 3D collagen gel scaffolds. The minimum applicable strain that can be applied is 0.1% and the maximum is 33% in the 3 mentioned systems. The 'Flex Jr.' is a single

chamber device, designed to be used in conjunction with microscopy to enable real-time imaging and analysis of cells responding to strain.

Strexcell (<https://strexcell.com/>) has two main types of devices, one of which, like Flexcell is a high-throughput, long term stretching machine; the other device is also a microscope mountable option for live-cell imaging. Both Strexcell systems are designed to apply strain to their own designed PDMS chambers in a cyclic motion, and the machines have prewritten programmes meaning that the flexibility to create a unique programme to slowly stretch a substrate is not there or would need customisation through the company. Furthermore, the minimum strain that can be applied is high at 1.5% compared to the Flexcell devices and the maximum strain it can apply to substrates is 20%, again performing significantly worse than the Flexcell devices.

As the Flexcell and Strexcell devices come with built in substrate platforms they would require substantial modification to use in the application of strain to cell-cultured PCL. There are however 2 CellScale (<https://cellscale.com>) systems which unlike the above systems cater for interchangeable substrate testing. Therefore, PCL would be able to be tested without excessive device manipulation. The MCJ1 Bioreactor has six chambers, each coming with its own load cell for real-time measurement of force change during substrate stretching (Figure 3.2A). Although the device is built to test specimens by applying load cyclically, small displacements may be able to be applied and held, however this is not outlined in the specification. The smallest displacement this machine can apply seems load dependant; 0.02N. The clear advantage in using this device would be that force-displacement graphs would be able to be seen in real time as substrates are stretched and each sample can be strained at different rates/increments. The second CellScale device which is applicable for the purposes of this project is the MCT6. This device is designed for the purposes of stretching long rectangular 3D constructs, however the clamping mechanism (Figure 3.2B) for the device may well be applied to hold thin PCL films. This device is however primarily used for cyclic stretching at high magnitudes relative to what this project aims to look at; the lower end of strain that can be applied through this device is not specified, and several studies use this device to apply strains of 5-20% (Ali et al., 2019; D. Kumar et al., 2019). Furthermore, as the samples are all attached to one block

(Figure 3.2B) which displaces all the substrates simultaneously upon moving, all samples will be subjected to the same deformations.

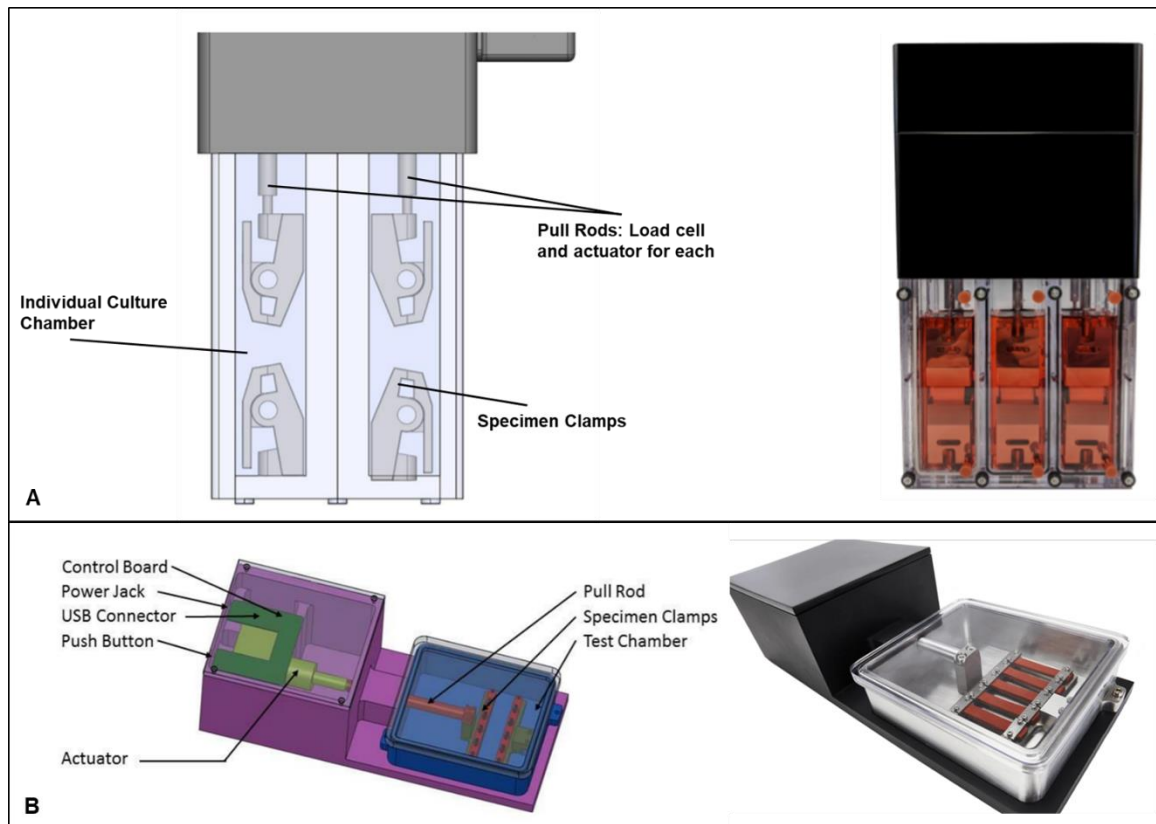


**Figure 3-2. CellScale devices used to uniaxially stretch cell cultured substrates. A) The MCJ1 has vertically orientated culture chambers with a load cell attached to each chamber alongside individual actuators. substrates are attached via outlined clamps. B) The MCT6 has horizontally orientated chambers with one actuator for all chambers, substrates are attached via outlined clamps (images taken from: <https://cellscale.com/products/>).**

Each of the above systems have their own mechanisms which control substrate stretching, the main mechanism used to drive the displacement or load applied is called actuation. The Flexcell systems are all actuated pneumatically. This means that substrate strain is controlled via pressure changes. Pneumatic actuators have been widely used in in-house devices as well as the commercial Flexcell systems to induce mechanical stress or strain to cells via substrates in-vitro. Both positive and negative pressure sources have been utilised for stretching membranes. Research has been conducted on cells cultured on serially connected balloons which apply strain on inflation (increase in pressure) (Shimizu et al., 2011) (Figure 3.3A), as well as on substrates stretched using a vacuum source to deform a wall attached to the sides of the substrate (Huang & Nguyen, 2013) (Figure 3.3B). This concept has been further developed to stretch membranes biaxially where four

independently controlled low-pressure compartments are used instead of 2, to pull membranes in directions perpendicular to one another.

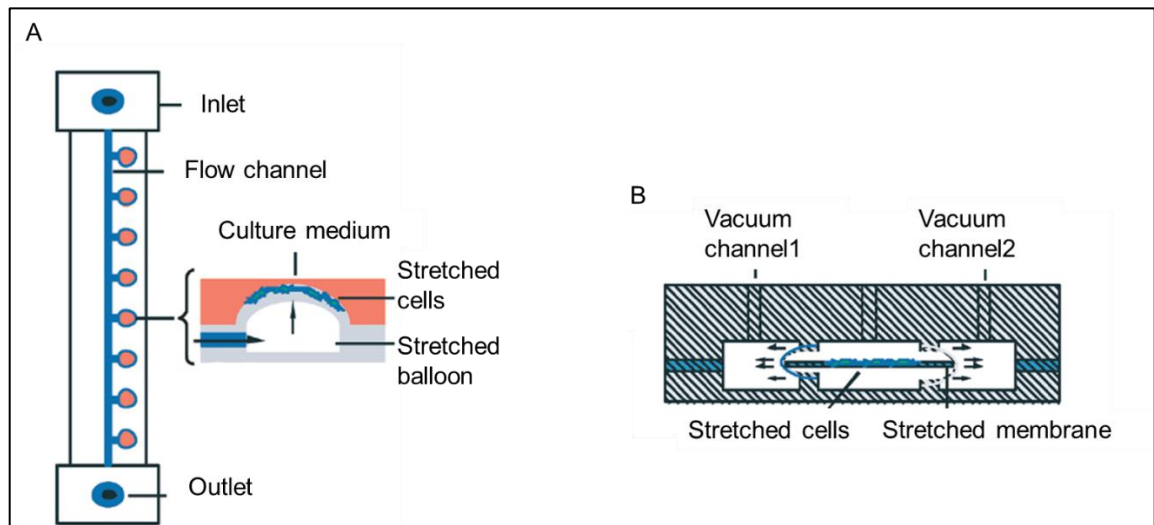


**Figure 3-3. Example pneumatic actuator mechanisms. A) Positive pressure used to inflate series of balloon membranes, thereby stretching cell cultures. B) Negative pressure applied to each end of cell cultured membrane to stretch from each end.**

The desired overall deformation may not be achievable with pneumatic systems, as in the Flexcell devices the smallest achievable substrate strain is 0.1%. However even if the minimum strain of 0.025% strain was achievable with a pneumatic system, there would still be problems related to deforming PCL in small increments over 24 hours. This is because the deformation would rely on a negative pressure calibrated to give a certain amount of displacement. This would bring about sample variation in displacement if mechanical properties between samples slightly varied, but furthermore problems would be encountered after deformation has been applied using a negative pressure; when the substrate is held at a specified deformation, it will stress relax. This would result in the substrate continuing to deform if held at that negative pressure. To avoid this, a sophisticated feedback loop would be required; however regardless of a feedback loop being developed the inaccuracy that would have the potential to accumulate after several increments would make samples incomparable.

Piezoelectric devices have also been used to deform cell-cultured substrates. Piezoelectric manipulators using a high displacement resolution have been included in a number of studies to induce cell stretching, where the key

advantages have been precision while being able to apply a broad range of controllable strains, from a few microns to tens of microns (Kamble et al., 2016). Generally piezoelectric actuators require a direct physical contact with cells which limits their application, however indirect stretching through microstructures has been used to overcome this problem; microwells with a flexible bottom membrane have been placed over piezoelectrically actuated pins to apply stress/strain to cells. Pins were independently actuated using a customised computer program that pushed the bottom membrane to achieve membrane deformation (Figure 3.4A) (Kamotani et al., 2008). Other devices have used piezoelectric actuators in conjunction with linear fixtures to deform PDMS membranes (Figure 3.4B), where the maximum applied substrate displacement was 89 $\mu$ m (Deguchi et al., 2015).

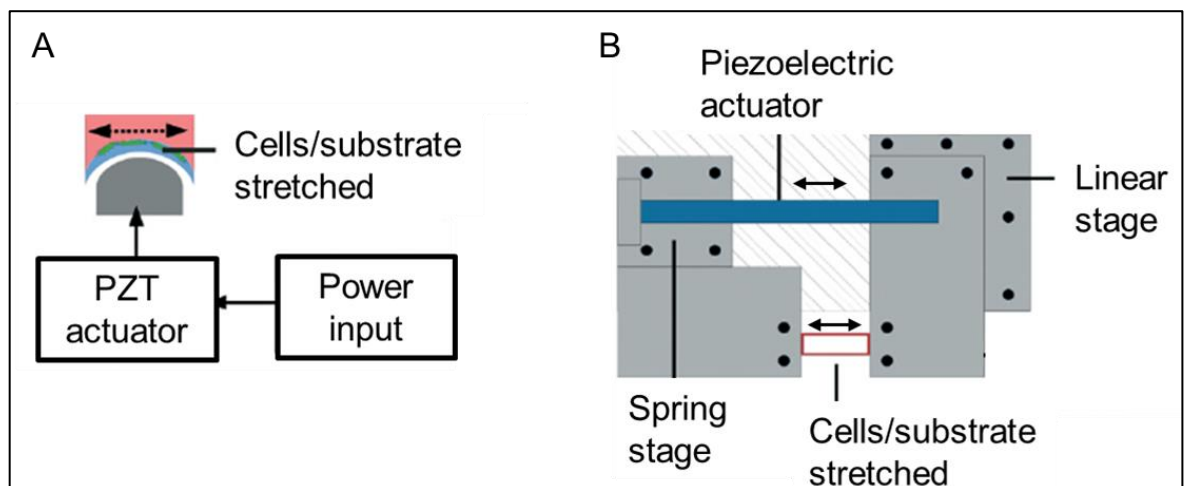


**Figure 3-4. Example piezoelectric actuator mechanisms to stretch cell cultured substrates. A) Microwell substrates placed over piezoelectric pin, displacement controlled via power input. B) Stretching of cell cultured PDMS membrane through moving stages; the linear stage moves away from the spring stage upon piezoelectric actuation, upon relaxation, the spring helps the PDMS recoil back to its original shape.**

Piezoelectric actuators would provide accuracy in displacement, however, are unviable for the purposes of this project as they cannot easily enable incremental displacement; the range in which they do displace would suffice for approximately one-tenth of the overall displacement required per substrate (1mm).

Motors are the most common method of actuation when considering linear displacement due to their relatively simplicity in running and cheap cost. The Strexcell and CellScale devices previously mentioned use motors as the method

for actuation for their systems. The movements and forces generated by motors can be precisely monitored and controlled. Rotary stepper motors can rotate  $0.09^\circ/\text{step}$ , and displacements in one microstep linearly have been shown to be as low as  $\sim 0.1\mu\text{m}$  (Metzler et al., 2012). However, parts connected to motors often must be inserted into the culture chamber to drive substrate displacement, which increases the possibility of contamination and can transfer heat generated by the motor during operation, so it must be ensured that the motor does not sit close to the culture as not to effect the culture chamber temperature.

As motors operate via rotation, rotation must be converted to linear actuation through certain mechanisms. A summary of these mechanisms can be seen in Figure 3.5. Timing-belt pulleys and engaged gears have linear speeds and motion determined by the size of the pulleys or gears (Feng et al., 2005; Masoumi et al., 2014). Cam-shafts can generate high force at high speeds. A cam can be shaped to be axisymmetric such as a 4-sinusoid waveform superimposed around the circumference of a circle (Gupta et al., 2008). Thus, it can stretch the substrates multiple times with each cam rotation at high frequencies. However, these methods can only apply a set displacement cyclically. For the purposes of this project a rotating lead screw mechanism should be considered, where small displacements are achievable due to a combination of small motor steps in rotation as well as fine pitch dimensions of lead screws (Lei & Ferdous, 2016). Precision can then be achieved by driving the motor through a software platform.

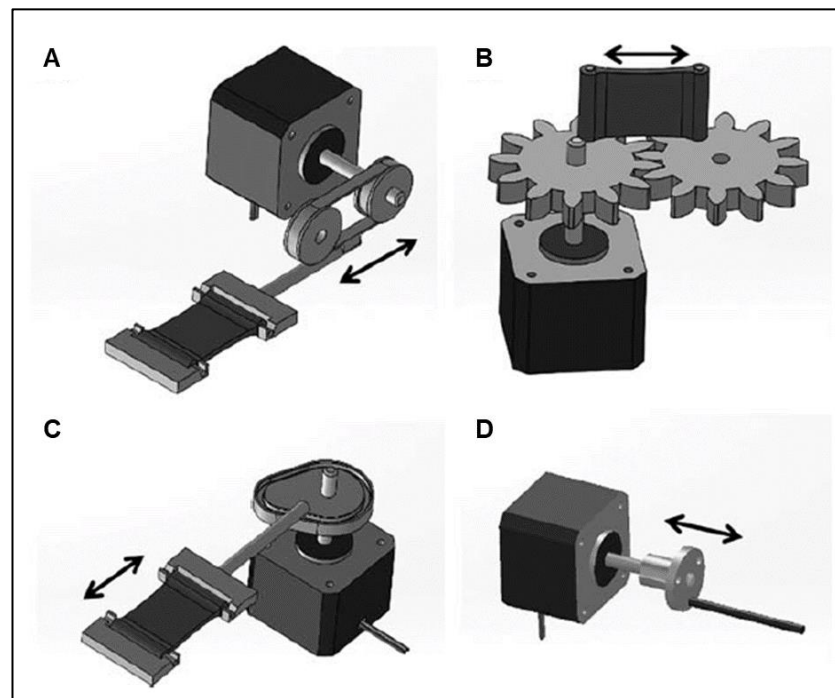


**Figure 3-5. Motor mechanisms to create linear displacements. A) Timing-belt pulley; size of pulley dictates displacement. B) Engaged gears; size of gears dictates displacement. C) Camshaft; Non-concentricity of cam dictates displacement. D) Screw pitch, length, and direction of motor rotation dictate displacement (Lei & Ferdous, 2016).**

As pneumatic actuation is an unsuitable mechanism in this situation due to small displacements of PCL requiring extensive pressure calibration to accommodate for material stress relaxation, and the fact that piezoelectric actuation would not enable a large range of overall deformation, motors were selected as the mechanism of actuation. Furthermore, as precision can be achieved for small displacements in a controlled manner, independent of the tension which PCL would be under, a stepper motor leadscrew mechanism was selected to be used in the design of the main device for this project.

### 3.1.3 Devices to be Developed

This project is targeted at analysing the active stretching of confluent cell layers on plastically deformable substrates to develop a model for stretching/growing soft tissue. Therefore, the key difference within this project, in comparison to existing set ups currently used is that the intention is for the substrate to be continuously stretched uniaxially rather than being stretched cyclically where substrates are stretched and then relaxed at a set frequency. Therefore, devices developed relating to this project were to incorporate precision in stretching uniaxially. Based on devices outlined in this section, 2 devices are to be designed for stretching PCL substrates in cell culture conditions for the following reasons:

- 1) To stretch several substrates at 1mm/sec up to a displacement of 10mm before continuing to stretch these substrates under culture conditions at a minimum stepped displacement of 0.025mm, 4 times over 24 hours.
- 2) To stretch a single substrate precisely and manually with the view of tracking cells on it under a microscopy set up.

Components designed to be 3D printed were designed in AutoCAD as 'dwg' files. These were then converted to 'stl' files which were then opened in a software called 'Cura'. The printing parameters input to Cura are outlined in the table below. Once set, the file is saved as a G-code on an SD card which is then inserted into an Ultimaker 2 3D printer. The material used for all prints was ABS (2.85mm diameter, Innofil3D).

## 3.2 Results

### 3.2.1 Cell Sheet Stretching Device

The aim of the first device developed was to enable precision stretching of multiple polymer films in cell culture conditions. Requirements for the device were that:

- It was to be able to incorporate a 4-well plate into the design so that separate conditions could be tested (if need be) within a single experiment.
- The media within the wells had to be easily accessible so that cells on substrates within the device could easily be fed, and so that immunostaining methods (as well as other likewise methods) could easily be conducted.
- The device should be easily dismantlable so that substrates could readily be removed for imaging.
- The part of the device that would hold the substrates should be compatible with a microscope in case substrates were to be held in tension whilst imaging.
- The device should be able to reside in an incubator (37°C, 5% CO<sub>2</sub>) for the duration of cell culture experiments.
- Linear actuation should be easily input and quantifiable to know how much strain has been applied to substrates.

The concept to be developed here was to create a framework to build a platform which could hold a 4-well-plate above the height of a motor/leadscrew unit, and then to make a lid which could be driven forward/backwards by the leadscrew over the attached well plate to stretch substrates in the well-plate. Blocks attached to either end of the substrates could be used where one end would remain fixed and the other would attach to the lid and hence move forward stretching the substrate upon turning of the leadscrew (Figure 3.6).

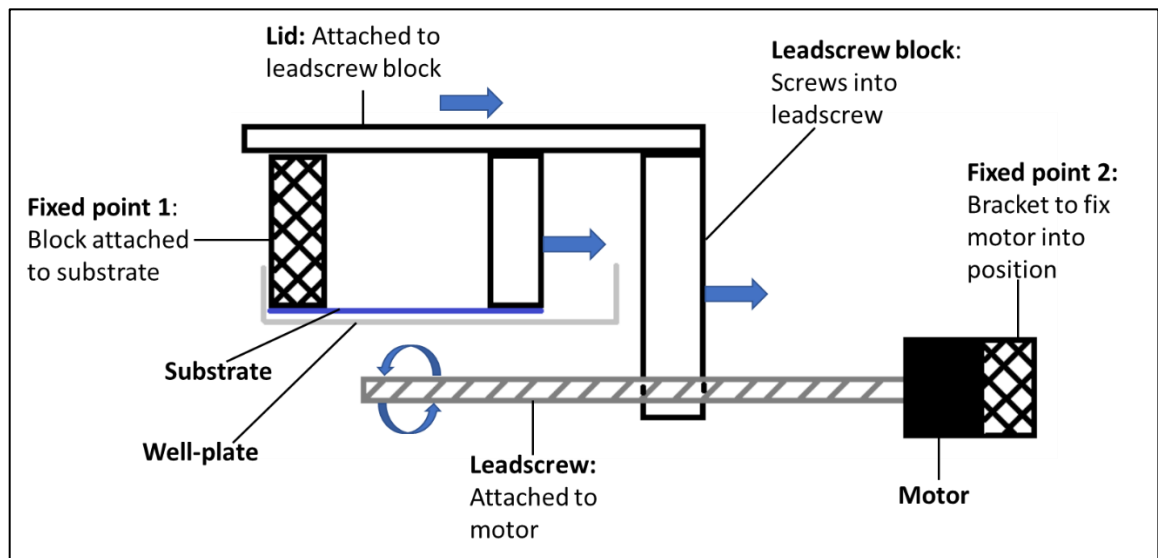


**Figure 3-6. Schematic depicting a concept of how a substrate material for cells may be stretched with precision.**

### 3.2.1.1 Motor and Leadscrew Selection and Control

Motor and leadscrew selection were important factors in developing the device due to these components governing the precision of the system over large time frames. Stepper motors are consistently used in mechanisms where linear precision is required. They're found in printers, machine tools, and process control systems and are built for high-holding torque which in this case would ensure substrates would be held in tension once stretched.

Every revolution of the stepper motor is divided into a discrete number of steps, and the motor is sent a separate pulse for each step. The stepper motor can only take one step at a time and each step is the same size. As each pulse causes the motor to rotate a precise angle (typically  $1.8^\circ$ ), the motor's position can be controlled without a feedback mechanism. As digital pulses increase in frequency, the step movement changes into continuous rotation, with the speed of rotation directly proportional to the frequency of the pulses (Sija, 2000). The rotation angle of the motor being proportional to the input pulse gives the motor high precision positioning and repeatability of movement.

The torque required to lift or lower a load can be calculated by unwrapping one revolution of a thread. The unwrapped thread forms a right-angle triangle where the base is  $\pi dm$  long and the height is the lead. The force of the load is directed

downward, the normal force is perpendicular to the hypotenuse of the triangle, the frictional force is directed in the opposite direction of the direction of motion (perpendicular to the normal force or along the hypotenuse), and a reaction force is acting horizontally in the direction opposite the direction of the frictional force. The torque required to stretch 4 substrates can therefore be calculated from equation 1 for different leadscrews, and a stepper motor can then be chosen accordingly.

$$T = \frac{Fd_m}{2} \left( \frac{l + \pi\mu d_m}{\pi d_m - \mu l} \right) \quad (1)$$

Where  $F$  is lateral force;  $d_m$  is diameter of the lead screw;  $l$  is the lead length;  $\mu$  is the coefficient of friction of the lead screw. It is known from tensile testing (Chapter 2) that the maximum load required to stretch one substrate is 5N; therefore, to stretch 4, the force applied must be at least 20N.

The motor selected for the purposes of this project was a NEMA 17 stepper motor with an attached 6.35mm diameter lead screw which had a lead length of 2mm (Stepperonline). This motor was to be controlled by an Arduino Board (Arduino/Genuino-Uno-R3) alongside a motorshield (Adafruit-motorshield-V2) which was soldered to it (Figure 3.7 a). There are 2 sets of ports (M1-M2, and M3-M4) which can be used to run 2 stepper motors simultaneously. The motorshield is powered via a 12v, 2A output adapter, and the Arduino is powered via a 5v, 2a output USB adapter. The rate at which the motor turns; how much it turns by; and how it does it, is controlled by a script uploaded to the Arduino Uno (Figure 3.8).

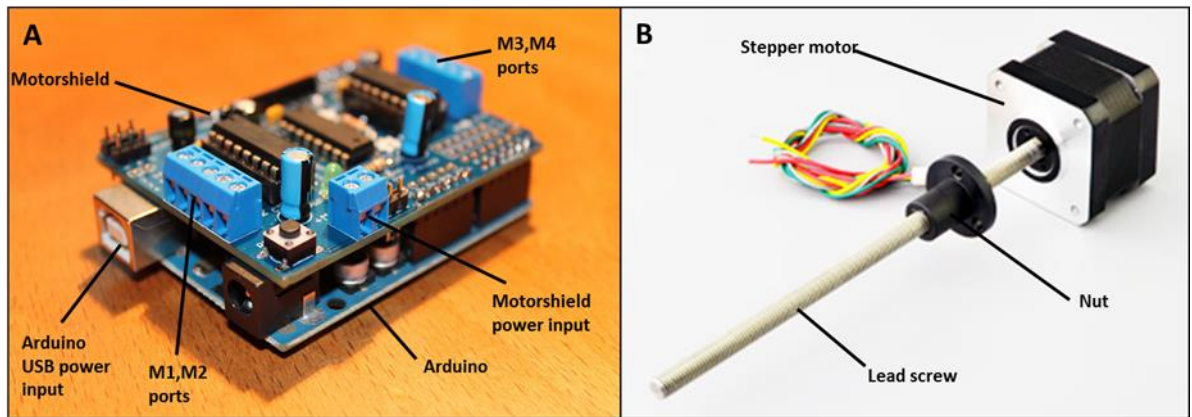


**Figure 3-7. Stepper motor driven by arduino to achieve precision stretching of cell culture substrates. A) Arduino configuration with Adafruit V2 motorshield fitted on top. B) Nema-17 Stepper motor with welded leadscrew (6.35mm diameter, 2mm lead length).**

This motor/lead screw/microcontroller configuration was chosen as it suffices the holding torque requirement based on equation 1 above. The lead length ( $l$ ) is 2mm; the coefficient of friction ( $\mu$ ) is  $\sim 0.15$ ; the diameter of the lead screw ( $d_m$ ) is 6.35mm. This results in a maximum torque ( $T$ ) of 0.97N.cm (0.099kg.cm) being required. The holding torque generated by the NEMA 17 stepper motor 2.6kg.cm, and it therefore suffices the requirements of being equal to or more than 0.099kg.cm.

The minimum required displacement for the system was outlined as 0.025mm (0.1mm overall stretch in 4 increments), and the minimum linear displacement achievable with this motor-leadscrew combination is 0.01mm. Furthermore, the maximum rate of displacement that the actuation mechanism was to achieve was 1mm per second (through a displacement period of 10mm); as this motor has a minimum rotary speed of 4688RPM and the lead length of the attached screw is 2mm, this rate is easily achievable.

```

File Edit Sketch Tools Help
_1mm_24hr $
#include <Wire.h>
#include <Adafruit_MotorShield.h>
#include "utility/Adafruit_MS_PWM_ServoDriver.h"
// Create the motor shield object with the default I2C address
Adafruit_MotorShield AFMS = Adafruit_MotorShield();
// Or, create it with a different I2C address (say for stacking)
// Adafruit_MotorShield AFMS = Adafruit_MotorShield(0x61);

// Connect a stepper motor with 200 steps per revolution (1.8 degree)
// to motor port #2 (M3 and M4)
Adafruit_StepperMotor *myMotor = AFMS.getStepper(200, 2);
void setup() {
  Serial.begin(9600); // set up Serial library at 9600 bps

  AFMS.begin(); // create with the default frequency 1.6KHz
  //AFMS.begin(1000); // OR with a different frequency, say 1KHz

  myMotor->setSpeed(3); // 3 rpm
}
void loop() {
  delay(60000);
  myMotor->step(2, FORWARD, MICROSTEP);
  delay(3600000);
}
38 Arduino/Genuino Uno on COM3

```

Figure 3-8. Example script uploaded to Arduino to provide 1mm stretch over 24 hours. Before the 'void loop' line, certain libraries are being selected, and the motor and which port it's connected to have been defined, as well as the speed that it will go through the amount of steps that are input within the 'void loop'. The delay function stops the motor from turning and is defined in milliseconds. The line highlighted defines how many steps (2) it takes in one cycle before the next delay; which way the motor rotates the lead screw (FORWARD), and which method it uses to turn the lead screw (MICROSTEP).

### 3.2.1.2 Device Design

MakerBeam is an open source construction set which utilises a miniature version of larger T-slot building systems. The kit consists of various lengths in extruded aluminium beams, 10mm by 10mm in width and height with various connectors and panels that slot into the sides of the beam. The kit was used to create a frame which the motor/leadscrew unit could sit in below a platform for a 4-well plate (Figure 3.8).

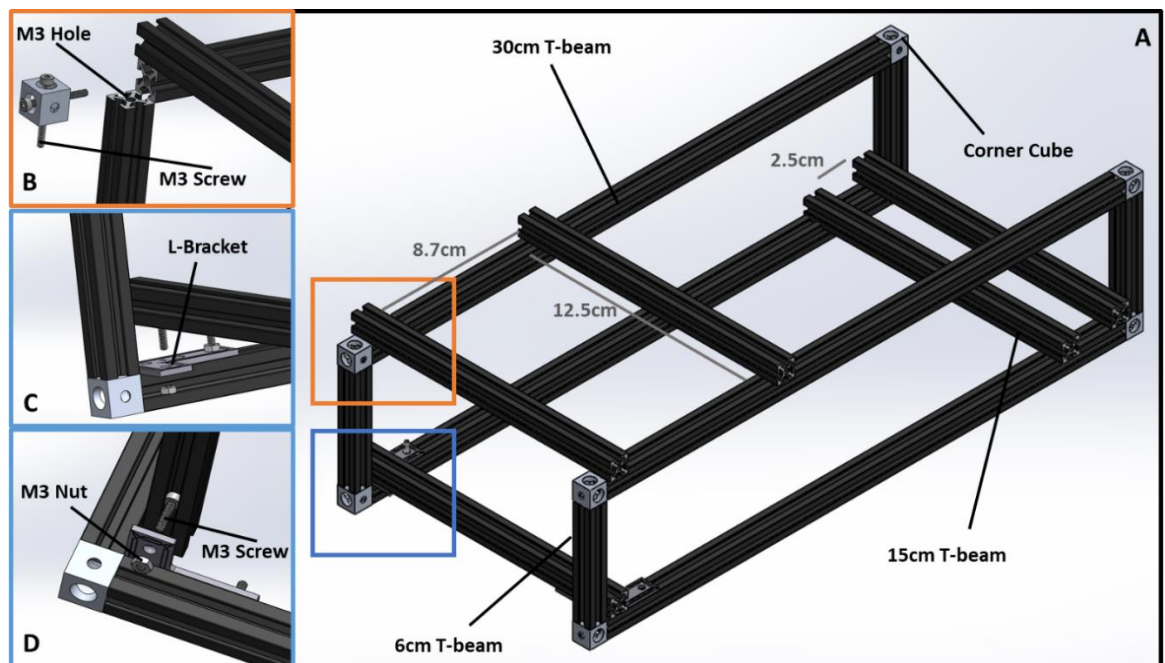


**Figure 3-9.** Frame assembly for cell substrate stretcher. A) Assembled Makerbeam beams (30cm x 4, 15cm x 5, 6cm x 4), corner cubes (x8), M3 12mm square headed screws (12mm x 20, 6mm x 16), and L-brackets (x10). B) Blowout of a corner joint to connect 2 beams at a right angle. 2 x 6mm M3 screws are required. They are each pushed in through the large hole on the cube through to the small which sits against an M3 threaded hole on the end of the beam. C) Blowout of how an L-bracket connects the 15cm beams to the 30cm ones. A screw slotted into each beam goes through one of the holes on the bracket and is kept in place by screwing down a nut on each screw. D) Blow of the L-bracket joint again. Different view to show how screws slot into T-beams.

As depicted by Figure 3.6, the concept was being generated so that the motor would sit on a level below the well plate. A Nema-17 bracket was bought alongside the stepper motor from Stepperonline and fitted onto the bottom two 15cm beams (Figure 3.10).

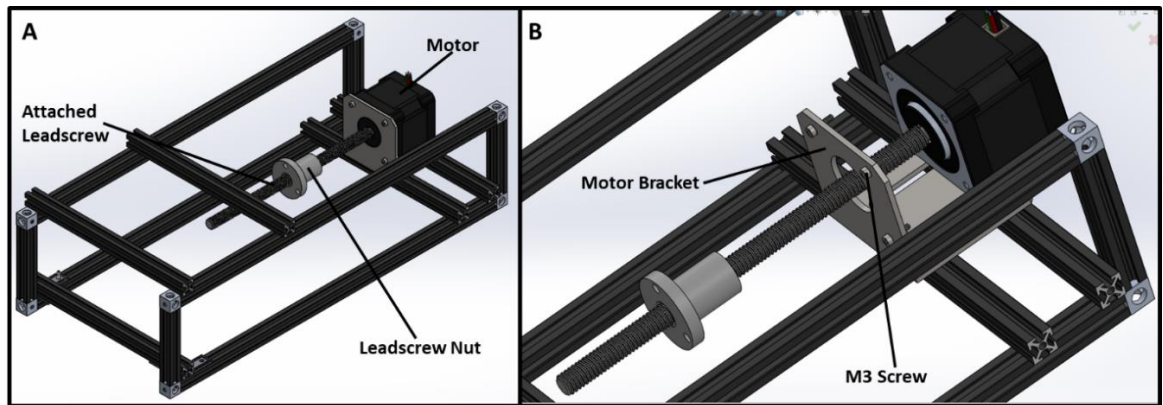


**Figure 3-10. Motor/leadscrew assembly on frame. A) Full assembly with motor fitted onto bottom 2 15cm brackets. B) Blowout showing how the motor attaches to the brackets, 4x 12mm M3 screws go through 4 corners of the front of the bracket into 4 threaded corners into the motor. The bracket is attached via 4x 6mm M3 screws (2 slotted in each 15 cm beam before being tightened with M3 nuts).**

3D printed parts were then designed on AutoCad to fit around the frame and in the well-plate. Various studies have shown cell viability not to be effected by the 3D-printed material ABS (Hyde et al., 2014; Rosenzweig et al., 2015). The frame was dimensioned to hold a 4-wellplate (Thermofischer) on its top level. A 4-well-plate frame was designed, and 3D printed to sit flush against the MakerBeam framework put together with a 4-well-plate underneath (Figure 3.11). The holes on the 4 corners of the fixture are 4mm in diameter and would allow screws placed through the T-slot of beams underneath through; M3 nuts can then be used to tighten the 4-well-plate frame to its corresponding beam. When 3D printed, the M4 threaded holes are printed at a 3mm diameter and are then manually threaded in. The ridges allow the M4 threaded holes to sit in the well-plate.

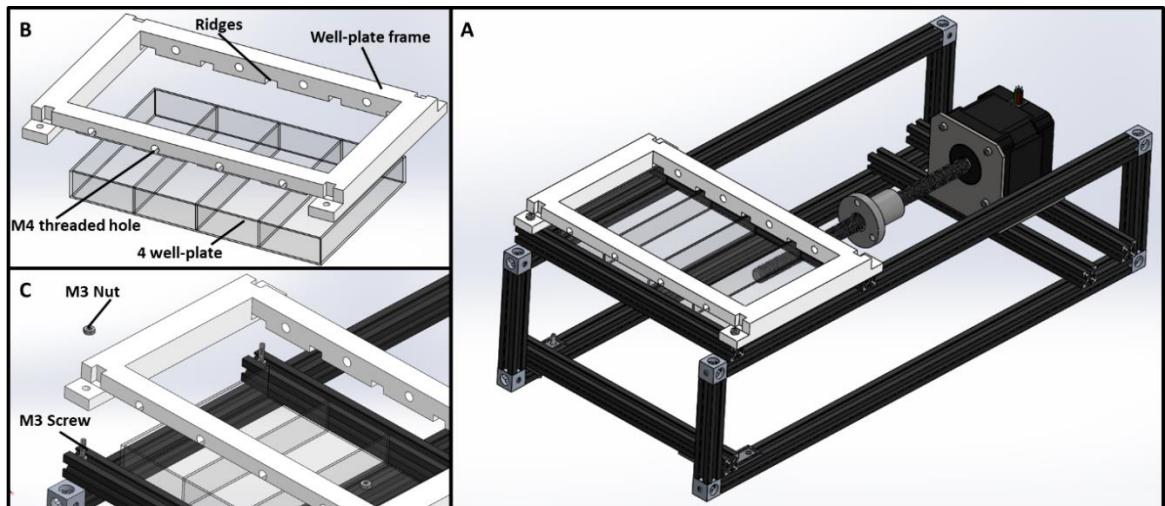


**Figure 3-11. 4-well-plate assembly on frame. A)** Full assembly with well-plate fitted on. **B)** Blowout of just the well-plate and the frame fixture which keeps the well-plate locked onto the frame. The ridges of the fixture fit over the spacers between each well. The M4 threaded holes are for components described next. **C)** Blowout depicting how the well-plate frame, well-plate and Makerbeam frame fit together. 2x 12mm flat headed M3 screws are slotted into the 2 15cm beams surrounding the well-plate. The 4 holes on the corners of the well-plate frame are placed over the screws and bolted down onto the frame.

The next component designed, and 3D printed was an attachment for the leadscrew nut (Leadscrew block). This component needed to fit onto the nut and resist the nut from turning as the leadscrew turns for lateral movement of the part to occur. The way in which this happens is that it sits on top of the two 30cm beams (Figure 3.12).

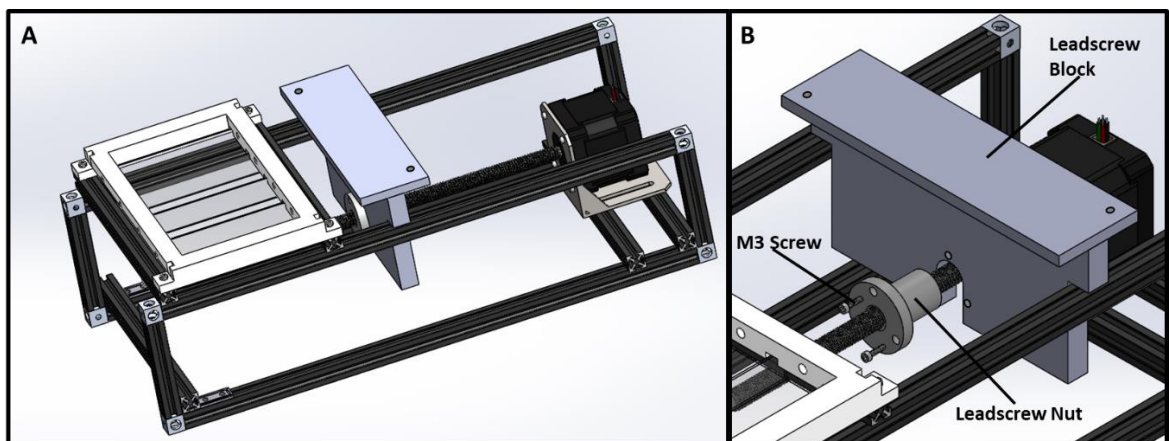


**Figure 3-12. Leadscrew block assembly on frame. A)** Full assembly with leadscrew block fitted. **B)** Blowout showing how the block attaches to the leadscrew nuts. The leadscrew nut has 3 holes on it 120 degrees apart on the larger circle side of it. The block has 3 holes corresponding to them. The arch of the block fits over the smaller part of the leadscrew nut; the holes are aligned and 3x 12mm M3 screws are pushed through the aligned holes before being bolted off.

A lid was then designed to be fixed on top of the leadscrew block and over the well-plate, where it would sit against the well-plate frame (Figure 3.13). The lid was designed in 2D on AutoCAD and saved as a dxf file before being lasercut from a piece of Perspex 5mm thick (Technologies Supply ltd.). After being laser cut, the part was annealed at 90°C to relieve internal stresses from the material.

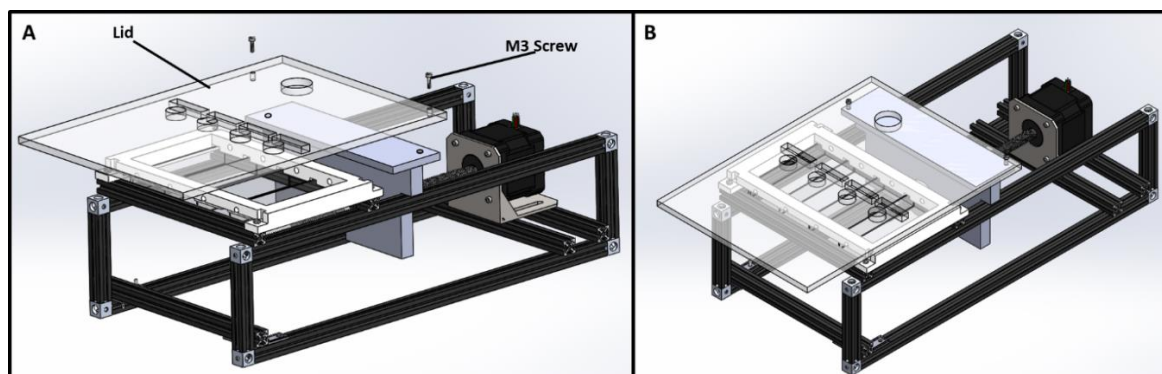


**Figure 3-13. Assembly of lid on frame. A) Blowout diagram to show how lid fits onto the leadscrew block. Holes between the 2 are aligned. The 2 holes on the leadscrew block are manually threaded to allow a 12mm M3 screw to be screwed in. B) Full assembly with lid.**

The M4 threaded holes which sit inside the well-plate provide a fixation point for blocks (small blocks) attached to substrates to screw into (Figure 3.14).

The lid can be seen to consist of circular and rectangular shaped holes sitting over each well in the well-plate. The circular holes are there to enable media feeding of cells during experiments. When not being fed, parafilm is used to keep them covered. The rectangular holes are what enable the movement of the lid to stretch cell substrates. Large blocks which attach to the substrate (opposite end of the substrate to small blocks which fix into the well-plate frame) fit through the lid and therefore move with it as the leadscrew turns (Figure 3.14). The large blocks were designed longer in length to protrude through the lid for the device. The PCL substrates would be attached by dipping the bottom of these blocks into molten PCL on a hotplate and pressing them onto the PCL substrates cut to specific lengths.

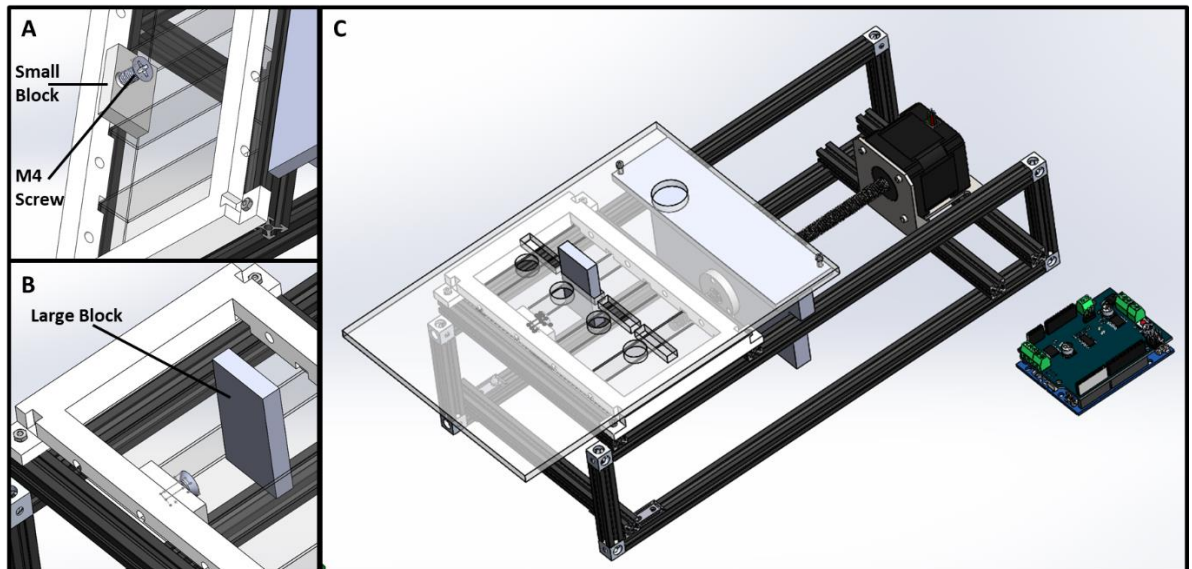


**Figure 3-14. Assembly of how substrates fit into the well plate. A) View of how a small block (a substrate would be attached) screws into the frame. B) The larger block sits opposite the fixed in small block (the other end of the substrate would be attached to it. C) The full assembly; the lid fits over, where the large block protrudes through one of the lid's rectangular holes.**

The Arduino/Motorshield unit then connects to the stepper motor via 4 wires (into a motor port on the shield) and the assembly is complete (Figure 3.15 A). The amount of lateral movement per step is known as the motor completes one rotation through 200 steps, and the lead length is 2mm; therefore, the lateral movement of the lead screw attachment per step is 0.01mm. The response ratio of the large block is 1:1, and this can be seen in Figure 3.15 where 20 rotations of the leadscrew resulted in a 40mm deformation of PCL attached to each of the 4 wells on the device. Therefore, dimension of substrate stretch is precisely known by the amount of steps input into the Arduino script.

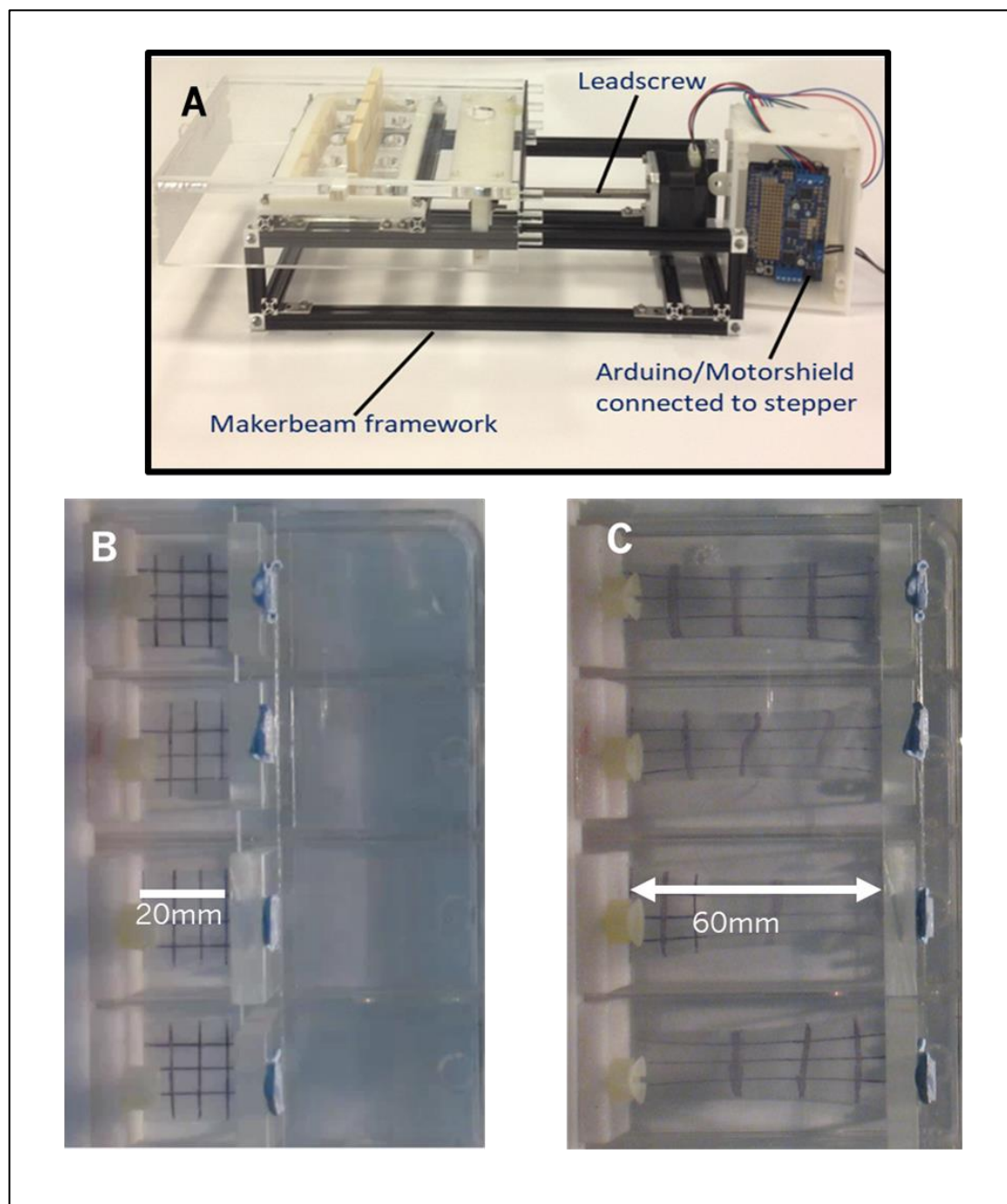


**Figure 3-15. Overall assembly and functionality of the device designed. A) Picture of components assembled to make stretcher. B) Top view of device with PCL (20mm length) attached in all 4 wells of the well-plate. C) Top view of stretcher after 20 rotations of the lead screw is applied through 4000 steps of the stepper motor.**

The device created here enables testing of multiple samples within a single experiment; enables media access; and has an easy disassembly process to enable imaging of samples used on it. Furthermore, it can be placed and run in cell culture incubators and applied strain to materials on it are known as a function of what is put into its Arduino script. This device does not however cater for live imaging whilst stretching of single substrates.

### 3.2.2 Live Cell Sheet Stretching Device

The previous device outlined enabled stretching of multiple sheets under separate conditions over extensive culture times. However, there are research benefits in having a device which can be used under a microscope to image the cell response to strain in real-time.

The key area that this device was designed to research was the effect of localised strain in the material on cell response (e.g. migration/remodelling). This was seen as a potential issue based on the DIC material analysis in the previous chapter where highly localised strain regions could be seen through plastic deformation of PCL, particularly with the C-PCL. Therefore, key features of the device to be designed were that it should be:

- Portable to be able to be moved easily from culture conditions to microscope.
- Able to stretch cell substrates by a known amount whilst under microscopy.
- Stationary when being stretched and imaged for tracking purposes.
- Cell culture compatible.

The concept to be developed (Figure 3.16) was to essentially scale down the initial 4-well-plate device into a 52mm petri dish and use manual actuation to turn a small lead screw with a high-resolution lead length. A fixed block and moveable block would still be used to stretch the substrate, and an interference fit would be used keep the device components in the petri dish upon media addition as well as actuation. A clamping set up would also be required to ensure the petri dish does not move through imaging during stretching of substrates.

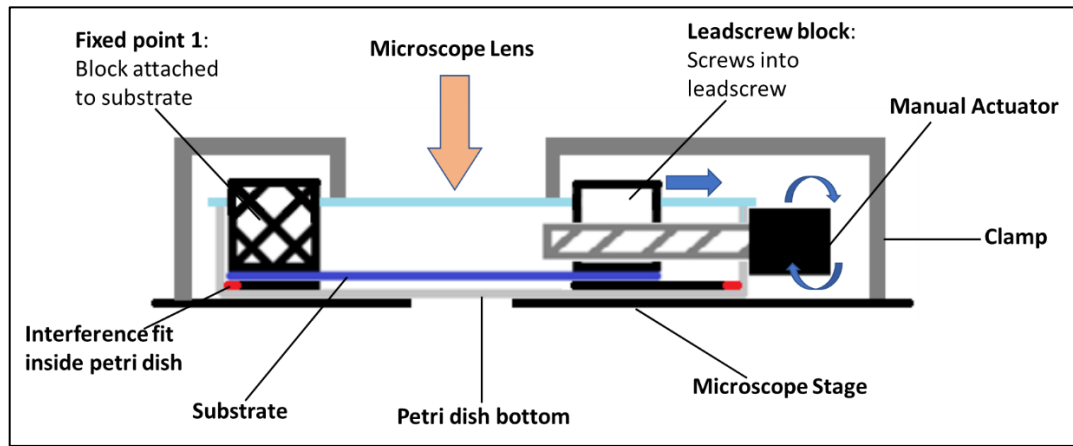


**Figure 3-16. Schematic depicting a concept of how a substrate material for cells may be stretched with precision under a microscope for live imaging.**

### 3.2.2.1 Device Design

A substrate guide component was made to fit tightly inside a 50mm petri dish (Thomas Scientific) (Figure 3.17). The component was designed to enable controllable stretching of substrates in one plane in a petri dish. A designed slider fits on top; this part enables a clamping point for one end of substrates as well as keeping a large contact area to the substrate guide component. This is important as it stops a pivot point from developing where the material would lift in response to turning of the leadscrew. The leadscrew fits through the substrate guide component all the way till the end of the knob comes into contact with the column part of the substrate guide component (Figure 3.17). The column on the substrate guide component has a slight curve in it to stop leakage of media via capillary action between the column and the inside edge of the petri-dish.

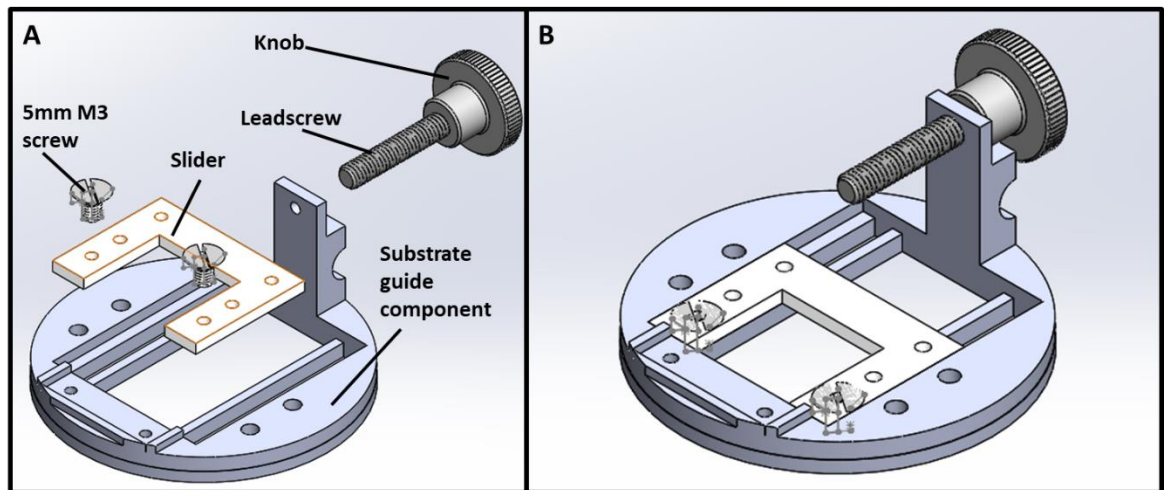


**Figure 3-17.** Partial assembly of petri-dish device. A) Blowout diagram; A substrate guide component is used to keep substrates in the petri-dish. The OD of this (50.5mm) is slightly larger than the petri-dish's (50mm), and this allows for an interference fit in the dish. A slider component screws down into the tramlines of the substrate guide component, and the leadscrew pushes through the hole in the column. B) Assembly showing that the leadscrew pushes all the way through till the knob is against the column.

Two blocks were designed to attach the substrate to the substrate guide component. The bottom of the large sliding block attaches to one end of the substrate, and the block is screwed into the slider (Figure 3.18).

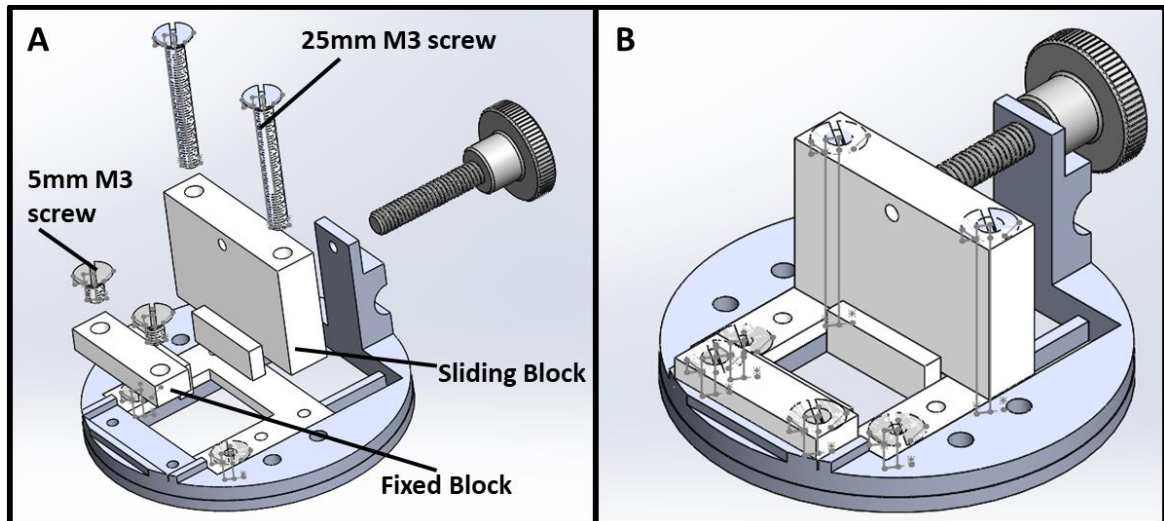


**Figure 3-18.** Subassembly of components in petri-dish. A) Blowout diagram showing how blocks clamping the substrate down attach. The sliding block screws into the slider, and the fixed block screws into the substrate guide component. The leadscrew then screws into the sliding block after it has been pushed up against the column of the substrate guide component.

The fixed block attaches to the substrate at the other end and clamps it to the substrate guide component. Both blocks have a front end which folds the substrate downwards at its clamping sit so that it would sit at the bottom of the petri dish rather than towards the top (Figure 3.19). If the substrate did fit towards the top

end of the petri dish, it is likely the top of the substrate would not receive sufficient media to maintain cell growth over long time periods.

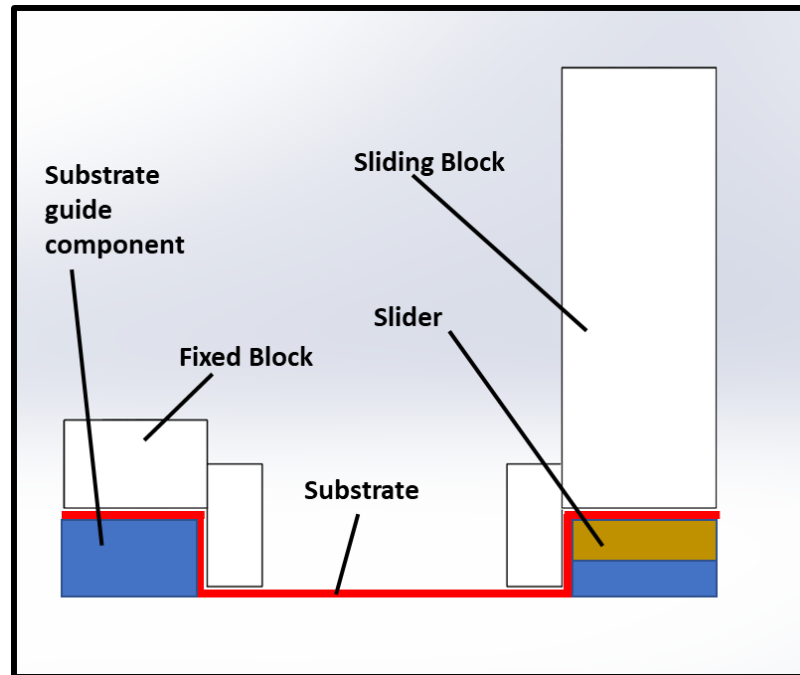


**Figure 3-19.** Side view of components attached to substrate. On both blocks, there is a part designed to make the substrate sit at the bottom of the petri-dish.

The M2.5 leadscrew (obtained from Thorrlabs is 20mm in length) has a fine lead length of 0.2mm which enables precision stretching; one turn of the knob attachment (also obtained from Thorrlabs) would stretch the substrate by 0.2mm. The leadscrew screws into a threaded hole in the sliding block (Figure 3.18), and as the knob of the screw is pushed up against the column on the substrate guide component, tightening of the screw pulls the sliding block back, hence stretching the substrate.

The components mentioned so far fit inside a 50mm plastic petri dish (Figure 3.20). Cells can therefore be cultured on and incubated within the device. To enable real-time imaging of substrates a fixture for the Olympus microscope stage was made for the device to stably sit in whilst allowing imaging. The ring on the stage fixture fits around the petri-dish, and the smaller ring below provides a platform for the dish. To ensure no moving of the petri dish during imaging and turning of the leadscrew, clamps were designed to hold the petri dish down against the microscope stage fixture (Figure 3.20).

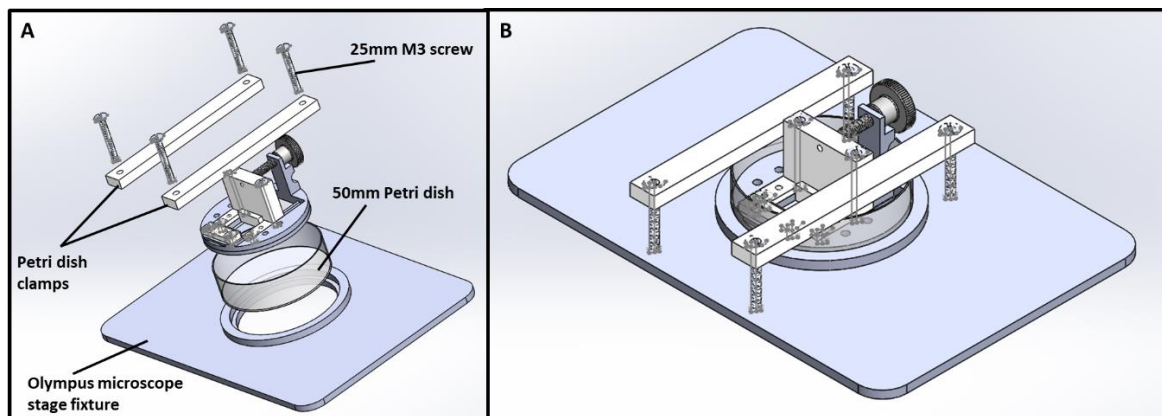


**Figure 3-20. Assembly of Petri-dish device stretcher.** A) Blowout of components fitting together. The well plate with the subassembly that fits inside it's in the ring of the microscope stage fixture. The sides of the petri-dish are clamped down by being screwed to the microscope stage fixture, which fits directly onto the microscope stage. B) Diagram of the petri-dish device fully assembled.

The amount of lateral movement per rotation of the leadscrew is 0.2mm. The response ratio of the sliding block was tuned through iterations of the design to be 1:1 (incorporation of the slider and changes to the column of the substrate guide component) therefore lateral stretching of substrates is precisely known from marks that can be put on the knob to know how much it has been turned. Figure 3.21 illustrates the 1:1 response obtained by turning of the leadscrew; when rotated ten times PCL polymer is stretched by 2mm ( $0.2\text{mm} \times 10 = 2\text{mm}$ ).

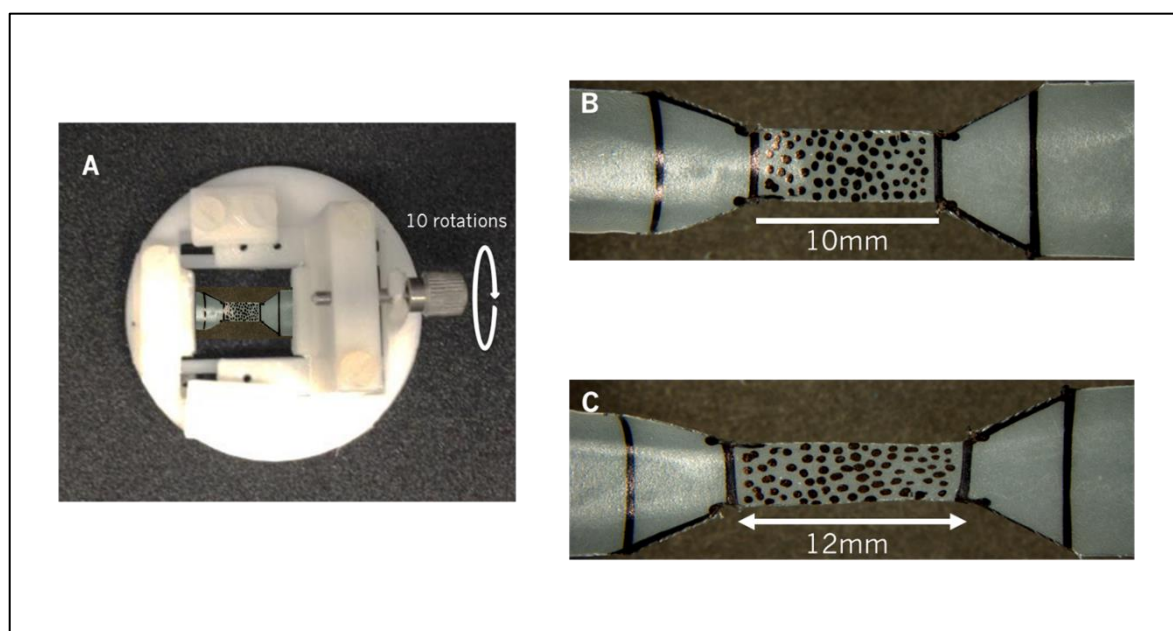


**Figure 3-21. Overall assembly and functionality of the live-imaging stretcher device designed.** A) Top view of stretcher with PCL film attached. B) Image and length of PCL film before being stretched through 10 rotations of the leadscrew. C) Image and length of PCL film after being stretched through 10 rotations of leadscrew. The film stretched by 2mm.

The device created here enables testing of single substrates, cultured with cells under a microscopy set up. The device has been optimised to enable determination of applied strain to the substrate via counting of leadscrew turns, and this strain can be administered during imaging due to the custom designed clamps and microscope stage for the device.

### 3.3 Discussion and Conclusion

The devices designed and made have been customised for the purposes of this project where PCL substrates will be required to initially be strained into their plastic flow region (10mm displacement) at a rate of 1mm/sec (as this correlates to testing done on PCL substrates in chapter 2), before being slowly and precisely deformed in their plastic flow regions.

The minimum displacement after plastic deformation and cell culture that needs to occur is 0.025mm every 6 hours, and the maximum deformation is 0.042mm every hour. The only commercially available device that may have been able to meet the needs of this project with regards to a multi-well system is the CellScale MCJ1 system; however this is based from a minimum applicable load specification, whereas the important parameter to consider for the purposes of stretching PCL is a precise displacement control. Using a load control in conjunction with small stretch hold cycles would be inaccurate due to further displacement occurring during a held load as a result of stress relaxation in the material. For this reason a customised stepper motor leadscrew combination was utilised as described in the above to meet these requirements without the need for a feedback loop; Arduino software is used to drive how many steps are taken by the stepper motor and when they are taken.

The surrounding framework of the multi-well device enables addition and removal of media and solutions with regards to immunostaining and prevents media contamination. As the motor is far from the culture plate, heat stimulation of cultures is not a problem. Furthermore, the device is able to be disassembled with substrates kept in tension to view under microscopy post-fixation if necessary.

The second device works via manual turning of a finely threaded lead screw (0.2mm pitch) and can be used for live analysis of substrate stretching on cells. Substrates can still be pre-stretched on this device manually to be in the plastic flow region, and again this device holds the advantage of being able to apply and hold small (<0.2mm) displacements accurately. In the case of commercial devices described which enable stretching of cell cultures under microscopy (for example Flexcell, Strexcell), the devices tend to come with their own custom well plates which have in-built PDMS or collagen substrates, therefore these devices would

require custom modification to be used with PCL. The one advantage these devices do hold over the custom designed one in this chapter is that they are not manually actuated, therefore, future work around this device would involve attaching an automated actuation mechanism.

## 4 Fibroblast Response to a Continuously Stretched Substrate

### 4.1 Introduction

Fibroblasts are required for structure and maintenance of soft tissue as they secrete ECM components, such as collagen. Mechanosensitivity is essential to fibroblast function as they counteract extracellular tension by exerting contractile force on the ECM to maintain tensional homeostasis of the tissue (Brown et al, 1998). Increased mechanical tension in combination with biochemical signals can induce fibroblast differentiation into a highly contractile phenotype; myofibroblasts (Tomasek et al, 2002). Myofibroblasts are characterised by increased proliferation, secretion of collagen and expression of  $\alpha$ -smooth muscle actin ( $\alpha$ SMA), which is integrated into intracellular stress fibres and contributes to their contractility. These features allow myofibroblasts to remodel surrounding tissue, after which they normally undergo apoptosis (Humphrey et al, 2014). Continuously upregulated secretory activity and failure to enter apoptosis causes formation of scars and other fibrotic pathologies (Sewell-Loftin et al, 2017). Due to such impacts that fibroblasts can have on soft tissues, they will be focussed on as a first cell type to be investigated on continuously stretched PCL in this chapter.

Chapter 3 of this thesis determined that the stretching regime will be uniaxial (as during DO the stretching is done in one axis) and stepped in small hourly increments summing to 1mm over 24hours. The rate of stretch during DO is 1mm over 24 hours across approximately 4 stepped increments (G. Kumar & Narayan, 2014), and although substrates will be significantly smaller than bone (50mm compared to ~500mm) this will be the starting rate of stretching substrates after cells have been cultured on. The significantly higher relative deformation (x10 relatively) alongside the increase in amount of steps that the deformation is conducted in should then provide a noticeable signal when analysing cell responses to PCL plastic deformation; ensuring that the mechanism does have a detectable effect on cell populations. Both PCL types (C-PCL and A-PCL) investigated in Chapter 2 will be investigated as cell substrates; differences in cell responses can then be elucidated to relevant material properties such as topography, stiffness,

stress-relaxation and strain localisation. Investigating fibroblasts is one component from several impacting soft tissue growth in response to being stretched; by isolating the fibroblast response a top down approach is being taken, where the long term idea is to investigate a range of individual cell lines/soft tissue components using similar stretching regimes to build an overall model for tissue growth via stretch.

#### **4.1.1 Fibroblast Mechanotransduction and Cell Morphology**

Mechanical signal transduction from the external environment of a cell in general to its cytoplasm and nucleus relies on an intact actin cytoskeleton and cell-ECM attachments via focal adhesions as discussed in Chapter 1. Ras homolog family member A (RhoA) belongs to the Rho family of small guanosine triphosphatases (GTPases). Rho GTPases are small signalling G-proteins involved in the regulation of cytoskeletal organization; they switch between the active guanosine triphosphate (GTP) and the inactive guanosine diphosphate (GDP) bound states. They affect multiple cellular functions, including cell motility, polarity and division. (Maeda et al., 2011).

RhoA can be activated by biomechanical stimuli or a variety of signalling molecules, such as the cytokine TGF- $\beta$  (Ji et al., 2014). In all cases, the switching of RhoA between the inactive GDP-bound form to the active GTP-bound form is regulated by guanine nucleotide exchange factors (GEFs), GTPase activating proteins (GAPs) and guanine dissociation inhibitors (GDIs) (Figure 4.1).

RhoGAPs support the intrinsic GTPase activity of RhoGTPases, converting them from a GTP-bound state to a GDP-bound state, thereby leading to their deactivation. RhoGEFs on the other hand help maintain RhoGTPases in the active state by facilitating their switch from the GDP-bound form to the GTP-bound form. RhoGDIs, stabilize the RhoGTPases in the inactive GDP form (Thomas et al., 2019).

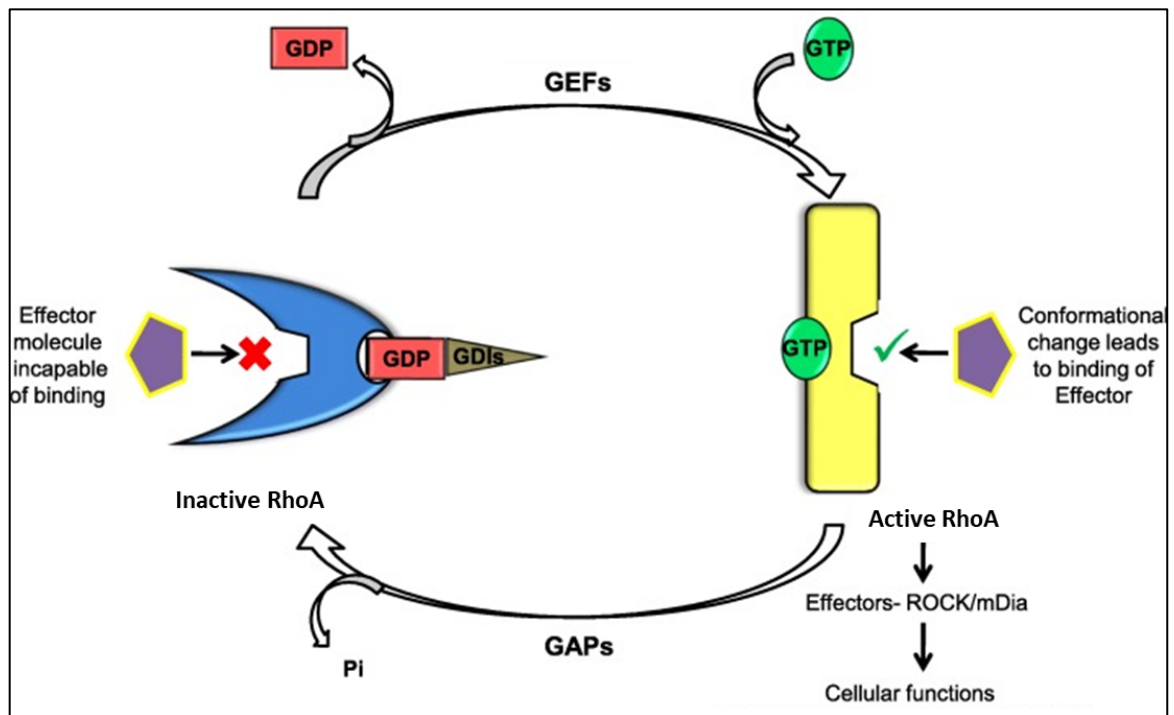


**Figure 4-1. Cycling of RhoA between active and inactive forms: Switching of RhoA between inactive GDP-bound form to the active GTP-bound form is regulated by GEFs, GAPs and GDIs. Binding to GTP changes the conformation of the molecule, thus allowing the binding of various downstream effectors of RhoA such as ROCK, thereby facilitating various downstream signalling pathways (Figure adapted from Thomas et al., 2019).**

Binding to GTP changes the conformation of the molecule, thus allowing the binding of various downstream effectors of RhoA. One such example is GTP-RhoA activating rho associated kinase (ROCK), which facilitates activating of LIM kinase (LIMK) by phosphorylation (Figure 4.2) (Ohashi et al., 2000). Active LIMK targets cofilin for inactivation by phosphorylation and therefore inhibits actin filament depolymerisation (Ohashi et al., 2000). Another target protein of GTP-RhoA is mDIA1. mDIA1 is a formin family protein, that binds the fast-growing end of actin fibres and protects these from capping proteins, allowing F-actin extension. It also recruits profilin to the polymerising end of actin fibres, which associates with monomeric actin and accelerates filament assembly (Shekhar et al., 2015).

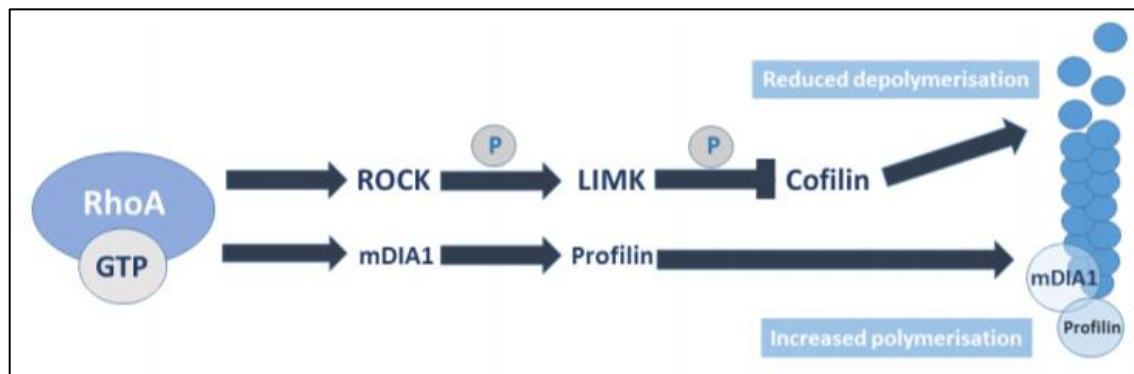


**Figure 4-2. Schematic representation of RhoA mediated formation of F-Actin. RhoA-GTP activates ROCK, which phosphorylates LIMK, resulting in its activation. Active LIMK phosphorylates actin depolymerising protein cofilin, inactivating it and stabilising forming actin fibres. In addition, RhoA activates formin mDia1, which binds the fast-growing ends of fibres and recruits profilin to fibre assembly site. Profilin brings monomeric actin to the fast growing end of the fibre, while mDia1 protects it from capping proteins, resulting in accelerated actin polymerisation. Adapted from Parmacek (2007).**

The actin cytoskeleton is an important regulator of cell shape, and therefore activation of RhoA can lead to changes in cell morphology. Reorientation of a cell's long axis in direction of the lowest perceived strain has been observed in several cell types and is important for maintenance of stable focal adhesions and stress fibres (Qian et al., 2013). Cell reorientation in response to stretch has been shown to determine the axis of cell division and could regulate tissue growth into a particular direction (E. H. Kim et al., 2015).

RhoA influences actin fiber organisation and actin fibers have been shown to impact morphological changes in the cell nucleus. This may be as a result of stress fibers running over the nucleus putting it under compression, or lateral pulling by the direct coupling between adhesion proteins and nuclear membrane via cytoskeletal components (Jean et al., 2004; Khatau et al., 2009). Experiments where cells are grown on adhesive islands of different shapes or adhesive strips show that variation in cell spreading is transmitted to the nucleus by actin stress fibers and results in nuclear deformation (Khatau et al., 2009; Roca-Cusachs et al., 2008; Versaevel et al., 2012). It has been demonstrated that when cells are spread on highly anisotropic patches, the nucleus is elongated along the long axis of the pattern and actin stress fibers running on either sides of the nucleus are responsible for the observed deformation (Versaevel et al., 2012). Stress fibers have also been observed to run over the nucleus, and ablation of these fibers

result in reorganization of nuclear structures (Khatau et al., 2009; Nagayama et al., 2011). Furthermore, integrin manipulation used for cytoskeletal reorientation was linked to nuclei distortion along the axis of tension. It was found that at low strain, F-actin mediated force transfer to the nucleus however, it is important to realise intermediate filaments mediated force transfer to the nucleus under high strains (after tearing of F-actin) and low strains, where microtubules acted to hold open the intermediate filament lattice and to stabilize the nucleus against lateral compression (Maniotis et al., 1997).

All these results point towards a mechanical connection between the actin cytoskeleton and nucleus which could regulate nuclear deformations. RhoA induced F-actin reorganization can therefore affect nuclear shape (Haase et al., 2016).

This mechanism is likely to be key when stimulating cells to grow using a stretching mechanism. Pharmacologic inhibition of MLCK or disruption of the actin cytoskeleton for example has shown to inhibit cell proliferation (Huang et al., 1998). Inhibiting RhoA activity with C3 exoenzyme or dominant-negative mutants of RhoA has also been shown to block cell proliferation, whereas microinjection of constitutively active RhoA has been shown to promote DNA synthesis (Pirone et al., 2006). Looking further downstream, RhoA and actin impact fibroblast differentiation into myofibroblasts via activation of myocardin related transcription factor A (MRTF-A).

#### **4.1.2 Myocardin related transcription factor A**

MRTF-A is a co-activator of serum response factor (SRF), which can be involved in controlling expression of over 900 genes, the majority of which are also MRTF regulated (Esnault et al., 2014). As SRF is expressed at constant levels and always associated with serum response elements (SRE) of the DNA, MRTF-A activation is the key regulatory step in MRTF-A/SRF induced gene expression. MRTF-A has a g-actin binding site and a nuclear localisation sequence; when bound to g-actin MRTF-A cannot localise to the nucleus and stays inactive, sequestered in the cytoplasm. Dissociation of actin monomers from MRTF-A molecule causes its

translocation to the nucleus. In the nucleus, MRTF-A enhances SRF binding to the SRE and activates the transcription of its target genes (Velasquez et al., 2013). RhoA activation results in increased F-actin polymerisation and reduced availability of G-actin in the cytoplasm, causing G-actin release from MRTF and allowing its nuclear transport (Olson & Nordheim, 2010).

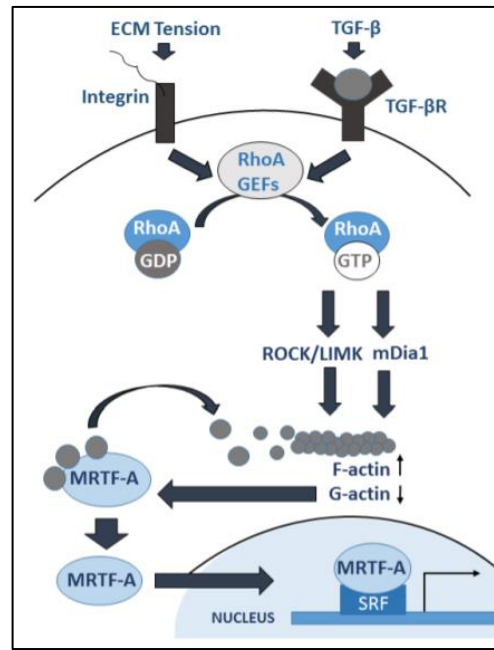


**Figure 4-3. Schematic representation of MRTF-A activity regulation by ECM tension and TGF- $\beta$  signalling via activation of RhoA GTPase. In response to stimulation, integrins and TGF- $\beta$  receptors activate Rho GEFs. Active Rho GEFs mediate exchange of GDP for GTP activating RhoA. RhoA-GTP upregulates actin polymerisation via mDia1 and downregulates depolymerisation via ROCK pathway. Increased actin filament growth reduces concentration of monomeric actin in the cytoplasm, leading to G-actin dissociation from MRTF-A. MRTF-A is translocated to the nucleus, where it binds SRF and activates gene transcription (Olson & Nordheim, 2010) .**

MRTF is 99 kDa protein comprised of 929 amino acids. It contains a N-terminal RPEL domain, consisting of three RPEL motifs connected by 22 amino acid spacer sequences. Each RPEL motif binds one actin monomer, and RPEL2 and RPEL3 motifs also recruit two additional G-actin molecules to spacer regions (Mouilleron et al., 2011). RPEL domain also contains two basic sequences, which can interact with importin complexes on the nucleus and serve as nuclear localization signals. Located near actin binding sites, these sequences are not accessible for importin interaction in G-actin bound MRTF-A (Pawłowski et al., 2010). Any G-actin bound MRTF-A that is imported into the nucleus is quickly removed by exportin crm-1. A low rate of import and a high rate of export results in mainly cytoplasmic

localisation of the protein (Vartiainen et al., 2007). Phosphorylation of several serine residues of MRFT-A also plays a role in its localisation. Ser98, located within RPEL domain, was shown to be phosphorylated by extracellular signal-regulated kinases upon dissociation from G-actin. Ser98 phosphorylation promotes MRTF-A nuclear localisation and activity by preventing G-actin rebinding. Ser33 phosphorylation was shown to have the opposite role and facilitate MRTF-A export from the nucleus (Panayiotou et al., 2016).

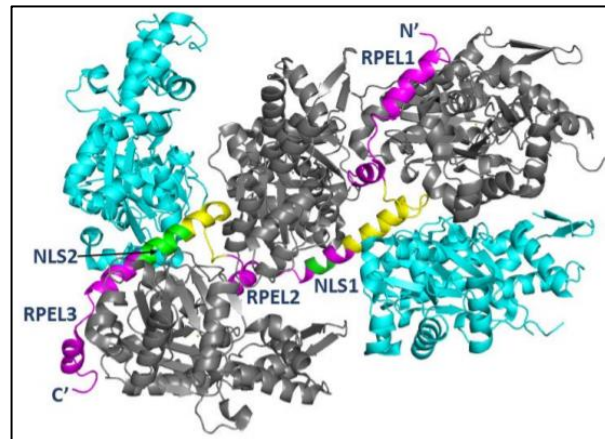


**Figure 4-4.** Cartoon representation of MRTF-A RPEL domain bound to 5 actin monomers. Actin monomers that are bound to RPEL motifs 1-3 are shown in grey, monomers recruited to spacer regions – in cyan. RPEL motifs are shown in magenta, spacer regions in yellow and nuclear localization sequences 1 and 2 (NLS) in green (Mouilleron et al., 2011).

Nuclear MRTF-A in fibroblasts increases the expression of CARG box-containing contractile genes such as  $\alpha$ -smooth muscle actin ( $\alpha$ SMA) and caldesmon (Latif et al., 2015). Upregulation of  $\alpha$ SMA by MRTF-A/SRF pathway is key in identifying differentiation of fibroblasts to myofibroblasts. An in-between stage where cells differentiate into protomyofibroblasts can be identified by the presence of  $\beta$ - and  $\gamma$ -actins in cytoplasmic stress fibers (Darby et al., 2014).

Incorporation of  $\alpha$ SMA into stress fibres increases intracellular tension and fibroblast contractility. Contractile stress fibers are also required for supermature focal adhesion formation (B. Hinz, 2003) and reinforcement of adherens junctions (B. Hinz, 2004) in myofibroblasts. Increased adhesion and contractility allow myofibroblasts to efficiently exert force on the surrounding ECM. Applying force to the ECM through integrins can also potentiate inactive TGF- $\beta$  stored in the ECM, further increasing RhoA activity and creating a positive feedback loop for promoting and maintaining the myofibroblast phenotype (Klingberg et al., 2014).

### 4.1.3 Chapter Aims and Objectives

Based on the above literature, the aim of this chapter is to define fibroblast behaviour and their phenotypical changes in response to a novel stretching regime which is characteristic of stretching soft tissue in vivo for the purposes of distraction osteogenesis.

In order to achieve this the following objectives must be sequentially met:

1. Develop a scale-down method to optimise PCL surface treatment to support fibroblast growth and to produce a growth curve for fibroblasts cultured on PCL at a low density using the scale-down method and optimal surface treatment.
2. Scale-up the finalised growth curve onto the stretching device and develop a protocol where the cell-seeded substrates are stretched to produce a comparable mechanical mechanism to when soft tissue is stretched.
3. Define mechanical differences between C-PCL and A-PCL through the stretching regime to be implemented.
4. Use immunofluorescence to analyse cell morphological responses (i.e. cell elongation and orientation), and actin dynamics (i.e. MRTF translocation,  $\alpha$ SMA expression, and F-actin characterisation) on the two different PCL (C-PCL and A-PCL) substrates being stretched.

There are two hypotheses addressed in the following chapter:

- It was hypothesised that C-PCL and A-PCL differ in their response to unidirectional stretch in small stepped increments.
- It was hypothesised that cells respond to passive unidirectional stretch in a way similar to passive cyclic stretch or active extension on patterned substrates, adapting their cytoskeleton and activation of mechanosensitive signalling pathways.

The materials response to the stretching mechanism defined was addressed by:

- Analysing force response to displacement of each substrate.
- FE analysis of each material.

The reaction of the cells to stepped unidirectional stretch was addressed by determining:

- Cell morphological changes such as elongation.
- Alignment of cells to the axis of stretch.
- MRTF-A nuclear translocation.
- Actin texture changes

## 4.2 Methods

### 4.2.1 Mechanical Testing of PCL

As a stretching regime had now been determined, further tensile testing of C-PCL and A-PCL was conducted to evaluate how the materials differ through small displacements during their plastic flow phases.

Samples were cut from PCL developed films using a mould (15mm x 70mm rectangle) and scalpel before the thickness of each sample was measured using a micrometer screw gauge. For the tensile test each sample was clamped using pneumatic rubber grips in the tensile testing system used in Chapter 2 (Figure 2.7) (Zwick Roell z2) so that the gauge length (length between the 2 grips) was 30mm. Samples were then stretched by 10mm at a rate of 60mm per minute, before being stretched by a further 1mm at a rate of 1mm per 10 seconds.

### 4.2.2 Finite Element Analysis

DIC was used as a means of analysing localised strains in C-PCL and A-PCL in Chapter 2 during mechanical testing. DIC enables analysis of the optical flow of the material undergoing deformation allowing the calculation of finite strains (through FEA) within the material as it is undergoing deformation.

Material deformation can be described by depicting the material to be a collection of small line elements. As the material is deformed, the line elements stretch, or get shorter and can also rotate in space relative to each other. Strain at a point is characterised by the movement of any two mutually perpendicular line-segments. If it is known how these perpendicular line segments are stretching, contracting and rotating, it will be possible to determine how any other line element at the point is behaving, by using a strain transformation rule. This is analogous to the way the stress at a point is characterised by the stress acting on perpendicular planes through a point, and the stress components on other planes can be obtained using the stress transformation formulae (Kelly, 2015).

The surface of the PCL film is a two-dimensional case. If 2 perpendicular line-elements emanating from the same point are considered during a deformation, two things happen in conjunction: The line segments will change length; and the angle between the line-segments can change. The change in length of line elements is called normal strain and the change in angle between initially perpendicular line segments is called shear strain (Kelly, 2015). Normal strain in direction  $x$  is denoted as  $\epsilon_{xx}$ , whereas normal strain in  $y$  direction is denoted as  $\epsilon_{yy}$ . Shear strain is then denoted by  $\epsilon_{xy}$ . Figure 2.8 in Chapter 2 depicts  $\epsilon_{yy}$ ,  $\epsilon_{xx}$  and  $\epsilon_{xy}$  for a single point when a material has been deformed.

To generate a speckle for the DIC, Holts car spray paint (matt black) was used. Samples were placed flat on a table and the spray can was held approximately 50cm away from the samples. The spray was lightly applied by applying a small amount of pressure on the nozzle while moving the spray can from left to right. The sample was then clamped between rubber grips in the Zwick Roell z2, and a digital camera was set up on a tripod to image specimens (2048×2448 pixels, Vic-Snap, Correlated Solutions, Inc., Columbia, SC). A white sheet was placed behind the specimen to maximise the contrast on the speckle pattern.

For the purposes of DIC testing in this chapter, samples (both C-PCL and A-PCL) were set up at a gauge length of 30mm before being stretched by 10mm at a rate of 60mm per minute. The reference region of interest was selected on this stretched sample before further stretching it by 1mm at a rate of 1mm per 10 seconds. The strain profile was mapped for both C-PCL and A-PCL using this stretching mechanism.

### 4.2.3 Optimising Cell Proliferation on PCL

From Chapter 2 it can be seen that water contact angle changes between different plasma treatment times (Figure 2.25). Treating PCL with plasma is required for media ECM proteins to adsorb (and hence cell attachment) due to the material being naturally hydrophobic. Therefore, an experiment was designed to look at cell proliferation on PCL at different plasma treatment times to determine the optimum plasma treatment time for cells to attach and proliferate to confluence.

As only 4 samples can be cultured on at a time when using the stretching system, a scale down model was to be used to optimise cell attachment on PCL. This required a method to be developed where many PCL samples with differing plasma treatment times could be analysed at several time points after cells had been cultured on them. As PCL is a 20  $\mu\text{m}$  thick film, it is difficult to handle and image due to it not remaining flat in a well plate. Furthermore, the stretching device will initially keep the PCL taut when cells are being cultured on. Therefore, to determine optimum culture conditions the PCL was to be kept taut for these experiments. Wells which were able to fit in a 24-well plate were 3D printed on PCL to overcome these problems.

#### 4.2.3.1 Method Development

PCL films of 20  $\mu\text{m}$  thickness were made by spincoating as described in Chapter 2. A cylinder of 20 mm external diameter, 10 mm height and 2 mm wall thickness was designed on AutoCAD (Figure 4.5) and 3D printed out of acrylonitrile butadiene styrene (ABS) on top of PCL after it was taped down flat onto the printing build plate (ULTIMAKER 2). The printing nozzle was kept at a far enough distance from the PCL in order not to melt it, and the printing speed was kept low to ensure the process did not rip the film. Furthermore, the fan speed on the printer was set at maximum, again to prevent the PCL from melting. These measures were taken in a trial and error approach until the parameters in Table 4.1 were decided upon.

**Table 4.1. Optimum parameters used on the Ultimaker 2 3D printer for printing wells onto PCL**

Parameter	Setting
Layer height	0.2 mm
Shell thickness	0.4 mm
Fill density	90%
Print speed	10 mm/s
Nozzle temperature	260°C
Build Plate temperature	0°C
Fan Speed	100%
Nozzle distance from PCL	2 mm

As the PCL was taped down onto the build plate of the 3D printer while the rings were printed on, the material within the rings remained flat and taut (Figure 4.5).

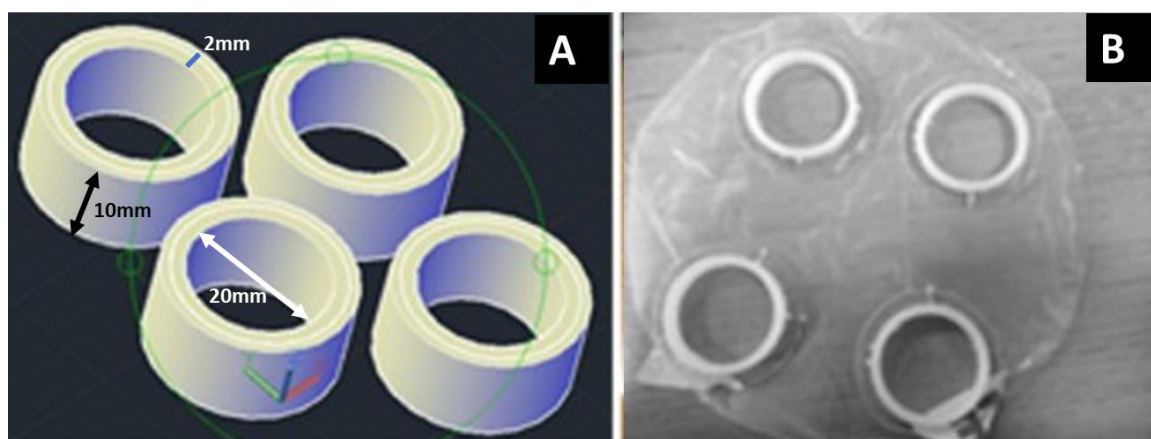


**Figure 4-5. Wells developed to keep PCL taut for cell culture. A) AutoCAD design of the wells. B) How the wells look printed onto the PCL.**

For each plasma treatment time 10 wells were required per experiment. Glass coverslips were used as a positive control. The wells were cut out with a scalpel before being plasma treated for various times ranging between 0 and 2 minutes. They were then left in a beaker filled with 70% ethanol for 30 minutes alongside the coverslips. After being removed from ethanol in the culture hood, the wells and coverslips were dipped in RO water 3 times before being air dried. The samples were then placed in a 24-well plate before hTERT immortalised human dermal fibroblasts cells were seeded on at a density of 127 cells/mm<sup>2</sup> in Dulbecco's

Modified Eagle's medium (Sigma-Aldrich, D5671) supplemented with 20% (v/v) Medium 199 (ThermoFisher Scientific, 31150-022), sodium pyruvate solution (Sigma-Aldrich, S8636) and 10% (v/v) fetal bovine serum, at 37°C. Half the media in each well was removed after 2 days and replaced with new media. Two samples from each condition were fixed using 10% (v/v) formaldehyde and permeabilized using 0.2% (v/v) Triton X in phosphate buffered saline (PBS) at time points of 2 hours, 1 day, 2 days, 3 days and 4 days after culture, before being stained with DAPI (Vector Laboratories, H-1200) to visualise cell nuclei.

A fluorescent microscope (Olympus BX51) was used to image the stained cells and as the cells were contact inhibited and did not grow on top of each other the area coverage of nuclei to the surface expressed as percentage coverage was used to quantify cell proliferation.

After establishing an optimal treatment time, the same experiment was repeated, however cell adhesion, spreading and proliferation was analysed at 5 minutes, 2 hours, 2 days, 3 days, 5 days, 8 days, 10 days, 12 days and 14 days. This allowed cell seeding density to be optimised and proliferation followed until the plateau phase was reached. Percentage coverage of nuclei to the surface was again used to quantify proliferation in this experiment, however after fixing and permeabilizing samples as above, rhodamine phalloidin (ThermoFisher Scientific, R415) diluted 1:100 in PBS/1%BSA was used to stain F-actin. These images were used to assess cell coverage of the surface, as all cells contain F-actin. If 100% confluence had been reached the entire surface would be covered with F-actin containing cells.

### 4.2.3.2 Method Development Results

Plasma treatment times between 0 and 2.5 were shown to adequately support cell growth (Figure 4.6). The optimal treatment time was taken as 1 minute due to it marginally supporting a higher cell proliferation rate.

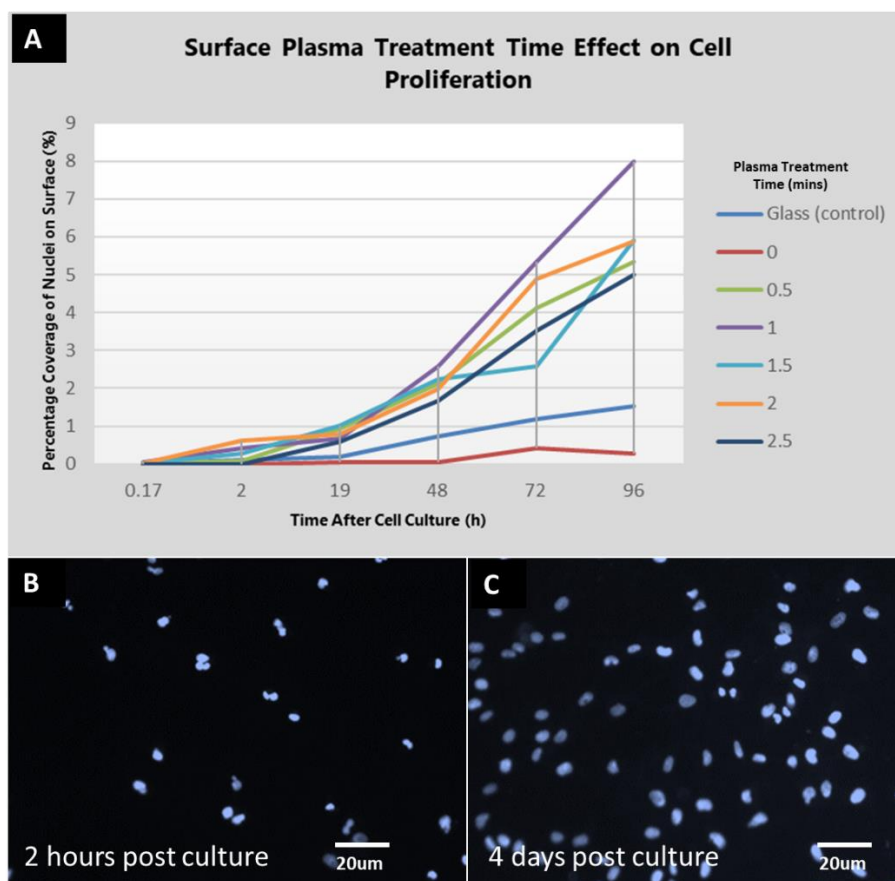


**Figure 4-6.** Optimising plasma treatment time of C-PCL for cell growth. **A)** Graph depicting percentage nuclei coverage on C-PCL plasma treated between 0.5 and 2.5 minutes (Glass = positive control, 0 = negative control). **B)** Image of cell nuclei on PCL (plasma treated for 1 minute); nuclei attachment after 2 hours. **C)** Image of cells on PCL (plasma treated for 1 minute); cells have increased markedly after 4 days. Curves show mean of 3 repeats.

Cell compatibility on 1 minute plasma treated C-PCL was therefore further tested over a period of two weeks with the aim to assess hTERT fibroblast proliferation and the time point when 100% confluence was reached. Figure 4.7 illustrates how C-PCL, treated for 1 minute under plasma, supports cell attachment and proliferation over a two-week period.

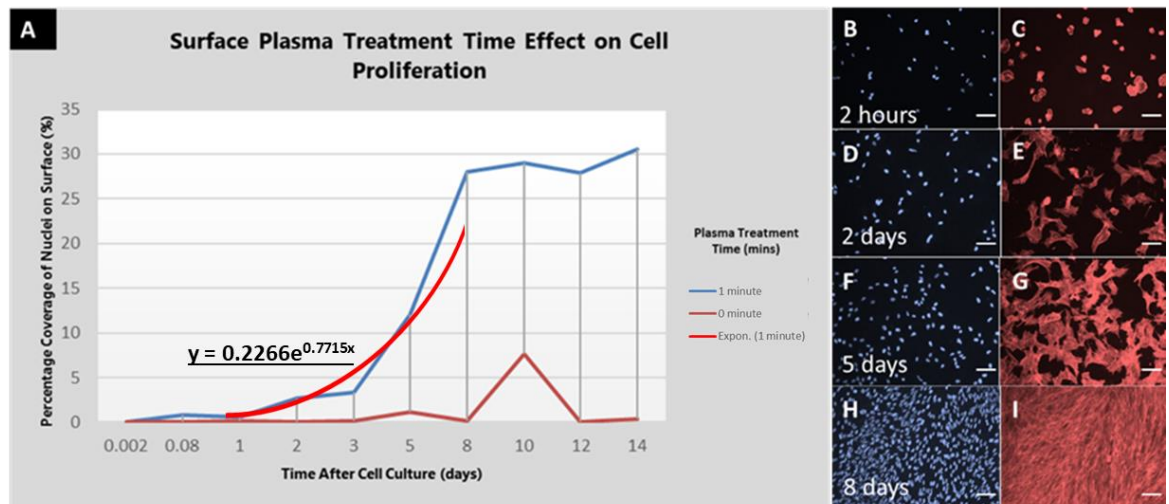


**Figure 4-7.** Cell proliferation on C-PCL, plasma treated for 1-minute vs 0 minutes over 2 weeks. **A)** Graph showing cell numbers increase over a 2-week period when cells cultured onto C-PCL which has been plasma treated for 1 minute. The exponential curve provides a fit for the data till it reaches a plateau (confluence) where cell density ( $y$ ) can be approximated by culture time ( $x$ ). **B), C)** Immunofluorescent images at 2 hours after culture, DNA and F-actin respectively. **D), E)** Immunofluorescent images at 2 days after culture, DNA and F-actin respectively. **F), G)** Immunofluorescent images at 5 days after culture, DNA and F-actin respectively. **H), I)** Immunofluorescent images at 8 days after culture, DNA and F-actin respectively. All scale bars are 50 $\mu$ m. Curves show mean of 3 repeats.

Results here suggest that C-PCL, treated for 1 minute under plasma enable cells to proliferate to 100% confluence in approximately 1 week after being cultured on at a density of 127 cells/mm<sup>2</sup>. The same cell density was used when culturing on substrates in the '4-well plates' used in conjunction with the motorised stretching device described in chapter 3. The exponential curve (Figure 4.7 A) can be utilised to estimate cell density populations when lower cell densities are to be analysed.

#### 4.2.4 Cell Culture and Analysis Methods in Relation to the Stretching Device

Having developed a growth curve for hTERTs on C-PCL, the next aim was to upscale this to the stretching system. As the global aim of the project is to develop a model for 'growth by stretch', it was decided that the substrates would be stretched beyond their elastic deformation point into the area of plastic deformation before cells were cultured on. The cells could then be left to grow to confluence and substrates could then be stretched at a low rate which would resemble a typical stretching profile of soft tissue.

#### 4.2.4.1 Cell Culture on Stretching Device

C-PCL and A-PCL were made by spincoating as described in Chapter 2. A stencil and scalpel were used to cut the substrates into 50 mm by 10 mm rectangles. The blocks were attached to the substrates by being dipped into molten PCL before being placed on each end of the rectangular shaped substrates (gauge length of PCL is therefore 40mm at this point). The substrates with their attached blocks were then plasma treated for 1 minute, before being sterilised in 70% ethanol for 30 minutes alongside the 3D printed well-plate frame, cover for the stretcher, and plastic screws for the small blocks.

The sterilised components were removed from 70% ethanol inside the culture hood and dipped in RO water three times before being air-dried. The substrates with their attached blocks were placed in a 4-well plate which was placed on a stretcher. The well-plate frame was placed on top of the well plate and screwed down using a sterile nut driver. The small blocks attached to the substrates were then screwed into the well-plate frame using sterile plastic screws and a sterile screwdriver. The large blocks were placed upright in the 4-well plate, and the cover was placed on top, allowing the large blocks to fit through. The cover was then screwed down onto the 'Leadscrew-hood attachment'. A script was uploaded to the Arduino/Motorshield unit to turn the stretcher's stepper motor at a speed of 3 rpm so that the substrate would be stretched at a rate of 6 mm per minute. The substrates were stretched by 10 mm to ensure each substrate was in the plastic deformation stage before the Arduino/Motorshield unit was disconnected (substrate gauge length is therefore 50mm at this point). For each experiment 2 stretchers were used; the first stretcher was to be used as a control where the substrates would not be further stretched after cells had been cultured on; the second stretcher was used to further stretch substrates after cells had been cultured on.

hTERT immortalized human dermal fibroblasts were cultured onto the substrate at a concentration of 127 cells/mm<sup>2</sup> in Dulbecco's Modified Eagle's medium (Sigma-Aldrich, D5671) supplemented with 20% (v/v) Medium 199 (ThermoFisher Scientific, 31150-022), sodium pyruvate solution (Sigma-Aldrich, S8636) and 10% (v/v) fetal bovine serum, at 37°C. Parafilm was stretched over the cover of the

stretcher to ensure media was not left exposed, thereby decreasing the risk of contamination. Stretchers were then left in an incubator at 37°C 5% CO<sub>2</sub>. Half the media in each well was removed after 2 days and replaced with new media. After 7 days, a new script was uploaded to the Arduino/Motorshield unit to stretch the substrates 1 mm over 24 hours; 4 steps per hour (0.04mm per hour) (Figure 4.8). This was connected to one of the stretchers whilst substrates on the other stretcher were not further deformed (control samples).

```

File Edit Sketch Tools Help

_1mm_24hr$

#include <Wire.h>
#include <Adafruit_MotorShield.h>
#include "utility/Adafruit_MS_PWM_ServoDriver.h"
// Create the motor shield object with the default I2C address
Adafruit_MotorShield AFMS = Adafruit_MotorShield();
// Or, create it with a different I2C address (say for stacking)
// Adafruit_MotorShield AFMS = Adafruit_MotorShield(0x61);

// Connect a stepper motor with 200 steps per revolution (1.8 degree)
// to motor port #2 (M3 and M4)
Adafruit_StepperMotor *myMotor = AFMS.getStepper(200, 2);
void setup() {
  Serial.begin(9600);          // set up Serial library at 9600 bps

  AFMS.begin(); // create with the default frequency 1.6KHz
  //AFMS.begin(1000); // OR with a different frequency, say 1KHz

  myMotor->setSpeed(3); // 3 rpm
}
void loop() {
  delay(600000);
  myMotor->step(4, FORWARD, MICROSTEP);
  delay(3600000);
}

36 Arduino/Genuino Uno on COM3

```

**Figure 4-8.** Example script uploaded to Arduino to provide 1mm stretch over 24 hours. Before the 'void loop' line, certain libraries are being selected, and the motor and which port it's connected to have been defined, as well as the speed that it will go through the amount of steps that are input within the 'void loop'. The delay function stops the motor from turning and is defined in milliseconds (3600000 = 1hour). The line highlighted defines how many steps (4) it takes in one cycle before the next delay; which way the motor rotates the lead screw (FORWARD), and which method it uses to turn the lead screw (MICROSTEP).

#### 4.2.4.2 Cell Culture on Petri dish Device

For experiments requiring culture on the petri dish stretching device, the same protocol was used as for the larger stretching device. However, the substrate was attached between the 2 clamping sections using molten PCL, and the entire internal piece to sit in the petri dish was plasma cleaned prior to being placed in ethanol with the substrate attached. Pre-stretching of the substrate was then done manually using the actuation knob and lead screw. Cells were cultured on at the same density as the larger stretcher device 127 cells/mm<sup>2</sup>.

#### 4.2.4.3 Immunostaining on Stretched Samples

Cells were fixed using 10% (v/v) formaldehyde and permeabilized using 0.2% (v/v) Triton X in phosphate buffered saline (PBS). Stretched PCL samples were stained using rabbit polyclonal antibodies for either MRTF-A (Abcam, ab49311) or  $\alpha$ SMA (Abcam, ab5694) diluted 1:100 in PBS with 1% (w/v) bovine serum albumin (BSA), with secondary biotinylated anti-rabbit antibody (Vector Laboratories, BA-1100) and fluorescein-streptavidin (Vector Laboratories, SA-5001), both diluted 1:50 in PBS/1%BSA. Rhodamine phalloidin (ThermoFisher Scientific, R415) diluted 1:100 in PBS/1%BSA was used to visualise F-actin.

Following the addition of antibodies, the cover was unscrewed from the 'Leadscrew-hood attachment' and carefully lifted off ensuring that the substrates were not further stretched. The small blocks were then unscrewed from the well-plate frame before both blocks were cut away from each substrate using a scalpel. A drop of DAPI was placed on each substrate before they were turned onto coverslips. Each coverslip was placed on a microscope slide for imaging.

#### 4.2.4.4 Live/Dead Staining on Petri Dish Device

A LIVE/DEAD® Viability/Cytotoxicity kit was used to image cells fluorescently in real time and to determine cell viability under extensive strains. The assay is a two-colour fluorescence assay that allows simultaneous staining in both live and dead cells (via calcein AM and ethidium homodimer respectively). After cells had been grown to confluence in the petri dish device stretcher, media was removed and PBS at 37°C was used to wash media out (x3), before 10 mL of new media consisting of 1 µL calcein-AM and 1 µL ethidium homodimer was added. The device was then incubated for 1 hour (37°C, 5% CO<sub>2</sub>).

After incubation, media was removed, and samples were washed twice in new media (at 37°C). After the second wash CO<sub>2</sub> independent media consisting of 100 µM ascorbic acid (AA) was added to prevent light induced cell-death. The excitation/emission wavelengths were 485/515 nm for calcein AM and 525/590 for EthD-1 and were therefore viewed with FITC and TRITC filters on the Olympus microscope with the clamp set up described in Chapter 3.

#### 4.2.4.5 Imaging

Imaging was conducted on an Olympus BX51 with a Prior filter wheel, x-, y-, z-stage, 10x/0.30 magnification lens and a QSense cooled CCD camera. Surveyor software was used for automated image acquisition using a x10 0.3NA LD Olympus objective. Samples on microscope slides were fixed to the stage using a platform built to hold slides. The top left corner of each sample was focussed to provide the software with coordinates for the sample 'origin'. Using the joystick controller, the bottom right of each sample was brought under the objective, and a grid was set on the software between the 2 points. Due to the sample being a thin film, creases and folds caused them to lie unevenly on their slides; therefore, the samples were imaged through the z plane as well as in the x, y direction. The aim of the imaging protocol used was to create one image of the entire sample after taking a series of images in the x, y and z axes.

After setting the exposure and gain for each channel to be imaged, the range of images required to be taken through the z axis was determined by focussing at the lowest and highest focus point for a range of positions on the film. The lowest and highest z value were taken, and the difference between them was divided by 7 to give a step size which was put into the software (alongside the value 7 as the number of steps). The microscope stage was then set back to its origin, and the z-coordinate was set to halfway between the lowest and highest focal points. The scan button was then selected to take z-stack images all the way through the film. Upon scan completion, the workspace was saved so that the individual images that were taken could be opened in various other software packages.

#### **4.2.4.6 Live/Dead Imaging**

For live/dead imaging of the petri dish device stacks were not required to be taken as the material is observed in tension where it remains relatively flat in comparison to substrates no longer held in tension. The petri dish device was clamped down as described in chapter 2, and the actuating knob was turned however many times necessary for certain strain values to be transmitted to the material. Images were taken at x10 for FITC (live) and TRITC (dead) directly after strain was applied and every 10 minutes from there on in.

#### **4.2.4.7 Image Processing**

Once the workspace had been saved, all TIFF images could be accessed. Each image is labelled 'Tile' followed by a number. The first objective was to convert each z-stack into a single focussed image. To do this, the software FIJI (imageJ) was used alongside an extended depth of field filter (EDF) (Aguet et al., 2008; Schindelin et al., 2012). A macro was created on the software to open a z-stack, process it, and save the resulting image in an output folder before moving onto the next stack (Figure 4.9). The macro would start at the lowest tile number and work consecutively through them; the stack size was set at 7 but could be adjusted if bigger/smaller stack sizes were taken.

<pre> 1 2 input = getDirectory("Input directory"); 3 4 output = getDirectory("Output directory"); 5 6 Dialog.create("File type"); 7 Dialog.addString("File suffix: ", ".tif"); 8 Dialog.show(); 9 suffix = Dialog.getString(); 10 //suffix = ".tif"; 11 starter = -1; 12 stacksize=9; 13 14 processFolder(input, output); 15 </pre>	<p>Where to open images from and where to save them to.</p>
<pre> 16 function processFolder(input, output) { 17     list = getFileList(input); 18     for (i=0; i&lt;list.length - stacksize; i++) { 19         if(File.isDirectory(list[i])){ 20             processFolder("" + input + list[i]); 21             print("reading in at File.isDir: " + list[i] + " and i =" + i); 22         } 23         if(endsWith(list[i], suffix)){ 24             if(starter == -1) { 25                 starter=i; 26                 print("Here it is starting: " + starter); 27             } 28             print("Here it is starting 1: " + list[i]); 29             print("Here it is starting 2: " + list[i+0]); 30 31             for(ii=0; ii&lt;stacksize; ii++) 32                 open(input + list[i+ii]); 33             run("Images to Stack", "name=Stack title=[] use"); 34 </pre>	<p>Opens initial image and the rest of the stack (On a loop till it reaches the end of the input folder).</p>
<pre> 35         run("Easy mode...", "quality='4' topology='0' show-topology='off' show-view='off'"); 36 37         while(nSlices&gt;1) 38             wait(500); 39 </pre>	<p>Processes the stack using the EDF plugin to give one image.</p>
<pre> 40         saveAs("TIFF", output + list[i]); 41 42         close(); 43         close(); 44 45         i=i+stacksize-1; 46         print("Here it did process: " + list[i] + " and i =" + i); 47     } 48 } 49 } 50 </pre>	<p>Saves the image as a TIFF with the filename corresponding to the initial image name.</p>

**Figure 4-9.** FIJI Macro used to open image stacks and process them into one focussed image for an entire sample. Text on the right explains key elements of the macro.

After the z stacks were converted into single images, the fluorescent channels were separated by opening each channel as an image sequence before saving this image sequence to another new output folder. Once the channels had been separated out, the images within the channel could be stitched together using the stitching 'Add on' on the software FIJI; this resulted in one complete image of cells (or cell components tagged using immunofluorescence) on the entire sample; Figure 4.10 is a segment of such an image (6 images produced from 6 stacks of images stitched together).

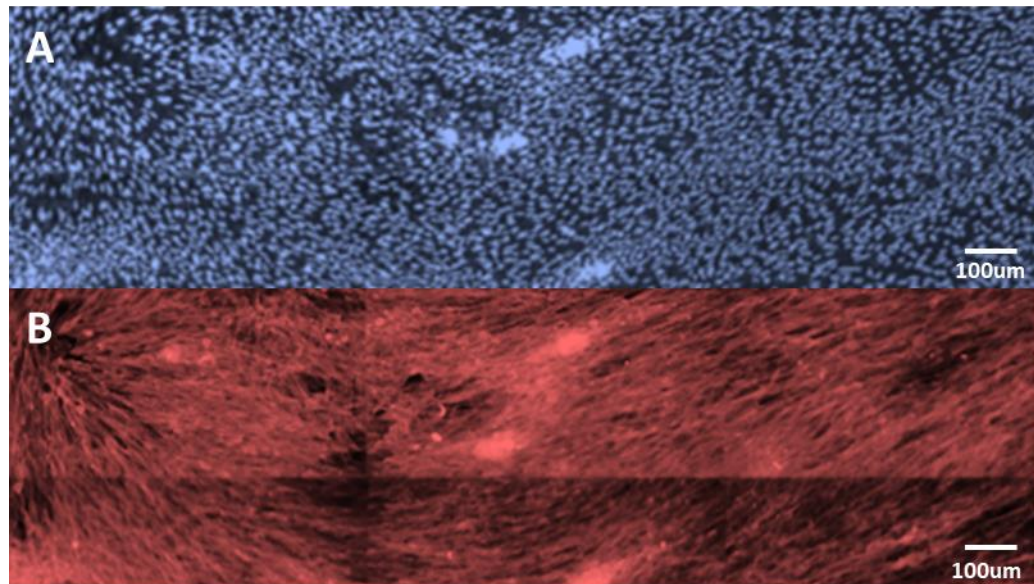


**Figure 4-10.** Example of processed image of cells cultured to confluence on stretched C-PCL. A) DNA and B) F-actin. Six consecutive image stacks have been processed using an EDF filter here for images taken at two different wavelengths of light 405nm, to image DAPI bound to DNA and 561.4nm to image F-actin.

However, due to the size of the sample there is often an uneven illumination of the cells or a background illumination. This causes problems when analysing the morphology of the cells as well as the fact that many cells become lost in the background. Contrast limited adaptive histogram equalisation (CLAHE) was therefore applied to stitched images and used (Figure 4.11) to solve the problem of uneven illumination. The way in which CLAHE does this, is by using histogram equalisation (bin count: defines amount of bins used for this equalisation) in local regions (block size: input as a larger pixel size than the minimum feature in the image); a slope size parameter can be used to increase the local contrast output ([https://imagej.net/Enhance\\_Local\\_Contrast\\_\(CLAHE\)](https://imagej.net/Enhance_Local_Contrast_(CLAHE))). It then uses them to redistribute the lightness values of the image. This results in improved local contrast and enhances definitions of edges in each region of an image. The parameters used for the purposes of processing the stitched images were 2.5 for the slope size, 31 for the block size and 256 for the number of bins.

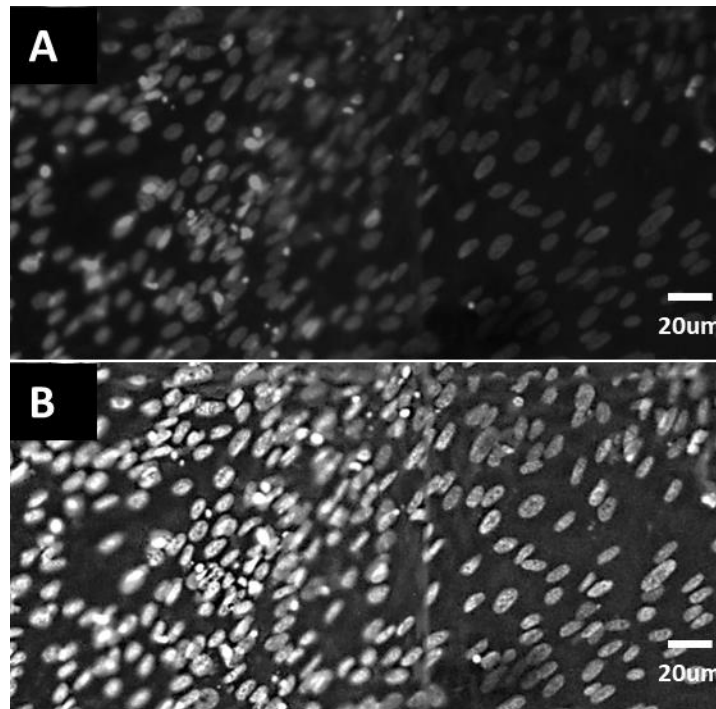


**Figure 4-11.** Example of part of PCL substrate with cells attached. A) Image of nuclei (DAPI stained) after images have been run through macro and stitched. This image highlights how some nuclei blend in with the background. B) Same image processed through CLAHE.

#### 4.2.4.8 Further Image Processing to Analyse Cell Morphological Response

F-Actin staining of cell bodies cannot be separated out to analyse the morphology of each cell when cell layers are highly confluent, and determining a morphological response was important as a first step to knowing whether the stretching of the substrate was providing a general response from the cells. Cell elongation and orientation was therefore an important starting point, as many studies have shown that under certain mechanical stress or strain regimes many adherent cell types respond by aligning parallel to the deformation direction or perpendicular to it (Boccafroschi et al., 2007; Peters et al., 2014; J. H. C. Wang et al., 2004a; Y. C. Wang et al., 2010). The analysis of the F-Actin filaments is a common way in which this is done, however due to the confluency of the samples, the filaments are very condensed on each sample. This makes it hard to separate filaments from the background to analyse. Another way in which cellular orientation and elongation can be analysed is by looking at the morphology of each nuclei. The Feret angle of a nucleus is the angle at which the maximum diameter lies to a set axis, and this angle correlates to the orientation of a cell body (B.

Chen et al., 2015). The aspect ratio of the nuclei can also be used to determine whether nuclei are elongating in response to stretch. The aspect ratio is found by dividing the 'Ferret' by the 'Min Feret' as illustrated in Figure 4.12.

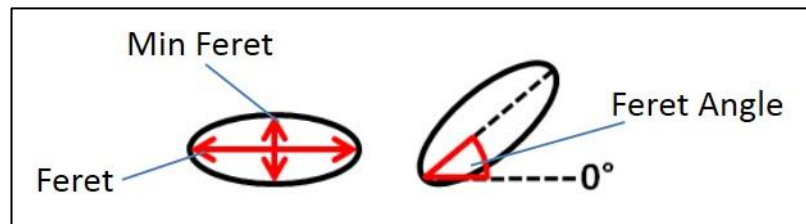


**Figure 4-12.** Illustration of what the Ferret, Min Feret and Feret Angle are. The Ferret is the maximum diameter of the particle. The Min Feret is the smallest diameter of the particle. The Feret Angle is the angle between the Feret and Normal.

To analyse nuclei for the with respect to the parameters described above , the final nuclei image for each sample was put through 'particle analysis' on FIJI, where anything smaller than 100 pixels or larger than 600 was filtered out (in separate runs it was determined that the average nucleus imaged with the above described settings has a size of  $350 \pm 250$  pixels, thus allowing to apply a size discrimination to separate out background noise and /cell clusters). The parameters selected to be analysed were the Feret angle, minimum Feret and Feret.

#### 4.2.4.9 Image Process Development to Analyse Translocation of Cytoplasmic Protein

When analysing images regarding the translocation of protein (in this case MRTF) from the cytoplasm into the nucleus in response to stretching of the substrate, a similar problem to the one encountered for morphological analysis occurred for confluent samples. As the cell body in this case is important, the data obtained cannot just be from the nuclei as was the case for the morphological analysis. Therefore, the decision to grow samples to a tenth of their confluence was taken, purely to analyse protein translocation in cells. The culture density was kept the same, but the total cell culture time was 3 days; therefore, stretched samples were stretched from 2 days after culture to 3.

To analyse whether MRTF is being translocated to the nucleus in response to substrate stretching, a ratio was to be taken from the stitched immunofluorescent images for MRTF between the fluorescent intensity in the cytoplasm and nucleus per cell. As it is fluorescent intensity which is being analysed, it was important that the image analysed was not processed in any way where the pixel intensity would be affected. Therefore, the CLAHE step previously mentioned in the general processing section could not be used. A software called 'Cell Profiler' was used to conduct this analysis (McQuin et al., 2018); Appendix A details how it was used for the purposes of this analysis.

#### **4.2.5 Statistical Analysis**

Analysis of statistical differences between conditions in all experiments was performed using Minitab 17 software (Minitab Inc., USA), with a Mann-Whitney U test for non-normal data and Welch's t test for normal data with unequal variances as appropriate. Prior to this, the data distribution was determined to be either normal or non-normal using an Anderson-Darling normality test. Statistical differences were defined by P values and confidence intervals were indicated with a \*. As a guide for confidence intervals of P values: ns > 0.05, \* ≤ 0.05, \*\* ≤ 0.01, \*\*\* ≤ 0.001. Other statistical analyses were performed as required, using the methods provided by the software. To ensure robust statistical analysis all experiments were performed at least 3 times independently (3 biological repeats).

Data analysed with the Mann-Whitney U test uses the median as the centre point for data; the 'Point Difference' is the difference between the 2 means and the 'Confidence Interval' provides a range of likely values for the population difference.

## 4.3 Results

### 4.3.1 Mechanical Characterisation of Crystalline and Amorphous Polycaprolactone

Stress-strain curves of C-PCL and A-PCL were analysed in Chapter 2, where C-PCL was defined to be initially stiffer in the elastic region than A-PCL and required a higher force to deform it through its ‘plastic flow’ stage. However, what has not been determined is how the tension in each material changes through 1mm stepped stretching after the material has yielded and is in its plastic flow stage (after pre-stretch). Figure 4.13 below shows the difference in force required to stretch each material by 1mm over 10 seconds after 40mm (30mm gauge length) strips of C-PCL and A-PCL were stretched by 10mm.

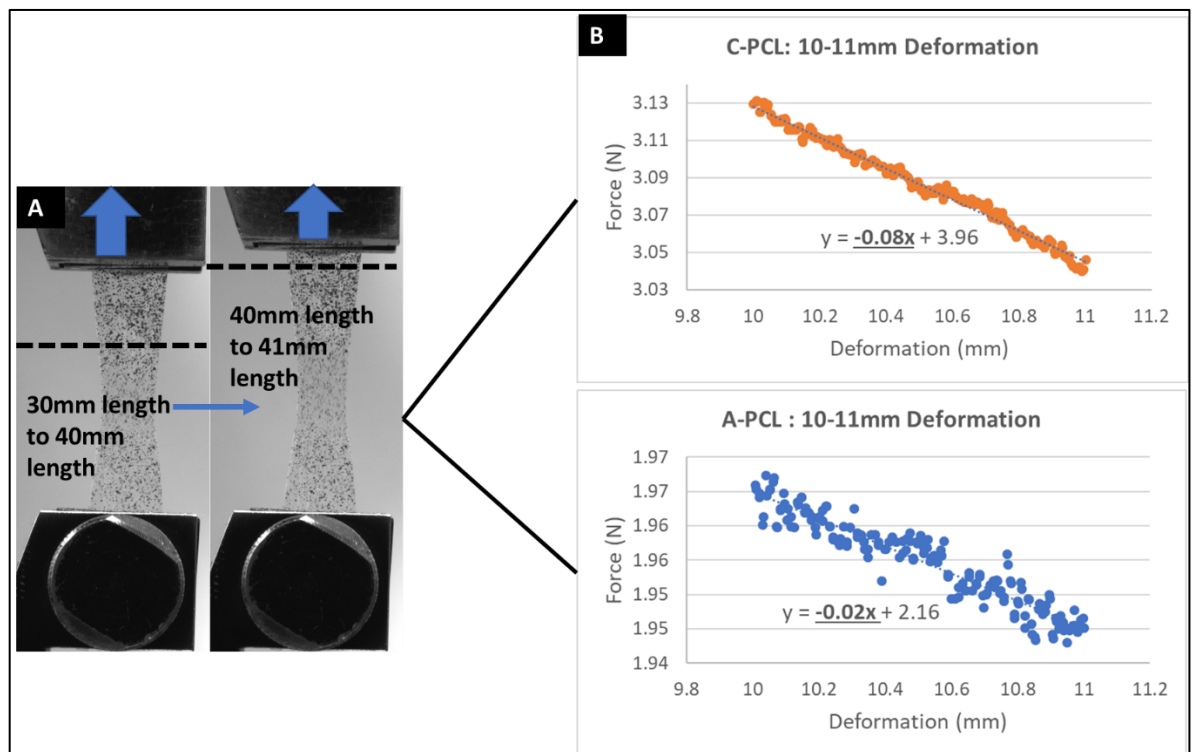


**Figure 4-13.** Stress relaxation in C-PCL and A-PCL when stretching materials by 1mm after pre-stretch has been applied. A) Image of A-PCL being stretched from 30-40mm, before being stretched by 1mm to 41mm. B) Top: Force drop (stress-relaxation) deforming 40mm C-PCL to 41mm. Bottom: Force drop (stress-relaxation) deforming 40mm A-PCL to 41mm. Stress-relaxation gradient for is 0.08N/mm for C-PCL and 0.02 for A-PCL.

What can be seen here in Figure 4.13, is that although a lower force is required to stretch the A-PCL as much as the C-PCL, the stress-relaxation that takes place over 1mm is four times greater in the C-PCL (gradient of stress relaxation is 0.08

in C-PCL and 0.02 in A-PCL). This means that in a stepped system of extension such as the one used where the polymer is being stretched 0.04mm each hour, C-PCL will have a greater fluctuation of tension in the material than A-PCL.

Further to analysing the material tension differences in the stretching regimen to be applied to fibroblasts, FEA was also conducted on both materials when each was stretched over 1 mm after being pre-stretched by 10mm using the MATLAB plugin NCorr (Blaber et al., 2015). This was done to evaluate whether there is a difference in deformation behaviour between C-PCL and A-PCL in order to understand differences which may be observed in cell responses between the 2 materials. Eulerian strain analysis was conducted as an evaluation of each material. Figure 4.14 below depicts the Eulerian strain field ( $\epsilon_{yy}$ ,  $\epsilon_{xy}$ ) for C-PCL and A-PCL for when both materials are extended by 1mm after being pre-stretched. The reference image in each case is therefore the pre-stretched film.

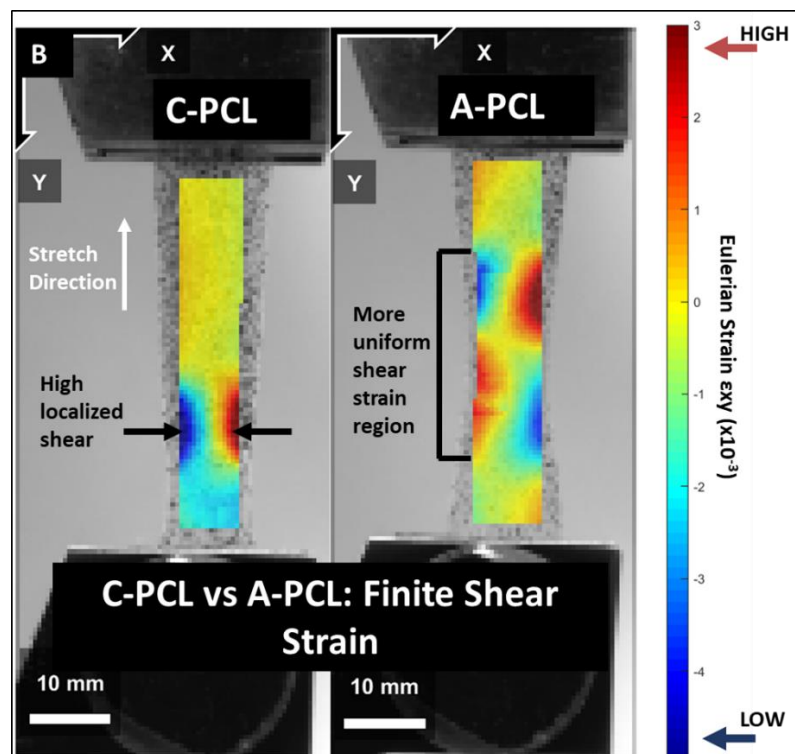
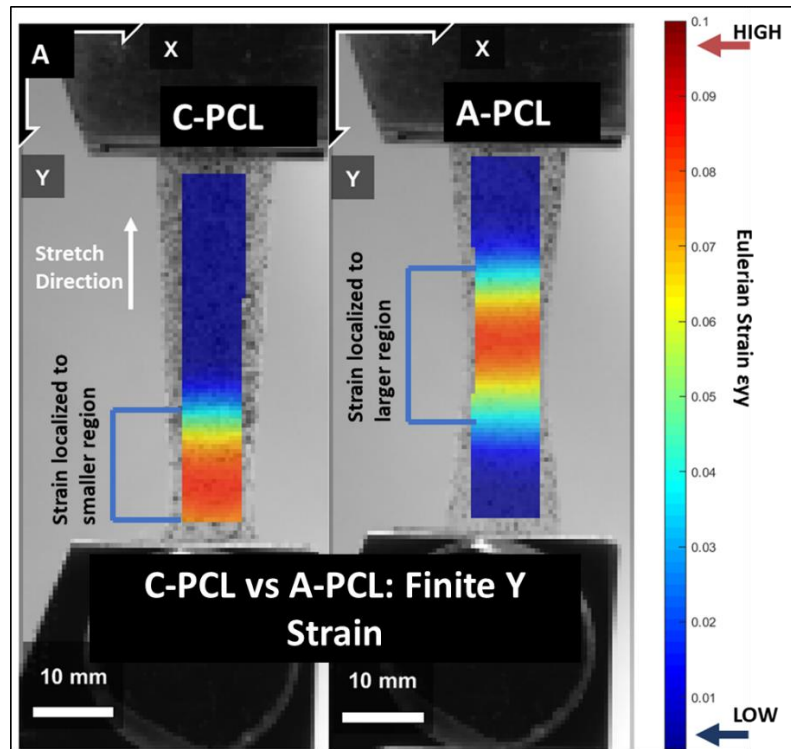


Figure 4-14. Finite strain analysis comparison between C-PCL and A-PCL when both materials are stretched by 1mm after being pre-stretched by 10mm from a 30mm gauge length. A) Finite element Y-strain ( $\epsilon_{yy}$ ) plotted in the Eulerian configuration shows a more localised strain region on C-PCL to A-PCL. The strain propagates on from one point on C-PCL. Although strain is still localised to the necked region on A-PCL, the profile is more homogenous in comparison to C-PCL (see light blue and yellow regions on films). B) Finite element shear-strain ( $\epsilon_{xy}$ ) plotted in the Eulerian configuration again shows to highly localised points of shear on C-PCL, whereas shear strain is more evenly distributed on A-PCL).

C-PCL can be seen to have a more localised  $\gamma$ -strain and shear strain region in the material when being stretched in comparison to the A-PCL. For both materials the strain is highest in the region where it necks, however the strain field extends beyond that region for A-PCL, showing that the strain is more homogeneously spread through the material than in C-PCL.

### **4.3.2 Nuclei morphological analysis**

Aspect ratio and orientation of nuclei on pre-stretched and further stretched samples of C-PCL and A-PCL were the first cell related parameters to be investigated to gain an initial read as to whether the stretching conditions of utilising the plastic flow of the material were mechanically stimulating confluent fibroblasts.

#### **4.3.2.1 Aspect Ratio**

As aspect ratio is a measure of maximum diameter divided by minimum diameter (as detailed in the methods section), the higher the aspect ratio of a nucleus, the more elongated it is. The aspect ratio of nuclei on C-PCL and A-PCL samples was first analysed. Aspect ratio for each experiment was plotted as a histogram where the data for the control pre-stretch condition was overlaid onto the response stretch condition. As large quantities of cells were being analysed per experiment (>35,000 cells), it was important to plot the data in this way to understand how the data was distributed and how this distribution changed in response to the stretch variable. Figure 4.15 below is an example of one experiment on C-PCL; the importance of viewing the distributions in analysing these results is illustrated here by labelling of the means and medians of nuclei aspect ratio on the pre-stretch and stretch conditions. Both data sets are right-skewed, which causes the mean to fall to the right of where the centre point (peak) of the data would be expected. However, the median in this instance is a better representation of the centre point for both data sets in the experiment (falls closer to peak in both instances).

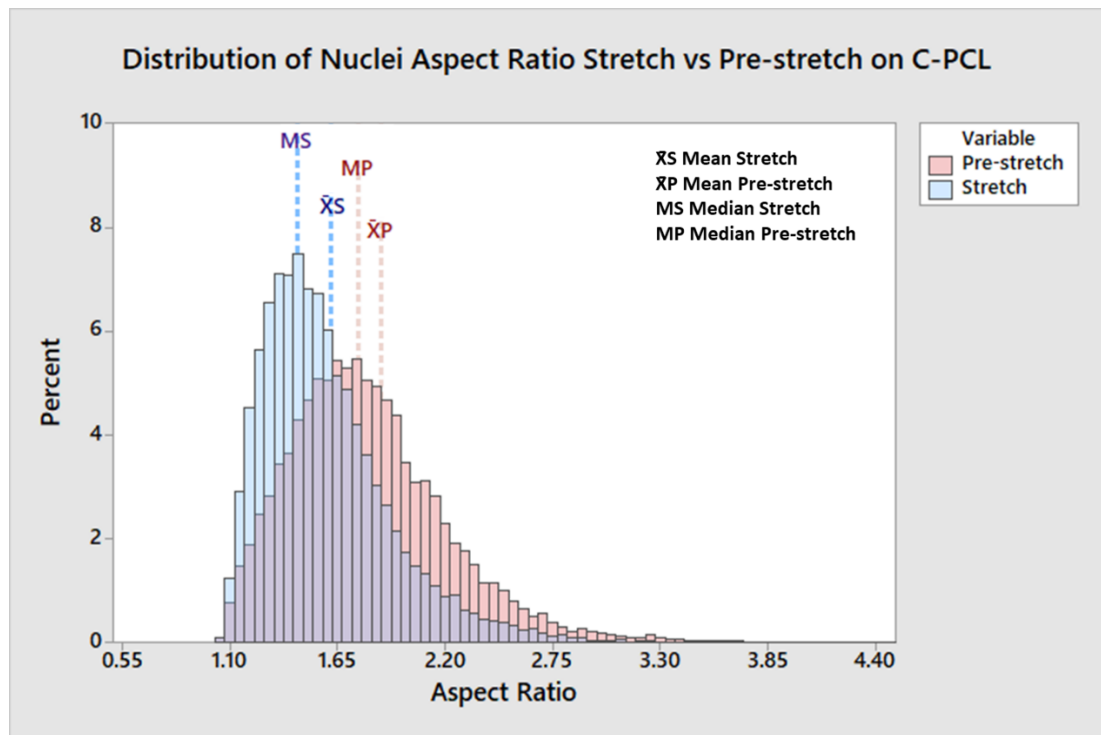


**Figure 4-15.** Histogram plotting aspect ratio of cell nuclei when cells grown to confluence on C-PCL that has been pre-stretched, and then C-PCL which has been pre-stretched, then further stretched for 1mm over 24 hours for one experiment. The distribution of nuclei aspect ratio for both conditions indicates that the median should be used to gauge the centre point of the data rather than the mean as the median in both cases is closer to the peak of the data than the mean.

Analysing how/if the aspect ratio changes in response to stretch on C-PCL first; it can be seen in Figure 4.16 that there is consistency between the control distributions of each experiment (blue). In each experimental case the control distribution appears slightly right skewed. The further stretch condition causes the distribution to become more right-skewed (red), which indicates the opposite of what was hypothesised. The cell nuclei start more elongated on the pre-stretched C-PCL, and as a result of a further stretch, cell nuclei become rounder.

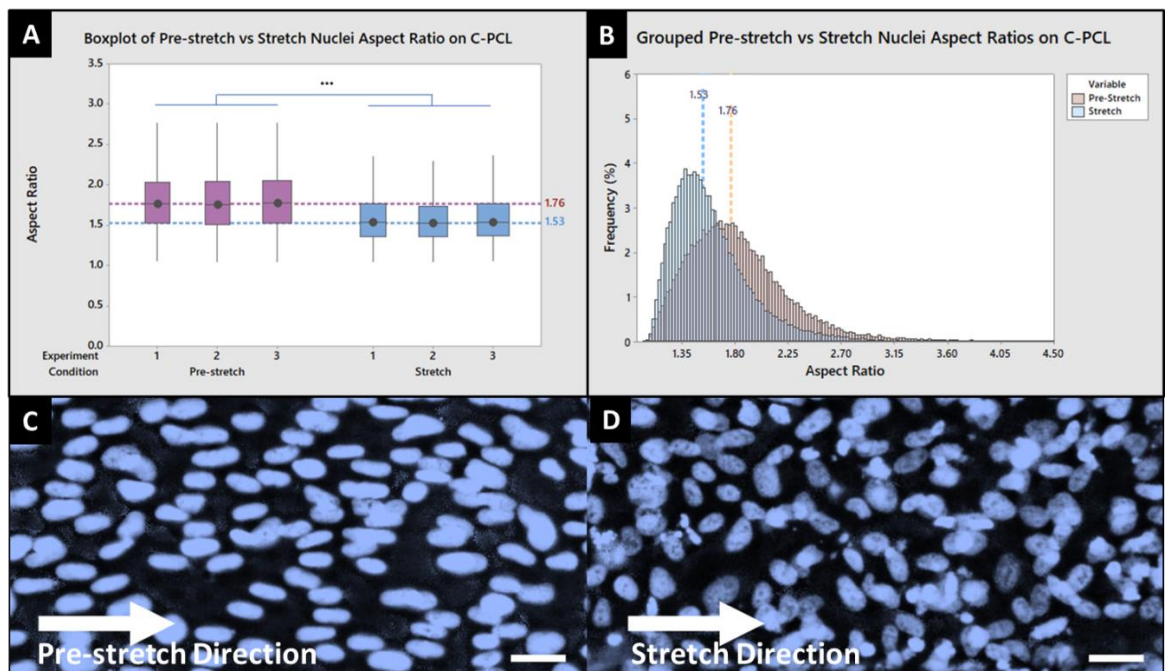


**Figure 4-16.** Summarised data for aspect ratio of cell nuclei when cells grown to confluence on C-PCL that has been pre-stretched, and then further stretched for three experiments. **A)** Boxplot of individual experiments. The bottom of each box represents the first quartile and the top is the third quartile. The centre point in each box is the median for each experiment. The whiskers extend from either side of the box. The whiskers represent the ranges for the bottom 25% and the top 25% of the data values. The median of the pre-stretch data is 1.76 and the median of the further stretched data is 1.53. These median aspect ratios are significantly different ( $p < 0.001$ , using the Mann-Whitney Test)).  $n_{\text{cells}} = 61836$  for pre-stretch and  $n_{\text{cells}} = 74482$  for the further stretched condition. Point estimate for  $\eta_1 - \eta_2$  is 0.2087, 99.9 Percent CI for  $\eta_1 - \eta_2$  is (0.2025, 0.2149), Test of  $\eta_1 = \eta_2$  vs  $\eta_1 \neq \eta_2$  is significant at 0.0000. **B)** Histogram of pooled aspect ratios of nuclei on pre-stretched C-PCL vs further stretched C-PCL. An overall shift can be seen where nuclei are more elongated in the pre-stretch condition in comparison to the further stretched condition. **C)** Example of nuclei analysed in pre-stretched condition on C-PCL. **D)** Example of nuclei analysed in further stretched condition on C-PCL. Nuclei can be seen to be more elongated in C) than D). Scalebars in white in C and D are  $20\mu\text{m}$  in length.

Based on the above aspect ratio results it was expected that the aspect ratio behaviour of the nuclei would be similar on the A-PCL as it was for the C-PCL. However, upon analysing the distributions of aspect ratios for each experiment the opposite can be seen; the aspect ratio is right skewed for control samples for each experiment, and this distribution becomes less skewed in the stretch condition. This means that cell nuclei are elongating in response to the further stretch condition. Aspect ratio goes from low to high for this material with regard to the median (1.61 to 2.00), and a Mann-Whitney test was again used to show that there is a significant change in aspect ratio here (Figure 4.17).

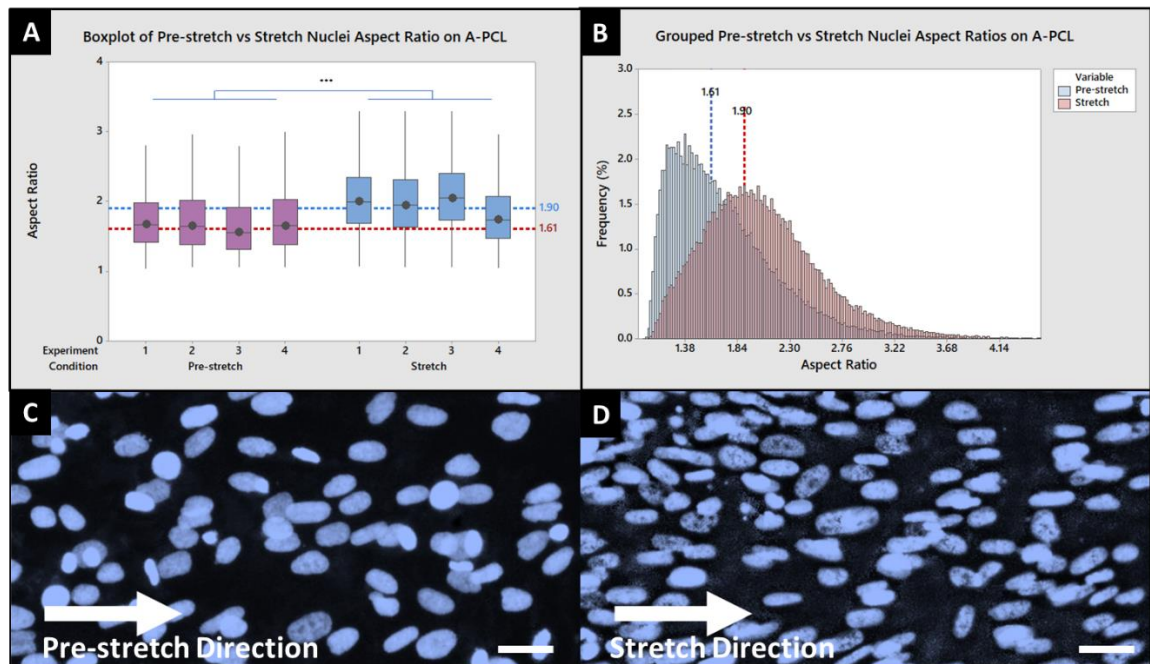


**Figure 4-17.** Aspect ratio of nuclei of cells grown to confluence on pre-stretched A-PCL, compared to cells grown to confluence on pre-stretched A-PCL and then further stretched. **A)** Boxplot of individual experiments. The bottom of each box represents the first quartile and the top is the third quartile. The centre point in each box is the median for each experiment. The whiskers extend from either side of the box. The whiskers represent the ranges for the bottom 25% and the top 25% of the data values. When pooled median aspect ratios are significantly different ( $p < 0.001$ , Mann-Whitney U test).  $n_{\text{cells}} = 92864$  for the pre-stretch condition and  $n_{\text{cells}} = 91514$  for the further stretched condition. Point estimate for  $\eta_1 - \eta_2$  is  $-0.3477$ , 99.9 Percent CI for  $\eta_1 - \eta_2$  is  $(-0.3548, -0.3406)$ , Test of  $\eta_1 = \eta_2$  vs  $\eta_1 \neq \eta_2$  is significant at  $0.0000$ . **B)** Histogram of pooled aspect ratios of nuclei on pre-stretch A-PCL vs further stretched A-PCL. An overall shift can be seen where nuclei are more elongated in the further stretched condition in comparison to the pre-stretched condition. **C)** Example of nuclei analysed in pre-stretched condition on A-PCL. **D)** Example of nuclei analysed in further stretched condition on A-PCL. Nuclei can be seen to be more elongated in **D)** than **C)**. Scalebars in white are  $20\mu\text{m}$  in length.

#### 4.3.2.2 Orientation Analysis

To analyse whether cells had an orientation response to each material being stretched, the Feret angle of all nuclei was analysed where the normal direction was taken to be the direction of stretch. The Feret angle gives values in the range of  $0-180^\circ$ , where anything between  $\sim 0-20^\circ$  and  $\sim 160-180^\circ$  is nuclei aligning to the direction of strain and anything in the range of  $\sim 70-110^\circ$  is aligning perpendicular to the direction of strain. Therefore, to avoid bimodal distributions, nuclei Feret angle values between  $180$  and  $90^\circ$  were reflected back into a value between  $0$  and  $90^\circ$  by subtracting the original value from  $180$  (Figure 4.18).

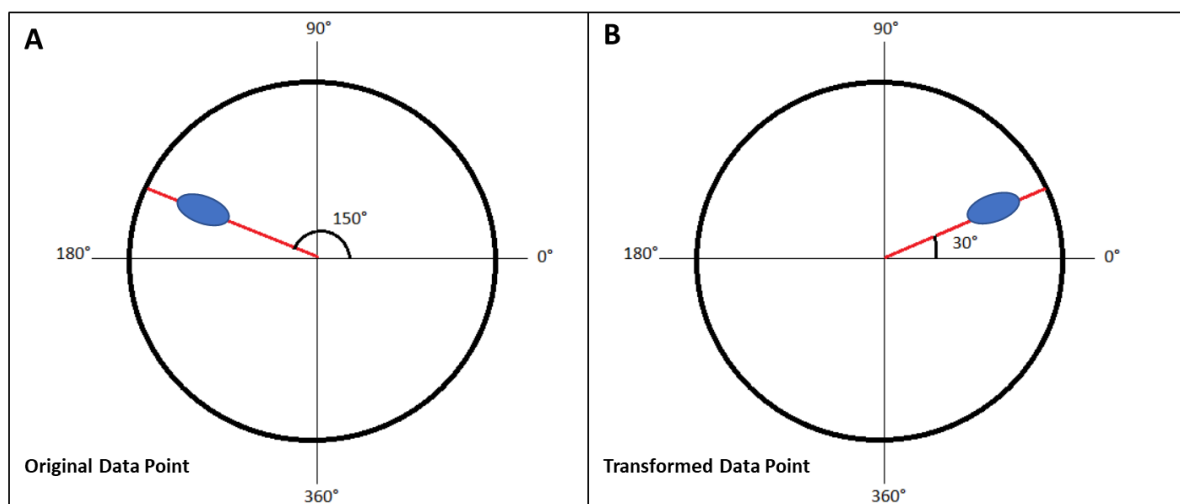


**Figure 4-18. Transformation of orientation Feret angle values. A) Example data point to be transformed to avoid bimodal data sets. B) Data point from A) transformed by subtracting original value from 180°.**

Cells align to the direction of strain on the pre-stretched C-PCL material (median 19.9°, Figure 4.19), and when the material is further stretched over 1mm in 24 hours, cells begin to orient more perpendicularly to the strain direction (median 50.2°, Figure 4.19). This response is consistent through 3 separate experiments, and the median was taken as a comparison due to the data being skewed. The circular histograms indicate the overall direction change of the nuclei when the data between experiments is pooled.

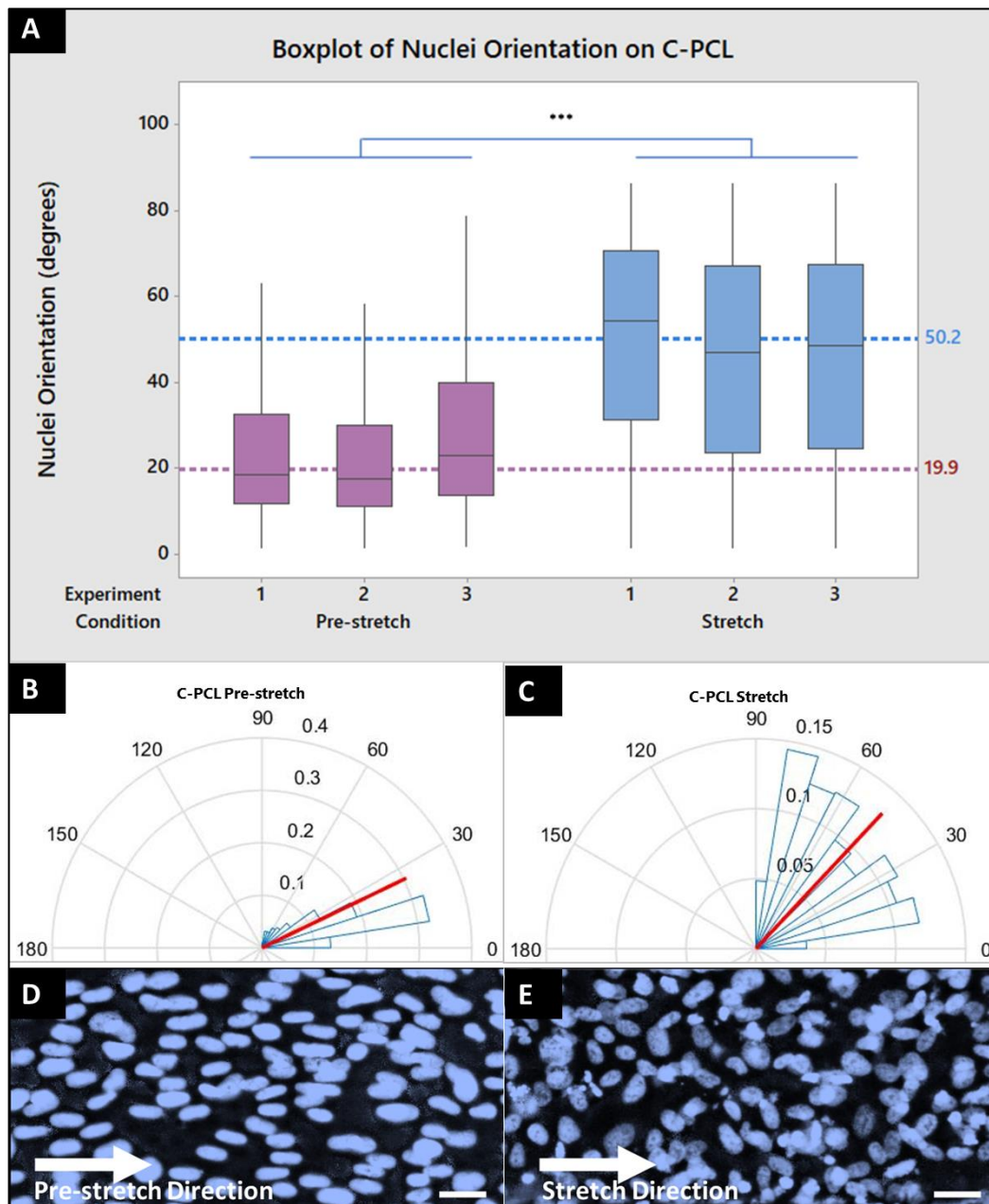


**Figure 4-19.** Orientation of cell nuclei grown to confluence on pre-stretched C-PCL, compared to cells grown to confluence on pre-stretched C-PCL and then further stretched. **A)** Boxplot of individual experiments. The bottom of each box represents the first quartile and the top is the third quartile. The centre point in each box is the median for each experiment. The whiskers extend from either side of the box. The whiskers represent the ranges for the bottom 25% and the top 25% of the data values. When pooled, median orientation angles are 19.9° in pre-stretch, and 50.2° when further stretched ( $p < 0.001$ , Mann-Whitney U-test).  $n_{\text{cells}} = 61836$  for pre-stretch and  $n_{\text{cells}} = 74482$  for the further stretched condition. Point estimate for  $\eta_1 - \eta_2$  is -21.404, 99.9 Percent CI for  $\eta_1 - \eta_2$  is (-21.866, -20.947). Test of  $\eta_1 = \eta_2$  vs  $\eta_1 \neq \eta_2$  is significant at 0.0000. **B)** and **C)** are circular histograms for C-PCL, pre-stretched and stretched data respectively; the red line is a mean vector indicating how well the distribution is spread around the mean. **D)** Example of cells orienting in the direction of stretch on the pre-stretched material and **E)** Example of cells losing orientation to stretch direction when C-PCL is further stretched. Scalebars in white are 20  $\mu\text{m}$ .

Cell nuclei alignment to the strain direction in the pre-stretch condition on A-PCL is not as pronounced as was for the C-PCL (median of  $30.5^\circ$  compared to  $19.9^\circ$  on C-PCL) and there is more variability between experiments when analysing the stretched response (medians of  $25^\circ$ ,  $32^\circ$ ,  $76^\circ$ ,  $31^\circ$ ). Pooling the experiments shows a response where cell orientation starts to slightly shift in aligning perpendicular to the strain direction (median of  $38^\circ$ ) (Figure 4.20).

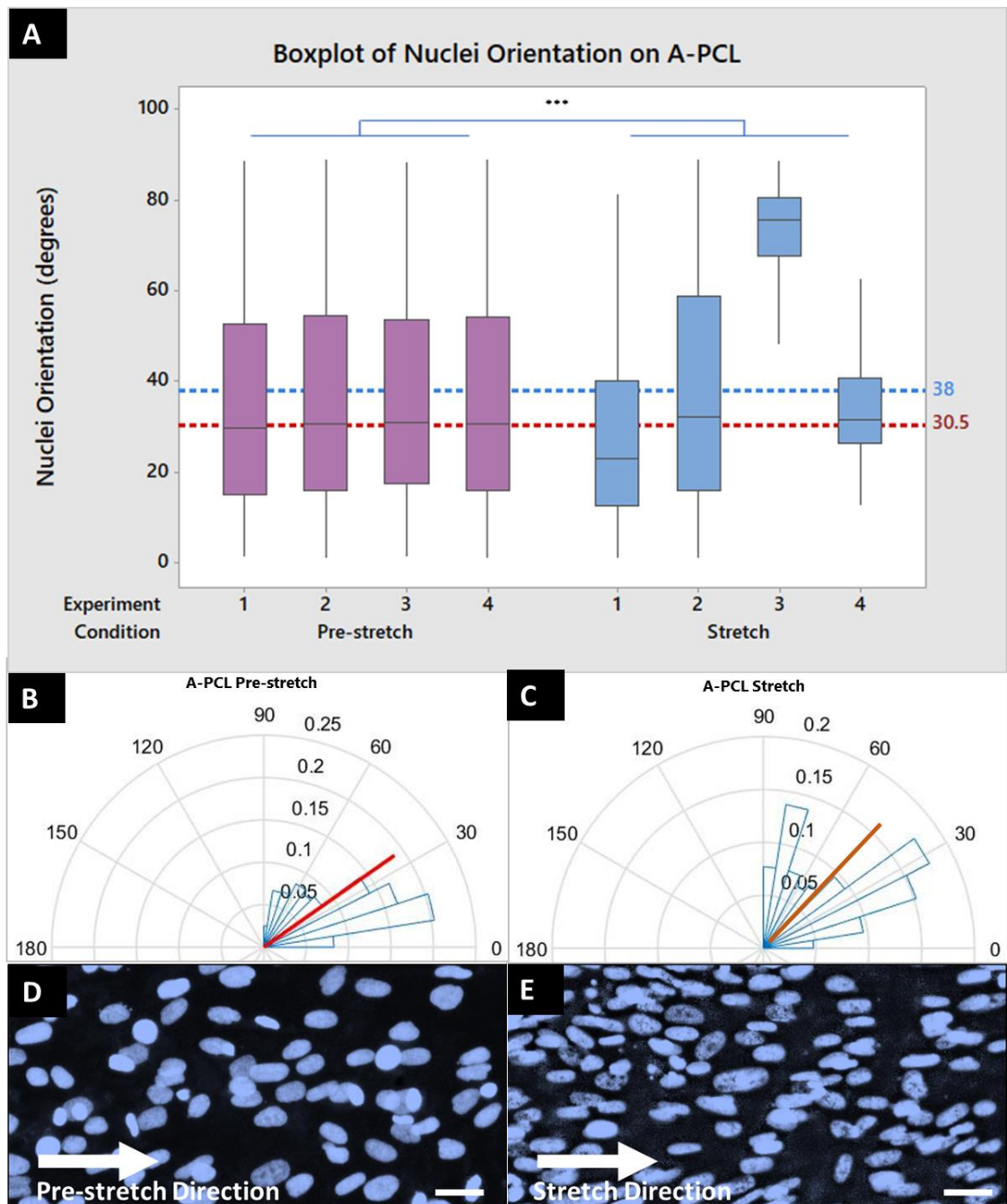


**Figure 4-20.** Orientation of cell nuclei grown to confluence on pre-stretched A-PCL, compared to cells grown to confluence on pre-stretched A-PCL and then further stretched. **A)** Boxplot of individual experiments. The bottom of each box represents the first quartile and the top is the third quartile. The centre point in each box is the median for each experiment. The whiskers extend from either side of the box. The whiskers represent the ranges for the bottom 25% and the top 25% of the data values. When pooled, median orientation angles are 30.5° in pre-stretch and 38° when further stretched ( $p < 0.001$ , Mann-Whitney U-test).  $n_{\text{cells}} = 92864$  for the pre-stretch condition and  $n_{\text{cells}} = 91514$  for the further stretched condition. Point estimate for  $\eta_1 - \eta_2$  is  $-8.54$ . 99.9 Percent CI for  $\eta_1 - \eta_2$  is  $(-8.8, -8.2)$ . Test of  $\eta_1 = \eta_2$  vs  $\eta_1 \neq \eta_2$  is significant at 0.0000. **B), C)** Circular histograms for A-PCL, pre-stretched and stretched data respectively; the red line is a mean vector indicating how well the distribution is spread around the mean. **D)** Example of cells on pre-stretched A-PCL orienting towards stretch direction. **E)** Example of cells on further stretched A-PCL continuing to orient in the direction of stretch. Scalebar in white are 20  $\mu\text{m}$ .

To validate whether the morphological and directional changes observed above translated to cell bodies, staining of F-actin was qualitatively compared to staining of DNA in all quantified samples. The below image in Figure 4.21 indicates that directional changes quantified in the above section are representative of F-actin fiber directionality on the substrates.

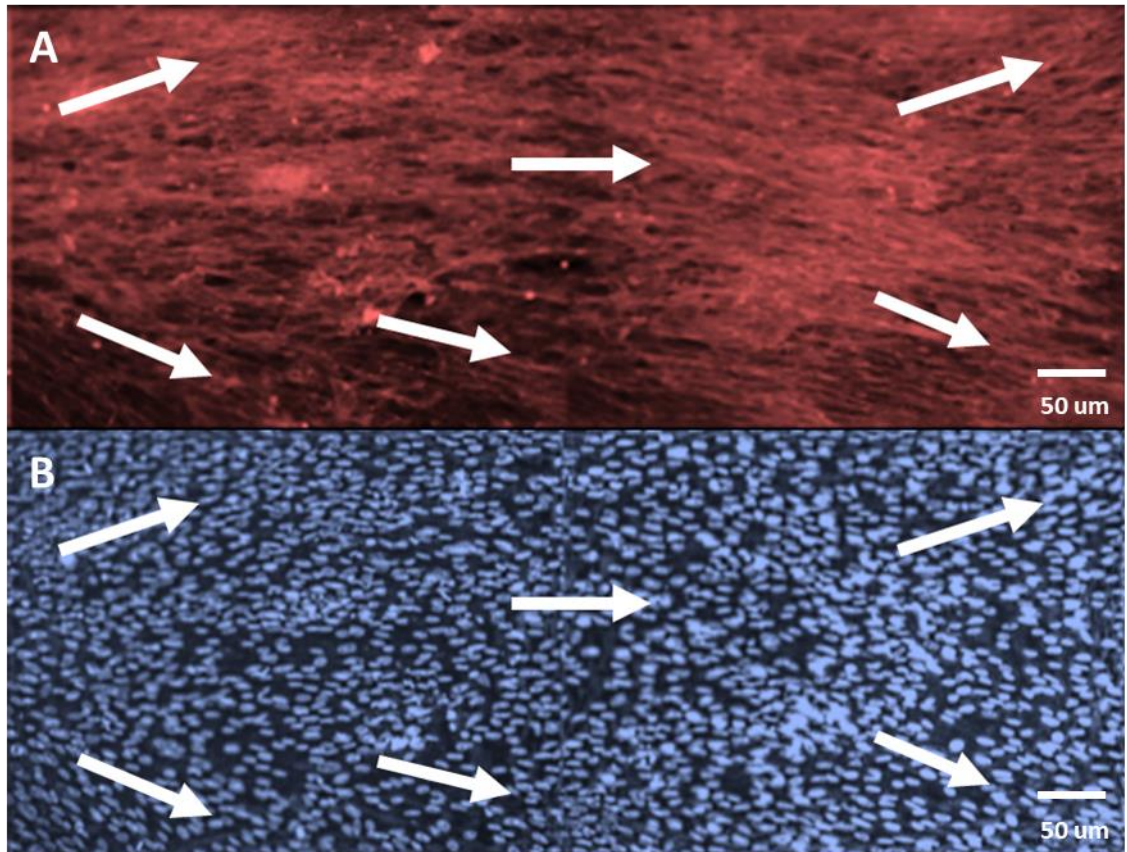


**Figure 4-21. Nuclei direction analysis indicative of F-actin fiber direction. A)** Immunofluorescent F-actin staining of confluent cells cultured on A-PCL, stretched for 1mm over 24hours after pre-stretching of material. Arrows indicate direction of nearby fibers. **B)** Immunofluorescent DNA staining of confluent cells in the same region as A). Arrows indicate direction of nuclei represents direction of F-actin fibers.

As two separate effects were observed on cells cultured on each polymer (C-PCL and A-PCL), the data was to be evaluated to determine if cells are contracting as a result of the strain applied or elongating on each material.

### 4.3.2.3 Aspect Ratio vs Orientation

To understand if there was a trend between aspect ratio and orientation, one was plotted against the other for each condition and material as binned heat maps on MATLAB. For C-PCL, high nuclei aspect ratios could be observed in the direction of stretch (Figure 4.22 A) however upon further stretching of the substrate the decrease in aspect ratio couples with a shift in the orientation of where the highest aspect ratio is found (Figure 4.22 B).

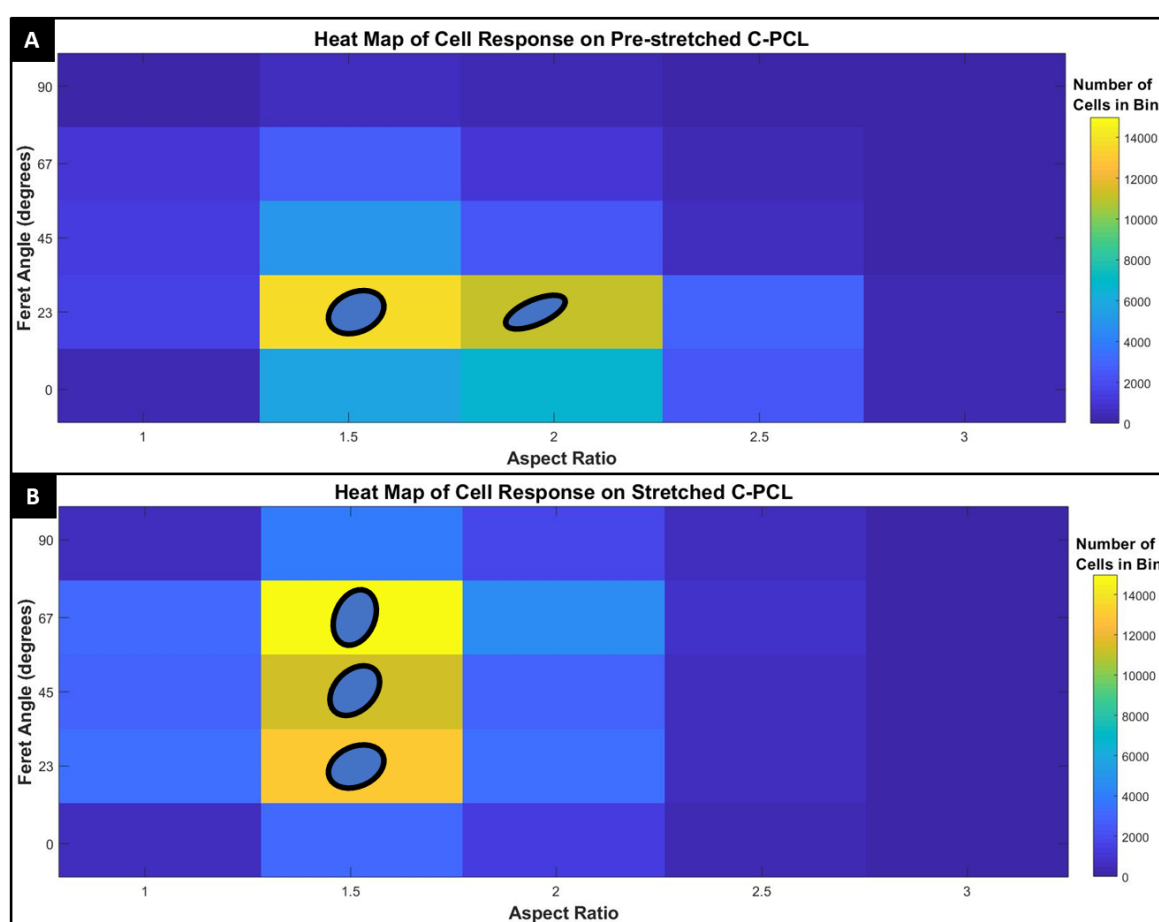


**Figure 4-22.** Heat maps plotting Feret angle of cells to their aspect ratios on C-PCL. A) For all pre-stretched samples ( $n_{\text{cells}}=61836$ ), and B) for all further stretched samples ( $n_{\text{cells}}=74482$ ). Schematic nuclei have been drawn into the them most populated bins. Their circularity and orientation represent circularity and orientation for the bin that they are in. The schematic nuclei show that cells are responding to the surface being plastically stretched by becoming more circular and orienting against the direction of stretch.

For A-PCL, there is a difference in how the cells respond to substrate strain. In the pre-stretched condition, the high aspect ratio values can be seen to be in parallel with the direction of stretch (Figure 4.23 A, yellow bin) and this is similar

to how cells react on the pre-stretched C-PCL; although cells cultured on C-PCL have a higher aspect ratio in parallel to stretching direction (Figure 4.22 B, orange bin). However a difference in comparison to how cells react on C-PCL can be seen in response to when the substrate is further stretched; a shift occurs where nuclei aspect ratio increases in the direction parallel to strain as well as perpendicular to it (Figure 4.23 yellow/orange bin).

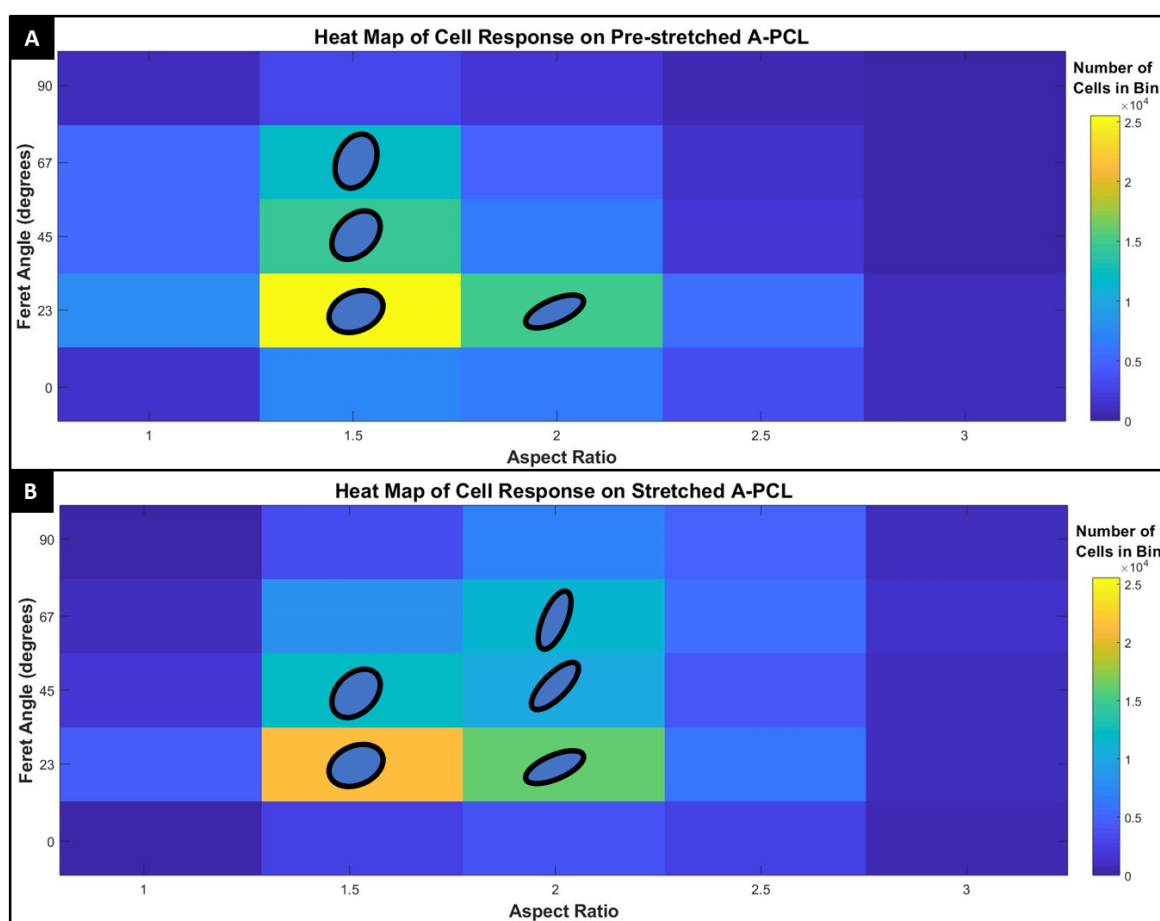


**Figure 4-23.** Heat maps plotting Feret angle of cells to their aspect ratios on A-PCL. A) For all pre-stretched samples ( $n_{\text{cells}}=92864$ ), and B) for all further stretched samples ( $n_{\text{cells}}=91514$ )  $n=3$  biological repeats. Schematic nuclei have been drawn into the them most populated bins. Their circularity and orientation represent circularity and orientation for the bin that they are in. The schematic nuclei show that cells are responding A-PCL being plastically stretched by becoming more elongated and are slightly orienting against the direction of stretch.

It can be seen that cells behaved differently on C-PCL compared to A-PCL in response to being stretched under the same regimen. Stress relaxation and local strain regions were defined as differences between C-PCL and A-PCL and were next investigated in relation to cell culture.

### 4.3.3 Live Imaging of Cell Remodelling

To understand the impact of the finite element analysis data and the cell aspect ratio/orientation response seen on C-PCL, cells cultured on the petri-dish stretching device were analysed in real-time in the necked region of the polymer after being stained with a live/dead stain (Figure 4.24). Due to the short length of time that cells can survive using this kit, the stretching regime was accelerated in order to determine whether cell contraction could be displayed under live imaging on C-PCL. Two strain values were applied in separate experiments (4%, 15%).

Figure 4.24 outlines two images of cells on a pre-stretched C-PCL substrate in the necked region. In the first case the material is strained by 4% in one motion, and in the second case, the material is strained by 15% in one motion. Images for each were taken every 10 minutes (FITC and TRITC for live/dead respectively). For both strain values the first image is directly after strain is applied with the next being the image taken at 30 minutes after the strain application. The blue/green combination image displayed for each is the difference between the original image and the image at 30 minutes. The green highlights regions missing from the image at 30 minutes after strain in comparison to the image taken straight after application of strain.

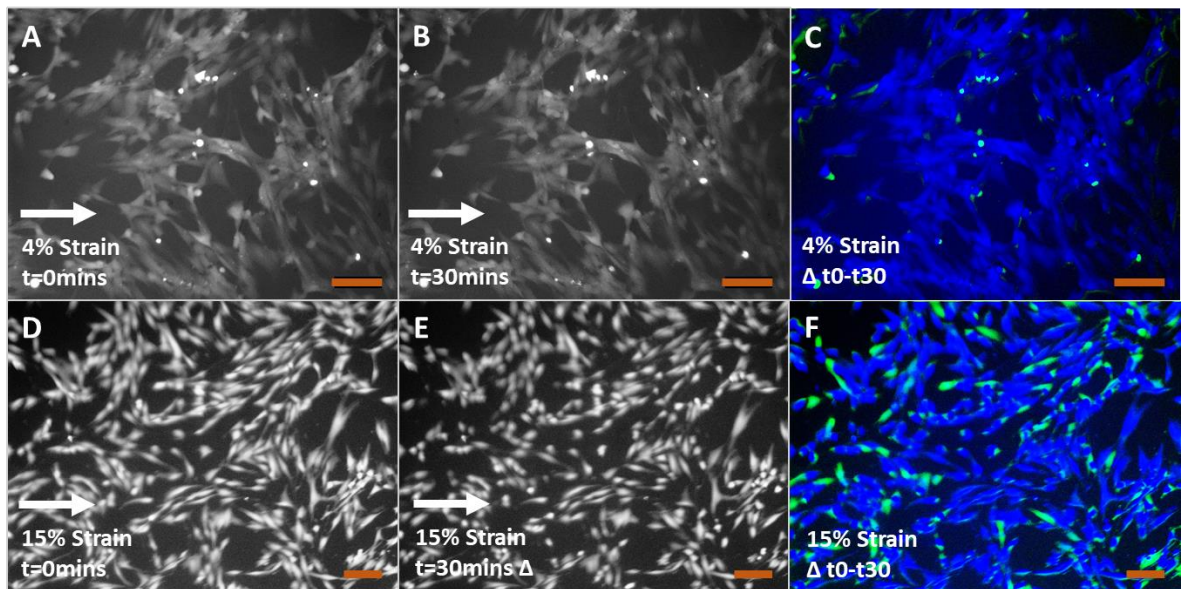


**Figure 4-24.** Live images using a live/dead stain of: A) Directly after 4% strain has been applied to C-PCL substrate, B) 0.5 hours after image A taken. C) Is the same image as B, but with remodelled areas outlined in green, cells are made blue so that the green is better visualised. The green areas are a subtraction of image B from A. D) Directly after 15% strain has been applied to substrate, E) 0.5 hours after image D taken. F) Is the same image as E, but with remodelled areas outlined in green. Scalebars in red are 50 $\mu$ m.

It can be seen that at 4% strain there is less shape change and contraction of cells than at 15% when images are taken half an hour after applying strain. Cells could visibly be seen to contract and become smaller after application of 15% strain, whereas at 4% strain cells seem to move and remodel rather than contract depicting the importance of strain rate and material tension in inducing cell responses. The observation of cell contraction here, alongside the numerical data determining an aspect ratio decrease in cell nuclei cultured on C-PCL in response to substrate stretching demonstrates that the change in tension coupled with localised strain in response to being stretched for C-PCL leads to a contraction mechanism in cells on the substrate.

C-PCL has a pre-orienting effect on cells cultured on it and this causes a change in the cell response to the direction of stretch/growth compared to flat substrates. Cells grown on pre-stretched A-PCL grow not as aligned as they do on the C-PCL. Therefore, A-PCL was selected as the material to be further investigated for the purposes of developing a soft tissue growth/stretch model.

#### 4.3.4 MRTF-A Nuclear Translocation

A-PCL samples were next seeded at the same cell density to the prior nuclear aspect ratio and orientation experiments, however stretching was initiated 2 days after culture as opposed to 7 which was used for nuclei aspect ratio and orientation analysis. Both the pre-stretch and stretch condition cells were fixed 3 days after culture (~5-10% nuclei coverage). This was to enable MRTF-A translocation analysis. A low cell density on the surface was required so that cells could be separated so that nuclear to cytoplasmic ratio could accurately be evaluated per cell (as described in the “Image Process Development to Analyse Translocation of Cytoplasmic Protein” methods section of this chapter).

Images were analysed using Cell Profiler where MRTF-A translocation was determined by its nuclear to cytoplasmic ratios in pre-stretched and further stretched samples. Mean intensity measurements, which show sum of all pixel intensity values divided by the number of pixels within an object were obtained from CellProfiler analysis. The mean intensity of the nucleus was divided by mean intensity of the cytoplasm of the same cell.

It was observed that in both the stretched and pre-stretched control cells MRTF-A predominantly localised to the cytoplasm as median nuclear/cytoplasmic MRTF-A ratio did not exceed 1 in either group. However, the stretched condition did show a significant increase in uptake of MRTF-A into the nucleus cells where the ratio increased by almost 3-fold when comparing the medians of the 2 data sets (0.35 pre-stretch to 0.99 in the further stretched condition). Figure 4.25 displays translocation of MRTF-A occurring due to the stretching mechanism applied to A-PCL. Furthermore, plotting each cell from both conditions against their nucleus aspect ratio demonstrates nuclei becoming more elongated in response to the stretch condition, showing the mechanical effect seen earlier in confluent samples remains consistent on less confluent samples.

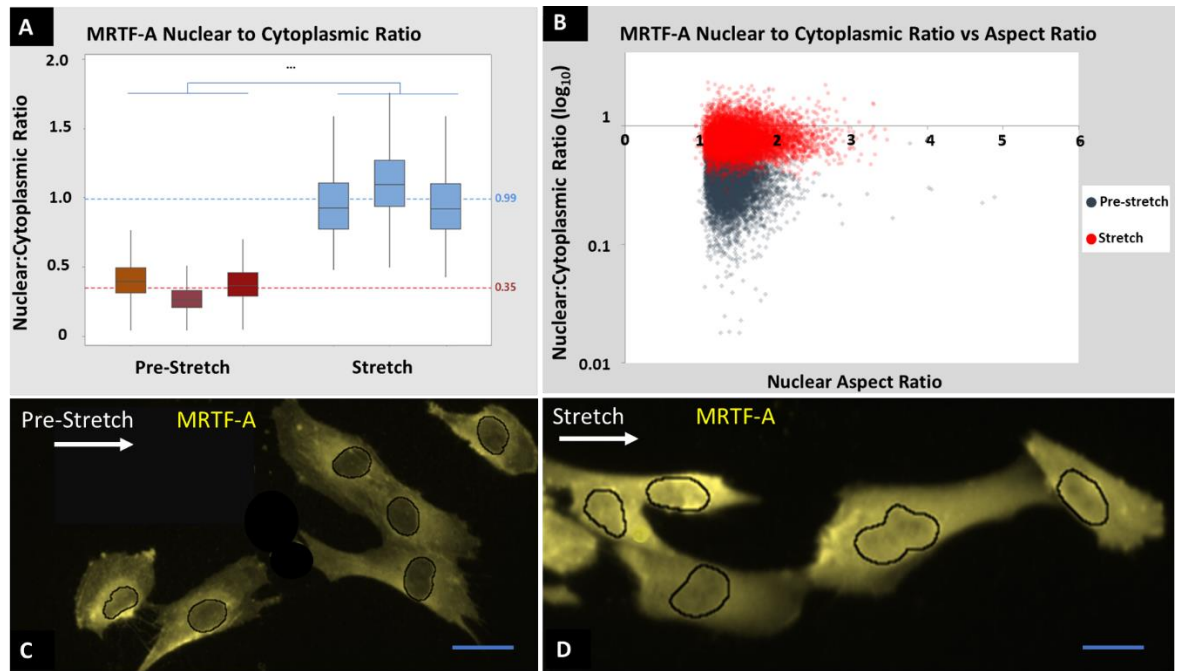


**Figure 4-25.** MRTFF-A translocation from cytoplasm to nuclei for cells grown to one-tenth confluence on pre-stretched A-PCL, compared to translocation on further stretched A-PCL. **A)** Box plot showing when 3 experiments pooled, median MRTFF-A ratio from nucleus to cytoplasm in the pre-stretch control condition is 0.35 whereas when stretch is further applied this increases to 0.99 ( $p < 0.001$ , Mann-Whitney U-test).  $n_{\text{cells}} = 7238$  for the pre-stretch condition and  $n_{\text{cells}} = 7606$  for the further stretched condition. The bottom of each box represents the first quartile and the top is the third quartile. The centre point in each box is the median for each experiment. The whiskers extend from either side of the box. The whiskers represent the ranges for the bottom 25% and the top 25% of the data values. Point estimate for  $\eta_1 - \eta_2$  is -0.63947. 99.9 Percent CI for  $\eta_1 - \eta_2$  is (-0.65097, -0.62806). Test of  $\eta_1 = \eta_2$  vs  $\eta_1 \neq \eta_2$  is significant at 0.0000. **B)** All cells MRTFF-A translocation ratio ( $\log_{10}$ ) plotted against aspect ratio showing there is still an increase in aspect ratio of nuclei in response to stretch. **C)** MRTFF-A in the cytoplasm with very little in the nucleus in the pre-stretch condition. **D)** MRTFF-A in the cytoplasm as well as the nucleus in the further stretched condition. (Nuclear regions for images C and D defined by black outline, scalebar is  $10\mu\text{m}$ ).

As MRTFF-A translocation is dependent on F-actin polymerisation and as actin fibers have been shown to impact morphological changes in the cell nucleus, F-actin texture analysis was next investigated to see if cytoskeletal changes were occurring in response to plastic deformation of the A-PCL substrate.

### 4.3.5 F-Actin Texture Analysis

A-PCL samples were seeded at the same cell density, however stretching was initiated 2 days after culture (the same as the MRTF-A section above). Both the pre-stretch and stretch condition cells were fixed 3 days after seeding cells on to substrates. This lower culture period was required to enable quantification per cell of changes in F-actin due to stretching of the substrate. F-actin cell changes were quantified using Haralick's texture features analysis, which was developed in the 1970s for image classification based on greytone spatial dependencies (Haralick et al, 1973).

This type of analysis uses the Grey-Level Co-Occurrence Matrix (GLCM) which is a statistical method of examining texture that considers the spatial relationship of pixels at the grey level (Haralick, 1973). The example below in Figure 4.26 is a 4 by 4 region of interest (ROI) where 3 grey levels (for example purposes) are represented by numerical values from 1 to 3. The GLCM is constructed by considering the relation of each pixel with its neighbouring pixel. The below example is only looked at in terms of the neighbour to the right. The GLCM acts like a counter for every combination of grey level pairs in the image. For each pixel, its value and the neighbouring pixel value are counted in a specific GLCM element (Löfstedt et al., 2019). The value of the reference pixel determines the column of the GLCM and the neighbour value determines the row. In the Figure 4.26 example, there are two instances when a reference pixel of 3 occurs with a neighbour pixel of 2, (indicated in blue), and there is one instance of a reference pixel of 3 with a neighbour pixel of 1 (indicated in dashed red); the normalized GLCM represents the frequency or probability of each combination to occur in the region of interest in a given direction (Löfstedt et al., 2019).

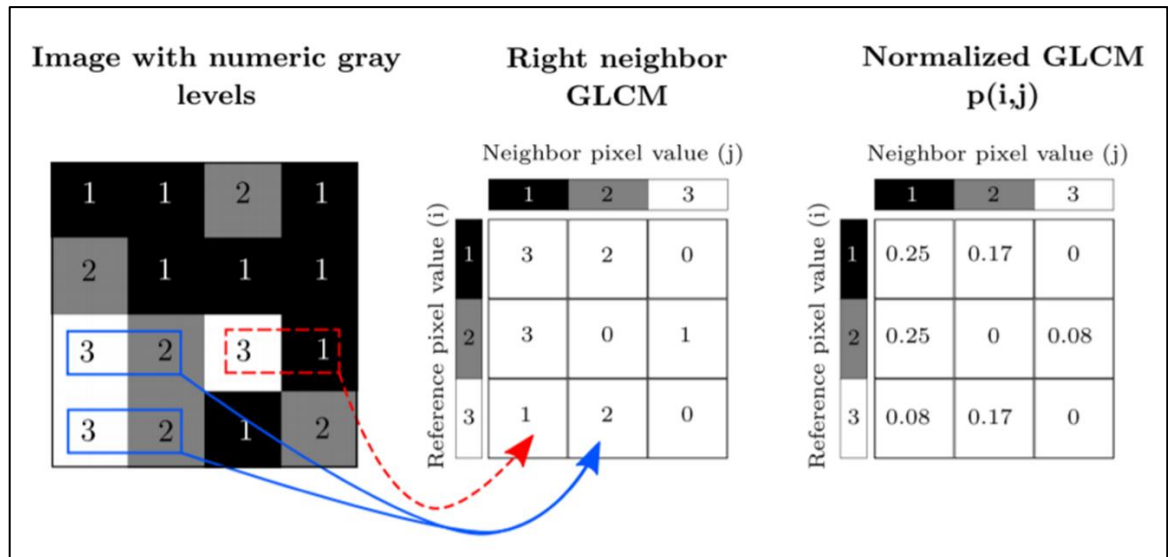


**Figure 4-26. Schematic of how a normalised GLCM is developed.** A region of interest is selected, and each pixel is assigned a grey value. A GLCM is developed with respect to neighbouring pixels in a specified direction (in this case to the right); for each pixel, its value and the neighbouring pixel value are counted in a specific GLCM element. The value of the reference pixel determines the column (i) of the GLCM and the neighbour value determines the row (j). As an example, there are two instances when a reference pixel of 3 “co-occurs” with a neighbour pixel of 2 (blue), and there is one instance of a reference pixel of 3 with a neighbour pixel of 1 (red). The normalised GLCM represents the estimated probability of each combination to occur in the image (Figure adapted from Löfstedt, Brynolfsson, Askund, Nyholm, & Garpebring, 2019).

All of the texture features are differing functions of the normalized GLCM, which take into account different combinations of the grey level distribution in the ROI. For example, in Figure 4.26, the diagonal elements in the GLCM have pixel pairs with equal grey levels; ‘contrast’ here will value these a low weight but will value elements with differing grey level value a high weight (3 and 1).

Using the same pipeline on ‘Cell Profiler’ as was used to separate out cells for MRTF-A analysis alongside the ‘Orange’ data mining toolbox (<https://orange.biolab.si/>), four Haralick texture features (homogeneity, contrast, entropy, correlation) were analysed for F-actin stained, pre-stretched and further stretched A-PCL samples. Table 4.2 outlines the formulae for how each feature is calculated. Breaking down the formulae for each feature, it can be seen that homogeneity is a measure for uniformity throughout the GLCM. If variation is low, then homogeneity will be high; values range from 0-1 for this feature. Contrast as previously described measures local variation in the GLCM; high contrast values would be expected when an image has heavy edged textures,

and conversely, low values would be expected for smooth edged textures. In the context of GLCM entropy, is a measure used to determine the unpredictability of the grey level distribution; a completely random distribution would have very high entropy. Finally, the correlation feature shows the linear dependency of grey level values in the GLCM.

**Table 4.2. Haralick texture features and how they are calculated on ‘Orange’.** Mathematical formulae (right column) using the GLCM values (see Figure 4.26) can be used to determine defined texture measurements (left column).  $P(i,j)$  is the probability value at position  $(i,j)$  in the generated GLCM.  $P_{ij}$  values in the GLCM are therefore a measure of commonness of occurrence between neighbouring pixel values; as it is a probability measure, the value ranges between 0 and 1. Contrast (CO) measures similarity of pixels. When  $i$  and  $j$  are equal,  $(i-j=0)$ , this represents pixels entirely similar to their neighbour, so they are given a weight of 0 (no contrast). The weights increase exponentially as  $(i-j)$  increases. Homogeneity (HO) increases with less contrast as essentially homogeneity weights values by the inverse of the contrast weight. Entropy (EN) is a measure used to determine the unpredictability of the grey level distribution; the  $\ln$  of the probability will always be 0 or negative as the probability range is between 0 and 1. The  $(-1)$  multiplier makes each term positive. Therefore, the smaller the  $P_{ij}$  value, the greater the weight, and the greater the value of entropy. The GLCM Mean (ME) is not simply the average of all the original pixel values in the image window. The pixel value is weighted by its frequency of its occurrence in combination with a certain neighbour pixel value. The equation can calculate the mean based on the reference pixels ( $i$ ) or the neighbour pixels ( $j$ ). GLCM variance (VA) uses the GLCM, therefore it deals specifically with the combinations of reference and neighbour pixel; it is not the same as the variance of grey levels in the original image. The Correlation (CO) texture measures the linear dependency of grey levels on those of neighbouring pixels; it is expressed by the regression equation.

Texture Measures	Formula
Contrast	$CO = \sum_{i,j=0}^{n-1} i \cdot P_{i,j} (i - j)^2$
Homogeneity	$HO = \sum_{i,j=0}^{n-1} i \cdot \frac{P_{i,j}}{1 + (i - j)^2}$
Entropy	$EN = \sum_{i,j=0}^{n-1} i \cdot P_{i,j} (-\ln P_{i,j})$
Mean	$ME = \sum_{i,j=0}^{n-1} i \cdot (P_{i,j})$
Variance	$VA = \sum_{i,j=0}^{n-1} i \cdot P_{i,j} (i - ME)^2$
Correlation	$CC = \sum_{i,j=0}^{n-1} i \cdot P_{i,j} \left( \frac{(i - ME)(j - ME)}{VA_i VA_j} \right)$

Contrast and entropy can be seen to significantly increase in the actin cytoskeleton of the fibroblasts in response to stretching of the substrate after pre-stretch in Figure 4.27. As both of these values depend on the range in grey pixel values to a certain degree, and as these in turn are correlated to the relative amount of F-actin, which can be assessed using fluorescently labelled phalloidin (Verderame et al., 1980). Therefore, this increase in contrast and entropy can be linked to F-actin formation in response to stretch, as F-actin formation leads to higher grey intensities in certain regions of the imaged cells. Texture correlation decreased after stretching which links to the entropy results in that pixels are more randomly distributed in response to the stretch condition.

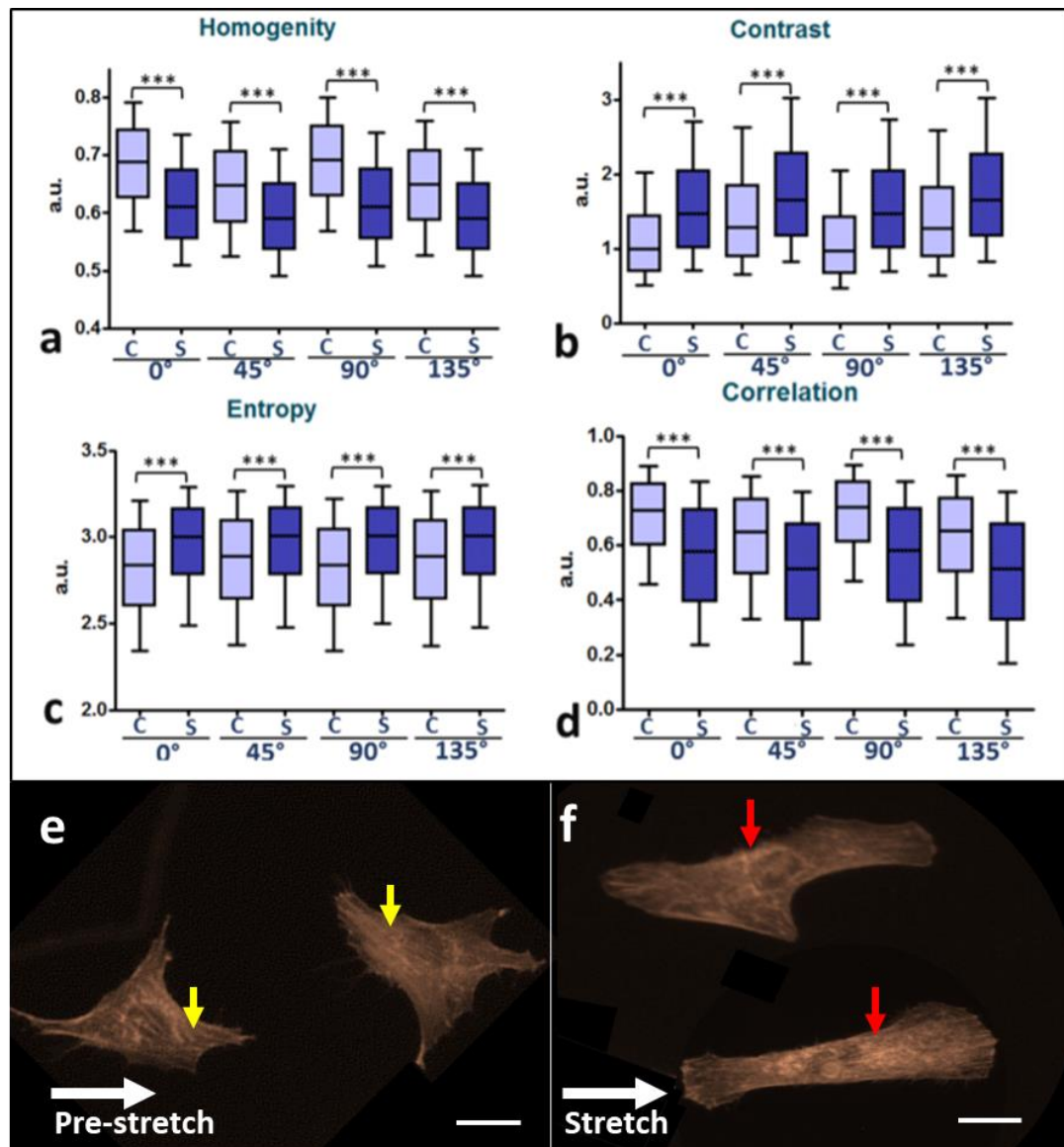


**Figure 4-27.** F-actin texture difference on A-PCL, pre-stretch vs further stretch. Texture homogeneity (a), contrast (b), entropy (c) and correlation (d) values were measured in 4 different directions. Homogeneity (a) and correlation (d) decreased after stretching, while contrast (b) and entropy (c) increased. All measurements, except for entropy, also varied dependent on direction. Box plots show inter-quartile range (25% above and below the median), whiskers show 10-90 percentile of the data, \*\*\* indicates  $p < 0.0001$  by Welch's t-test. Data shown from 2 independent repeats and 22095 cells. (Figure and data courtesy of Egle Antanaviciute, undergraduate project student at the time). Image (e) is an image of 2 phalloidin stained cells on the pre-stretch control condition. The areas indicated by the yellow arrows are areas that are highly homogenous which would have a low entropy. Image (f) is an image of 2 phalloidin stained cells on the further stretched condition. The areas indicated by the red arrows are areas that will lead to higher contrast and entropy values. Scalebar is  $10\mu\text{m}$  in each case.

The fact that homogeneity also decreases in response to stretch, leads to the conclusion that the stretching condition is increasing actin polymerisation, leading towards the formation of stress fibers. No specific trend was seen in terms of direction of the GLCM.

## 4.4 Discussion

In relation to the orientation and aspect ratio data evaluated on C-PCL and A-PCL, previous research where MSC cells were cultured on PCL films where microgrooves were purposely created via stretching of crystals has demonstrated self-aligning along the ridges into a more elongated morphology. Furthermore these grooves resulted in the MSCs obtaining a contractile SMC-like phenotype with upregulation and ordered organization of  $\alpha$ -SMA (Z. Y. Wang et al., 2014). In chapter 2, it can be seen that stretching C-PCL creates 'waves' in the membrane in parallel to the long axis that act like microgroove topography to orient cell alignment; this is the state of the membranes when these membranes have undergone 'pre-stretch'. The intention of this work was not to induce cell responses via topography and allow that to be a dominating factor; microtopographies on PDMS have also shown to affect alignment of cells more than the stretching direction of PDMS (J. H. C. Wang et al., 2004b).

The C-PCL nuclei results also demonstrated a decrease in aspect ratio in response to further stretching suggesting that fibroblasts cultured on pre-stretched C-PCL have a high cytoskeletal tension which is released upon further stretching of the substrate; reorientation has been shown to involve F-actin depolymerisation and RhoA dependent reassembly into stress fibres (Kaunas et al, 2005) as well as remodelling of focal adhesions (Jungbauer et al, 2008). This results in a temporary loss of intracellular tension and reduced tension after the reorientation. This effect can be seen in the live imaging characterisation where a large strain is applied to the substrate and cells are seen to contract over a half hour period. The remodelling demonstrated here supports findings on elastic silicone substrates where a continuous 5% stretch and hold caused a decrease in overall cell aspect ratio when cells were observed over a 40 minute period after stretch was applied (Y. Chen et al., 2013). This exaggerated response in a short time frame is likely to resemble the cell reaction to 1mm stretch over 24 hours on the C-PCL, where an overall negative shift in aspect ratio distribution was quantified in response to stretch. However, the question remains as to why this is seen to be the case on the C-PCL and not the A-PCL.

Measuring the force required to stretch A-PCL and C-PCL by a further 1mm after they have been pre-stretched past their respective yield points shows that more force is required to displace the C-PCL than the A-PCL. However, the stress relaxation when the material is being continuously stretched by 1mm is greater in C-PCL than for A-PCL (Figure 4.13). This gradient is likely to be more exaggerated in the stepped stretch regime used to stretch substrates by 1mm over 24 hours (material stretched 0.04mm every hour) as the material would further relax when being held at each step (Mirani et al., 2009). The main point is that the C-PCL has a higher gradient for stress relaxation than the A-PCL (0.08 compared to 0.02). Therefore, cells cultured on this material are experiencing higher tension upon a step as well as more relaxation between steps thereby giving 2 possible reasons (or a combination of reasons) as to why an increase in cell contraction is seen as a response on this surface.

The mechanism of substrate stretching clearly differs here when compared to cyclic stretching on elastic surfaces such as PDMS; research showed cyclic stretching not to have an effect on cell orientation when grooves were perpendicularly aligned to strain direction (8% at 0.5Hz for up to 3 days) as well as parallel (J. H. C. Wang et al., 2004b). In the case of the C-PCL in this experiment, cell orientation starts to shift away from the direction of the grooves despite the relatively low strain rate (0.1%/hr). This could either be due to high tension or relaxation of the material (or both). When looking at the physical process of generating contractile force in non-muscle cells, activation of non-muscle myosin-II motors, which act to crosslink, organize and affect sliding between actin microfilaments is key (Landsverk and Epstein, 2005). In the presence of strong adhesion against an underlying substrate, these filaments tend to coalesce into stress fibers that are tethered at sites of adhesion (Chrzanowska-Wodnicka and Burridge, 1996). Numerous findings have demonstrated that mechanotransduction of applied forces is often lost when myosin-based contractility is inhibited (Zhao et al., 2007; Sarasa-Renedo et al., 2006; Torsoni et al., 2005). One explanation for this finding is that cell-generated forces and applied forces must act together on a mechanosensor to generate a response.

Research has shown a loss in substrate rigidity modulated cell spreading and focal adhesion size. FAK activation and serum-induced ERK phosphorylation increased

with rising substrate rigidity as did expression of  $\alpha$ -SMA, whereas myocilin and  $\alpha$ -B-crystallin expression increased on soft substrates, suggesting this could be a likely effect of the overall drop in stiffness of the C-PCL substrate after undergoing 1mm stretch (Schlunck et al., 2008). Pre-strained collagen lattices have shown cells to appear more elongated within them, whereas when these lattices are relaxed, cells can be seen to have a more rounded and less stretched morphology (Kessler et al., 2001). The shift in nucleus aspect ratio is subtle (median of 1.77 decreasing to 1.53 in response to stretch) but does imply rounding of cells between the pre-stretch and further stretch conditions.

However recent work on fibroblasts has suggested high regions of tension cause proliferation of fibroblasts from myofibroblasts with a deposition of a less strained matrix (Kollmannsberger et al., 2018). This maybe applicable to the C-PCL material where cells were already pre-strained due to the topography, and then when further stretch is applied, the strain is likely to have been very localised (Figure 4.14); it could be in these regions where new rounded fibroblasts are developing causing the shift in aspect ratio.

It may therefore be beneficial to track material deformation and cell morphological response simultaneously, however there may also be the component of ECM proteins to consider; for example fibronectin may unfold due to substrate deformation and then may potentially be remodelled by cells when the substrate is undergoing stress relaxation (Antia et al., 2008; Ao et al., 2015). To investigate these interactions through live imaging, the petri dish device stretcher set up must be further developed to enable live imaging for longer time periods.

The A-PCL also demonstrated alignment of nuclei in the pre-stretch direction to a certain degree. This may be explained by fibroblasts aligning to the direction of tension (Hyun et al., 2006). Results from chapter 2 (polarised light microscopy) indicate that fibres in the A-PCL align in the direction of stretch during pre-stretching of the material; there may therefore be an element of topography being involved in the alignment of cells during pre-stretch. Further stretching of the material over 24 hours, showed there was a degree of strain shielding (more cells orienting away from the direction of stretch, although this was variable between

experiments). In general, the response of the cells was to extend in the direction of strain where higher nuclear aspect ratios could be seen. It is difficult to compare these results with previous observations due to the difference in stretching regime in this study. However cyclically stressed collagen matrices (10%, 0.1Hz, 24 hrs) have demonstrated cell alignment in parallel to strain direction. The heat map (Figure 4.23) showing an increase in nuclei aspect ratio in the stretched direction implies cells are being polarised and stretch in the plane of the substrate's stretch (Versaevel et al., 2012). This is an important factor in producing a model for growing a tissue via stretch as tissues will not form correctly if cell polarity formation is impaired (Maninová et al., 2013).

To demonstrate that the change in morphology represented an effect which can be seen in soft tissue (in tension), analysis of MRTF-A translocation to the nucleus was conducted on the A-PCL under the same stretching conditions. The results of the MRTF-A experiments confirm fibroblasts were sensitive to the stretching regime applied. Higher nuclear to cytoplasmic ratios were quantified when substrates were further stretched from pre-stretch than pre-stretch controls. The aspect ratio of nuclei was also higher in the stretched condition (Figure 4.25). This result is not as exaggerated as results seen on cyclically stretched PDMS pillar surfaces where ratios of up to 3 were reported in response to 2 hours cyclic stretching at 5% with a frequency of 0.1Hz on mouse fibroblast. As the stretching regime is continuous in small stepped increments over 24 hours, it is not surprising that the cellular response is not as acute as under cyclical stretch, when cells undergo sudden deformations repeatedly. Both MRTF-A nuclear translocation and polarising of cells towards the stretch axis are cellular responses dependant on changes in the intracellular actin dynamics and structure (Goldyn et al, 2009). Differences seen in actin texture results indicate that the actin cytoskeleton is affected by slow continuous stretch, where polymerisation of actin is occurring (Haralick, 1973). F-actin polymerisation in response to passive stretching is a known response, and further proves that cells are responding to substrate stretching via remodelling of cytoskeletal structures (Pot et al., 2010). In comparison to stimulating fibroblasts through cyclic stretching (Gadhari et al., 2013; Montel et al., 2019) or substrate topographical changes (Ahmed et al., 2010), the changes found in this study (with respect to MRTF-A nuclear translocation and F-actin changes mentioned) are of a smaller magnitude but more

representative of the cell response when tissue is placed under slow increasing tension.

The fact that these changes can be induced through the process of step stretching A-PCL substrate plastically over 24 hours is novel; the next step then is to determine when these changes have a negative impact. For example, with respect to MRTF-A nuclear translocation, MRTF-A has been reported to have a negative effect on cell proliferation as it upregulates the transcription of some antiproliferative proteins (Descot et al, 2009, Gualdrini et al, 2016). Furthermore, it has also been shown that  $\alpha$ SMA positive cells do not actively proliferate, suggesting that contractile and proliferative activities of myofibroblasts are not regulated by mutually exclusive pathways (Grotendorst, Rahmanie, & Duncan, 2004). This is further supported by work which suggested that myofibroblast proliferation, required for skin expansion, is regulated by another SRF co-activator ternary complex factor, which directly competes with MRTF-A for SRF binding sites (Gualdrini et al., 2016). The point/magnitude at which these changes have negative impacts on key pathways is where this model must next go.

#### **4.4.1 Conclusion**

This chapter has shown the application of a stretch regimen, where the plastic flow of polymer is utilised to apply stretch to a combination of cells and their extracellular matrix. The utilisation of plastic flow here is novel in relation to modelling stretching of soft tissue for the purposes of surgical techniques such as distraction osteogenesis. Fibroblast behaviour on 2 variations of PCL (C-PCL and A-PCL) has been defined; each version of the material may be useful to serve different purposes.

The C-PCL has a more localised strain region when stretched, this version of the PCL may therefore be useful to model scenarios such as wound healing, where the necked region in the polymer acts as the wound site. Fibroblast behaviour on this material is characterised by an initial alignment to the pre-stretch direction where high nuclear aspect ratios can be seen indicating cells elongating in the direction of stretch (Figure 4.22). When a stepped stretching regime of 1mm is applied over a 24 hour period, cell nuclei begin to round and orient perpendicular to stretch.

This effect is likely due to a combination of localised strain on the material when 1mm stretch is applied after pre-stretch; and high stress relaxation occurring between each step of stretching.

The A-PCL has a more homogenous strain region when stretched in comparison to the C-PCL; this version of the PCL may therefore be useful to use more generically as a model for stretching soft tissue for growth purposes. Fibroblast behaviour on this material is characterised by an initial alignment to the pre-stretch direction, and when a stepped stretching regime of 1mm is applied over a 24 hour period, cell nuclei elongate in the direction of stretch (Figure 4.23).

This overall effect of stimulating cells to elongate in the direction of stretch is a representative scenario of tissue growing due to application of stretch. Furthermore, a mechanotransductive response was seen in fibroblasts where MRTF-A translocated from the cytoplasm to the nuclei of cells, as well as F-actin texture changing (indicating actin polymerisation in response to stretch). Therefore, variables such as rate and amount of deformation could be optimised to fine tune the fibroblast response (or other cellular responses) to, for example promote proliferation while decreasing MRTF-A translocation.

## 5 Final Discussion and Project Perspectives

PCL polymer films were used as a substrate for investigating the effects of stretch on cells with a view to building towards a model for soft tissue damage incurred during surgical DO. Initial work involved tailoring a material to resemble a deformation profile close to what can be seen in a typical soft tissue in tension. This was met by investigating mechanical changes in tension of PCL after altering its crystallinity (C-PCL and A-PCL). Although C-PCL was more rigid than A-PCL through tensile testing, both materials demonstrated that they plastically deform after being stretched past their yield points and this stress/strain profile after the yield point is representative of how soft tissue responds to tension (Payne et al., 2014). Custom devices were then created to analyse fibroblasts behaviour in relation to the two materials being stretched in their plastic flow regions (1 mm over 24 hours after 33% strain pre-stretch). A difference in fibroblast response was quantified in relation to both materials (pre-stretch and further stretch conditions) and this had implications for the study of fibroblast mechanotransduction in relation to the impact of: substrate topography; material rigidity and stress-relaxation during stretching mechanisms; and localisation of strain through stretching mechanisms. This chapter will discuss the impact of this work on each of these topics before providing an overall perspective on the findings of this project. Future work which can be conducted to further understand concepts discussed in this work will then be explained.

### 5.1 Material Topography

C-PCL and A-PCL characterisation in Chapter 2 showed how the materials differ in their structure where crystallites in C-PCL cause the material to appear translucent with a rougher surface structure (crystal size  $\sim 400 \mu\text{m}^2$ ). Previous work has demonstrated that crystallinity has an effect on cell response where the rougher crystalline surface has caused hepatocytes to form spheroids faster (A. Park & Cima, 1996) and cells in general to grow at a slower rate when compared to growing on amorphous versions of poly-L-lactide (PLLA) (A. Park & Cima, 1996; Washburn et al., 2004). However, decrease in growth rate did not significantly

effect cell area, number of adhesions, or degree of actin polymerisation in osteoblasts (Washburn et al., 2004); this study also reported no change in adhesion protein accessibility, suggesting a direct topographical effect from crystallites.

In this work, the developed amorphous 'smooth' polymer (A-PCL) was compared as a cell culture substrate to the frequently used semicrystalline PCL (C-PCL) (Izquierdo et al., 2008; Puig-De-Morales et al., 2001; Sarkar et al., 2008; Uto et al., 2014) in stretched configurations prior to and post cell seeding. Previous work has been conducted on pre-stretched semicrystalline PCL, where groove like features characterised substrate topography (Z. Y. Wang et al., 2014). Consistent with this data hTERT fibroblasts aligned in the direction of these stretched grooves in this study. Research has also demonstrated the impact of microgrooves on cell alignment in the same way through different materials (Dalby et al., 2007; Meredith et al., 2007; Oakley et al., 1997). Further work in relation to fibroblasts implies that after cells flatten and spread, active filaments form longitudinal stress fibers parallel to topographical grooves (Walboomers et al., 2000). Such changes and the variability in alignment have been related to the depth of grooves, where deeper grooves have a more pronounced effect on orientation (Loesberg et al., 2005; Teixeira et al., 2004), highlighting a possible cause as to why cell nuclei were more elongated on pre-stretched C-PCL than A-PCL, where features induced by stretching of the substrate past its yield point were more pronounced.

Despite cells aligning to structural features in the pre-stretch condition, further stretching of both C-PCL and A-PCL led to differing responses. Previous data would suggest that topography would be the main driver of cell orientation when paired with cyclic stretching of substrates (Loesberg et al., 2005; J. H. C. Wang et al., 2004a). However, the cellular response to the stepped stretching regime in this work suggests an initial cell response is determined by topography, before further stepped stretching induces a separate response. In the case of this work fibroblasts begin to orient away from substrate structural features in both C-PCL and A-PCL (although variably in the case of A-PCL). However, there is a difference in cell elongation, where cells elongate in the direction of stepped stretch (on A-PCL), or contract against it (C-PCL). Although fibroblasts do not align away from microgrooves on cyclically strained substrates, they have expressed higher levels

of  $\alpha$ -smooth muscle actin when they were oriented parallel to the stretching direction (using topographical cues) compared to when they were oriented perpendicularly to the stretching direction (J. H. C. Wang et al., 2004b), implying that topography must be taken into account alongside the strain regime applied to cells.

The implication of this work with regards to topography is that it highlights a new area to be explored; where cells do not remain completely aligned to their substrate topographical features under a stepped stretching regime. Furthermore, cells can be cultured in alignment and stressed using pre-stretched C-PCL or aligned under no/limited stress using A-PCL before application of further stretch which can be based on the in vivo situation aimed to be investigated. However, it is important to remember that topography is one influencing factor in determining the fibroblast cell response in both pre-stretch and further stretch conditions on C-PCL and A-PCL. With regards to the fibroblasts appearing to be stressed before contracting due to stepped stretch on C-PCL, change in material rigidity in particular could be an influencing factor.

## **5.2 Material Rigidity and Stress-Relaxation**

PCL is known to behave like a viscoelastic material which stores and dissipates energy within the complex molecular structure, producing hysteresis and allowing creep and stress relaxation to occur (Duling, 2008). C-PCL was seen to be more rigid than A-PCL in tensile testing where it had a higher elastic modulus, and during its plastic phase required higher stress than A-PCL to deform, however it was also shown to stress-relax more than A-PCL when both polymers are stretched in their plastic phase. For amorphous polymers (such as A-PCL), entanglements are the only connecting points in the material, and the atoms are free to twist on carbon-carbon bonds. The elastic properties are mainly due to the entropy of variation of the positions of entanglements (Schirrer, 2001). The stronger rigidity in the crystalline polymer (C-PCL) is because molecular motion does not occur to the same degree in the crystalline section due to the intermolecular and/or intramolecular forces holding the ordered groups of atoms and molecules together (Wagner et al., 2014).

Research has shown a loss in substrate rigidity modulated cell spreading and focal adhesion size. FAK activation and serum-induced ERK phosphorylation increased with rising substrate rigidity as did expression of  $\alpha$ -SMA, whereas myocilin and  $\alpha$ -B-crystallin expression increased on soft substrates, suggesting this could be a likely effect of the overall drop in stiffness of the C-PCL substrate after undergoing 1mm stretch (Schlunck et al., 2008). Pre-strained collagen lattices have shown cells to appear more elongated within them, whereas when these lattices are relaxed cells can be seen to have a more rounded and less stretched morphology (Kessler et al., 2001).

The shift in nucleus aspect ratio on C-PCL substrates here indicates rounding of cells through the 24 hour stretching period. To support this recent research has shown switchable PCL films (which can be switched from rigid to soft) cause myofibroblasts to become rounded when switching from a rigid to soft configuration, and this change in shape did not translate to fibroblast cultures (Uto et al., 2014); this indicates that fibroblasts cultured on pre-stretched C-PCL may have differentiated into myofibroblasts due to the topography and tension in the material (Uto et al., 2014; J. H. C. Wang et al., 2004b), before stress-relaxation of the material (when it was further stretched by 1mm over 24 hours) caused these myofibroblasts to become rounded to a degree. Conversely, in the case of A-PCL, topography may not have had the same level of impact in terms of straining fibroblasts upon culture. Furthermore, the material undergoes less stress-relaxation between stretching steps, generating a different response altogether. The key point here is that, the topography of each substrate, alongside the rigidity and stress-relaxation properties of them seem to all impact fibroblast behaviour from the point of when they are cultured onto each substrate.

### 5.3 Material Strain Homogeneity

Both materials (C-PCL and A-PCL) were characterised through strain via DIC to determine homogeneity of the strain profile through being stretched. An important finding here was that A-PCL displayed a more homogenous profile through strain than C-PCL, and this is likely due to multiple nucleation points developing upon the material being stretched, acting as multiple anchor points (Kamal et al., 2012).

Recent work on fibroblasts has suggested high regions of tension cause proliferation of fibroblasts from myofibroblasts with a deposition of a less strained matrix over time (Kollmannsberger et al., 2018). This may be applicable to the C-PCL material where cells may have already been pre-stretched due to the topography, and then when further stretch is applied over long periods where there is a localised strain point, new rounded fibroblasts could be developing.

Overall, it can be seen that topography has an initial impact on fibroblast alignment and stress. Analysing the fibroblast response on C-PCL to further stretch then has two factors which may be responsible for what is seen as an overall cell population result of rounding: stress relaxation during stretching step causing a shift towards rounding in the overall population; and the fact that strain is applied in a localised region of the cell population, which would cause the population median (C-PCL nuclei aspect ratio in Chapter 4) to shift towards being more rounded. A-PCL was therefore the material taken forward to analyse with respect to MRTF-A nuclear translocation and F-actin texture analysis in relation to being used as a model for stretching soft tissue; however the fact that fibroblasts are stressed when cultured on pre-stretched C-PCL and then have a localised strain region in stretch, make this system suitable for a wound healing model (Kollmannsberger et al., 2018; Moulin et al., 1996), where the localised strain region can be used as the highly tensed wound site where fibroblasts transition into myofibroblasts (Kollmannsberger et al., 2018; Moulin et al., 1996).

As the strain profile was more homogenous on A-PCL, and the initial orientation and aspect ratio results (Chapter 4) were more indicative of a soft tissue stretch model, MRTF-A and F-actin texture were analysed in response to the stepped stretching regime. Both MRTF-A nuclear translocation and orientation towards the

stretch axis (Goldyn et al., 2009) are cellular responses dependant on changes in the intracellular actin dynamics and structure. That the actin cytoskeleton is affected by slow continuous stretching is further supported by changes in the F-actin texture measurements. Although nuclear elongation in the plane of stretch on A-PCL implies cells are being polarised in the right direction (Versaevel et al., 2012), it has also been shown that nuclear elongation can lead to more condensed chromatin and reduced DNA synthesis (Versaevel et al, 2012). Furthermore, MRTF-A has been reported to have a negative effect on cell proliferation, as it upregulates the transcription of some antiproliferative proteins (Descot et al., 2009; Gualdrini et al., 2016). It has also been shown that  $\alpha$ SMA positive cells do not actively proliferate, suggesting that contractile and proliferative activities of myofibroblasts are regulated by mutually exclusive pathways (Grotendorst et al., 2004). This is further supported by work showing that myofibroblast proliferation, required for skin expansion, is regulated by another SRF co-activator ternary complex factor, which directly competes with MRTF-A for SRF binding sites (Gualdrini et al., 2016). It is unclear if such moderate nuclear MRTF-A increase in response to stepped stretching could have affected cell proliferation, and furthermore research has shown in cyclical systems at higher strains than described in this work to initiate cell proliferation (Cui et al., 2015; Friedrich et al., 2019).

## 5.4 Overall Perspective on Utilising Plastic Flow to Stretch Cell-Substrates

Due to the stretching profiles observed and compared to literature soft tissue profiles, an effective conditioning step (material strained to 33%) was performed on both materials before cells were cultured on; this was to take the material past its yield point, so that when it's further stretched the material remains plastically deformed and hence resembles growth to a certain extent.

This is novel in comparison to other uniaxial/biaxial studies where elastic substrates are used and either cyclically stretched or stretched and held at defined strains and frequencies. The fact that both forms of PCL exhibit a certain degree of stress relaxation when held in tension after yield point added another similarity between the material's deformation and soft tissue deformation characteristics where soft tissues display viscoelastic behaviour. Cells are consistently experiencing a dynamic matrix environment, and this is captured in cyclic experiments where the frequency of stretch often resembles in vivo conditions. In the case of this work, the stress-relaxation characteristic helped develop a model resembling characteristics of slow continuous growth by stretch of soft tissue.

The difference in rigidity, microstructure and localised strain accumulation between A-PCL and C-PCL resulted in cell response differences between the two materials. Cells started elongated and oriented in the direction of stretch in the pre-stretch condition on C-PCL before a shift in aspect ratio indicated that cell tension was progressively being lost in response to the 24 hour stepped stretching of the material. Cells grown on A-PCL responded in the opposite way where cells had a lower aspect ratio in the pre-stretch condition; this increased in response to the 24 hour stepped stretching.

A combination of three reasons were outlined for the possible contractile behaviour of cells on the C-PCL in response to the stepped stretching regime in this work (summarised in Figure 5.1):

- The first being that elongated crystal microgrooves pre-stretched them, and further stretching resulted in a loss in tensional homeostasis.

- The second being that stress relaxation of the material resulted in the loss of stable focal adhesions.
- The third reason being that high localised points of strain on the material, may have resulted in myofibroblasts differentiating back towards fibroblasts.

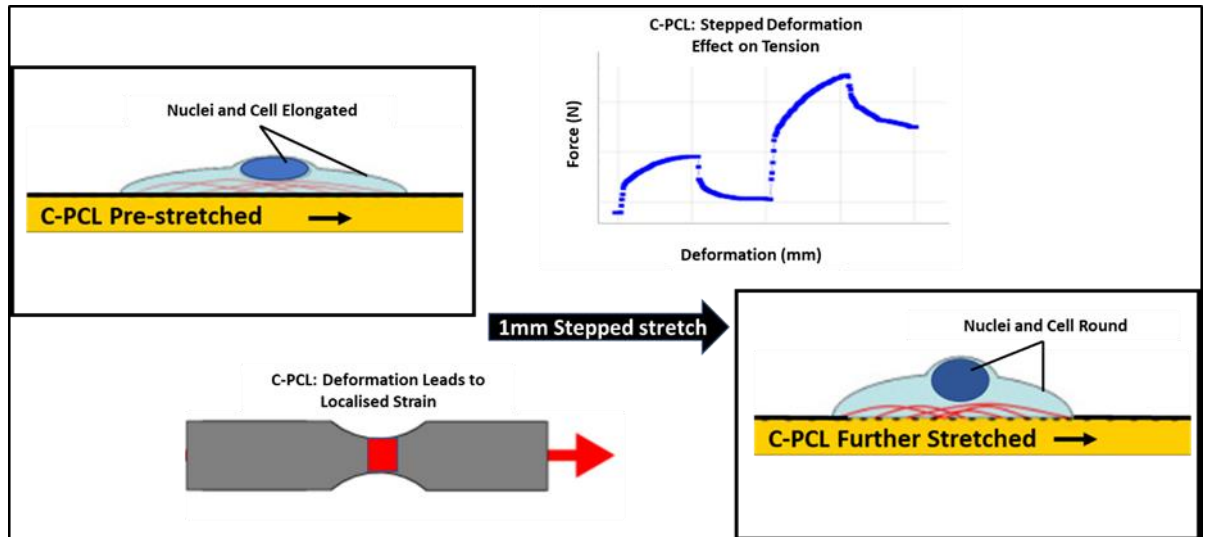


**Figure 5-1. Schematic depicting fibroblast behaviour on C-PCL.** When C-PCL is pre-stretched, fibroblasts align to the direction of pre-stretch in an elongated manner. When a further 1mm stretch is applied over a 24 hour period in a stepped manner of 0.04mm each hour, C-PCL undergoes large changes in tension due to stress-relaxation occurring between steps; furthermore, the strain transferred is very localised on the material. This leads to cells rounding on the material as a result.

These points do not affect A-PCL as the cells do not appear to be in a pre-tensed state as they do on C-PCL when the material is in pre-stretch. Although A-PCL does show stress relaxation after its yield point, it does not exhibit as much hysteresis and the material is also held in tension at a lower force than C-PCL; the combined result of these factors is that fibroblasts elongate in the axis of stretch in response to 24 hour stepped stretching (Figure 5.2).

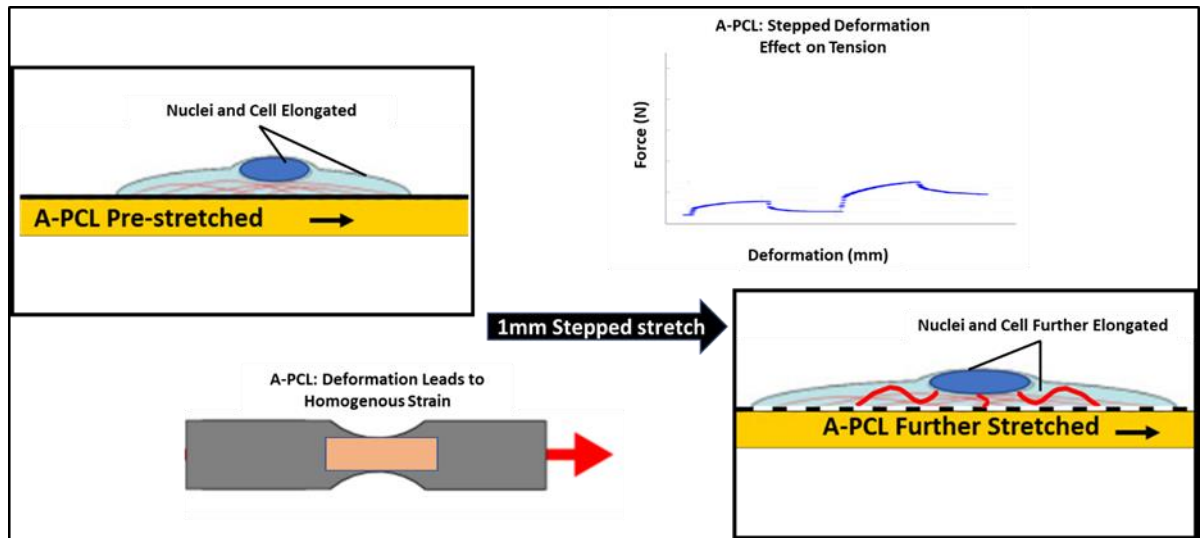


**Figure 5-2. Schematic depicting fibroblast behaviour on A-PCL. When A-PCL is pre-stretched, fibroblasts align to the direction of pre-stretch. When a further 1mm stretch is applied over a 24 hour period in a stepped manner of 0.04mm each hour A-PCL undergoes small changes in tension as stress-relaxation is lower in comparison to C-PCL between steps; furthermore the strain transferred is more homogenous on the material in comparison to C-PCL. This leads to cells elongating on the material as a result.**

A discussion point generated from the data in this thesis is perhaps whether the transduction of stiffness to a response actually involves sensing stress. The existing data are consistent with the possibility that focal adhesions (or other sensors) alter their structure and function simply as a result of changes in stress when cells are attached to substrates of different stiffnesses. For example, Engler et al. used pure collagen-I gels as well as polyacrylamide gels to show that cellular responses were equivalent on gels of equivalent stiffness (Engler et al., 2004). Although these data support a strong case for a mechanical basis for sensing, they do not exclude several other plausible mechanisms. As all of these studies use polymers with varying degrees of crosslinking to alter stiffness, it is impossible to decouple the nanomolecular changes in polymer-chain mobility, flexibility and hydration.

The MRTF-A data then seen on the A-PCL validates the material as a substrate to be further investigated as a model for growth by stretch. Although differentiation to a myofibroblast lineage may not be desired in vivo, it must be remembered that the rate at which these substrates are being stretched is still much higher than what is seen in DO (1mm/day for a much longer length than 3cm). Furthermore, tissue is not densely populated with fibroblasts, it is likely a more migratory effect would be seen with respect to fibroblasts before they start to

proliferate and induce matrix changes if the rate of distraction is too high (Boris Hinz, 2007). However, the fact that they elongate and start displaying a known differential change bodes well for other cell line pathways to be investigated in the future. Results have been seen where nuclear to cytoplasmic ratio of MRTF-A increases to 3, whereas the data set presented here peaked at 1; it may therefore be a good idea to stretch through consecutive days and analyse whether a further increase in change is seen.

## 5.5 Future Work to Further Elucidate Findings

To develop an understanding of the difference between C-PCL and A-PCL for the purposes of this project; tensile testing, DIC, SEM and PLM analysis were used. However, to highlight changes in A-PCL structure once it has undergone stretch and to investigate mechanisms to which cells may be responding to at the FA level, another stretcher device to be used under atomic force microscopy can be developed. An initial prototype of such a device can be seen below in Figure 5.3. The useful outputs from such a device would be the ability to investigate structural changes at the nanoscale when both C-PCL and A-PCL are being stretched, which could be related back to the cell response.

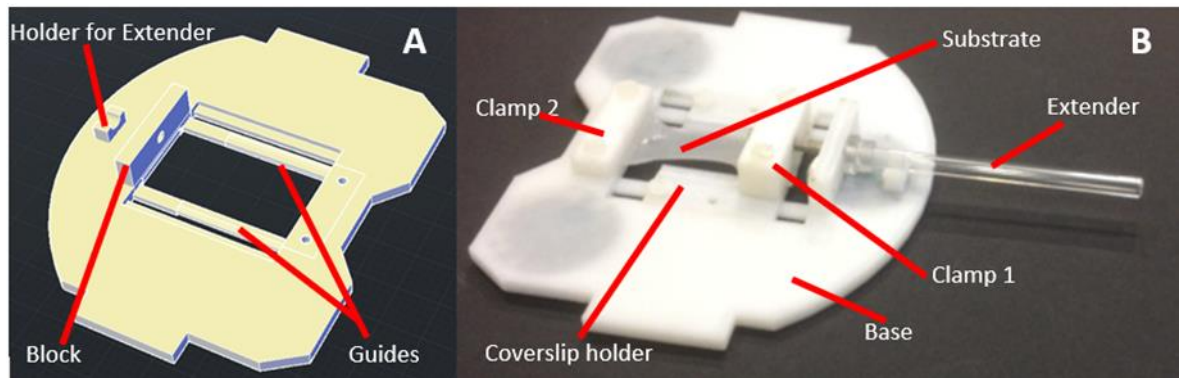


**Figure 5-3. Prototype AFM stretcher Device. A) CAD drawing of the main base which was 3D printed (Ultimaker 2). B) Final version of the device with attached parts. The base fits on top of the Nanowizard 4 (jpk.com). The PCL is clamped between 'Clamp 1' and 'Clamp 2'. 'Clamp 2' has a thread through the middle of it, through which a screw with a lead of 1mm is tightly fitted; the end of this screw also goes through a loose hole in the 'Block', where it is met by a threaded hole in the 'Extender'. When the 'Extender' is turned clockwise the screw tightens, increasing the gap between 'Clamp 1' and 'Clamp 2', thereby stretching the PCL by 1mm/rotation. The 'Coverslip holder' fits on the bottom of 'Clamp 1' and has screws going through the holes on its margins which connect to the 'Guides' ensuring smooth movement.**

Such a device would also enable further feature characterisation of A-PCL topography after pre-stretch. This data would feed into whether the tension in the material drives cells to align in the direction of pre-stretch or whether it was more a topographical influence.

Further work would involve developing the petri dish device for live imaging over long periods of time where fiducial markers would be used in the substrate, as well as live cell tags for focal adhesions to track cell remodelling in real time in response to marker movement (Strain field); this would enable a direct

quantification of strain transferred to cells on both C-PCL and A-PCL, and would then further understanding of the interaction between stress relaxation and cell remodelling. Furthermore, this would enable the development of a conclusive answer as to whether strain localisation on the C-PCL substrate is causing fibroblasts to round in response to the stepped stretching regime.

Additional work and analysis must also be conducted on the ECM and how it responds to substrate deformation; a point of interest here would be to see whether cells remodel the matrix in response to stretch or vice versa/both. Previous work for example has shown that fibronectin may unfold due to substrate deformation and then may potentially be remodelled by cells when the substrate is undergoing stress relaxation (Antia et al., 2008; Ao et al., 2015). To investigate these interactions through live imaging, the petri dish device stretcher set up must be further developed to enable live imaging for longer time periods. After breaking down these components, different cell lines and co-cultures can then be investigated with a view to deriving important components related to soft tissue damage in distraction osteogenesis.

## Appendices

### Appendix A- Image Processing to Analyse MRTF-A Nuclear to Cytoplasmic Ratio

An imaging 'pipeline' was made on 'Cell Profiler' to measure MRTF-A fluorescent intensity in the nucleus and cytoplasm. The objectives of the pipeline were to:

- 1) Develop a mask for the nucleus of the cells, ensuring the nuclear masks do not overlap into cell cytoplasm.
- 2) Develop a mask for the cytoplasm of the cells, ensuring neighbouring cells are adequately separated.
- 3) Calculate the intensity ratio for MRTF between the cytoplasm and nucleus for each cell.
- 4) Identify/link other morphological parameters to MRTF translocation if it is occurring.

Figure A.1 is a screen shot from the Cell Profiler software outlining the components of the pipeline, Each heading has a drop down where parameters were defined on a trial and error basis to extract accurate information; for example, ensuring most nuclei were selected, and that cells were adequately separated in clusters. The parameters for each heading can be seen in Figures A.2-A.5.

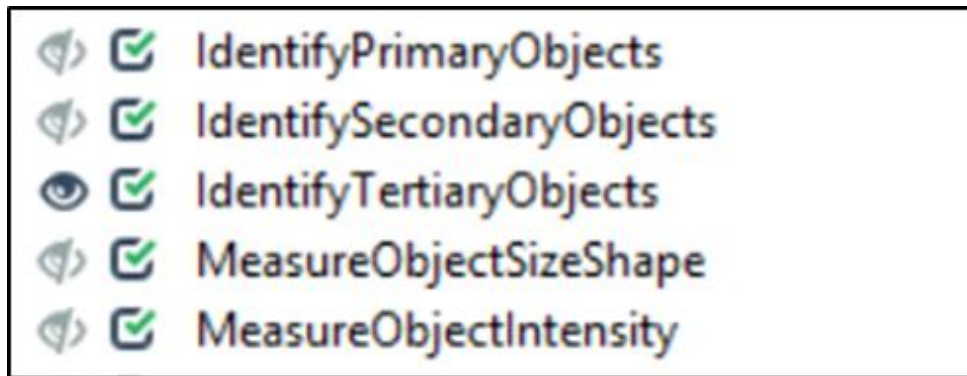


Figure A.1. Imaging pipeline main components. Primary objects were to be cell nuclei masks. Secondary objects were to be entire cell masks (determined by MRTF images). Tertiary objects were to be cell cytoplasm masks where nuclei were subtracted from cell masks. Nucelus and cell dimensions were out put alongside MRTF intensities in the nuclei and cytoplasms.

Name the primary objects to be identified	Nuclei
Typical diameter of objects, in pixel units (Min,Max)	10 40
Discard objects outside the diameter range?	<input checked="" type="radio"/> Yes <input type="radio"/> No
Discard objects touching the border of the image?	<input checked="" type="radio"/> Yes <input type="radio"/> No
Threshold strategy	Global
Thresholding method	Otsu
Two-class or three-class thresholding?	Two classes
Threshold smoothing scale	1.3488
Threshold correction factor	1.0
Lower and upper bounds on threshold	0.0 1.0
Method to distinguish clumped objects	Shape
Method to draw dividing lines between clumped objects	Intensity
Automatically calculate size of smoothing filter for declumping?	<input checked="" type="radio"/> Yes <input type="radio"/> No
Automatically calculate minimum allowed distance between local maxima?	<input checked="" type="radio"/> Yes <input type="radio"/> No
Speed up by using lower-resolution image to find local maxima?	<input type="radio"/> Yes <input checked="" type="radio"/> No
Fill holes in identified objects?	After both thresholding and declumping
Handling of objects if excessive number of objects identified	Continue

Figure A.2. Primary objects parameters for cell profiler pipeline. The input here is a stitched image of nuclei on the film. When the pipeline is run, if an image is output at this point it will output a mask image for the nuclei input.

Select the input image	MRTF_Images	(from NamesAndTypes)
Select the input objects	Nuclei	(from IdentifyPrimaryObjects #05)
Name the objects to be identified	Cells	
Select the method to identify the secondary objects	Watershed - Gradient	
Threshold strategy	Adaptive	
Thresholding method	Otsu	
Two-class or three-class thresholding?	Two classes	
Threshold smoothing scale	1.3488	
Threshold correction factor	1.0	
Lower and upper bounds on threshold	0.0	1.0
Size of adaptive window	10	
Fill holes in identified objects?	<input checked="" type="radio"/> Yes <input type="radio"/> No	
Discard secondary objects touching the border of the image?	<input checked="" type="radio"/> Yes <input type="radio"/> No	
Discard the associated primary objects?	<input checked="" type="radio"/> Yes <input type="radio"/> No	
Name the new primary objects	FilteredNuclei	

**Figure A.3. Secondary objects parameters for cell profiler pipeline.** The input here is a stitched image of MRTF on the film. When the pipeline is run, if an image is output at this point it will output a mask image for the MRTF input. This was used as a mask representing the entire cell.

Select the larger identified objects	Cells
Select the smaller identified objects	FilteredNuclei
Name the tertiary objects to be identified	Cytoplasm
Shrink smaller object prior to subtraction?	<input checked="" type="radio"/> Yes <input type="radio"/> No

**Figure A.4. Tertiary objects, defining an output cytoplasmic mask via the subtraction of the nuclei mask from its corresponding cell mask.**

Select an image to measure  (from NamesAndTypes)

---

Select objects to measure  (from IdentifySecondaryObjects #06)

Select objects to measure  (from IdentifyTertiaryObjects #07)

Select objects to measure  (from IdentifySecondaryObjects #06)

**Figure A.5. MRTF intensity measurements output defined.**

Below, Figure A.6 is an example of what the pipeline does. The images on the left are the Nuclei and actin input images, the MRTF one is to be analysed for grey intensity. The images on the right are the output masks where the bottom one is the result of subtracting the nuclei masks from the cell masks to give a cytoplasmic mask.

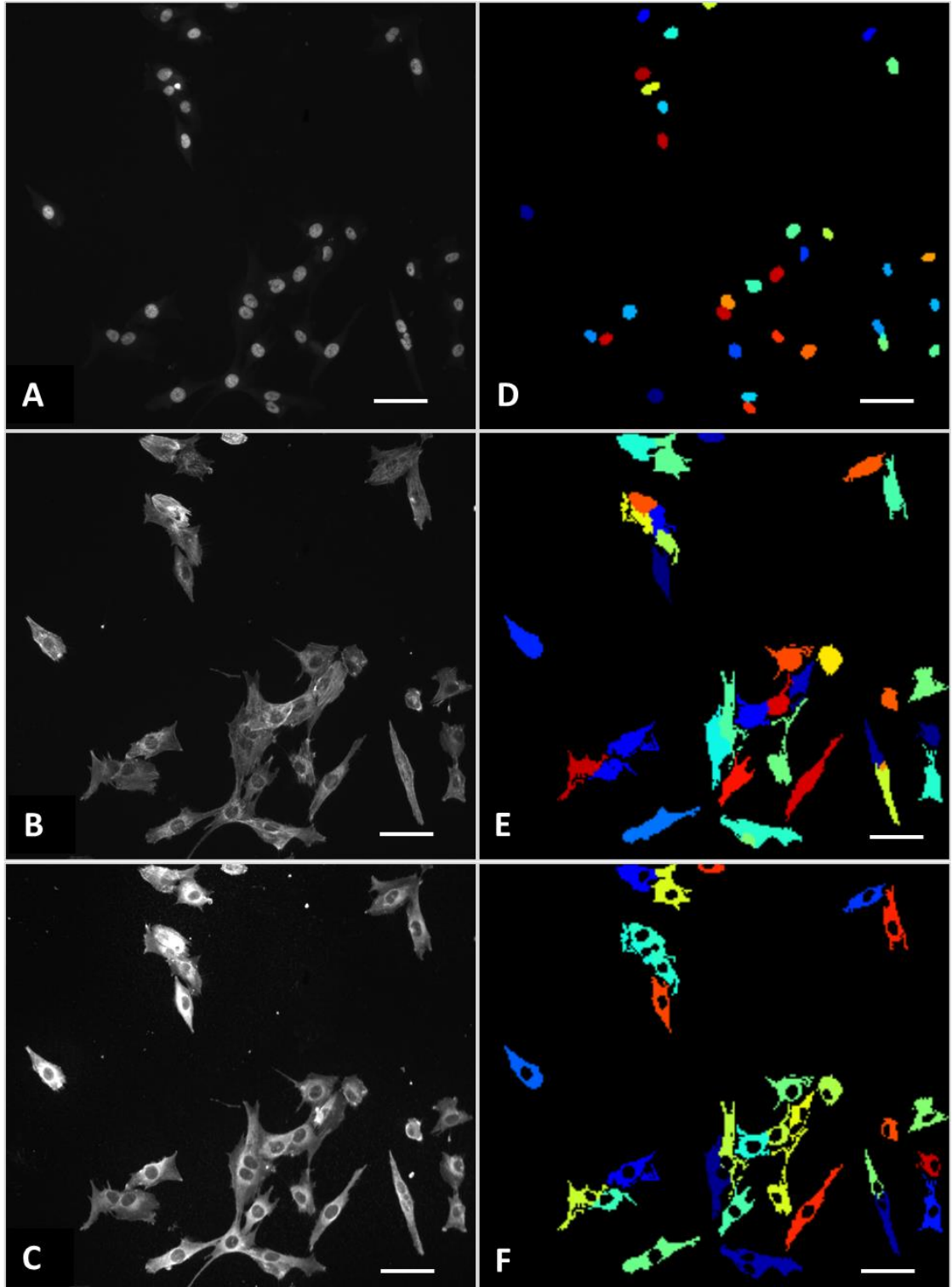


**Figure A.6.** Example of Cell Profiler image pipeline outputs. A) Input nuclei image. B) Input F-Actin image. C) MRTF to have cytoplasmic and nuclear intensity measured. D) Output nuclei mask. E) Output cell mask. F) Output cytoplasmic mask. All scale bars in white are 50 $\mu$ m.

The nuclear and cytoplasmic masks are laid over the original image and output grey intensities for their respective cell components.

## References

- Aguet, F., Van De Ville, D., & Unser, M. (2008). Model-based 2.5-D deconvolution for extended depth of field in brightfield microscopy. *IEEE Transactions on Image Processing*. <https://doi.org/10.1109/TIP.2008.924393>
- Ahmed, W. W., Wolfram, T., Goldyn, A. M., Bruellhoff, K., Rioja, B. A., Möller, M., Spatz, J. P., Saif, T. A., Groll, J., & Kemkemer, R. (2010). Myoblast morphology and organization on biochemically micro-patterned hydrogel coatings under cyclic mechanical strain. *Biomaterials*. <https://doi.org/10.1016/j.biomaterials.2009.09.047>
- Ali, M. S., Wang, X., & Lacerda, C. M. R. (2019). The effect of physiological stretch and the valvular endothelium on mitral valve proteomes. *Experimental Biology and Medicine*. <https://doi.org/10.1177/1535370219829006>
- Aliabadi, H. M., Mahmud, A., Sharifabadi, A. D., & Lavasanifar, A. (2005). Micelles of methoxy poly(ethylene oxide)-b-poly( $\epsilon$ -caprolactone) as vehicles for the solubilization and controlled delivery of cyclosporine A. *Journal of Controlled Release*. <https://doi.org/10.1016/j.jconrel.2005.02.015>
- Androsch, R., Di Lorenzo, M. L., Schick, C., & Wunderlich, B. (2010). Mesophases in polyethylene, polypropylene, and poly(1-butene). In *Polymer*. <https://doi.org/10.1016/j.polymer.2010.07.033>
- Ankersen, J. (1999). Puncture resistance and tensile strength of skin simulants. *Proceedings of the Institution of Mechanical Engineers, Part H: Journal of Engineering in Medicine*. <https://doi.org/10.1243/0954411991535103>
- Antia, M., Baneyx, G., Kubow, K. E., & Vogel, V. (2008). Fibronectin in aging extracellular matrix fibrils is progressively unfolded by cells and elicits an enhanced rigidity response. *Faraday Discussions*. <https://doi.org/10.1039/b718714a>
- Ao, M., Brewer, B. M., Yang, L., Franco Coronel, O. E., Hayward, S. W., Webb, D. J., & Li, D. (2015). Stretching fibroblasts remodels fibronectin and alters cancer cell migration. *Scientific Reports*. <https://doi.org/10.1038/srep08334>
- Aronson, J., & McCarthy, J. G. (1994). Experimental and clinical experience with distraction osteogenesis. *Cleft Palate-Craniofacial Journal*. [https://doi.org/10.1597/1545-1569\(1994\)031<0473:EACEWD>2.3.CO;2](https://doi.org/10.1597/1545-1569(1994)031<0473:EACEWD>2.3.CO;2)
- Askari, M., Gabbay, J. S., Tahernia, A., O'Hara, C. M., Heller, J. B., Azari, K., Hollinger, J. O., & Bradley, J. P. (2006). Favorable morphologic change of preosteoblasts in a three-dimensional matrix with in vitro microdistraction. *Plastic and Reconstructive Surgery*. <https://doi.org/10.1097/01.prs.0000197085.72380.e3>

- ASTM. (2002). Standard Test Method for Tensile Properties of Thin Plastic Sheeting, ASTM D882-02. *American Society for Testing and Materials*.
- Averous, L., Moro, L., Dole, P., & Fringant, C. (2000). Properties of thermoplastic blends: Starch-polycaprolactone. *Polymer*. [https://doi.org/10.1016/S0032-3861\(99\)00636-9](https://doi.org/10.1016/S0032-3861(99)00636-9)
- Banes, A. J., Gilbert, J., Taylor, D., & Monbureau, O. (1985). A new vacuum-operated stress-providing instrument that applies static or variable duration cyclic tension or compression to cells in vitro. *Journal of Cell Science*.
- Baneyx, G., Baugh, L., & Vogel, V. (2002). Fibronectin extension and unfolding within cell matrix fibrils controlled by cytoskeletal tension. *Proceedings of the National Academy of Sciences of the United States of America*. <https://doi.org/10.1073/pnas.072650799>
- Bao, G., & Suresh, S. (2003). Cell and molecular mechanics of biological materials. In *Nature Materials*. <https://doi.org/10.1038/nmat1001>
- Bartczak, Z. (2005). Effect of chain entanglements on plastic deformation behavior of linear polyethylene. *Macromolecules*. <https://doi.org/10.1021/ma050815y>
- Beaupere, N., Soupremanien, U., & Zalewski, L. (2018). Nucleation triggering methods in supercooled phase change materials (PCM), a review. In *Thermochimica Acta*. <https://doi.org/10.1016/j.tca.2018.10.009>
- Beaupré, G. S., Stevens, S. S., & Carter, D. R. (2000). Mechanobiology in the development, maintenance, and degeneration of articular cartilage. *Journal of Rehabilitation Research and Development*.
- Bershadsky, A. D., Balaban, N. Q., & Geiger, B. (2003). Adhesion-Dependent Cell Mechanosensitivity. *Annual Review of Cell and Developmental Biology*. <https://doi.org/10.1146/annurev.cellbio.19.111301.153011>
- Bhatt, K. A., Chang, E. I., Warren, S. M., Lin, S. e., Bastidas, N., Ghali, S., Thibboneir, A., Capla, J. M., McCarthy, J. G., & Gurtner, G. C. (2007). Uniaxial Mechanical Strain: An In Vitro Correlate to Distraction Osteogenesis. *Journal of Surgical Research*. <https://doi.org/10.1016/j.jss.2007.01.023>
- Birch, J. G., & Samchukov, M. L. (2004). Use of the Ilizarov method to correct lower limb deformities in children and adolescents. In *The Journal of the American Academy of Orthopaedic Surgeons*. <https://doi.org/10.5435/00124635-200405000-00002>
- Birnie, D. P. (2001). Rational solvent selection strategies to combat striation formation during spin coating of thin films. *Journal of Materials Research*. <https://doi.org/10.1557/JMR.2001.0158>
- Birnie, D. P., Hau, S. K., Kamber, D. S., & Kaz, D. M. (2005). Effect of ramping-up

rate on film thickness for spin-on processing. *Journal of Materials Science: Materials in Electronics*. <https://doi.org/10.1007/s10854-005-4973-6>

Blaber, J., Adair, B. S., & Antoniou, A. (2015). Ncorr: Open-Source 2D DIC Matlab Software. *Experimental Mechanics*. <https://doi.org/10.1007/s11340-015-0009-1>

Boccafoschi, F., Bosetti, M., Gatti, S., & Cannas, M. (2007). Dynamic fibroblast cultures: response to mechanical stretching. *Cell Adhesion & Migration*, 1(3), 124–128.

Brown, R. A., Prajapati, R., McGrouther, D. A., Yannas, I. V., & Eastwood, M. (1998). Tensional homeostasis in dermal fibroblasts: Mechanical responses to mechanical loading in three-dimensional substrates. *Journal of Cellular Physiology*. [https://doi.org/10.1002/\(SICI\)1097-4652\(199806\)175:3<323::AID-JCP10>3.0.CO;2-6](https://doi.org/10.1002/(SICI)1097-4652(199806)175:3<323::AID-JCP10>3.0.CO;2-6)

Camelliti, P., Borg, T. K., & Kohl, P. (2005). Structural and functional characterisation of cardiac fibroblasts. In *Cardiovascular Research*. <https://doi.org/10.1016/j.cardiores.2004.08.020>

Chakraborty, S., Banerjee, S., Raina, M., & Haldar, S. (2019). Force-Directed “mechanointeractome” of Talin-Integrin. In *Biochemistry*. <https://doi.org/10.1021/acs.biochem.9b00442>

Chanet, S., & Martin, A. C. (2014). Mechanical force sensing in tissues. In *Progress in Molecular Biology and Translational Science*. <https://doi.org/10.1016/B978-0-12-394624-9.00013-0>

Chen, B., Co, C., & Ho, C. C. (2015). Cell shape dependent regulation of nuclear morphology. *Biomaterials*. <https://doi.org/10.1016/j.biomaterials.2015.07.017>

Chen, C. C., Hsieh, P. C. H., Wang, G. M., Chen, W. C., & Yeh, M. L. (2009). The influence of surface morphology and rigidity of the substrata on cell motility. *Materials Letters*. <https://doi.org/10.1016/j.matlet.2009.05.073>

Chen, Y., Pasapera, A. M., Koretsky, A. P., & Waterman, C. M. (2013). Orientation-specific responses to sustained uniaxial stretching in focal adhesion growth and turnover. *Proceedings of the National Academy of Sciences*, 110(26), E2352–E2361. <https://doi.org/10.1073/pnas.1221637110>

Choi, K. M., & Rogers, J. A. (2003). A photocurable poly(dimethylsiloxane) chemistry designed for soft lithographic molding and printing in the nanometer regime. *Journal of the American Chemical Society*. <https://doi.org/10.1021/ja029973k>

Cui, Y., Hameed, F. M., Yang, B., Lee, K., Pan, C. Q., Park, S., & Sheetz, M. (2015). Cyclic stretching of soft substrates induces spreading and growth. *Nature Communications*. <https://doi.org/10.1038/ncomms7333>

- Dalby, M. J., Gadegaard, N., Tare, R., Andar, A., Riehle, M. O., Herzyk, P., Wilkinson, C. D. W., & Oreffo, R. O. C. (2007). The control of human mesenchymal cell differentiation using nanoscale symmetry and disorder. *Nature Materials*. <https://doi.org/10.1038/nmat2013>
- Darby, I. A., Laverdet, B., Bonté, F., & Desmoulière, A. (2014). Fibroblasts and myofibroblasts in wound healing. In *Clinical, Cosmetic and Investigational Dermatology*. <https://doi.org/10.2147/CCID.S50046>
- Debelle, L., & Tamburro, A. M. (1999). Elastin: Molecular description and function. In *International Journal of Biochemistry and Cell Biology*. [https://doi.org/10.1016/S1357-2725\(98\)00098-3](https://doi.org/10.1016/S1357-2725(98)00098-3)
- Deguchi, S., Kudo, S., Matsui, T. S., Huang, W., & Sato, M. (2015). Piezoelectric actuator-based cell microstretch device with real-time imaging capability. *AIP Advances*. <https://doi.org/10.1063/1.4922220>
- Dekker, A., Reitsma, K., Beugeling, T., Bantjes, A., Feijen, J., & van Aken, W. G. (1991). Adhesion of endothelial cells and adsorption of serum proteins on gas plasma-treated polytetrafluoroethylene. *Biomaterials*. [https://doi.org/10.1016/0142-9612\(91\)90191-C](https://doi.org/10.1016/0142-9612(91)90191-C)
- Del Rio, A., Perez-Jimenez, R., Liu, R., Roca-Cusachs, P., Fernandez, J. M., & Sheetz, M. P. (2009). Stretching single talin rod molecules activates vinculin binding. *Science*. <https://doi.org/10.1126/science.1162912>
- Delvoye, P., Wiliquet, P., Levêque, J. L., Nusgens, B. V., & Lapière, C. M. (1991). Measurement of mechanical forces generated by skin fibroblasts embedded in a three-dimensional collagen gel. *Journal of Investigative Dermatology*. <https://doi.org/10.1111/1523-1747.ep12491651>
- Descot, A., Hoffmann, R., Shaposhnikov, D., Reschke, M., Ullrich, A., & Posern, G. (2009). Negative Regulation of the EGFR-MAPK Cascade by Actin-MAL-Mediated Mig6/Erff-1 Induction. *Molecular Cell*. <https://doi.org/10.1016/j.molcel.2009.07.015>
- Djasim, U. M., Mathot, B. J., Wolvius, E. B., van Neck, J. W., & van der Wal, K. G. H. (2009). Histomorphometric comparison between continuous and discontinuous distraction osteogenesis. *Journal of Cranio-Maxillofacial Surgery*. <https://doi.org/10.1016/j.jcms.2009.03.006>
- Djordjevic, I., Britcher, L. G., & Kumar, S. (2008). Morphological and surface compositional changes in poly(lactide-co-glycolide) tissue engineering scaffolds upon radio frequency glow discharge plasma treatment. *Applied Surface Science*. <https://doi.org/10.1016/j.apsusc.2007.07.199>
- Domke, J., & Radmacher, M. (1998). Measuring the elastic properties of thin polymer films with the atomic force microscope. *Langmuir*. <https://doi.org/10.1021/la9713006>

- Duling, R. R. (2008). Mechanical Characterization of Electrospun Polycaprolactone (PCL): A Potential Scaffold for Tissue Engineering. *Journal of Biomechanical Engineering*. <https://doi.org/10.1115/1.2838033>
- Dumbauld, D. W., Shin, H., Gallant, N. D., Michael, K. E., Radhakrishna, H., & García, A. J. (2010). Contractility modulates cell adhesion strengthening through focal adhesion kinase and assembly of vinculin-containing focal adhesions. *Journal of Cellular Physiology*. <https://doi.org/10.1002/jcp.22084>
- Eastwood, M., McGrouther, D. A., & Brown, R. A. (1998). Fibroblast responses to mechanical forces. *Proceedings of the Institution of Mechanical Engineers, Part H: Journal of Engineering in Medicine*, 212(2), 85–92. <https://doi.org/10.1243/0954411981533854>
- Eckert, C. E., Fan, R., Mikulis, B., Barron, M., Carruthers, C. A., Friebe, V. M., Vyavahare, N. R., & Sacks, M. S. (2013). On the biomechanical role of glycosaminoglycans in the aortic heart valve leaflet. *Acta Biomaterialia*. <https://doi.org/10.1016/j.actbio.2012.09.031>
- Emslie, A. G., Bonner, F. T., & Peck, L. G. (1958). Flow of a viscous liquid on a rotating disk. *Journal of Applied Physics*. <https://doi.org/10.1063/1.1723300>
- Engelberg, I., & Kohn, J. (1991). Physico-mechanical properties of degradable polymers used in medical applications: A comparative study. *Biomaterials*. [https://doi.org/10.1016/0142-9612\(91\)90037-B](https://doi.org/10.1016/0142-9612(91)90037-B)
- Engler, A. J., Sen, S., Sweeney, H. L., & Discher, D. E. (2006). Matrix Elasticity Directs Stem Cell Lineage Specification. *Cell*. <https://doi.org/10.1016/j.cell.2006.06.044>
- Esnault, C., Stewart, A., Gualdrini, F., East, P., Horswell, S., Matthews, N., & Treisman, R. (2014). Rho-actin signaling to the MRTF coactivators dominates the immediate transcriptional response to serum in fibroblasts. *Genes and Development*, 28(9), 943–958. <https://doi.org/10.1101/gad.239327.114>
- Evans, E., & Yeung, A. (1989). Apparent viscosity and cortical tension of blood granulocytes determined by micropipet aspiration. *Biophysical Journal*. [https://doi.org/10.1016/S0006-3495\(89\)82660-8](https://doi.org/10.1016/S0006-3495(89)82660-8)
- Falleroni, F., Torre, V., & Cojoc, D. (2018). Cell mechanotransduction with piconewton forces applied by optical tweezers. *Frontiers in Cellular Neuroscience*. <https://doi.org/10.3389/fncel.2018.00130>
- Farhadieh, R. D., Gianoutsos, M. P., Dickinson, R., & Walsh, W. R. (2000). Effect of distraction rate on biomechanical, mineralization, and histologic properties of an ovine mandible model. *Plastic and Reconstructive Surgery*. <https://doi.org/10.1097/00006534-200003000-00010>
- Feng, Z., Matsumoto, T., Nomura, Y., & Nakamura, T. (2005). An electro-tensile bioreactor for 3-D culturing of cardiomyocytes. *IEEE Engineering in Medicine*

and *Biology Magazine*. <https://doi.org/10.1109/MEMB.2005.1463399>

- Flanagan, L. A., Ju, Y. E., Marg, B., Osterfield, M., & Janmey, P. A. (2002). Neurite branching on deformable substrates. *NeuroReport*. <https://doi.org/10.1097/00001756-200212200-00007>
- Franchi, M., Raspanti, M., Dell'Orbo, C., Quaranta, M., De Pasquale, V., Ottani, V., & Ruggeri, A. (2008). Different crimp patterns in collagen fibrils relate to the subfibrillar arrangement. *Connective Tissue Research*. <https://doi.org/10.1080/03008200801913635>
- Friedrich, O., Merten, A. L., Schneiderreit, D., Guo, Y., Schürmann, S., & Martinac, B. (2019). Stretch in focus: 2D inplane cell stretch systems for studies of cardiac mechano-signaling. In *Frontiers in Bioengineering and Biotechnology*. <https://doi.org/10.3389/fbioe.2019.00055>
- Fulda, S., Gorman, A. M., Hori, O., & Samali, A. (2010). Cellular stress responses: Cell survival and cell death. In *International Journal of Cell Biology*. <https://doi.org/10.1155/2010/214074>
- Gadhari, N., Charnley, M., Marelli, M., Brugger, J., & Chiquet, M. (2013). Cell shape-dependent early responses of fibroblasts to cyclic strain. *Biochimica et Biophysica Acta - Molecular Cell Research*. <https://doi.org/10.1016/j.bbamcr.2013.10.012>
- Gallagher, A. J., Ní Anniadh, A., Bruyere, K., Otténio, M., Xie, H., & Gilchrist, M. D. (2012). Dynamic tensile properties of human skin. *2012 IRCOBI Conference Proceedings - International Research Council on the Biomechanics of Injury*.
- Gathercole, L. J., & Keller, A. (1991). Crimp Morphology in the Fibre-Forming Collagens. *Matrix*. [https://doi.org/10.1016/S0934-8832\(11\)80161-7](https://doi.org/10.1016/S0934-8832(11)80161-7)
- Geiger, B., Spatz, J. P., & Bershadsky, A. D. (2009). Environmental sensing through focal adhesions. In *Nature Reviews Molecular Cell Biology*. <https://doi.org/10.1038/nrm2593>
- Gelse, K., Pöschl, E., & Aigner, T. (2003). Collagens - Structure, function, and biosynthesis. *Advanced Drug Delivery Reviews*. <https://doi.org/10.1016/j.addr.2003.08.002>
- Goldyn, A. M., Rioja, B. A., Spatz, J. P., Ballestrem, C., & Kemkemer, R. (2009). Force-induced cell polarisation is linked to RhoA-driven microtubule-independent focal-adhesion sliding. *Journal of Cell Science*. <https://doi.org/10.1242/jcs.054866>
- Goth, W., Lesicko, J., Sacks, M. S., & Tunnell, J. W. (2016). Optical-Based Analysis of Soft Tissue Structures. *Annual Review of Biomedical Engineering*. <https://doi.org/10.1146/annurev-bioeng-071114-040625>

- Grashoff, C., Hoffman, B. D., Brenner, M. D., Zhou, R., Parsons, M., Yang, M. T., McLean, M. A., Sligar, S. G., Chen, C. S., Ha, T., & Schwartz, M. A. (2010). Measuring mechanical tension across vinculin reveals regulation of focal adhesion dynamics. *Nature*. <https://doi.org/10.1038/nature09198>
- Grotendorst, G. R., Rahmanie, H., & Duncan, M. R. (2004). Combinatorial signaling pathways determine fibroblast proliferation and myofibroblast differentiation. *The FASEB Journal*. <https://doi.org/10.1096/fj.03-0699com>
- GROTENDORST, G. R., RAHMANIE, H., & DUNCAN, M. R. (2004). Combinatorial signaling pathways determine fibroblast proliferation and myofibroblast differentiation. *The FASEB Journal*. <https://doi.org/10.1096/fj.03-0699com>
- Gualdrini, F., Esnault, C., Horswell, S., Stewart, A., Matthews, N., & Treisman, R. (2016). SRF Co-factors Control the Balance between Cell Proliferation and Contractility. *Molecular Cell*. <https://doi.org/10.1016/j.molcel.2016.10.016>
- Gupta, V., Werdenberg, J. A., Lawrence, B. D., Mendez, J. S., Stephens, E. H., & Grande-Allen, K. J. (2008). Reversible secretion of glycosaminoglycans and proteoglycans by cyclically stretched valvular cells in 3D culture. *Annals of Biomedical Engineering*. <https://doi.org/10.1007/s10439-008-9501-4>
- Haase, K., MacAdangdang, J. K. L., Edrington, C. H., Cuerrier, C. M., Hadjiantoniou, S., Harden, J. L., Skerjanc, I. S., & Pelling, A. E. (2016). Extracellular Forces Cause the Nucleus to Deform in a Highly Controlled Anisotropic Manner. *Scientific Reports*, 6. <https://doi.org/10.1038/srep21300>
- Hall, T. J., Bilgen, M., Insana, M. F., & Krouskop, T. A. (1997). Phantom materials for elastography. *IEEE Transactions on Ultrasonics, Ferroelectrics, and Frequency Control*. <https://doi.org/10.1109/58.656639>
- Hamilton, B. D., Ha, J. M., Hillmyer, M. A., & Ward, M. D. (2012). Manipulating crystal growth and polymorphism by confinement in nanoscale crystallization chambers. *Accounts of Chemical Research*. <https://doi.org/10.1021/ar200147v>
- Haralick, R. M. (1973). Glossary and index to remotely sensed image pattern recognition concepts. *Pattern Recognition*. [https://doi.org/10.1016/0031-3203\(73\)90029-0](https://doi.org/10.1016/0031-3203(73)90029-0)
- Hardingham, T., Tew, S., & Murdoch, A. (1999). Tissue engineering: chondrocytes and cartilage. *Biophysical Journal*. <https://doi.org/10.1186/ar561>
- Haston, W. S., Shields, J. M., & Wilkinson, P. C. (1983). The orientation of fibroblasts and neutrophils on elastic substrata. *Experimental Cell Research*. [https://doi.org/10.1016/0014-4827\(83\)90330-0](https://doi.org/10.1016/0014-4827(83)90330-0)
- Hinz, B. (2003). -Smooth Muscle Actin Is Crucial for Focal Adhesion Maturation in Myofibroblasts. *Molecular Biology of the Cell*, 14(6), 2508–2519.

<https://doi.org/10.1091/mbc.E02-11-0729>

- Hinz, B. (2004). Myofibroblast Development Is Characterized by Specific Cell-Cell Adherens Junctions. *Molecular Biology of the Cell*, 15(9), 4310–4320. <https://doi.org/10.1091/mbc.E04-05-0386>
- Hinz, Boris. (2007). Formation and function of the myofibroblast during tissue repair. In *Journal of Investigative Dermatology* (Vol. 127, Issue 3, pp. 526–537). <https://doi.org/10.1038/sj.jid.5700613>
- Hiss, R., Hobeika, S., Lynn, C., & Strobl, G. (1999). Network stretching, slip processes, and fragmentation of crystallites during uniaxial drawing of polyethylene and related copolymers. A comparative study. *Macromolecules*. <https://doi.org/10.1021/ma981776b>
- Htay, A. S., Teoh, S. H., & Hutmacher, D. W. (2004). Development of perforated microthin poly(E-caprolactone) films as matrices for membrane tissue engineering. *Journal of Biomaterials Science, Polymer Edition*. <https://doi.org/10.1163/156856204323046933>
- Huang, Y., & Nguyen, N.-T. (2013). A polymeric cell stretching device for real-time imaging with optical microscopy. *Biomedical Microdevices*, 15(6), 1043–1054. <https://doi.org/10.1007/s10544-013-9796-2>
- Humphrey, J. D., Dufresne, E. R., & Schwartz, M. A. (2014). Mechanotransduction and extracellular matrix homeostasis. In *Nature Reviews Molecular Cell Biology* (Vol. 15, Issue 12, pp. 802–812). <https://doi.org/10.1038/nrm3896>
- Hyde, J., MacNicol, M., Odle, A., & Garcia-Rill, E. (2014). The use of three-dimensional printing to produce in vitro slice chambers. *Journal of Neuroscience Methods*. <https://doi.org/10.1016/j.jneumeth.2014.09.012>
- Hyun, J., Chen, J., Setton, L. A., & Chilkoti, A. (2006). Patterning cells in highly deformable microstructures: Effect of plastic deformation of substrate on cellular phenotype and gene expression. *Biomaterials*, 27(8), 1444–1451. <https://doi.org/10.1016/j.biomaterials.2005.08.018>
- Ippolito, E., Peretti, G., & Bellocchi, M. (2011). HISTOLOGY AND ULTRASTRUCTURE OF ARTERIES, VEINS, AND PERIPHERAL NERVES DURING LIMB LENGTHENING. *Journal of Pediatric Orthopaedics*. <https://doi.org/10.1097/01241398-199505000-00028>
- Izquierdo, R., Garcia-Giralt, N., Rodriguez, M. T., Cáceres, E., García, S. J., Gómez Ribelles, J. L., Monleón, M., Monllau, J. C., & Suay, J. (2008). Biodegradable PCL scaffolds with an interconnected spherical pore network for tissue engineering. *Journal of Biomedical Materials Research - Part A*. <https://doi.org/10.1002/jbm.a.31396>
- Jabbari-Farouji, S., Rottler, J., Lame, O., Makke, A., Perez, M., & Barrat, J. L. (2015). Plastic deformation mechanisms of semicrystalline and amorphous

polymers. *ACS Macro Letters*. <https://doi.org/10.1021/mz500754b>

- Jean, R. P., Gray, D. S., Spector, A. A., & Chen, C. S. (2004). Characterization of the nuclear deformation caused by changes in endothelial cell shape. *Journal of Biomechanical Engineering*. <https://doi.org/10.1115/1.1800559>
- Ji, H., Tang, H., Lin, H., Mao, J., Gao, L., Liu, J., & Wu, T. (2014). Rho/Rock cross-talks with transforming growth factor- $\beta$ /Smad pathway participates in lung fibroblast-myofibroblast differentiation. *Biomedical Reports*. <https://doi.org/10.3892/br.2014.323>
- Jiang, X., Zou, S., Ye, B., Zhu, S., Liu, Y., & Hu, J. (2010). bFGF-Modified BMSCs enhance bone regeneration following distraction osteogenesis in rabbits. *Bone*. <https://doi.org/10.1016/j.bone.2009.12.017>
- Jones, B. F., Wall, M. E., Carroll, R. L., Washburn, S., & Banes, A. J. (2005). Ligament cells stretch-adapted on a microgrooved substrate increase intercellular communication in response to a mechanical stimulus. *Journal of Biomechanics*. <https://doi.org/10.1016/j.jbiomech.2004.07.027>
- Jordan, C. J., Goldstein, R. Y., McLaurin, T. M., & Grant, A. (2013). The evolution of the Ilizarov technique: part 1: the history of limb lengthening. *Bulletin of the Hospital for Joint Disease* (2013).
- Kamal, T., Shin, T. J., & Park, S. Y. (2012). Uniaxial tensile deformation of poly( $\epsilon$ -caprolactone) studied with SAXS and WAXS techniques using synchrotron radiation. *Macromolecules*. <https://doi.org/10.1021/ma301714f>
- Kamble, H., Barton, M. J., Jun, M., Park, S., & Nguyen, N. T. (2016). Cell stretching devices as research tools: Engineering and biological considerations. In *Lab on a Chip*. <https://doi.org/10.1039/c6lc00607h>
- Kamotani, Y., Bersano-Begey, T., Kato, N., Tung, Y. C., Huh, D., Song, J. W., & Takayama, S. (2008). Individually programmable cell stretching microwell arrays actuated by a Braille display. *Biomaterials*. <https://doi.org/10.1016/j.biomaterials.2008.02.019>
- Karaharju-Suvanto, T., Peltonen, J., Kahri, A., & Karaharju, E. O. (1992). Distraction osteogenesis of the mandible. An experimental study on sheep. *International Journal of Oral and Maxillofacial Surgery*. [https://doi.org/10.1016/S0901-5027\(05\)80547-8](https://doi.org/10.1016/S0901-5027(05)80547-8)
- Kelly, P. A. (2015). Solid Mechanics Part I: An Introduction to Solid Mechanics. In *Solid Mechanics part 1*.
- Keselowsky, B. G., Collard, D. M., & García, A. J. (2005). Integrin binding specificity regulates biomaterial surface chemistry effects on cell differentiation. *Proceedings of the National Academy of Sciences of the United States of America*. <https://doi.org/10.1073/pnas.0407356102>

- Kessler, D., Dethlefsen, S., Haase, I., Plomann, M., Hirche, F., Krieg, T., & Eckes, B. (2001). Fibroblasts in Mechanically Stressed Collagen Lattices Assume a “Synthetic” Phenotype. *Journal of Biological Chemistry*, 276(39), 36575–36585. <https://doi.org/10.1074/jbc.M101602200>
- Khatau, S. B., Hale, C. M., Stewart-Hutchinson, P. J., Patel, M. S., Stewart, C. L., Searson, P. C., Hodzic, D., & Wirtz, D. (2009). A perinuclear actin cap regulates nuclear shape. *Proceedings of the National Academy of Sciences of the United States of America*. <https://doi.org/10.1073/pnas.0908686106>
- Kim, E. H., Oh, N., Jun, M., Ko, K., & Park, S. (2015). Effect of cyclic stretching on cell shape and division. *Biochip Journal*, 9(4), 306–312. <https://doi.org/10.1007/s13206-015-9406-x>
- Kim, H. N., Kang, D. H., Kim, M. S., Jiao, A., Kim, D. H., & Suh, K. Y. (2012). Patterning methods for polymers in cell and tissue engineering. In *Annals of Biomedical Engineering*. <https://doi.org/10.1007/s10439-012-0510-y>
- Kim, W., Kim, J., Park, H. S., & Jeon, J. S. (2018). Development of microfluidic stretch system for studying recovery of damaged skeletal muscle cells. *Micromachines*. <https://doi.org/10.3390/mi9120671>
- King, G. J., Liu, Z. J., Wang, L. L., Chiu, I. Y., Whelan, M. F., & Huang, G. J. (2003). Effect of distraction rate and consolidation period on bone density following mandibular osteodistraction in rats. *Archives of Oral Biology*. [https://doi.org/10.1016/S0003-9969\(03\)00004-9](https://doi.org/10.1016/S0003-9969(03)00004-9)
- Klingberg, F., Chow, M. L., Koehler, A., Boo, S., Buscemi, L., Quinn, T. M., Costell, M., Alman, B. A., Genot, E., & Hinz, B. (2014). Prestress in the extracellular matrix sensitizes latent TGF- $\beta$ 1 for activation. *Journal of Cell Biology*, 207(2), 283–297. <https://doi.org/10.1083/jcb.201402006>
- Kollmannsberger, P., Bidan, C. M., Dunlop, J. W. C., Fratzl, P., & Vogel, V. (2018). Tensile forces drive a reversible fibroblast-to-myofibroblast transition during tissue growth in engineered clefts. *Science Advances*. <https://doi.org/10.1126/sciadv.aao4881>
- Kolodney, M. S., & Wysolmerski, R. B. (1992). Isometric contraction by fibroblasts and endothelial cells in tissue culture: A quantitative study. *Journal of Cell Biology*. <https://doi.org/10.1083/jcb.117.1.73>
- Kubow, K. E., Vukmirovic, R., Zhe, L., Klotzsch, E., Smith, M. L., Gourdon, D., Luna, S., & Vogel, V. (2015). Mechanical forces regulate the interactions of fibronectin and collagen i in extracellular matrix. *Nature Communications*. <https://doi.org/10.1038/ncomms9026>
- Kumar, D., Cain, S. A., & Bosworth, L. A. (2019). Effect of topography and physical stimulus on hMSC phenotype using a 3D in vitro model. In *Nanomaterials*. <https://doi.org/10.3390/nano9040522>

- Kumar, G., & Narayan, B. (2014). The tension-stress effect on the genesis and growth of tissues: Part II. The influence of the rate and frequency of distraction. In *Classic Papers in Orthopaedics*. [https://doi.org/10.1007/978-1-4471-5451-8\\_137](https://doi.org/10.1007/978-1-4471-5451-8_137)
- Latif, N., Sarathchandra, P., Chester, A. H., & Yacoub, M. H. (2015). Expression of smoothmuscle cellmarkers and co-activators in calcified aortic valves. *European Heart Journal*. <https://doi.org/10.1093/eurheartj/eh547>
- Leach, J. B., Brown, X. Q., Jacot, J. G., Dimilla, P. A., & Wong, J. Y. (2007). Neurite outgrowth and branching of PC12 cells on very soft substrates sharply decreases below a threshold of substrate rigidity. *Journal of Neural Engineering*. <https://doi.org/10.1088/1741-2560/4/2/003>
- Lee, D. Y., Han, T. R., Choi, I. H., & Lee, C. K. (2018). Changes of Somatosensory Evoked Potentials in Bone Lengthening: An Experimental Study on Rabbits' Tibiae. *Journal of the Korean Orthopaedic Association*. <https://doi.org/10.4055/jkoa.1990.25.4.1239>
- Lei, Y., & Ferdous, Z. (2016). Design considerations and challenges for mechanical stretch bioreactors in tissue engineering. *Biotechnology Progress*. <https://doi.org/10.1002/btpr.2256>
- Levental, I., Georges, P. C., & Janmey, P. A. (2007). Soft biological materials and their impact on cell function. In *Soft Matter*. <https://doi.org/10.1039/b610522j>
- Li, M., Liu, R., Gao, J., Lan, X., Wang, Z., Gao, Q., & Zeng, P. (2018). Ilizarov technique for treatment of distal radius deformity and bone defect after trauma. [Chinese]. *Zhongguo Xiu Fu Chong Jian Wai Ke Za Zhi = Zhongguo Xiufu Chongjian Waikexue Zazhi = Chinese Journal of Reparative and Reconstructive Surgery*. <https://doi.org/http://dx.doi.org/10.7507/1002-1892.201804088>
- Li, W. J., Cooper, J. A., Mauck, R. L., & Tuan, R. S. (2006). Fabrication and characterization of six electrospun poly( $\alpha$ -hydroxy ester)-based fibrous scaffolds for tissue engineering applications. *Acta Biomaterialia*. <https://doi.org/10.1016/j.actbio.2006.02.005>
- Liu, C., Baek, S., Kim, J., Vasko, E., Pyne, R., & Chan, C. (2014). Effect of static pre-stretch induced surface anisotropy on orientation of mesenchymal stem cells. *Cellular and Molecular Bioengineering*. <https://doi.org/10.1007/s12195-013-0300-0>
- Loesberg, W. A., Walboomers, X. F., Van Loon, J. J. W. A., & Jansen, J. A. (2005). The effect of combined cyclic mechanical stretching and microgrooved surface topography on the behavior of fibroblasts. *Journal of Biomedical Materials Research - Part A*. <https://doi.org/10.1002/jbm.a.30480>
- Löfstedt, T., Brynolfsson, P., Asklund, T., Nyholm, T., & Garpebring, A. (2019). Gray-level invariant Haralick texture features. *PLoS ONE*.

<https://doi.org/10.1371/journal.pone.0212110>

- Love, B. (2017). Property Assessments of Tissues. In *Biomaterials*.  
<https://doi.org/10.1016/b978-0-12-809478-5.00005-5>
- Lovekamp, J. J., Simionescu, D. T., Mercuri, J. J., Zubiato, B., Sacks, M. S., & Vyavahare, N. R. (2006). Stability and function of glycosaminoglycans in porcine bioprosthetic heart valves. *Biomaterials*.  
<https://doi.org/10.1016/j.biomaterials.2005.08.003>
- Loverde, J. R., Tolentino, R. E., & Pfister, B. J. (2011). Axon stretch growth: The mechanotransduction of neuronal growth. *Journal of Visualized Experiments*.  
<https://doi.org/10.3791/2753>
- Luo, D. Y., Wazir, R., Du, C., Tian, Y., Yue, X., Wei, T. Q., & Wang, K. J. (2015). Magnitude-dependent proliferation and contractility modulation of human bladder smooth muscle cells under physiological stretch. *World Journal of Urology*. <https://doi.org/10.1007/s00345-015-1509-4>
- Maeda, M., Hasegawa, H., Hyodo, T., Ito, S., Asano, E., Yuang, H., Funasaka, K., Shimokata, K., Hasegawa, Y., Hamaguchi, M., & Senga, T. (2011). ARHGAP18, a GTPase-activating protein for RhoA, controls cell shape, spreading, and motility. *Molecular Biology of the Cell*, 22(20), 3840–3852.  
<https://doi.org/10.1091/mbc.E11-04-0364>
- Makke, A., Lame, O., Perez, M., & Barrat, J. L. (2012). Influence of tie and loop molecules on the mechanical properties of lamellar block copolymers. *Macromolecules*. <https://doi.org/10.1021/ma301286y>
- Maninová, M., Klímová, Z., Parsons, J. T., Weber, M. J., Iwanicki, M. P., & Vomastek, T. (2013). The reorientation of cell nucleus promotes the establishment of front-rear polarity in migrating fibroblasts. *Journal of Molecular Biology*. <https://doi.org/10.1016/j.jmb.2013.02.034>
- Maniotis, A. J., Chen, C. S., & Ingber, D. E. (1997). Demonstration of mechanical connections between integrins, cytoskeletal filaments, and nucleoplasm that stabilize nuclear structure. *Proceedings of the National Academy of Sciences of the United States of America*. <https://doi.org/10.1073/pnas.94.3.849>
- Masoumi, N., Howell, M. C., Johnson, K. L., Niesslein, M. J., Gerber, G., & Engelmayer, G. C. (2014). Design and testing of a cyclic stretch and flexure bioreactor for evaluating engineered heart valve tissues based on poly(glycerol sebacate) scaffolds. *Proceedings of the Institution of Mechanical Engineers, Part H: Journal of Engineering in Medicine*.  
<https://doi.org/10.1177/0954411914534837>
- Mathur, A. B., Collinsworth, A. M., Reichert, W. M., Kraus, W. E., & Truskey, G. A. (2001). Endothelial, cardiac muscle and skeletal muscle exhibit different viscous and elastic properties as determined by atomic force microscopy. *Journal of Biomechanics*. [https://doi.org/10.1016/S0021-9290\(01\)00149-X](https://doi.org/10.1016/S0021-9290(01)00149-X)

- McQuin, C., Goodman, A., Chernyshev, V., Kametsky, L., Cimini, B. A., Karhohs, K. W., Doan, M., Ding, L., Rafelski, S. M., Thirstrup, D., Wiegraabe, W., Singh, S., Becker, T., Caicedo, J. C., & Carpenter, A. E. (2018). CellProfiler 3.0: Next-generation image processing for biology. *PLoS Biology*. <https://doi.org/10.1371/journal.pbio.2005970>
- Meijer, G. J., De Bruijn, J. D., Koole, R., & Van Blitterswijk, C. A. (2007). Cell-based bone tissue engineering. *PLoS Medicine*. <https://doi.org/10.1371/journal.pmed.0040009>
- Mellbring, O., Øiseth, S. K., Krozer, A., Lausmaa, J., & Hjertberg, T. (2001). Spin coating and characterization of thin high-density polyethylene films. *Macromolecules*. <https://doi.org/10.1021/ma000094x>
- Meng, F., Suchyna, T. M., Lazakovitch, E., Gronostajski, R. M., & Sachs, F. (2011). Real time FRET based detection of mechanical stress in cytoskeletal and extracellular matrix proteins. *Cellular and Molecular Bioengineering*. <https://doi.org/10.1007/s12195-010-0140-0>
- Meredith, D. O., Eschbach, L., Riehle, M. O., Curtis, A. S. G., & Richards, R. G. (2007). Microtopography of metal surfaces influence fibroblast growth by modifying cell shape, cytoskeleton, and adhesion. *Journal of Orthopaedic Research*, 25(11), 1523–1533. <https://doi.org/10.1002/jor.20430>
- Mescher, A. (2010). Junqueira's Basic Histology, 12th Edition. In *Neurosci Lett*.
- Metzler, S. A., Digesu, C. S., Howard, J. I., To, S. D. F., & Warnock, J. N. (2012). Live en face imaging of aortic valve leaflets under mechanical stress. *Biomechanics and Modeling in Mechanobiology*. <https://doi.org/10.1007/s10237-011-0315-1>
- Meyerhofer, D. (1978). Characteristics of resist films produced by spinning. *Journal of Applied Physics*. <https://doi.org/10.1063/1.325357>
- Mih, J. D., & Tschumperlin, D. J. (2008). Lung Fibroblast Behavior Is Tuned by Substrate Stiffness. *Proceedings of the American Thoracic Society*.
- Milisavljević, J., Petrović, E., Ćirić, I., Mančić, M., Marković, D., & Dordević, M. (2012). Tensile testing for different types of polymers. *29th DANUBIA-ADRIA Symposium on Advances in Experimental Mechanics, DAS 2012*.
- Mirani, R. D., Pratt, J., Iyer, P., & Madhally, S. V. (2009). The stress relaxation characteristics of composite matrices etched to produce nanoscale surface features. *Biomaterials*. <https://doi.org/10.1016/j.biomaterials.2008.10.023>
- Mithieux, S. M., & Weiss, A. S. (2005). Elastin. *Advances in Protein Chemistry*. [https://doi.org/10.1016/S0065-3233\(05\)70013-9](https://doi.org/10.1016/S0065-3233(05)70013-9)
- Montel, L., Sotiropoulos, A., & Hénon, S. (2019). The nature and intensity of

mechanical stimulation drive different dynamics of MRTF-A nuclear redistribution after actin remodeling in myoblasts. *PLoS ONE*.  
<https://doi.org/10.1371/journal.pone.0214385>

- Moore, S. W., Roca-Cusachs, P., & Sheetz, M. P. (2010). Stretchy Proteins on Stretchy Substrates: The Important Elements of Integrin-Mediated Rigidity Sensing. *Developmental Cell*, *19*(2), 194–206.  
<https://doi.org/10.1016/j.devcel.2010.07.018>
- Mouilleron, S., Langer, C. A., Guettler, S., McDonald, N. Q., & Treisman, R. (2011). Structure of a pentavalent G-actin•MRTF-A complex reveals how G-actin controls nucleocytoplasmic shuttling of a transcriptional coactivator. *Science Signaling*, *4*(177). <https://doi.org/10.1126/scisignal.2001750>
- Moulin, V., Castilloux, G., Jean, A., Garrel, D. R., Auger, F. A., & Germain, L. (1996). In vitro models to study wound healing fibroblasts. *Burns*.  
[https://doi.org/10.1016/0305-4179\(95\)00167-0](https://doi.org/10.1016/0305-4179(95)00167-0)
- Naemi, R., Behforootan, S., Chatzistergos, P., & Chockalingam, N. (2016). Viscoelasticity in Foot-Ground Interaction. In *Viscoelastic and Viscoplastic Materials*. <https://doi.org/10.5772/64170>
- Nagase, H., Visse, R., & Murphy, G. (2006). Structure and function of matrix metalloproteinases and TIMPs. In *Cardiovascular Research*.  
<https://doi.org/10.1016/j.cardiores.2005.12.002>
- Nagayama, K., Yahiro, Y., & Matsumoto, T. (2011). Stress fibers stabilize the position of intranuclear DNA through mechanical connection with the nucleus in vascular smooth muscle cells. *FEBS Letters*.  
<https://doi.org/10.1016/j.febslet.2011.11.006>
- Natu, S. S., Ali, I., Alam, S., Giri, K. Y., Agarwal, A., & Kulkarni, V. A. (2014). The biology of distraction osteogenesis for correction of mandibular and craniomaxillofacial defects: A review. *Dental Research Journal*.
- Neidlinger-Wilke, C., Wilke, H. J., & Claes, L. (1994). Cyclic stretching of human osteoblasts affects proliferation and metabolism: a new experimental method and its application. *Journal of Orthopaedic Research : Official Publication of the Orthopaedic Research Society*, *12*(1), 70–78.
- Nemir, S., & West, J. L. (2010). Synthetic materials in the study of cell response to substrate rigidity. *Annals of Biomedical Engineering*.  
<https://doi.org/10.1007/s10439-009-9811-1>
- Niemeyer, F., Claes, L., Ignatius, A., Meyers, N., & Simon, U. (2018). Simulating lateral distraction osteogenesis. *PLoS ONE*.  
<https://doi.org/10.1371/journal.pone.0194500>
- Oakley, C., Jaeger, N. A. F., & Brunette, D. M. (1997). Sensitivity of fibroblasts and their cytoskeletons to substratum topographies: Topographic guidance and

topographic compensation by micromachined grooves of different dimensions. *Experimental Cell Research*. <https://doi.org/10.1006/excr.1997.3625>

- Olson, E. N., & Nordheim, A. (2010). Linking actin dynamics and gene transcription to drive cellular motile functions. In *Nature Reviews Molecular Cell Biology* (Vol. 11, Issue 5, pp. 353–365). <https://doi.org/10.1038/nrm2890>
- Panayiotou, R., Miralles, F., Pawlowski, R., Diring, J., Flynn, H. R., Skehel, M., & Treisman, R. (2016). Phosphorylation acts positively and negatively to regulate MRTF-A subcellular localisation and activity. *ELife*, 5(JUN2016). <https://doi.org/10.7554/eLife.15460>
- Park, A., & Cima, L. G. (1996). In vitro cell response to differences in poly-L-lactide crystallinity. *Journal of Biomedical Materials Research*. <https://doi.org/10.1002/jbm.1996.820310103>
- Park, J. Y., & McKenna, G. B. (2000). Size and confinement effects on the glass transition behavior of polystyrene/o-terphenyl polymer solutions. *Physical Review B - Condensed Matter and Materials Physics*. <https://doi.org/10.1103/PhysRevB.61.6667>
- Patel, B., Gingras, A. R., Bobkov, A. A., Fujimoto, L. M., Zhang, M., Liddington, R. C., Mazzeo, D., Emsley, J., Roberts, G. C. K., Barsukov, I. L., & Critchley, D. R. (2006). The activity of the vinculin binding sites in talin is influenced by the stability of the helical bundles that make up the talin rod. *Journal of Biological Chemistry*. <https://doi.org/10.1074/jbc.M508058200>
- Pawlowski, R., Rajakylä, E. K., Vartiainen, M. K., & Treisman, R. (2010). An actin-regulated importin  $\alpha/\beta$ -dependent extended bipartite NLS directs nuclear import of MRTF-A. *EMBO Journal*, 29(20), 3448–3458. <https://doi.org/10.1038/emboj.2010.216>
- Payne, T., Mitchell, S., Bibb, R., & Waters, M. (2014). Initial validation of a relaxed human soft tissue simulant for sports impact surrogates. *Procedia Engineering*. <https://doi.org/10.1016/j.proeng.2014.06.092>
- Peters, A. S., Brunner, G., Krieg, T., & Eckes, B. (2014). Cyclic mechanical strain induces TGF $\beta$ 1-signalling in dermal fibroblasts embedded in a 3D collagen lattice. *Archives of Dermatological Research*, 307(2), 191–197. <https://doi.org/10.1007/s00403-014-1514-2>
- Petruska, J. A., & Hodge, A. J. (2006). A SUBUNIT MODEL FOR THE TROPOCOLLAGEN MACROMOLECULE. *Proceedings of the National Academy of Sciences*. <https://doi.org/10.1073/pnas.51.5.871>
- Pot, S. A., Liliensiek, S. J., Myrna, K. E., Bentley, E., Jester, J. V., Nealey, P. F., & Murphy, C. J. (2010). Nanoscale topography-induced modulation of fundamental cell behaviors of rabbit corneal keratocytes, fibroblasts, and myofibroblasts. *Investigative Ophthalmology and Visual Science*. <https://doi.org/10.1167/iovs.09-4074>

- Puig-De-Morales, M., Grabulosa, M., Alcaraz, J., Mullol, J., Maksym, G. N., Fredberg, J. J., & Navajas, D. (2001). Measurement of cell microrheology by magnetic twisting cytometry with frequency domain demodulation. *Journal of Applied Physiology*. <https://doi.org/10.1152/jappl.2001.91.3.1152>
- Qian, J., Liu, H., Lin, Y., Chen, W., & Gao, H. (2013). A Mechanochemical Model of Cell Reorientation on Substrates under Cyclic Stretch. *PLoS ONE*, 8(6). <https://doi.org/10.1371/journal.pone.0065864>
- Ragaert, K., Cardon, L., De Baere, I., & Degrieck, J. (2014). Bulk Mechanical Properties of Thermoplastic PCL. *6th Polymers & Moulds Innovations Conference*.
- Reina-Romo, E., Gómez-Benito, M. J., García-Aznar, J. M., Domínguez, J., & Doblaré, M. (2009). Modeling distraction osteogenesis: Analysis of the distraction rate. *Biomechanics and Modeling in Mechanobiology*. <https://doi.org/10.1007/s10237-008-0138-x>
- Roca-Cusachs, P., Alcaraz, J., Sunyer, R., Samitier, J., Farré, R., & Navajas, D. (2008). Micropatterning of single endothelial cell shape reveals a tight coupling between nuclear volume in G1 and proliferation. *Biophysical Journal*. <https://doi.org/10.1529/biophysj.107.116863>
- Rognoni, L., Stigler, J., Pelz, B., Ylänné, J., & Rief, M. (2012). Dynamic force sensing of filamin revealed in single-molecule experiments. *Proceedings of the National Academy of Sciences of the United States of America*. <https://doi.org/10.1073/pnas.1211274109>
- Rosenzweig, D. H., Carelli, E., Steffen, T., Jarzem, P., & Haglund, L. (2015). 3D-printed ABS and PLA scaffolds for cartilage and nucleus pulposus tissue regeneration. *International Journal of Molecular Sciences*. <https://doi.org/10.3390/ijms160715118>
- Rowe, N. M., Mehrara, B. J., Dudziak, M. E., Steinbreck, D. S., Mackool, R. J., Gittes, G. K., McCarthy, J. G., & Longaker, M. T. (1998). Rat mandibular distraction osteogenesis: Part I. Histologic and radiographic analysis. *Plastic and Reconstructive Surgery*. <https://doi.org/10.1097/00006534-199811000-00033>
- Sacks, M. S., David Merryman, W., & Schmidt, D. E. (2009). On the biomechanics of heart valve function. In *Journal of Biomechanics*. <https://doi.org/10.1016/j.jbiomech.2009.05.015>
- Safinia, L., Wilson, K., Mantalaris, A., & Bismarck, A. (2007). Atmospheric plasma treatment of porous polymer constructs for tissue engineering applications. *Macromolecular Bioscience*. <https://doi.org/10.1002/mabi.200600175>
- Sarkar, S., Isenberg, B. C., Hodis, E., Leach, J. B., Desai, T. A., & Wong, J. Y. (2008). Fabrication of a layered microstructured polycaprolactone construct for 3-D tissue engineering. *Journal of Biomaterials Science, Polymer Edition*.

<https://doi.org/10.1163/156856208786052371>

- Saunders, M. M., Simmerman, L. A., Reed, G. L., Sharkey, N. A., & Taylor, A. F. (2010). Biomimetic bone mechanotransduction modeling in neonatal rat femur organ cultures: Structural verification of proof of concept. *Biomechanics and Modeling in Mechanobiology*. <https://doi.org/10.1007/s10237-010-0195-9>
- Schindelin, J., Arganda-Carreras, I., Frise, E., Kaynig, V., Longair, M., Pietzsch, T., Preibisch, S., Rueden, C., Saalfeld, S., Schmid, B., Tinevez, J. Y., White, D. J., Hartenstein, V., Eliceiri, K., Tomancak, P., & Cardona, A. (2012). Fiji: An open-source platform for biological-image analysis. In *Nature Methods*. <https://doi.org/10.1038/nmeth.2019>
- SCHIRRER, R. (2001). Damage Mechanisms in Amorphous Glassy Polymers: Crazing. In *Handbook of Materials Behavior Models*. <https://doi.org/10.1016/b978-012443341-0/50055-7>
- Schlunck, G., Han, H., Wecker, T., Kampik, D., Meyer-ter-Vehn, T., & Grehn, F. (2008). Substrate rigidity modulates cell-matrix interactions and protein expression in human trabecular meshwork cells. *Investigative Ophthalmology and Visual Science*. <https://doi.org/10.1167/iovs.07-0956>
- Schmelzer, J., Möller, J., Gutzow, I., Pascova, R., Müller, R., & Pannhorst, W. (1995). Surface energy and structure effects on surface crystallization. *Journal of Non-Crystalline Solids*. [https://doi.org/10.1016/0022-3093\(94\)00643-1](https://doi.org/10.1016/0022-3093(94)00643-1)
- Schultz, J. M. (2001). Polymer Crystallization: The Development of Crystalline Order in Thermoplastic Polymers. In *Processing of Polymers*. <https://doi.org/10.1021/ja015359h>
- Shen, H., Hu, X., Yang, F., Bei, J., & Wang, S. (2007). Combining oxygen plasma treatment with anchorage of cationized gelatin for enhancing cell affinity of poly(lactide-co-glycolide). *Biomaterials*. <https://doi.org/10.1016/j.biomaterials.2007.06.004>
- Shen, N., Knopf, A., Westendorf, C., Kraushaar, U., Riedl, J., Bauer, H., Pöschel, S., Layland, S. L., Holeiter, M., Knolle, S., Brauchle, E., Nsair, A., Hinderer, S., & Schenke-Layland, K. (2017). Steps toward Maturation of Embryonic Stem Cell-Derived Cardiomyocytes by Defined Physical Signals. *Stem Cell Reports*. <https://doi.org/10.1016/j.stemcr.2017.04.021>
- Shen, Z. L., Dodge, M. R., Kahn, H., Ballarini, R., & Eppell, S. J. (2008). Stress-strain experiments on individual collagen fibrils. *Biophysical Journal*. <https://doi.org/10.1529/biophysj.107.124602>
- Shimizu, K., Shunori, A., Morimoto, K., Hashida, M., & Konishi, S. (2011). Development of a biochip with serially connected pneumatic balloons for cell-stretching culture. *Sensors and Actuators, B: Chemical*. <https://doi.org/10.1016/j.snb.2011.04.048>

- Sochol, R. D., Higa, A. T., Janairo, R. R. R., Li, S., & Lin, L. (2011). Unidirectional mechanical cellular stimuli via micropost array gradients. *Soft Matter*. <https://doi.org/10.1039/c1sm05163f>
- Strobl, G. (2007). The physics of polymers: Concepts for understanding their structures and behavior. In *The Physics of Polymers: Concepts for Understanding Their Structures and Behavior*. <https://doi.org/10.1007/978-3-540-68411-4>
- Strong, M., Hruska, J., Czyrny, J., Heffner, R., Brody, A., & Wong-Chung, J. (1994). Nerve palsy During Femoral lengthening: MRI, Electrical, and Histologic Findings in the central and peripheral Nervous systems—a Canine Model. *Journal of Pediatric Orthopaedics*. <https://doi.org/10.1097/01241398-199405000-00014>
- Teixeira, A. I., Nealey, P. F., & Murphy, C. J. (2004). Responses of human keratocytes to micro- and nanostructured substrates. *Journal of Biomedical Materials Research - Part A*. <https://doi.org/10.1002/jbm.a.30089>
- Thomas, P., Pranatharthi, A., Ross, C., & Srivastava, S. (2019). RhoC: a fascinating journey from a cytoskeletal organizer to a Cancer stem cell therapeutic target. In *Journal of experimental & clinical cancer research : CR*. <https://doi.org/10.1186/s13046-019-1327-4>
- Turnbull, D. (1950). Formation of crystal nuclei in liquid metals. *Journal of Applied Physics*. <https://doi.org/10.1063/1.1699435>
- Tzvetkova-Chevolleau, T., Stéphanou, A., Fuard, D., Ohayon, J., Schiavone, P., & Tracqui, P. (2008). The motility of normal and cancer cells in response to the combined influence of the substrate rigidity and anisotropic microstructure. *Biomaterials*. <https://doi.org/10.1016/j.biomaterials.2007.12.016>
- Urbanczyk, M., Layland, S. L., & Schenke-Layland, K. (2019). The role of extracellular matrix in biomechanics and its impact on bioengineering of cells and 3D tissues. In *Matrix Biology*. <https://doi.org/10.1016/j.matbio.2019.11.005>
- Usami, S., Chen, H. H., Zhao, Y., Chien, S., & Skalak, R. (1993). Design and construction of a linear shear stress flow chamber. *Annals of Biomedical Engineering*. <https://doi.org/10.1007/BF02368167>
- Uto, K., Ebara, M., & Aoyagi, T. (2014). Temperature-responsive poly( $\epsilon$ -caprolactone) cell culture platform with dynamically tunable nano-roughness and elasticity for control of myoblast morphology. *International Journal of Molecular Sciences*. <https://doi.org/10.3390/ijms15011511>
- Van der Giessen, W. J., Lincoff, A. M., Schwartz, R. S., Van Beusekom, H. M. M., Serruys, P. W., Holmes, D. R., Ellis, S. G., & Topol, E. J. (1996). Marked inflammatory sequelae to implantation of biodegradable and nonbiodegradable polymers in porcine coronary arteries. *Circulation*.

<https://doi.org/10.1161/01.CIR.94.7.1690>

- Vartiainen, M. K., Guettler, S., Larijani, B., & Treisman, R. (2007). Nuclear actin regulates dynamic subcellular localization and activity of the SRF cofactor MAL. *Science*, *316*(5832), 1749–1752.  
<https://doi.org/10.1126/science.1141084>
- Velasquez, L. S., Sutherland, L. B., Liu, Z., Grinnell, F., Kamm, K. E., Schneider, J. W., Olson, E. N., & Small, E. M. (2013). Activation of MRTF-A-dependent gene expression with a small molecule promotes myofibroblast differentiation and wound healing. *Proceedings of the National Academy of Sciences of the United States of America*, *110*, 16850–16855.  
<https://doi.org/10.1073/pnas.1316764110>
- Verderame, M., Alcorta, D., Egnor, M., Smith, K., & Pollack, R. (1980). Cytoskeletal F-actin patterns quantitated with fluorescein isothiocyanate-phalloidin in normal and transformed cells. *Proceedings of the National Academy of Sciences of the United States of America*.  
<https://doi.org/10.1073/pnas.77.11.6624>
- Versaevel, M., Grevesse, T., & Gabriele, S. (2012). Spatial coordination between cell and nuclear shape within micropatterned endothelial cells. *Nature Communications*. <https://doi.org/10.1038/ncomms1668>
- Vogler, E. A. (1998). Structure and reactivity of water at biomaterial surfaces. *Advances in Colloid and Interface Science*. [https://doi.org/10.1016/S0001-8686\(97\)00040-7](https://doi.org/10.1016/S0001-8686(97)00040-7)
- Wagner, J. R., Mount, E. M., & Giles, H. F. (2014). Polymer Structure. In *Extrusion*. <https://doi.org/10.1016/b978-1-4377-3481-2.00019-3>
- Walboomers, X. F., Ginsel, L. A., & Jansen, J. A. (2000). Early spreading events of fibroblasts on microgrooved substrates. *Journal of Biomedical Materials Research*. [https://doi.org/10.1002/1097-4636\(20000905\)51:3<529::AID-JBM30>3.0.CO;2-R](https://doi.org/10.1002/1097-4636(20000905)51:3<529::AID-JBM30>3.0.CO;2-R)
- Wan, Y., Qu, X., Lu, J., Zhu, C., Wan, L., Yang, J., Bei, J., & Wang, S. (2004). Characterization of surface property of poly(lactide-co-glycolide) after oxygen plasma treatment. *Biomaterials*.  
<https://doi.org/10.1016/j.biomaterials.2003.11.051>
- Wang, H., Ip, W., Boissy, R., & Grood, E. S. (1995). Cell orientation response to cyclically deformed substrates: Experimental validation of a cell model. *Journal of Biomechanics*. [https://doi.org/10.1016/0021-9290\(95\)00101-8](https://doi.org/10.1016/0021-9290(95)00101-8)
- Wang, J. H. C., Yang, G., & Li, Z. (2005). Controlling cell responses to cyclic mechanical stretching. *Annals of Biomedical Engineering*.  
<https://doi.org/10.1007/s10439-005-1736-8>
- Wang, J. H. C., Yang, G., Li, Z., & Shen, W. (2004a). Fibroblast responses to

cyclic mechanical stretching depend on cell orientation to the stretching direction. *Journal of Biomechanics*, 37(4), 573–576.  
<https://doi.org/10.1016/j.jbiomech.2003.09.011>

Wang, J. H. C., Yang, G., Li, Z., & Shen, W. (2004b). Fibroblast responses to cyclic mechanical stretching depend on cell orientation to the stretching direction. *Journal of Biomechanics*.  
<https://doi.org/10.1016/j.jbiomech.2003.09.011>

Wang, Y. C., Tang, Z. M., Feng, Z. Q., Xie, Z. Y., & Gu, Z. Z. (2010). Stretched inverse opal colloid crystal substrates-induced orientation of fibroblast. *Biomedical Materials*, 5(3), 35011. <https://doi.org/10.1088/1748-6041/5/3/035011>

Wang, Z. Y., Teoh, S. H., Johana, N. B., Khoon Chong, M. S., Teo, E. Y., Hong, M. H., Yen Chan, J. K., & San Thian, E. (2014). Enhancing mesenchymal stem cell response using uniaxially stretched poly( $\epsilon$ -caprolactone) film micropatterns for vascular tissue engineering application. *Journal of Materials Chemistry B*. <https://doi.org/10.1039/c4tb00522h>

Washburn, N. R., Yamada, K. M., Simon, C. G., Kennedy, S. B., & Amis, E. J. (2004). High-throughput investigation of osteoblast response to polymer crystallinity: Influence of nanometer-scale roughness on proliferation. *Biomaterials*. <https://doi.org/10.1016/j.biomaterials.2003.08.043>

Wilhelmi, B. J., Blackwell, S. J., Mancoll, J. S., & Phillips, L. G. (1998). Creep vs. stretch: A review of the viscoelastic properties of skin. *Annals of Plastic Surgery*. <https://doi.org/10.1097/00000637-199808000-00019>

Wunderlich, B., & Mehta, A. K. (1974). Macromolecular nucleation. *Journal of Polymer Science: Polymer Physics Edition*.  
<https://doi.org/10.1002/pol.1974.180120203>

Yildirim, E. D., Ayan, H., Vasilets, V. N., Fridman, A., Guceri, S., & Sun, W. (2008). Effect of dielectric barrier discharge plasma on the attachment and proliferation of osteoblasts cultured over poly( $\epsilon$ -caprolactone) scaffolds. *Plasma Processes and Polymers*. <https://doi.org/10.1002/ppap.200700041>

Zhong, C., Chrzanowska-Wodnicka, M., Brown, J., Shaub, A., Belkin, A. M., & Burridge, K. (1998). Rho-mediated contractility exposes a cryptic site in fibronectin and induces fibronectin matrix assembly. *Journal of Cell Biology*.  
<https://doi.org/10.1083/jcb.141.2.539>